

The Deformation Capacity of Lap Splices in RC Walls: From Experimental Testing to Numerical Modelling

Thèse N° 9432

Présentée le 3 mai 2019

à la Faculté de l'environnement naturel, architectural et construit
Laboratoire du génie parasismique et dynamique des structures
Programme doctoral en génie civil et environnement

pour l'obtention du grade de Docteur ès Sciences

par

Danilo TARQUINI

Acceptée sur proposition du jury

Dr A. Vassilopoulos, président du jury
Prof. K. Beyer, Dr J. Saraiva Esteves Pacheco de Almeida, directeurs de thèse
Prof. B. Stojadinovic, rapporteur
Prof. L. Lowes, rapporteuse
Prof. A. Muttoni, rapporteur

2019

To my family...
...and to Vale

Preface

Reinforced concrete walls—either in buildings or as wall-type piers in bridges—are often tied to the foundation by means of starter bars, which are anchored in the foundation and spliced with the longitudinal wall reinforcement. Under seismic loading, plastic deformations concentrate at the base of the wall and therefore in the region of the lap splices. Poorly confined or short lap splices are known to limit the force transfer between the spliced bars and a large body of literature studied the parameters of splice configurations that influence the force transfer and developed models for estimating the maximum force that can be transferred. The seismic performance of structural elements with lap splices in plastic zones depends, however, not only on the force capacity but also on the deformation capacity of the lap splice and very little is known on the latter.

With his thesis, Danilo Tarquini provides new experimental evidence and models of the deformation capacity of lap splices subjected to monotonic and cyclic loading. Danilo Tarquini tested 24 axially loaded members with and without lap splices of various lengths and with different confinements, subjected to a range of loading histories. The test units were heavily instrumented, using optical measurements to determine the deformations along the element but also the slip between bars and concrete. From this data, Danilo Tarquini derived new deformation limits of lap splices. He extended the existing tension-chord model to axial members with lap splices, reproducing very well the experimentally observed force-displacement response as well as the crack width distribution along the member. To valorize fully the improved deformation capacity limits for lap splices when analyzing reinforced concrete elements, finite element models are required that estimate reliably the deformation demand in the lap splice region. For this purpose, Danilo Tarquini developed a displacement-based beam element but enforces axial equilibrium at the integration points. This results in a more realistic curvature profile and therefore in better estimates of strain demands.

With his experimental, numerical and analytical work, Danilo Tarquini advanced our understanding of the deformation capacity of lap splices under cyclic loading. By making all his research results including the experimental data and numerical models openly available, he facilitates and encourages future research on this challenging topic.

Lausanne, April 2019

Prof. Dr. Katrin Beyer

Prof. Dr. João Pacheco de Almeida

Funding

The Swiss Federal Roads Office (FEDRO) under the project AGB 2015/002 “Modelling the Seismic Response of RC Bridge Piers with Lap Splices in the Plastic Hinge Region” supported the work presented in this thesis. The content of the thesis does not necessarily reflect the position of FEDRO.

Acknowledgements

First off, I would like to thank Prof. Katrin Beyer, which gave me the opportunity of carrying out the present research project and supervised me all along the way. Your hard work and dedication have been a true inspiration to me, definitely contributing to my personal and professional growth. I wish that the EESD laboratory continues to thrive under your management. A huge thank you goes then to my co-supervisor, freshly assistant professor João Saraiva Esteves Pacheco Almeida. The fact that I remember by heart all your names says already a lot on the time that we've spent together. Or better, that you spent correcting my Itanglish, teaching me the fundamentals of beam theory, introducing me to the nonlinear analysis of structures, reviewing my manuscripts and listening to all sorts of ravings from my side. I apologize for not having heled you with your Italian, but there is no hope for that. I wish you all the best for the continuation of your academic career and, above all, I wish you to find some time to go swimming.

I would like to thank the members of my thesis jury: Dr. Anastasios Vassilopoulos (president) and Prof. Aurelio Muttoni from EPFL, Prof. Laura Lowes from University of Washington and Professor Bozidar Stojadinovic from ETH Zurich. I was honoured by your interest in my work and grateful for the insightful comments and the overall positive assessment.

A hearthfelt thank is for our laboratory secretary Yvonne, for her extreme competence, ability of solving problems and for organizing all events to which I participated over the last four years, from dinners to skidays to conference stayings.

Grateful appreciation goes to the laboratory technicians for the help that they provided during my lab work, as well as for the fun moments that we shared over the several skidays or bbqs organized by the lab. Merci Armin, Gerald, Sylvain, Serge, Gilles and Frederique.

Thank to my previous colleagues at the EESD laboratory of EPFL with whom I shared part of this path and which are now all succesfull engineers; in chronological order from their departure, we have: Pia, Sarah, Alessandro, Raluca, Angelica. A big thank goes also to the studenst I supervides and that helped me in the lab: first and foremost Tiagu and Maria, then Cristiano, Emanuele, Marlene, Pierre and Celine

A big thank goes to my current office-mates. Starting from the crocodile-dundee-pink-yoghurt eater Ryan, thanks m8 for being such a nice and fun person and for having agreed in proofreading part of my work (I definitely got lazier knowing that I had a native/slang speaker in the office). I will miss the Friday afternoon beers routine. Then Francesco, companion of (among others) several life-threatening hikes, skidays, via ferrata and unfortunate trips to San Siro. It was a pleasure sharing the office with you and having the possibility, between a numerical and mechanical model, to discuss about science, politics, mountains and our true passion: Inter.

More broadly, I would like to thank all my current labmates at EESD, from the students Aaron, Paolo, Giuseppe, Serena and Ayoub to the PhDs Igor, Ennio, Amir, Mahmoud, to the postdocs Bastian, Shenghan and Michele. We shared many moments together, from lunches to coffee brakes to dinners and they will be definitely part of my happy memories. Additionally, I would also like to thank the Ibetonians Raffaele, Francesco, Darko, Patrick and Max which never failed to help when I needed it, either in the lab or in the office for some tension chord related questions.

During these years in Lausanne I met some truly amazing people which I was honoured to share time with and with whom I hope to remain friend for long time ahead: Fabio, Alepap, il Tasso, il Bosio, il Tondo, Cantun e Victor, all members of the the Italian MontagnaCuloRoto group. Moreover, in this period, I developed a true passion for rockclimbing, and I want to thank my ropemate Davide for have caught me in the few fall I dare to take and Seb for having showed me the way of bouldering outdoor.

One downside of Lausanne was being away from my family, which I love and which is the main reason I manged to get this far. Mom, Dad, Sister, Granpa, Grandmas and Uncles, I will never be able to tell you how important you are, but you are, a lot. A huge thank is also for Rossella and Valeria, which sweetened a couple of Swiss Christmas and for my childhood friends (Fras, Rob, Mosk, Cip, Nash, Trek, Beato te...), which always welcomed me home and made me all the time leave Montappone with a heavy hearth.

Finally yet most importantly, my Vale...your incredible smile makes every day a happy day. I love you like no other.

Lausanne, le 6 mars 2019

Danilo Tarquini

Ringraziamenti

Innanzitutto vorrei ringraziare la prof.ssa Katrin Beyer, che mi ha dato l'opportunità di portare a termine questo progetto di ricerca e mi ha costantemente supervisionato per gli ultimi quattro anni. Il tuo duro lavoro e la tua dedizione sono stati una vera fonte di ispirazione per me, contribuendo sicuramente alla mia crescita personale e professionale. Mi auguro che il laboratorio EESD continui a prosperare sotto la tua gestione. Un enorme ringraziamento va poi al mio co-supervisore, da poco promosso assistente professore, João Saraiva Esteves Pacheco Almeida. Il fatto che io ricordi a memoria tutti i tuoi nomi dice già molto sul tempo che abbiamo trascorso insieme. O meglio, sul tempo che hai passato a correggere il mio Englino, ad insegnarmi i fondamenti della teoria degli elementi finiti, ad aiutarmi con l'analisi delle strutture non lineari, a rivedere i miei papers e ad ascoltare ogni sorta di deliri che hanno attraversato la mia mente. Mi scuso per non esserti stato d'aiuto con il tuo italiano, ma non credo ci sia speranza per questo. Ti auguro il meglio per la continuazione della tua carriera accademica e, soprattutto, ti auguro di trovare un po' di tempo per nuotare.

Vorrei ringraziare i membri della giuria di tesi: Dott. Anastasios Vassilopoulos (presidente) e Prof. Aurelio Muttoni dell'EPFL, Prof.ssa Laura Lowes dell'Università di Washington e Prof. Bozidar Stojadinovic dell'ETHZ. Il vostro interesse per il mio lavoro di tesi è stato enormemente apprezzato e vi ringrazio per i commenti e la valutazione positiva.

Un sentito ringraziamento va alla segretaria del nostro laboratorio Yvonne, per la sua estrema competenza, capacità di risolvere problemi e per l'organizzazione di tutti gli eventi a cui ho partecipato negli ultimi quattro anni, dalle cene agli skidays, alle conferenze.

Grato apprezzamento va ai tecnici per l'aiuto che hanno fornito durante il mio lavoro di laboratorio, così come per i momenti divertenti che abbiamo condiviso nel corso dei numerosi skidays o bbq organizzati dall'EESD. Merci Armin, Gerald, Sylvain, Serge, Gilles e Frederique.

Grazie ai miei precedenti colleghi del laboratorio EESD con cui ho condiviso parte di questo percorso e che ora sono tutti ingegneri di successo; in ordine cronologico dalla loro partenza, abbiamo: Pia, Sarah, Alessandro, Raluca, Angelica. Un grande ringraziamento va anche agli studenti che ho supervisionato e che mi hanno aiutato in laboratorio: Tiagu e Maria in primis, poi Cristiano, Emanuele, Marlene, Pierre e Celine

Un grande ringraziamento va ai miei attuali compagni di ufficio. A partire dal crocodile-dundee-mangiatore-di-yogurt-rosa Ryan, grazie m8 per la tua simpatia e per aver riletto parte del mio lavoro (sono decisamente diventato più pigro sapendo di avere un madrelingua in ufficio). Mi mancherà la routine delle birre del venerdì pomeriggio. Poi Francesco, compagno di (tra gli altri) numerosi trekking, skidays, vie ferrate e sfortunati viaggi a San Siro. È stato un piacere condividere l'ufficio con te e avere la possibilità, tra un modello numerico e meccanico, di discutere di scienza, politica, montagna così come della nostra vera passione: l'Inter.

Più in generale, vorrei ringraziare tutti i miei attuali colleghi dell'EESD, dagli studenti Aaron, Paolo, Giuseppe, Serena e Ayoub ai dottorandi Igor, Ennio, Amir, Mahmoud, ai postdoc Bastian, Shenghan e Michele. Abbiamo condiviso molti momenti insieme, dai pranzi alle pause caffè alle cene, che rimarranno sempre parte delle mie memorie felici. Inoltre, vorrei anche ringraziare gli Ibetonians Raffaele, Francesco, Darko, Patrick e Max che sono stati sempre disponibili per dare una mano, sia in laboratorio che in ufficio per alcune domande legate al tension chord.

Durante questi anni a Losanna ho incontrato persone davvero fantastiche con le quali spero di rimanere amico per molto tempo: Fabio, Alepap, il Tasso, il Bosio, il Tondo, Cantun e Victor, tutti membri del gruppo italiano MontagnaCuloRoto. Inoltre, in questo periodo, ho sviluppato una vera passione per il climbing, e voglio ringraziare il mio compagno di corda Davide per avermi ripreso nelle poche volte che ho osato cadere e Seb per avermi mostrato la via del bouldering all'aperto.

Uno svantaggio di Losanna è stato l'allontanarmi dalla mia famiglia, che adoro e che è il motivo principale che mi ha spinto ad arrivare così lontano. Mamma, papà, Debby, nonno, nonne e zii, non sarò mai in grado di dirvi quanto siete importanti, ma lo siete, e molto. Un grande ringraziamento va anche a Rossella e Valeria, che hanno addolcito un paio di natali svizzeri e per i miei amici d'infanzia (Fras, Rob, Mosk, Cip, Nash, Trek, Beato te ...), che rendono ogni mio ritorno a casa un periodo felice e mi fanno sempre lasciare Montappone col cuore pesante.

Ultimo ma non per importanza, mia Vale ... il tuo sorriso incredibile rende ogni giorno un giorno speciale. Ti amo come nessun altro.

Lausanne, le 6 mars 2019

Danilo Tarquini

Abstract

Field observations as well as experimental tests have shown that both the strength and displacement capacity of reinforced concrete (RC) members might be significantly reduced by the presence of lap splices. This degradation applies in particular if the longitudinal reinforcement is spliced in regions where inelastic deformations concentrate, which is frequently the case for RC building walls or bridge piers. In fact, these members often feature lap splices above the foundation level, where seismic demands are largest and damage is likely to occur.

In performance-based earthquake engineering (PBEE), which now sets the standards for seismic assessment, deformation rather than force capacities are compared to the demand; however, past experimental studies on spliced members have focused on the characterization of the strength rather than the deformation capacity of lap splices. Furthermore, these tests were primarily performed on spliced RC beam and column specimens, typically subjected to monotonic loading. Experimental investigations on the deformation capacity of members with lap splices under cyclic loading are underrepresented. This applies in particular to walls, despite the fact that splicing of longitudinal reinforcement in their plastic hinge regions is common construction practice. In line with the available experimental work, most of the developed empirical and analytical expressions aim solely at quantifying the force capacity of lap splices.

The preceding observations have motivated the following objectives of the present work: (i) investigate the displacement capacity of spliced RC walls through experimental tests; (ii) propose expressions characterizing the deformation capacity of lap splices subjected to monotonic and cyclic loading; and (iii) develop numerical and mechanical models suitable for practicing engineers to simulate the behaviour of RC members with lap splices.

Existing experimental programmes on spliced RC walls, including the cyclic test of two units recently carried out at the structural laboratory of the École Polytechnique Fédérale de Lausanne (EPFL), are first reviewed, organized and collected in a database. The review of the experimental data shows that the failure of the outermost lap splices, located in the boundary element, typically triggers the failure of the RC wall. Moreover, the main parameters influencing the deformation capacity of lap splices are identified, corresponding to the confining reinforcement ratio and the ratio of shear span to lap splice length. Building on these findings, an experimental programme on spliced RC wall boundary elements is designed using lap-splice length, confining reinforcement, and loading history as variable parameters. From the obtained results, an empirical expression for the lap-splice strain capacity is derived.

The presence of lap splices is typically simulated with finite elements through complex bond-slip interface models where local bond-slip laws are generally adjusted from pull-out tests on anchored rebars. In this work, a 2D shell element model is first developed to simulate the global force-displacement response of the walls in the aforementioned database. The lap splice response is considered through a new equivalent uniaxial steel stress-strain law, therefore bypassing the need for interface bond-slip elements. Secondly, an axially equilibrated displacement-based beam element model is proposed, which indirectly accounts for tension shift effects in RC structures. This element maintains the simplicity of beam formulations and improves the simulation of local-level quantities in RC members, which are better related to structural damage. The lap splice response can be included by using the derived strain limit expression.

Finally, by utilizing the experimental data, a novel mechanical model describing the behaviour of spliced RC wall boundary elements is presented. The model extends the tension chord model by accounting for anchorage slip and the presence of lap splices. It allows the determination of the global force-displacement response of the boundary element and the crack distribution and width, as well as the concrete and steel stress and strain distributions along the structural member. The mechanical model also provides the steel stress and strain distribution of the pair of spliced rebars until lap splice failure.

Keywords: RC wall; Database; Boundary element; Lap splice; Deformation capacity; Experimental test; Shell element model; Constitutive law; Displacement-based beam element; Mechanical model; Tension chord.

Résumé

Les observations sur le terrain ainsi que les résultats expérimentaux ont montré que la résistance et la capacité de déformation des éléments en béton armé sont réduites de manière significative en présence de barres de recouvrement. Cette dégradation s'avère particulièrement importante si la barre de renforcement longitudinale est placée dans une zone où les déformations plastiques se concentrent. En effet, cela est fréquemment rencontré dans le cas des murs en béton armé ou des piles de pont. Ces derniers présentent des barres de recouvrement au-dessus du niveau de fondation où la demande sismique y est la plus élevée et où les dommages sont susceptibles de se produire.

Dans l'ingénierie sismique basée sur la performance (*performance-based*), entité qui énonce les articles de la norme qui traite de la vérification sismique, les déformations en terme de capacité plutôt que les forces en terme de résistance sont comparées à la demande. En revanche, les études expérimentales qui ont été réalisées par le passé se sont penchées sur la caractérisation de la résistance en termes de force plutôt qu'en termes de déformations des barres de recouvrement. De plus, la plupart des tests ont été réalisés sur des poutres et colonnes en béton armé, typiquement sujets à des chargements monotoniques. Ainsi, les investigations expérimentales qui traitent de la capacité de déformation des éléments avec des barres de recouvrement sous chargement cyclique sont sous-représentées. Cela s'applique particulièrement aux murs malgré le fait que le recouvrement des barres longitudinales dans leurs zones plastiques est une pratique courante. Le même défaut que ceux des résultats expérimentaux à disposition peut être retrouvé dans la littérature théorique. En effet, la plupart des modèles empiriques et expressions analytiques développés ont pour unique but de quantifier la capacité en termes de forces des barres de recouvrement.

Les observations présentées ci-dessus ont motivé les objectifs suivants du présent travail : (i) étude de la capacité de déformation des murs en béton armé avec barres de recouvrement par le biais de tests expérimentaux; (ii) proposition d'expressions caractérisant la capacité de déformation des barres de recouvrement sujettes à des chargements monotoniques et cycliques; et (iii) développement de modèles numériques et mécaniques adaptés pour les ingénieurs praticiens afin de simuler le comportement des éléments en béton armé avec barres de recouvrement.

Les programmes expérimentaux existants réalisés sur les murs en béton armé avec barres de recouvrement et les tests cycliques réalisés récemment dans le laboratoire de l'EPFL sont d'abord étudiés puis classés dans une base de données. L'étude des données expérimentales montre que la rupture des barres de recouvrement le plus à l'extérieur sur la frontière de l'élément provoque la rupture du mur en béton armé. De plus, les paramètres les plus importants contrôlant la capacité de déformation des barres de recouvrement sont identifiés: la proportion du confinement des armatures et le rapport de la longueur du moment nul sur la longueur des barres de recouvrement. Avec ces trouvailles, un programme expérimental sur les éléments aux bords des murs en béton armé avec barres de recouvrement a été défini en utilisant la longueur des barres de recouvrement, l'armature de confinement ainsi que l'historique du chargement comme paramètres variables. A partir des résultats obtenus, une expression traitant de la capacité de déformation des barres de recouvrement a été déduite.

En général, lorsque l'usage d'éléments finis est choisi pour la modélisation de barres de recouvrement, une loi d'interface adhérence-glissement est utilisée qui est normalement calibrée sur la base des tests d'arrachement des barres ancrées. Dans ce travail, d'abord une modélisation avec des éléments coque 2D est développée pour simuler la réponse globale force-déplacement des murs présents dans la base de données. La réponse des barres de recouvrement est prise en compte par l'intermédiaire d'une loi uni-axiale équivalente contrainte-déformation afin de contourner le besoin d'utiliser une interface adhérence-glissement. Ensuite, un élément poutre définie par la méthode cinématique (*displacement-based*) et équilibré axialement qui tient compte de l'effet du décalage en traction est proposé. Ce dernier permet de garder la simplicité de la formulation d'un élément poutre et en même temps, il améliore la simulation des quantités locales dans les éléments en béton armé, qui sont mieux liés aux dommages structuraux. La réponse des barres de recouvrement peut aussi être incluse par l'usage de l'expression dérivée qui tient compte de la limite de déformation.

Enfin, en utilisant les données expérimentales, un modèle mécanique nouveau qui décrit le comportement des éléments aux bords des murs en béton armé avec barres de recouvrement est présenté. Le modèle affine le modèle du tirant tendu en tenant compte de la longueur d'ancrage et de la présence des barres de recouvrement. Cela permet la détermination de la réponse globale force-déplacement des éléments aux bords, la distribution des fissures et leur ouverture, ainsi que la distribution des contraintes-déformations dans le béton et l'acier le long des éléments structuraux. Le modèle mécanique fournit également la distribution des contraintes-déformations dans l'acier des barres de recouvrement jusqu'à leurs ruptures.

Mots-clés: Mur en béton armé ; Élément de bord ; Barre de recouvrement ; Capacité de déformation ; Test expérimental; Modèle coque ; Loi constitutive ; Élément définie cinématiquement ; Modèle mécanique ; Modèle du tirant tendu.

Sommario

Ricognizioni in sito e test in laboratorio hanno dimostrato che la presenza di giunzioni per sovrapposizione di barre (*lap splice*) può ridurre in maniera significativa sia la forza massima che la capacità di spostamento di elementi strutturali in cemento armato. Ciò si verifica in particolar modo se la sovrapposizione delle barre viene effettuata in regioni dove possono concentrarsi le deformazioni plastiche, come spesso succede in muri e pile da ponte in cemento armato. In questi elementi strutturali infatti, l'armatura longitudinale è spesso sovrapposta immediatamente al di sopra del livello di fondazione, dove si verificano le massime le azioni sismiche e l'occorrenza di lesioni strutturali è più probabile.

Nel contesto dell'ingegneria sismica basata sulle prestazioni (*performance-based*), che attualmente rappresenta lo standard per la verifica sismica, sono gli spostamenti e non le forze resistenti ad essere confrontate con le azioni. Tuttavia, in passato, nella ricerca in materia di elementi strutturali con giunzioni per sovrapposizione di barre, si è data maggiore importanza alla caratterizzazione della loro forza massima che deformazione massima. Inoltre, la maggior parte dei test che si possono reperire in letteratura sono stati eseguiti su provini di tipo trave o colonna, per lo più sottoposti a carico monotono incrementale fino a rottura. Gli esperimenti su prove cicliche finalizzati alla valutazione della capacità di deformazione delle giunzioni per sovrapposizione di barre sono limitati; ciò vale in particolar modo per quel che riguarda test su pareti in cemento armato, nonostante la presenza di barre sovrapposte nella loro cerniera plastica sia comune pratica costruttiva. Analogamente alla controparte sperimentale, la maggioranza delle espressioni empiriche e analitiche disponibili sono volte alla quantificazione della massima forza resistente dei cosiddetti '*lap splices*' mentre la determinazione della loro capacità di spostamento viene per lo più ignorata.

Le osservazioni contenute nel paragrafo precedente hanno motivato gli obiettivi di questo lavoro di tesi che sono: (i) analizzare la capacità di spostamento di muri in cemento armato con giunzioni per sovrapposizione di barre nella zona plastica; (ii) proporre delle relazioni empiriche atte a quantificare la massima deformazione delle giunzioni per sovrapposizione di barre; e (iii) sviluppare dei modelli numerici ed analitici per simulare il comportamento di elementi strutturali con giunti per barre sovrapposte.

Inizialmente, i test esistenti su pareti in cemento armato con sovrapposizione di barre longitudinali sono stati selezionati e organizzati in un database. Due test recenti effettuati nel laboratorio strutturale dell'École Polytechnique Fédérale de Lausanne (EPFL) sono presentati. L'analisi dei dati sperimentali ha messo in luce che la rottura globale delle pareti viene innescata dalla rottura locale dei giunti collocati alle loro estremità, nei cosiddetti 'elementi di bordo' (*boundary elements*). Inoltre è stato possibile evidenziare i principali parametri che influenzano il massimo spostamento dei *lap splices*, e cioè il rapporto tra la lunghezza di sovrapposizione e il punto d'applicazione della forza equivalente orizzontale (*shear span*) e la quantità di armatura a confinamento. Sulla base di queste osservazioni, è stata progettata e portata a termine una serie di test su degli elementi di bordo di pareti in cemento armato. Le variabili sperimentali sono rappresentate dalla lunghezza di sovrapposizione delle barre longitudinali, la quantità di armatura trasversale e la storia di carico imposta. Dai risultati ottenuti è stata calibrata un'equazione per calcolare la massima deformazione dei giunti per sovrapposizione di barre.

La presenza di barre sovrapposte in elementi in cemento armato viene spesso simulata in modelli ad elementi finiti per mezzo di complessi elementi interfaccia; questi ultimi implementano delle leggi costitutive aderenza-scorrimento (*bond-slip*) che sono adattate da test pull-out su barre ancorate. Durante il presente lavoro di ricerca, è stato sviluppato un modello a elementi shell bidimensionali che permette di considerare l'effetto dei *lap splices* per mezzo di una innovativa legge costitutiva equivalente, di fatto bypassando l'uso di elementi interfaccia. Tale modello viene poi utilizzato con successo per simulare i risultati sperimentali dei muri nel database. In seguito, è sviluppato e proposto anche un nuovo modello di tipo trave che permette di catturare indirettamente gli effetti *tension shift*. Quest'ultimo, pur mantenendo la semplicità di un modello trave, permette di migliorare sensibilmente il calcolo di quantità locali come deformazioni e curvature, che meglio caratterizzano il danno strutturale. La presenza di giunti per sovrapposizione di barre vi può essere tenuta in conto per mezzo dell'espressione empirica discussa in precedenza.

Infine, sulla base dei risultati ottenuti in laboratorio, è presentato un modello meccanico che descrive il comportamento degli elementi di bordo di pareti in cemento armato. Esso rappresenta un'estensione del modello a tirante fessurato (*tension chord*) in quanto, rispetto a quest'ultimo, permette di prendere in considerazione lo scorrimento delle barre ancorate in fondazione così come la presenza dei giunti per sovrapposizione. Tramite questo modello è possibile calcolare la risposta globale (forza-spostamento) dell'elemento di bordo, la disposizione e apertura delle fessure e, infine, la distribuzione degli sforzi e deformazioni nel cemento e nell'acciaio lungo l'elemento strutturale; in particolare è possibile determinare sforzi e deformazioni nella coppia di barre formanti il giunto per sovrapposizione, fino alla sua rottura.

Parole chiave: Muri in cemento armato; Database; Elemento di bordo; Giunto per sovrapposizione di barre; Capacità di deformazione; Test di laboratorio; Modelli shell; Relazione costitutiva; Elemento trave basato sugli spostamenti; Modello meccanico; Modello di tirante fessurato.

Kurzfassung

Beobachtungen in der Praxis sowie Versuche haben gezeigt, dass sowohl die Kraft- als auch die Verformungs-Kapazität von Stahlbetonbauteilen signifikant durch vorhandene Übergreifungsstöße verringert werden kann. Diese Widerstands-Verringerung wird besonders schlagend, wenn der Übergreifungsstoß in Regionen von inelastischen Deformationen auftritt. Dies ist oft bei aussteifenden Stahlbetonwänden in Gebäuden sowie Brückenpfeilern der Fall. Tatsächlich werden diese Bauteile regelmäßig mit Übergreifungsstößen direkt über dem Fundament-Niveau, wo die stärksten seismischen Belastungen auftreten und daher die zu erwartenden Schäden am größten sind, konstruiert.

In der leistungs-basierten Bemessung auf Erdbeben (Performance-based Earthquake Engineering), die inzwischen der Standard für die seismische Bewertung von Bauwerken geworden ist, werden Verformungs- statt Kraft-Kapazitäten mit der Belastung verglichen. Jedoch haben sich bisherige experimentelle Untersuchungen auf die Charakterisierung der Kraft- anstelle der Verformungs-Kapazität konzentriert. Des Weiteren wurden diese Versuche vornehmlich auf monoton belasteten Träger- und Säulen-Elementen durchgeführt. Untersuchungen der Verformungs-Kapazität von zyklisch belasteten Bauteilen mit Übergreifungsstößen sind daher unterrepräsentiert. Dies gilt im Besonderen für Wände, obwohl hier das Stoßen der Längsbewehrung in der Region des plastischen Gelenks weit verbreitete Konstruktionspraxis ist. Wie für experimentelle Untersuchungen ist die Mehrzahl der entwickelten empirischen und analytischen Formulierungen einzig auf die Quantifizierung der Kraft-Kapazität ausgerichtet.

Die genannten Punkte repräsentieren die Motivation für die folgenden Ziele der vorliegenden Arbeit: (i) die experimentelle Untersuchung der Verformungs-Kapazität von Stahlbetonwänden mit Übergreifungsstößen; (ii) die Erarbeitung von Formulierungen, welche die Verformungs-Kapazität von Übergreifungsstößen unter monotonen und zyklischen Belastungen beschreiben; (iii) die Entwicklung von numerischen und mechanischen Modellen für Ingenieure in der Praxis zur Simulation des Verhaltens von Stahlbetonbauteilen mit Übergreifungsstößen.

Bereits durchgeführte Versuchsprogramme von Stahlbetonwänden mit Übergreifungsstößen, wie beispielsweise die zwei kürzlich im Versuchslabor der École polytechnique fédérale de Lausanne (EPFL) getesteten zyklischen Versuche, werden zuerst analysiert und in einer Datenbank zusammengestellt. Die Untersuchung der Versuchsdaten zeigt, dass das Versagen der äussersten Übergreifungsstöße im Randelement typischerweise das Versagen der Wand auslöst. Des Weiteren werden die die Verformungs-Kapazität am stärksten beeinflussenden Faktoren identifiziert. Dazu gehört der einschnürende Bewehrungsgehalt und das Verhältnis von Schub-Spannweite zu Übergreifungsstoß-Länge. Basierend auf diesen Erkenntnissen wird eine Versuchsreihe an Stahlbeton-Randelementen mit Übergreifungsstößen geplant, wobei die Übergreifungsstoß-Länge, der einschnürende Bewehrungsgehalt und die Lastgeschichte als Variable gewählt werden. Basierend auf den Resultaten wird eine empirische Gleichung für die Übergreifungsstoß-Dehnungskapazität hergeleitet.

Übergreifungsstöße werden typischerweise mit Finiten-Elementen durch komplexe Verbund-Gleit-Gesetze simuliert, die normalerweise durch lokale Ausziehversuche von verankerten Bewehrungsstäben angepasst wurden. In der vorliegenden Arbeit wird als erster Schritt ein 2D-Schalenelement zur Simulation des globalen Kraft-Verformungsverhaltens der Wände aus der oben- genannten Datenbank entwickelt. Der Einfluss des Übergreifungsstoßes wird durch ein neues äquivalentes uniaxiales Spannungs-Dehnungs-Gesetz des Stahles berücksichtigt. Dadurch kann auf Interface-Verbund-Gleit-Elemente verzichtet werden. Zweitens wird ein axial-ausgeglichenes verformungs-basiertes Balkenelement eingeführt, das indirekt Tension-Shift-Effekte in Stahlbetonbauteilen abbildet. Dieses Element zeichnet sich durch die Einfachheit eines Balkenelements aus, während es die Simulation von lokalen Größen, die bessere Indikatoren von strukturellen Schäden darstellen, verbessert. Der Einfluss von Übergreifungsstößen kann durch die Benutzung des hergeleiteten Ausdrucks für die Dehnungskapazität berücksichtigt werden.

Schlussendlich wird ein neues mechanisches Modell zur Beschreibung des Verhaltens von Stahlbeton-Randelementen mit Übergreifungsstößen unter Berücksichtigung der analysierten Versuchsdaten präsentiert. Es baut das Zuggurtmodell durch Berücksichtigung von Verankerungsschlupf und den Effekt von Übergreifungsstößen aus. Dies erlaubt die Bestimmung des globalen Kraft-Verformungsverhaltens des Randelements, der Rissverteilung und Breite sowie der Beton- und Stahldehnungen und Spannungsverteilungen entlang des Bauteiles. Das mechanische Modell beschreibt außerdem die Stahldehnungs- und Spannungsverteilung des Paares gestoßener Bewehrungsstäbe bis zum Versagen des Übergreifungsstoßes.

Schlüsselwörter: Stahlbetonwand; Randelement; Übergreifungsstoß; Dehnungskapazität; Versuch; Schalenelement-Modell; konstitutives Gesetz; verformungs-basiertes Balkenelement; mechanisches Modell; Zuggurt.

Table of Contents

Preface	v
Funding.....	vii
Acknowledgements.....	ix
Ringraziamenti	xi
Abstract	xiii
Résumé.....	xv
Sommario	xvii
Kurzfassung	xix
Table of Contents.....	xxi
Introduction	25
1.1 Background and motivation	25
1.2 State of the art.....	26
1.3 Problem statement and research objectives	27
1.4 Methodology.....	28
1.5 Thesis layout.....	28
2 Reinforced Concrete Walls with Lap Splices: State of the Art, New Tests and Database Assembly	31
Abstract	31
2.1 Introduction	31
2.2 Review of field and experimental observations	32
2.2.1 Post-earthquake field observations.....	32
2.2.2 Past cyclic experimental tests on members with lap splices.....	33
2.3 New experimental tests on walls.....	38
2.3.1 Hysteretic behaviour and influence of lap splices	39
2.4 Inelastic cyclic response of lap splices in walls loaded in plane.....	42
2.4.1 Influence of lap splices on cyclic wall performance from tests and field observations.....	42
2.4.2 Factors affecting lap splice strength and strain at degradation onset	43
2.5 Conclusions	47
2.6 Acknowledgments	47
3 Equivalent Uniaxial Lap Splice Constitutive Law for the Simulation of Spliced RC Walls	49
Abstract	49
3.1 Introduction	49
3.2 State-of-the-art models for lap splice behaviour	50
3.2.1 Lap splice strength: literature review and application to wall database.....	50
3.2.2 Deformation capacity of lap splices	52

TABLE OF CONTENTS

3.2.3	Plastic hinge models for members with lap splices	52
3.2.4	Finite element simulations of members with lap splices	53
3.3	Detailed finite element models for response of walls with lap splices	53
3.3.1	Description of nonlinear shell models.....	53
3.3.2	Local-level validation of the shell element model up to the onset of lap splice degradation	54
3.3.3	Modelling lap splices as double reinforcement.....	57
3.4	Development of a simplified constitutive model for lap splices	59
3.4.1	Background and assumptions for development of equivalent uniaxial steel model	59
3.4.2	Lap splice strength	60
3.4.3	Strain at onset of strength degradation.....	61
3.5	Validation of model against wall database	64
3.6	Conclusions	67
3.7	Acknowledgments	68
4	An Enhanced Beam Element Model to Account for Tension Shift Effects in Reinforced Concrete	69
	Abstract	69
4.1	Introduction	69
4.2	Axially equilibrated displacement-based element: formulation and state determination.....	71
4.2.1	Axial equilibrium	72
4.2.2	Element state determination	74
4.2.3	Axially equilibrated vs classical DB element	75
4.3	Validation examples.....	78
4.3.1	Tests on RC bridge piers	78
4.3.2	Tests on RC structural walls.....	84
4.3.3	Limitations	87
4.4	Conclusions	88
4.5	Acknowledgements	88
5	Uniaxial Cyclic Tests on RC Wall Boundary Elements with Lap Splices.....	89
	Abstract	89
5.1	Introduction	89
5.2	Description of the test units	90
5.2.1	Geometry and reinforcement layout.....	90
5.2.2	Material properties.....	91
5.3	Test Setup, loading protocol and instrumentation.....	92
5.3.1	Test setup	92
5.3.2	Loading protocol.....	93
5.3.3	Instrumentation	94
5.4	Test observations.....	95

TABLE OF CONTENTS

5.4.1	Pre-failure behaviour	95
5.4.2	Observed failure modes	96
5.5	Organization of test data	101
5.5.1	LAP_P(i)/Lap_C(i) folders.....	101
5.6	Post-processed data and example plots.....	103
5.7	Summary.....	104
5.8	Acknowledgments	104
6	Evaluating the Ultimate Deformation Capacity of Lap Splices under Cyclic Loading.....	105
	Abstract	105
6.1	Introduction	105
6.2	Experimental tests on RC members with lap splices: literature review.....	106
6.3	New experimental programme on RC members with lap splices	107
6.3.1	Test setup, units, and loading	107
6.3.2	Experimental observations	109
6.4	Discussion of the experimental results	111
6.4.1	Definition of the average lap splice strain capacity	111
6.4.2	Influence of variable test parameters on the average strain capacity of lap splices.....	112
6.5	Prediction of the lap splice strain capacity	117
6.6	Conclusions	120
6.7	Acknowledgments	120
7	Mechanical Model for the Simulation of RC Wall Boundary Elements with Lap Splices	121
	Abstract	121
	List of symbols.....	121
7.1	Introduction	122
7.2	Tension chord model.....	123
7.2.1	Evolution of deformation in a tension chord subjected to increasing displacement.....	125
7.3	Mechanical model for boundary elements of RC walls with lap splices.....	126
7.3.1	Anchorage-slip element.....	126
7.3.2	Basic tension chord element.....	127
7.3.3	Lap-splice element.....	129
7.3.4	Model implementation: iterative procedure and failure criteria	130
7.4	Validation of the proposed model.....	131
7.4.1	TU with continuous reinforcement.....	132
7.4.2	TUs with lap splices.....	134
7.5	Conclusions	136
7.6	Acknowledgments	136
8	Conclusions.....	137

TABLE OF CONTENTS

8.1	Contributions and findings.....	137
8.1.1	Main findings from experimental tests.....	137
8.1.2	Developed numerical models	139
8.1.3	Developed mechanical model.....	140
8.2	Limitations and outlook	140
References.....		143
9	Appendix:.....	151
9.1	Implementation of the axially equilibrated displacement-based beam element in Opensees and application to dynamic analysis of structures.....	151
9.1.1	Nonlinear static analysis.....	151
9.1.2	Nonlinear time history analysis	153
9.2	Mechanical interpretation and calibration of the parameter α	154
CURRICULUM VITAE – DANILO TARQUINI.....		157

Introduction

1.1 Background and motivation

Lap splices are the most common method of obtaining a joint structural entity from two rebar segments [1]. They are created, as the name suggests, by overlapping and then wiring together two lengths of rebar. Due to shipping constraints as well as efficient material use, splicing of longitudinal reinforcement is found in almost all reinforced concrete (RC) structures and in all types of structural members such as beams, columns and walls [2]. The transfer of forces between spliced rebars relies fundamentally on the brittle mechanism of concrete-steel bond [3]; for this reason, in particular under tensile loading, the performance of lap splices differs substantially from the one of continuous rebars, potentially leading to undesired and fragile failures [4]. Namely, field observations (e.g. [5–7]) as well as past experimental tests (e.g. [8–13]) showed that inappropriate detailing or positioning of lap splices might cause a significant reduction in the strength and/or displacement capacity of structural members.

RC walls represent the main source of lateral resistance for bridges featuring wall-type piers and for buildings braced by shear walls. Although the current practice in bridge design is to avoid lap splices in regions undergoing plastic deformations (plastic hinges), in RC building walls longitudinal rebars continue to be typically spliced at the base of the member where stresses and strains are largest [14,15]. For these walls, specific safety provisions are adopted by international seismic guidelines including: (i) limits on the reinforcement percentage that can be spliced as a function of the ductility category of the plastic region [16]; (ii) location of splices away from high tensile stress regions [17–19]; and (iii) a minimum amount of confining reinforcement for lap splices in regions where inelasticity concentrates [18,19]. However, RC walls or piers constructed before the introduction of seismic codes do not respect such provision and may feature short and unconfined lap splices within their plastic hinge region.

In Switzerland, capacity design guidelines were introduced in the 2003 code generation [20]. According to a technical documentation issued by the Federal roads office (FEDRO) [21], only 10% of the existing Swiss bridge stock was built after that year. Of the remaining bridges, which can be assumed to have lap splices in the plastic hinge region of the piers, it is estimated 10-15% are represented by multi-span girder bridges with relatively short and squat wall-type piers [21]. Although Switzerland is a region with moderate seismicity (maximum horizontal peak acceleration on rock is $a_{gh} = 1.6 \text{ m/s}^2$), piers with such an aspect ratio may still undergo inelastic deformations to meet the imposed displacement demand.

In this framework, two research projects were funded by the FEDRO [22,23] aiming at establishing a displacement-based approach for the assessment of Swiss bridges. Seven half-scale RC wall-type piers were tested under quasi-static cyclic loading up to failure, of which three featured poorly detailed lap splices above the pier-foundation interface. The test parameters were the presence of lap splices, amount of longitudinal and transverse reinforcement and shear span. When comparing the response of the spliced specimens with the corresponding companion walls with continuous reinforcement, it was observed that the presence of lap splices always affected negatively the behaviour of the structural member. In the spliced units damage concentrated about the splices and, although the walls nominal force capacity was attained, failure occurred at reduced ductility levels with respect to units with continuous reinforcement. This can be observed in Figure 1.1 where the failure mode and the force-displacement response of two companion walls with and without lap splices are contrasted. In order to predict the overall behaviour of the tested units, Hannewald [24] proposed a plastic hinge model in which the ultimate displacement capacity was determined using strain limits. However, the latter were based on the results obtained from only three test units, therefore requiring further validation and investigation.

The above research projects revealed the scarcity of experimental studies focusing on the deformation capacity of lap splices. The characterization of this quantity, which involves additional experimental research, represents one first subject of the present thesis. The second topic regards instead the development of suitable models for practicing engineers to simulate the response of spliced RC walls, which are also underrepresented in current literature.

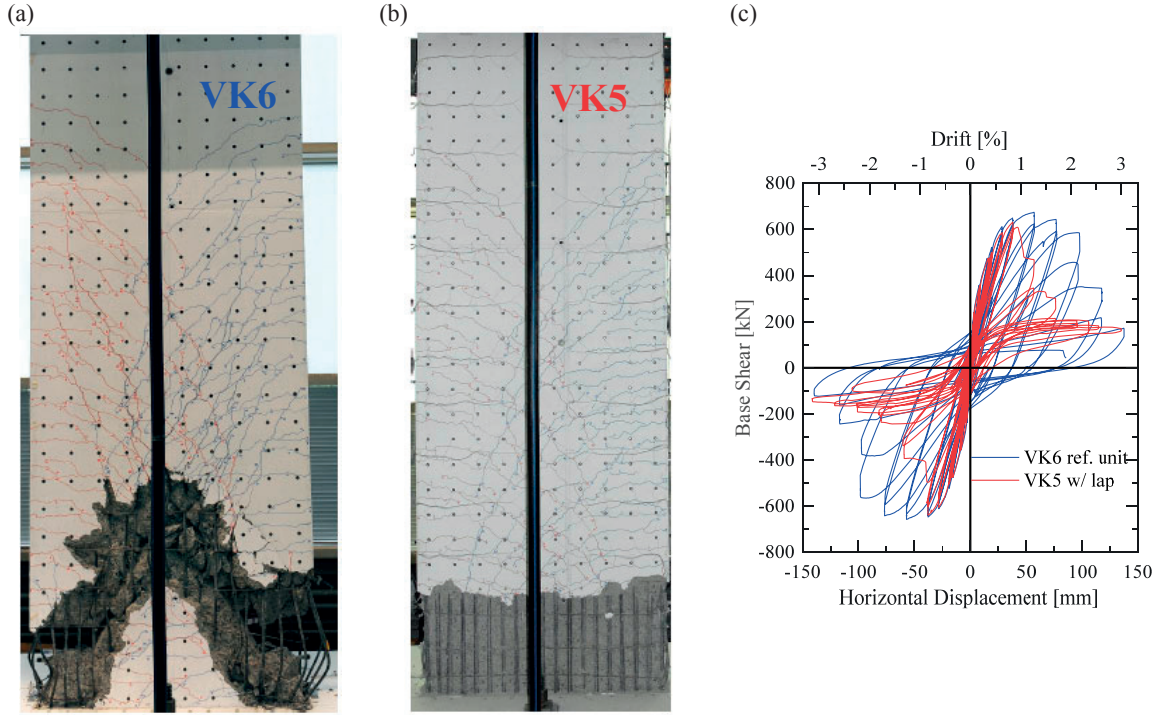


Figure 1.1: Effect of poorly detailed lap splice presence on the behaviour of RC walls: (a) failure mode of specimen VK6 with continuous reinforcement (figure from [25]); (b) failure mode of specimen VK5 with lap splices in the plastic hinge region (figure from [25]); (c) Comparison of the cyclic behaviour.

1.2 State of the art

The purpose of the following paragraphs is to provide a state-of-the-art overview of the different topics addressed in this thesis, i.e. experimental tests, numerical and mechanical modelling of RC walls with lap splices. A detailed literature review of the different subjects is performed in each Chapter, to which the reader is herein referred.

Although in performance based earthquake engineering (PBEE) deformation rather than force quantities are compared to seismic demand, past experimental studies primarily focused on the strength capacity of lap splices. Relatively less research was committed to the evaluation of the deformation capacity of lap splices. Moreover, experimental testing was mainly carried out on reinforced concrete beams and columns rather than wall specimens; this is in contrast with the fact that the use of lap splices is common in plastic hinge regions of bridge piers and walls, which was identified as a critical source of damage in recent earthquakes [26]. A detailed review of post-earthquake field observations as well as past experimental programmes on members with lap splices is presented in subsections 2.2.1 and 2.2.2, respectively.

Tests on RC walls are reviewed in subsection 2.2.2.2, which includes ductile specimens designed for high-seismic regions (e.g. [15,27]) as well as units detailed to simulate American and European non-ductile RC construction practice (e.g. [28,29]). When compared to the response of reference units with continuous reinforcement, the performance of spliced RC walls depended on the detailing. Sudden lap splice failure prior to reaching the member nominal yield force occurred in walls with short and unconfined lap splices [28,30]. On the other hand, in ACI-318 [17] code compliant specimens, the splices only affected the location of damage [15], with the plastic region relocating above and below the lap splice zone.

In line with the available experimental data, several expressions were proposed to predict the strength capacity of lap splices—reviewed in subsection 3.2.1, while only few models were put forward characterizing their deformation capacity—revised in subsection 3.2.3. Including the method suggested by Hannewald, to the author’s knowledge only three studies [24,31,32] provide an estimation of the deformation capacity of spliced members, which are all related to plastic hinge analysis. As for simulating the behaviour of spliced RC members with detailed finite elements models, outlined in subsection 3.2.4, interface bond-slip elements are typically employed to integrate numerically the lap splice response. This approach results in complex and computationally expensive models, which are typically not suitable for practicing engineers.

Plastic hinge analysis is the simplest modelling technique for representing the global response of RC walls. The inelasticity is lumped at pre-defined plastic hinge locations and the accuracy of the results strongly depends on the formula employed to evaluate the plastic hinge length. Yet, it can only capture the monotonic response of a single member and it does not provide information on local level quantities such as strains. Advanced 2D or 3D finite element models represent the most powerful simulation technique to predict the cyclic behaviour of RC members. The details of the structural member along its height can be explicitly modelled and the interaction between axial force, flexure and shear is directly accounted for at the material level through multidimensional constitutive relationships. However, the complexity involved in the model setup and interpretation of the results alongside with the computational burden usually limit the application of this modelling technique to research purposes or very specialized engineering applications. Nonlinear beam element models represent the best compromise between accuracy and computational cost and are often the preferred choice to perform nonlinear static or dynamic analysis of multi-element structures. They typically provide satisfactory results for members behaving mainly in flexure while their use in shear-dominated members still represent an active topic of research. Namely, the consideration of tension shift effects and shear deformations are the main causes of mismatch between experimental and numerical results. Nonlinear beam element formulations are revised in subsection 4.1 while a full review of the modelling techniques available to simulate the response of RC walls can be found in Almeida et al. [33].

Finally, mechanical models describing the transfer of forces between spliced rebars are also scarce. In fact, most of the research effort aimed at the characterization of local bond-slip relationship for anchored rebars (e.g. [34]), generally calibrated from pull-out tests. A first mechanical model predicting the force-displacement response of lap splices was proposed by Tastani et al. [35]—reviewed in subsection 7.1, which assumed an elasto-plastic bond-slip model along spliced rebars. However, the provided solution is limited to the elastic branch of the steel stress-strain relationship and therefore it is only applicable to very short lap splice lengths.

1.3 Problem statement and research objectives

Previous research on lap splices primarily focused on the evaluation of their force capacity. Few expressions are currently available characterizing the deformation capacity of lap splices, all derived from limited test data. The possible overearly strength degradation brought about by the presence of lap splices is particularly relevant for RC walls or piers, as these members often represent the bracing system of buildings and bridges. Moreover, lap splices in RC walls are usually located above the foundation interface, where seismic actions are largest and inelastic deformations may occur.

Due to their structural importance, an accurate prediction of the displacement capacity of RC walls is fundamental when performing the seismic assessment of a building or a bridge. Complex finite element models are typically employed to accomplish this task, where the response of lap splices is obtained by integrating local bond-slip laws through interface elements. These approaches require a high level of expertise and computational cost; therefore, they are only suitable for research or very specific engineering applications. On the contrary, a simple and dependable finite element model, convenient for practicing engineers, is at present not available. When approximate calculations are sufficient or required by time constraints, mechanical models are preferable to numerical models. However, as stated in the previous section, few of these approaches have been proposed simulating the behaviour of spliced rebars in RC members.

Based on the observations above, the objectives of the present thesis are:

- To identify the main parameters governing the displacement capacity of RC walls with poorly designed lap splices;
- To derive an expression quantifying the deformation capacity of lap splices as function of these parameters;
- To develop finite element models suitable for practicing engineers to simulate the cyclic response of RC walls with lap splices, namely capable of predicting their displacement capacity;
- To propose a mechanical model describing the behaviour of RC members with lap splices, which allows describing the stress transfer mechanism between spliced rebars, evaluating the crack evolution and width along the member, and computing the displacement at failure.

1.4 Methodology

Experimental programmes, numerical and mechanical modelling were performed throughout the present work in order to accomplish the objectives listed in the previous section. The main features of each research activity, alongside with the role and relevance played in attaining a specific goal, are separately discussed in the following three paragraphs.

Experimental activity: With the aim of identifying the parameters mostly influencing the displacement capacity of RC walls with lap splices, past cyclic tests on this type of structural member were reviewed, systematized and collected in a database. The dataset included 16 units with lap splices and 8 reference units with continuous reinforcement. Two wall specimens, one with lap splices and a reference unit with continuous reinforcement, were tested at the structural laboratory of EPFL. These two specimens featured the smallest shear span ratio among the RC walls in the database, therefore allowing to further investigate the influence of the moment gradient on the lap splice performance. Test results showed that lap splice failure was primarily governed by confining reinforcement and ratio of lap splice length to shear span; moreover, it was observed that the strength loss of the units was typically triggered by bond degradation occurring at the outermost lap splices, i.e. those located at the boundary elements. The above findings prompted a second experimental programme on spliced RC wall boundary elements carried out at the structural laboratory of EPFL. Out of 24 specimens, 22 featured lap splices above the foundation interface and two were reference units with continuous reinforcement. Variable parameters of the test series were lap splice length, confining reinforcement and loading history. The experimental data allowed to improve the understanding of the behaviour of lap splices under cyclic loading as well as to calibrate an empirical equation characterizing the deformation capacity of lap splices.

Numerical modelling: Two nonlinear finite element models were developed for the simulation of spliced RC walls: a two-dimensional shell element model and a beam element model. In the former, the presence of lap splices is considered through an equivalent, uniaxial, steel stress-strain law, therefore avoiding the use of complex interface bond-slip elements. The constitutive relationship represents the response of spliced rebars in RC walls up to the onset of strength degradation. The strain capacity is derived by means of a semi-empirical approach, and it is a function of the confining reinforcement ratio and the ratio of lap splice length to shear span. The validation was performed against the walls collected in the database demonstrating that the model is capable of adequately capturing the peak strength as well as the displacement capacity of the spliced units. The second finite element model presented in this thesis is a displacement-based beam element in which axial equilibrium is strictly enforced. The exact verification of axial equilibrium improves the poor performance of classical displacement based formulations while the assumed linear curvature profile allows to indirectly account for tension shift effects in RC members subjected to lateral loading. As previously discussed, the latter is amongst the main causes for the mismatch between experimental and numerical estimates of curvatures and strains obtained through existing beam formulations. Strain limits derived from experimental results can then be used to introduce the deterioration of the structural performance caused by the presence of inadequately designed lap splices.

Mechanical modelling: Based on the experimental findings, a mechanical model describing the behaviour of RC wall boundary elements with lap splices was also developed. This model shares the fundamental hypothesis of the tension chord model proposed by Marti et al. [36] yet extending it to account for the presence of lap splices and the strain penetration effect. Given an input global force or displacement, the model provides cracks location and width as well as the steel and concrete stress and strain distributions along the RC member. For a boundary element with lap splices, the ultimate displacement can be calculated through the direct application of the proposed relationship characterizing the deformation capacity of lap splices.

1.5 Thesis layout

This thesis is paper-based and includes a compilation of six articles, four published, one submitted and one under submission for publication in scientific journals, in agreement with the regulations of the doctoral school of EPFL (<https://phd.epfl.ch/publishedarticles>). The organization of the document, presented in the following, is illustrated schematically in Figure 1.2, where different background colors are used to distinguish the three main research activities performed, i.e. experimental work, numerical and mechanical modelling.

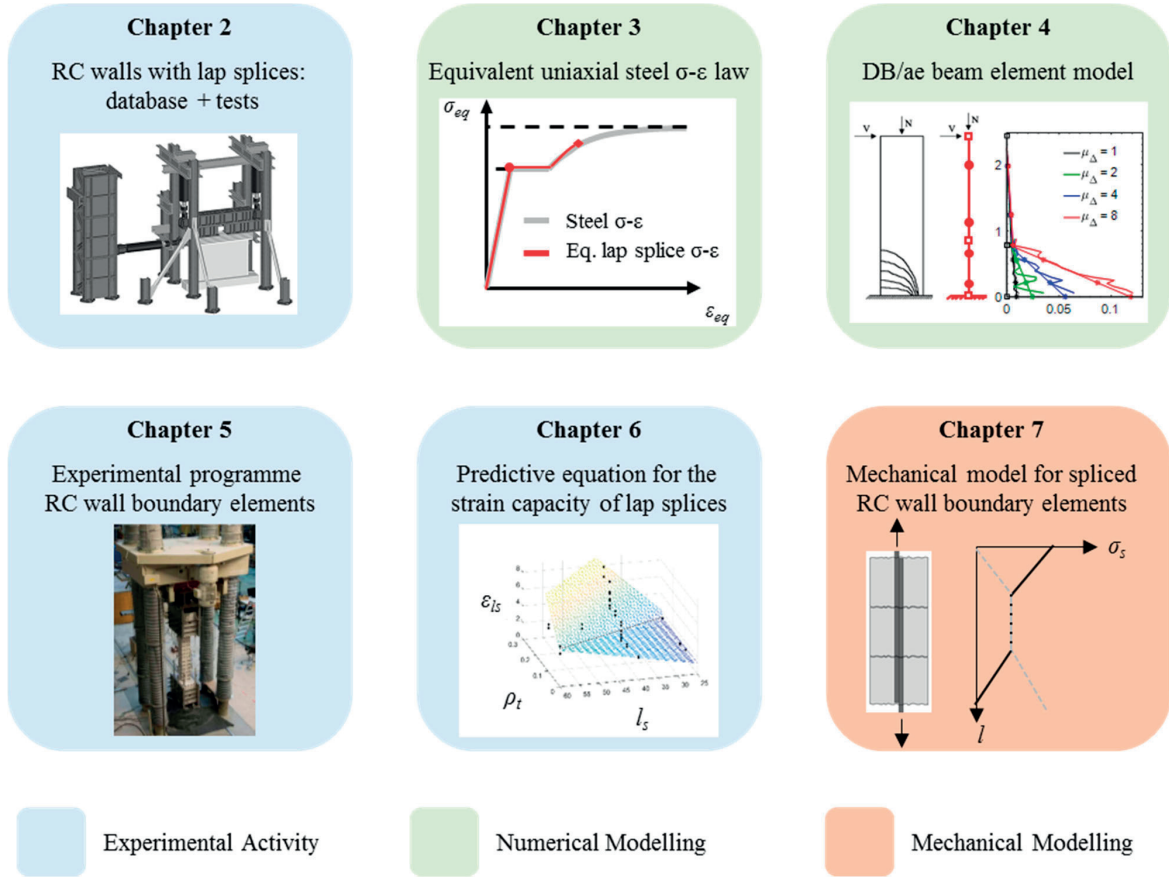


Figure 1.2: Sketch of the thesis layout

- Chapter 2 represents the post-print version of the journal paper:

“J.P. Almeida, O. Prodan, D. Tarquini, K. Beyer, 2017. *Influence of lap-splices on the cyclic inelastic response of reinforced concrete walls. I: Database assembly, recent experimental data, and findings for model development*, ASCE Journal of Structural Engineering 143 (12)”.

The Chapter presents a database of tests on spliced RC walls, which primarily aimed at collecting information on the deformation capacity of lap splices. Two new wall tests performed at the structural laboratory of EPFL are included. It is shown that confining reinforcement ratio and the ratio of shear span to lap splice length mostly influence the lap splice strain capacity.

- Chapter 3 represents the post-print version of the journal paper:

“D. Tarquini, J.P. Almeida, O. K. Beyer, 2017. *Influence of lap-splices on the cyclic inelastic response of reinforced concrete walls. II: Shell element simulation and equivalent uniaxial model*, ASCE Journal of Structural Engineering 143 (12)”.

In this Chapter, building on the information collected from the RC wall database of Chapter 2, a semi-empirical expression for the ultimate lap splice strain is derived. An equivalent uniaxial steel stress-strain law simulating the response of lap splices is first proposed and then successfully used, in conjunction with shell element models, to predict the force-displacement response of spliced RC walls.

- Chapter 4 represents the post-print version of the journal paper:

“D. Tarquini, J.P. Almeida, K. Beyer, 2017. *Axially equilibrated displacement-based beam element for simulating the cyclic inelastic behaviour of RC members*, Earthquake Engineering and Structural Dynamics 46 (9): 1471-1492”.

This Chapter presents a displacement-based beam element model improving the simulation, with respect to classical beam element formulations, of local-level quantities such as curvatures and strains, strictly related to structural damage. The proposed formulation consists in a displacement-based beam element in which axial equilibrium is strictly enforced along the element length; curvature profiles are assumed linear which allows the beam element to indirectly account for tension shift effects in RC structures (columns and walls).

- Chapter 5 represents the post-print version of the data paper:

“D. Tarquini, J.P. Almeida, K. Beyer, 2018. *Uniaxial cyclic tests on reinforced concrete members with lap splices*, accepted for publication in Earthquake Spectra, published online”.

In this Chapter, an experimental programme on RC wall boundary elements with lap splices is described. The test units were subjected to uniaxial cyclic loading with the objective of investigating the influence of lap splice length, confining reinforcement and loading history on the behaviour of lap splices.

- Chapter 6 represents the pre-print version of the journal paper:

“D. Tarquini, J.P. Almeida, K. Beyer, 2018. *Experimental investigation on the deformation capacity of lap splices under cyclic loading*, submitted to Bulletin of Earthquake Engineering (under review)”.

Based on the experimental data derived from the tests presented in Chapter 5, an empirical expression for the deformation capacity of lap splices is derived as function of lap splice length, loading history and casting position. The ultimate strain capacity of lap splices is determined considering only deformations originating within the lap splice zone.

- Chapter 7 represents the pre-print version of the journal paper:

“D. Tarquini, J.P. Almeida, K. Beyer, 2019. *Extended tension chord model for boundary elements of RC walls accounting for anchorage slip and lap splices presence*, under submission”.

This Chapter presents a mechanical model for the simulation of RC wall boundary elements with lap splices subjected to tensile loading. It allows to evaluate the steel and concrete stress-strain distributions as well as the crack distribution and opening along the structural member. For spliced boundary elements, the ultimate displacement is computed through the relationship proposed in Chapter 6.

- Finally, an overall summary of the experimental findings as well as general conclusions on the proposed numerical and mechanical models are provided in Chapter 8, which is concluded with an outlook of possible future works.

2 Reinforced Concrete Walls with Lap Splices: State of the Art, New Tests and Database Assembly

This Chapter collects a database of tests on RC walls with lap splices available in the literature including two tests performed at the structural laboratory of EPFL. It represents the post-print version of the article:

J.P. Almeida, O. Prodan, D. Tarquini, K. Beyer, 2017. “Influence of lap-splices on the cyclic inelastic response of reinforced concrete walls. I: Database assembly, recent experimental data, and findings for model development”, *ASCE Journal of Structural Engineering* 143 (12), DOI: [10.1061/\(ASCE\)ST.1943-541X.0001853](https://doi.org/10.1061/(ASCE)ST.1943-541X.0001853).

Figures and tables formatting, reference-, section-, and equation- numbering were adapted to the style of this document. The testing, post-processing and analysis of the experimental results were carried out by the first two authors under the supervision of the last author. The third author performed the literature review and collected the database of RC walls.

Abstract

Recent postearthquake missions have shown that reinforced concrete (RC) wall buildings can experience critical damage owing to lap splices, which led to a recent surge in experimental tests of walls with such constructional details. Most of the wall tests described in the literature thus far were carried out in the last six years. This Chapter presents a database with these wall tests, including the description of a new test on a wall with lap splices and a corresponding reference wall with continuous reinforcement. They complement the existing tests by investigating a spliced member with a shear span ratio smaller than two, which is the smallest among them. The objective of this database is to collect information not just on the force capacity but mainly on the deformation capacity of lap splices in reinforced concrete walls. It is shown that (1) well-confined lap splices relocate the plastic hinge above the lap splice, (2) lap splices with adequate lengths but insufficiently confined attain the peak force but their deformation capacity is significantly reduced, and (3) short and not well-confined lap splices fail before reaching the strength capacity. The analysis of the test results, which are used in Chapter 3 for the finite element simulation of walls with lap splices, indicates in particular that the confining reinforcement ratio and the ratio of shear span to lap splice length influence the lap splice strain capacity.

Keywords: Reinforced concrete (RC) walls; Lap splices; Database; Experimental tests.

2.1 Introduction

The transfer of forces between lap-spliced rebars relies fundamentally on the inherently brittle mechanism of concrete-steel bond. Although the common practice for the design of bridges is to avoid lap splices within plastic hinges, in reinforced concrete (RC) building walls, longitudinal rebars are typically spliced at the base of the member where stresses and strains are largest [14,15]. To avoid brittle failures, current standards impose limits on the reinforcement percentage that can be spliced as a function of the ductility category of the plastic region [16], promote the location of splices away from high tensile stress regions [17,18], or accept lap splices only at the extremity of the plastic region furthest away from the critical section [19]. Minimum confinement reinforcement for lap splices in regions undergoing plastic deformations is also prescribed [18,19]. Walls in buildings constructed before such guidelines were in place have often all their bars spliced at the base, short splice lengths and unconfined splices.

Performance-based seismic design and assessment requires estimates of the deformation capacity of members undergoing inelastic deformation. Previous research on lap splice performance focused largely on the strength capacity of lap splices (e.g. [37,38]). Experimental research on the deformation capacity of members with lap splices is scarce. Past tests were carried out on RC beams and columns (e.g. [31,32]), and on RC walls (e.g. [24]). This Chapter focuses on the latter.

The objective of this Chapter is threefold: (i) to establish a database of wall tests with lap splices, which collects and systematizes the experimental results on RC walls; (ii) to present the results of two new walls tests, one with lap splices and one without, which complement the existing tests by investigating for the first time a spliced member with shear span

ratio $L_s/h < 2$; and (iii) to discuss qualitatively and quantitatively on the basis of observations from post-earthquake reconnaissance missions and tests the influence of the individual factors previously outlined on the deformation capacity of lap splices.

The Chapter starts with a review of field and experimental observations on structural elements with lap splices, continues with the presentation of the new experimental results on two RC walls, and finally, based on these field and experimental results, considers the influence of lap splices on the cyclic response of RC walls. It concludes with a summary of the factors that have the most significant influence on lap splice displacement ductility.

2.2 Review of field and experimental observations

The force-transfer mechanism of lap splices involves bond stresses between concrete and rebars. The resultant bond force can be decomposed into a component parallel to the rebar axis and a radial one. The former causes shearing of the concrete between the rebar ribs, whereas the latter radial forces induce tensile stresses in the surrounding concrete [39]. These two components can be directly related with the two types of bond failures that are usually considered, namely pull-out—also described as ‘crushing and sleeving’ [31]—and splitting. If the rebar lugs are spaced far apart, the concrete cover is insufficient, the tensile strength is low, or the confinement provided by the transverse reinforcement does not suffice to keep cracks small, splitting failure will occur. In particular, concrete cover appears to be a critical factor when it is equal to or less than three rebar diameters—although splitting can also take place with larger covers [40]. Therefore, while anchored bars in foundations or well confined beam-column joints are more likely to sustain pull-out failures, rebars along the height of RC walls are more susceptible to splitting failure due to the small concrete cover characteristically employed in wall construction. Throughout this work, this will be the failure mode assumed. Note that a larger attention from the research community has been given to anchorage and bond-slip relations for anchored bars sustaining pull-out failure rather than splitting failure. For spliced rebars, researchers highlighted the role of transverse ties in enabling a shear friction mechanism to transfer forces from one spliced bar to the other, namely in sustaining a diagonal compression field across the spliced rebars [10]. Before splitting cracks form, the bond transfer relies largely on the tensile strength of the concrete while the shear friction plays a lesser role. Shear friction is activated after splitting cracks form and the confining reinforcement is subjected to significant tensile strains [31].

The detailing and content of the member longitudinal reinforcement will determine the orientation of the splitting cracks, and a typical division is often made in terms of side-splitting and face-splitting. According to ACI [40], for reinforcing layers with rebar spacing larger than twice the concrete cover, splitting cracks occur perpendicularly to the surface and along the rebar lengths (face-splitting). On the other hand, if the cover is larger than twice the bar spacing, cracks will form in the plane of the reinforcing layer (side-splitting). Additionally, Orangun et al. [37] illustrated how face-splitting cracks just before failure will develop either a ‘face-and-side split failure’ or a ‘V-notch failure’ (i.e., with further inclined cracking to the surface), the latter occurring if the bar spacing is several times larger than the concrete cover. This separation between face- and side-splitting has been considered in physically-based models to predict lap splice strength [3], the results of which compare well with those of other models developed from regression analyses alone [37,38].

When subjected to cyclic loading, cracks propagate in both loading directions and may eventually join up some distance away from the rebar surface, creating regions of disintegrated concrete and hence degraded bond. The effects of reversing curvatures on large diameter bars of flexural members may also have a weakening influence on the cover [8]. However, the same authors also point out that the onset of splitting does not constitute failure and that the confinement by the stirrups allows to carry loads up to concrete spalling.

2.2.1 Post-earthquake field observations

Different degrees of structural damage following past earthquakes, ranging from minor cracking to collapse, can be partly or totally attributed to the response of lap spliced wall regions. This Section presents examples of concrete structures that have undergone observable damage during recent earthquakes. Due to space limitations, column and beam damage is not included.

Damage to wall buildings associated with lap splices have been reported after some of the major earthquakes occurring during the last decade of the previous century. As examples, one can cite the damage to the *Guam Hilton Hotel* after the Guam 1993 earthquake [41], or the concrete spalling that occurred in the *Indian Hills Medical Center* during the Northridge earthquake of 1994. The RC walls in this building, which had already shown vertical splitting associated to

bond slip problems during the San Fernando earthquake of 1971, exhibited more extensive spalling over the height of the lap splice, evidencing the effects of the internal bond-slip mechanism that contributed to concrete splitting [42].

Chimneys do not have the redundancy of wall buildings and thus a failure at a critical section will inevitably lead to its partial or total collapse. This was highlighted by the performance of two RC chimneys that failed due to poor lap splice performance. Firstly, during the Marmara 1999 earthquake in Turkey a 115-m tall RC chimney collapsed. The failure occurred at a height of 30-35 m, where an opening and lap splices were present. The structure had been designed in 1978 according to the ACI provisions in force at the time. Kilic and Sozen [5] concluded that the most plausible cause for collapse was the association between the critical section for flexural yielding formed by the opening and the failure of lap splices at that location, which did not withstand the imposed stress reversals in the nonlinear response range. A 58-m tall chimney also failed during the Niigata-ken Chuetsu-Oki 2007 earthquake in Japan [7,43]. The chimney, constructed in 1994, had been designed according to the latest seismic standards, which imposed lap splice lengths of at least 40 times the diameter of the largest spliced bar. The damage concentrated at a height of approximately 17.5 m above the ground level where three constructional details contributed to a strength discontinuity that attracted large inelastic deformation demands: (i) splicing of the exterior layer of vertical bars, (ii) cut-off of the interior layer of longitudinal rebars, (iii) change from double to single transverse hoops.

More recently, damage to several of the more than one hundred high-rise RC wall buildings that were damaged during the Chile earthquake of February 27, 2010, can be traced back to lap splice failures [6]. The only building with more than three storeys that suffered total collapse during the earthquake was the 15-storey *Alto Rio* building, completed in 2009. Song et al. [6] analysed possible failure sequences of the building and concluded that lap splice failure was likely to have played a role. The same authors also claim to have observed splice failures, and failures at points where bars were cut off, in at least other eight buildings in Chile. However, they do not provide further information on the lap splice configurations in these buildings.

Finally, lap splice damage in RC walls was observed after the 2010-2011 earthquakes of Canterbury in New Zealand. Sritharan et al. [26] report the occurrence of damage about the lap splice in a 10-m long wall of a 13-storey apartment building (*Terrace on the Park*) built in 1999. The splice had poorly detailed shear reinforcement and lack of ties between the two layers of web reinforcement. It is noted that the lap splice was not located in the plastic hinge region.

2.2.2 Past cyclic experimental tests on members with lap splices

Many experimental and numerical studies have been performed on lap splice behaviour to date, the majority of which focused on lap splice strength under monotonic loading. There is less research on lap splice strength under cyclic loads, and even more so regarding the deformation capacity of lap splices, which are two fundamental quantities that are required when modelling the seismic response of members with lap splices. The present Section starts by reviewing the most relevant experimental tests carried out to date. In particular, a short summary of past cyclic tests on beams and columns is performed, followed by an extensive review of experimental tests on walls with lap splices.

2.2.2.1 Beams and columns

Up until the late 1970s and the extensive test programmes carried out at *Cornell University* on 68 beam and column specimens [44–46], there was an almost complete lack of experimental data on splice performance under cyclic loading. The work performed by these researchers brought forward that the main factor that affects the rate of bond deterioration and the deterioration propagation was the amount and spacing of transverse reinforcement along the splice and just beyond the splice end [8]. Building on the observation that maintaining stirrup strains substantially below yield improves splice strength and ductility, Paulay [10], Priestley et al. [31] and Sivakumar et al. [47] proposed design procedures and expressions to determine the amount of transverse confinement necessary to insure that lapped splices can sustain a large number of reversed cyclic loads just below yield level as well as some cycles into the inelastic range. Sparling and Rezansoff [48] observed, from 12 large-scale beam tests, that such recommendations allowed the specimens to achieve appreciable displacement ductilities. Rezansoff et al. [49], again building on the results of additional experimental tests, further underlined the need to account for the actual rebar yield strength—which can be appreciably larger than the specified yield strength—in designing the transverse reinforcement to ensure a reasonably ductile member response.

The behaviour of lap splices in compression was addressed in the first half of the 1990s [2], as well as the retrofit of columns with inadequate lap splices [50–52]. Lynn et al. [11] and Melek and Wallace [53] performed cyclic tests on columns with constant axial load and deficient lap splices (both in terms of splice length and confining reinforcement),

typical of old building design. Lynn et al. [11] showed that the more confined columns kept the moment capacity for larger displacement amplitude cycles, while the experimental program performed by Melek et al. [12] evidenced the influence of the applied loading history on post-peak strength degradation. More recently, Pam and Ho [54] studied the effects of the location of well-detailed lap splices on four RC columns. They concluded that the flexural strength increased slightly as the percentage of splices in the critical region also augmented, while the ductility capacity decreased due to an upward shift of the inelastic damaged region. Tests on beams with lap splices continue to date [14]. However, despite the many past tests that have been performed on beams and columns, few proposals can be found regarding the ductility capacity of lap splices expressed as a function of its detailing characteristics and mechanical properties [24,55].

2.2.2.2 Walls

Tests on walls with lap splices are recent when compared to those on beams and columns described in the previous sub-section. Although four wall units were tested before 2008 [30,56], the other 12 wall specimens with lap splices that are documented in the literature were tested over the past six years. The objective of the present sub-section consists in carrying out a compilation of data on walls with lap splices. The following Section describes also two new experimental tests (units TW2 and TW3) carried out at the structural laboratory of *EPFL* on companion walls with and without lap splices. They complement the existing tests by considering a large lap splice length to shear span ratio, hence allowing to investigate the influence of the moment gradient on lap splice performance. In this context, Table 2.1 presents a complete summary of the characteristics of the walls with lap splices that were experimentally tested under cyclic loads to date, along with the list of reference units with continuous reinforcement. The reinforcement layout and the main measured material properties of the specimens are depicted in Figure 2.1. Observations on the behaviour of each spliced test unit are provided in Table 2.2. As this summary can be useful to other researchers, all the information collected in Table 2.1, Table 2.2 and Figure 2.1, as well as the associated experimental force-displacement data, are available through the webpage www.zenodo.org using the DOI:10.5281/zenodo.19224.

Table 2.1: Review of experimental tests on walls with lap splices tested under cyclic loads.

Test Unit	Main Ref.	Ref. Unit	Geom.	Scale	<i>ls</i> (mm)	<i>dbl</i> (mm)	<i>nspl</i> (-)	<i>cb0</i> (mm)	<i>cs0</i> (mm)	<i>csi</i> (mm)	<i>s</i> (mm)	<i>dbl</i> (mm)	<i>Ls</i> (mm)	<i>h</i> (mm)	<i>FS</i> (-)	<i>SD</i> (-)	<i>δdeg</i> (%)
W1	Paterson and Mitchell (2003) [30]	[-]	Symm. Rectang.	1:1	900	25	2	63	40	60	350	11	3250	1200	N	Y	0.75
W2		[-]	Symm. Rectang.	1:1	900a	25	2	63	40	60	350	11	3750	1200	N	Y	1.75
CW2	Elnady (2008) [56]	[-]	Symm. Rectang.	1:3	360	16	2	27	27	17	180b	6b	5000	1000	Y	Y	0.2
CW3		[-]	Symm. Rectang.	1:3	360	16	2	27	27	17	180b	6b	2250	1000	N	Y	0.31
VK2	Bimschas (2010) [29]	VK1	Symm. Rectang.	1:2	600	14	4	26	26	31	200	6	3300	1500	N	Y	0.9
VK4	Hannewald et al. (2013) [57]	VK3	Symm. Rectang.	1:2	600	14	4	26	26	31	200	6	3300	1500	N	Y	0.9
VK5		VK6	Symm. Rectang.	1:2	600	14	4	26	26	31	200	6	4500	1500	N	Y	0.9
W1*	Layssi and Mitchell (2012) [28]	[-]	Symm. Rectang.	1:1	600	20	2	36	50	6	250c	11c	3250	1200	Y	Y	0.35
W2*		[-]	Symm. Rectang.	1:1	600	20	2	36	50	6	250c	11c	3250	1200	Y	Y	0.4
PW2**	Birely (2012) [42]	PW4	Symm. Rectang.	1:3	609	13	2	19	19	19	51d	6d	6710	3048	N	N	1.1
RWS	Aaleti et al. (2013) [27]	RWN	Unsymm. Rectang.	1:2	1140 1730	19 29	2 2	25 31	18 9	21 9	51d 62d	6d 9e	6096	2286	N	Y	1.2
W-60-C		W-MC-C	Symm. Rectang.	1:1	1520	25	2	30	19	56	64d	6d	3660	1520	N	Y	1.8
W-40-C	Villalobos (2014) [58]	W-MC-C	Symm. Rectang.	1:1	1020	25	2	30	19	56	64d	6d	3660	1520	N	Y	1.8
W-60-N		W-MC-N	Symm. Rectang.	1:1	1520	25	2	30	19	56	127f	10f	3660	1520	N	Y	1.35
W-60-N2		W-MC-N	Symm. Rectang.	1:1	1520	25	2	30	19	56	127g	10g	3660	1520	N	Y	1.35
TW3	Almeida et al. (2017) [59]	TW2	T-shaped	2:3	215	6	2	15	15	39	130h	6h	3150	2700	N	Y	0.75

Legend: **Ref. Unit**: reference unit with continuous reinforcement; **ls**: lap splice length; **dbl**: longitudinal reinforcement diameter; **nspl**: number of splices potentially crossed by a splitting crack; **cb0**: clear face cover; **cs0**: clear side cover; **csi**: half of the clear spacing between splices in the plane of a splitting crack; **s**: spacing of lateral or confining reinforcement (classical closed hoops or stirrups when not differently specified); **dbl**: horizontal reinforcement diameter (classical closed hoops or stirrups when not differently specified); **Ls**: shear span; **h**: wall length; **FS**: lap splice failure before the wall has reached the flexural capacity; **SD**: specimen experiences strength degradation due to the presence of lap splices; **δdeg**: Drift at degradation. **NOTE**: all quantities aforementioned are associated to the outmost reinforcement layer perpendicular to the plane of bending.

*Used to differentiate the 2 TUs from those of Paterson and Mitchell, which are equally labelled. ** PW1 and PW3 tested by the same authors showed a similar behaviour to PW2 (no lap splice failure) and were omitted. ^aLap splice zone starts 600 mm above the foundation level. ^bShear reinforcement consisting of 2 straight single leg rebars (no reinforcement preventing face splitting). ^cSingle leg rebar located in between the longitudinal reinforcement. ^dQuantity referred to the confining hoops present in the boundary element. ^eQuantity referred to the shear reinforcement. ^fShear reinforcement consisting of 2 single leg rebars with 135° hook. ^gShear reinforcement consisting of 2 single leg rebars with 90° hook. ^hHorizontal reinforcement inside the flexural reinforcement.

Almeida et al. (2016)	Villalobos (2014)	Birely (2013)	Layssi and Mitchell (2013)	Hamnevald et al. (2013)	Bimschas (2010)	Ehady (2008)	Paterson and Mitchell (2003)
TW3	W-MC-60/40C	RWS	W1*	VK4-VK5	VK2	CW2-CW3	W1-W2
W-MC-60C	W-MC-40C	North	W2*	VK4	CW2	W1	
$f'_c = 43.3 \text{ MPa}$ $f_y = 465 \text{ MPa}$ $f_u = 620 \text{ MPa}$ $\epsilon_{sh} = 2.5 \%$ $\epsilon_{sh} = 80 \%$	$f'_c = 31 \text{ MPa}$ $f_y = 461 \text{ MPa}$ $f_u = 655 \text{ MPa}$ $\epsilon_{sh} = 12 \%$ $\epsilon_{sh} = 180 \%$	$f'_c = 55.9 \text{ MPa}$ $f_y = 465 \text{ MPa}$ $f_u = 634 \text{ MPa}$ $\epsilon_{sh} = 9.6 \%$ $\epsilon_{sh} = 100 \%$	$f'_c = 31.2 \text{ MPa}$ $f_y = 460 \text{ MPa}$ $f_u = 637 \text{ MPa}$ $\epsilon_{sh} = 2.5 \%$ $\epsilon_{sh} = 91.2 \%$	$f'_c = 39.2 \text{ MPa}$ $f_y = 521 \text{ MPa}$ $f_u = 609 \text{ MPa}$ $\epsilon_{sh} = 28.6 \%$ $\epsilon_{sh} = 110 \%$	$f'_c = 39.0 \text{ MPa}$ $f_y = 521 \text{ MPa}$ $f_u = 609 \text{ MPa}$ $\epsilon_{sh} = 28.6 \%$ $\epsilon_{sh} = 110 \%$	$f'_c = 37.3 \text{ MPa}$ $f_y = 450 \text{ MPa}$ $f_u = 760 \text{ MPa}$ $\epsilon_{sh} = \text{N/A}$ $\epsilon_{sh} = \text{N/A}$	$f'_c = 25.9 \text{ MPa}$ $f_y = 423 \text{ MPa}$ $f_u = 667 \text{ MPa}$ $\epsilon_{sh} = \text{N/A}$ $\epsilon_{sh} = \text{N/A}$
		South				W2	
		$f'_c = 55.9 \text{ MPa}$ $f_y = 491 \text{ MPa}$ $f_u = 669 \text{ MPa}$ $\epsilon_{sh} = 9.6 \%$ $\epsilon_{sh} = 100 \%$				$f'_c = 37.5 \text{ MPa}$ $f_y = 450 \text{ MPa}$ $f_u = 760 \text{ MPa}$ $\epsilon_{sh} = \text{N/A}$ $\epsilon_{sh} = \text{N/A}$	$f'_c = 33.4 \text{ MPa}$ $f_y = 423 \text{ MPa}$ $f_u = 667 \text{ MPa}$ $\epsilon_{sh} = \text{N/A}$ $\epsilon_{sh} = \text{N/A}$

Notes: (i) the mechanical properties of the steel are relative to the rebar(s) of the controlling boundary reinforcement (represented in the zoomed-in section details); (ii) N/A = not available; (iii) Ø, π , M: tag for European, US and Canadian rebar sizes respectively.

Figure 2.1: Geometrical details of the walls presented in Table 2.1

Table 2.2: Main Observations on the Behavior of the Spliced Test Units Tested under Cyclic Loads.

Test Unit	Comments
W1	The specimen exhibited very poor ductility, failing soon after yielding at a lateral drift of 0.6%. There was a brittle failure of the lap splices at the tensile end of the wall that led to a significant drop in the wall capacity. A visible vertical side splitting crack along the entire length of the lap splice was visible prior to failure.
W2	The wall, which had a lap splice zone located 600 mm above the foundation, showed a ductile response until almost 2% drift. As inelasticity (and cracks) spread from the bottom and reached the height at which the splice started, a brittle tensile failure of the lap splices on one side of the specimen occurred, resulting in a large drop in the capacity of the wall.
CW2	At the very first loading cycle at a low drift of 0.05%, flexural cracks developed at the bottom of the wall and spread to near midheight. Upon increasing the lateral load, the existing cracks started to open up and a new horizontal crack developed just at the top end of the lap splice zone. At a drift below 0.1% (far below the yielding point) the wall failed prematurely due to bond slip of the lap splices.
CW3	At 0.5% drift two diagonal cracks were observed at inclined $\pm 45^\circ$ direction. While loading, cracks opened up and extended from corner-to-corner of the wall in both directions. At a horizontal drift of approximately 1.5% the wall failed due to bond slip of the lap splice.
VK2	The first side splitting cracks in the tensile edge of the wall appeared at 1.5% drift. At 2% drift, a large bond crack extended along the entire lap splice height. By the second cycle at this drift level the four reinforcement bars in the outmost layer of each tension zone of the cross section were essentially ineffective due to bond failure of the splices. With the increase of the lateral loading, more lap splices successively failed causing a subsequent progression of the cyclic strength degradation of the member.
VK4	At about 1% drift, while loading in one direction, compression cracks appeared at the wall edge. At the same drift level, upon reversal, splice failure occurred followed by a sensible drop of the wall strength. At the second peak at 1% drift, some splices at the tension side of the pier also failed. At 1.2% drift, all cover concrete along the splices sounded hollow. The wall had thus reached its residual capacity (25% of the peak force) and the force-displacement relationship remained rather flat even when higher displacement levels were imposed.
VK5	At 1% drift, vertical side splitting cracks were clearly visible along the splice length in the tension wall side. Also noticeable was a horizontal crack above the splice level. During loading to 1.5% drift, splice failure occurred followed by a decrease of the wall lateral strength. As for VK4, at this point the specimen had reached its residual strength capacity (30% of the peak force) which remained rather constant with the increase of the displacement demand.
W1*	The wall exhibited a non-ductile cyclic response due to brittle side splitting of the external lap splices prior to yielding. The specimen was able to withstand only 80% of the predicted flexural capacity.
W2*	Same behaviour as for wall W1 described above. However, specimen W2 was only able to carry 68% of its predicted flexural capacity.
PW2**	Cover spalling initiated above the splice region at 0.75% drift (determined from imposed top displacements at 3.66m). After 3 cycles at the same drift level the longitudinal reinforcement was exposed and longitudinal bars buckled in the boundary element above the splice region. At 1.05% drift concrete crushed where buckling had occurred and the damage extended to the web of the wall, propagating down towards the top of the of the web splices.
RWS	Noticeable strength degradation appeared at 1.2% drift with the fictitious flange in tension, probably due to slipping occurring in the splice region. Main cracks were located approximatively above the lap region and at the wall base. Bond degradation progressed increasingly with the demand. In the end, as the crack at the wall-foundation interface became wide enough, the relative slip between paired bars led to initial local buckling of the longitudinal reinforcement in the boundary element that contained rebars with $d_b=19\text{mm}$.
W-60-C	Splitting cracks were first observed at drift ratios ranging from 0.25% to 0.5%; the widest side splitting cracks occurred near the splice ends, being widest near the base. At the final imposed displacement, neither continuous splitting cracks along the entire splice length nor fully exposed splices were present. However, the loss in strength due to bond degradation in the splice regions is easily inferable from the global force displacement response of the specimen at 2% drift ratio.
W-40-C	Similarly to specimen W-60-C, tensile splitting cracks were observed at early stages of loading. However, before reaching the target drift ratio of 2.5% a crack along the entire length of the boundary splices opened. A drop in lateral load (10% and 4% of the peak lateral load respectively in each direction) occurred when this crack formed. With further displacement reversals the relative slip between splices on one face of the boundary elements led to further decrease of the wall strength until the boundary elements were fully exposed.
W-60-N	The response of W-60-N was similar to the one described above for the specimen W-60-C. However, the smaller amount of confining reinforcement present in W-60-N led to an anticipated onset of strength degradation occurring at a value of drift of 1.5% (0.5% less than the one observed in W-60-N).
W-60-N2	The cyclic behaviour of the specimen W-60-N2 was substantially identical to the one of W-60-N.
TW3	When loading towards the wall end without flange, the test unit failed due to crushing of the wall base. When loading towards the flange, the wall exhibited a softened response due to a progressive failure of the lap splices. Most deformations concentrated in a crack above and below the lap splice zone.

* Used to differentiate the 2 test units from those of Paterson and Mitchell (2003) which are equally labelled.

** PW1 and PW3 tested by the same authors showed a similar behaviour to PW2 (no lap splice failure) and were omitted.

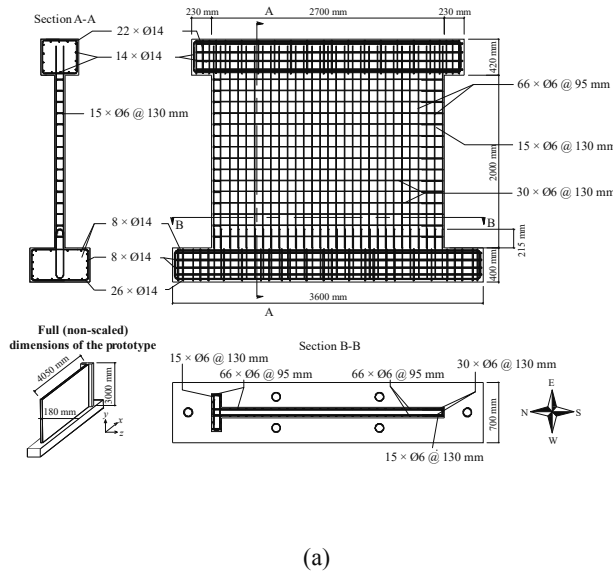
2.3 New experimental tests on walls

Five RC walls at 2:3 scale were tested under quasi-static cyclic loading at *École Polytechnique Fédérale de Lausanne* within an experimental program that aimed at analysing the effect of several parameters in the cyclic response of walls. Among them, the influence of lap splices on the in-plane structural behaviour was addressed by test units TW2 and TW3. A brief description of the test setup and of the wall response follows: the data of these tests and a more detailed description of the test setup is available in Almeida et al. [60].

Walls TW2 and TW3 were identical from the geometrical viewpoint and had a total length of 2700 mm, a thickness of 120 mm, and a height of 2000 mm. The specimens were cast with a 400×400×3600 mm RC foundation, which was prestressed to the laboratory strong floor, and a 2930×420×400 top RC beam to which the vertical and lateral loads were applied. Both units had a 440 mm flange at one extremity, which simulates the effect of a perpendicular wall on member stability. The reinforcement detailing, in which the flexural reinforcement was located on the outside of the shear reinforcement, intended to represent Central European construction practice between 1950 and 1970. The reinforcement layout of the two specimens was identical, apart from the presence of lap splices in test unit TW3, depicted in Figure 2.2 (a). The lap splice length was 215 mm, corresponding roughly to 35 times the diameter of the longitudinal bars. The material properties of TW2 and TW3 are summarized in Figure 2.2 (b).

A sketch of the general test setup is shown in Figure 2.3 (a). The walls were loaded by two vertical actuators, that applied a moment and an axial load, and by one horizontal actuator. The horizontal actuator imposed cyclic in-plane displacements according to the loading protocol shown in Figure 2.4. The vertical actuators were controlled such that the axial load and the shear span was constant throughout the test. The axial load was 690 kN and the shear span 3.15 m, which corresponds to a shear span ratio of 1.17.

The walls were instrumented using conventional (e.g. LVDTs) and optical measurement systems, a complete description of which can be found in Almeida et al. [60]. The deformations of the wall surface were measured using a grid of 29 columns × 18 rows of light-emitting diodes (LEDs) on the east face of the wall; see Figure 2.3 (b). On the west face of the wall the evolution of cracks was monitored with digital image correlation techniques.



Reinforcement ratios (TW2 & TW3)						
	$\rho_{vertical}$	$\rho_{horizontal}$	$\rho_{orthogonal}$			
Web	0.49%	0.35%	[-]			
Flange	0.64%	0.19%	0.35%			
Reinforcing steel properties (TW2 & TW3)						
	f_y	f_u	E_s	ϵ_{sy}	ϵ_{sh}	ϵ_{su}
460 MPa	625 MPa	200 GPa	2.5‰	2.5‰	80‰	
Concrete properties						
	f'_c	f'_t	E_c	ϵ_c		
TW2	50.7 MPa	2 MPa	31.8 GPa	2‰		
TW3	43.3 MPa	2 MPa	30.2 GPa	2‰		

(b)

Figure 2.2: (a) Geometrical and detailing characteristics of test unit TW3; (b) Material properties.

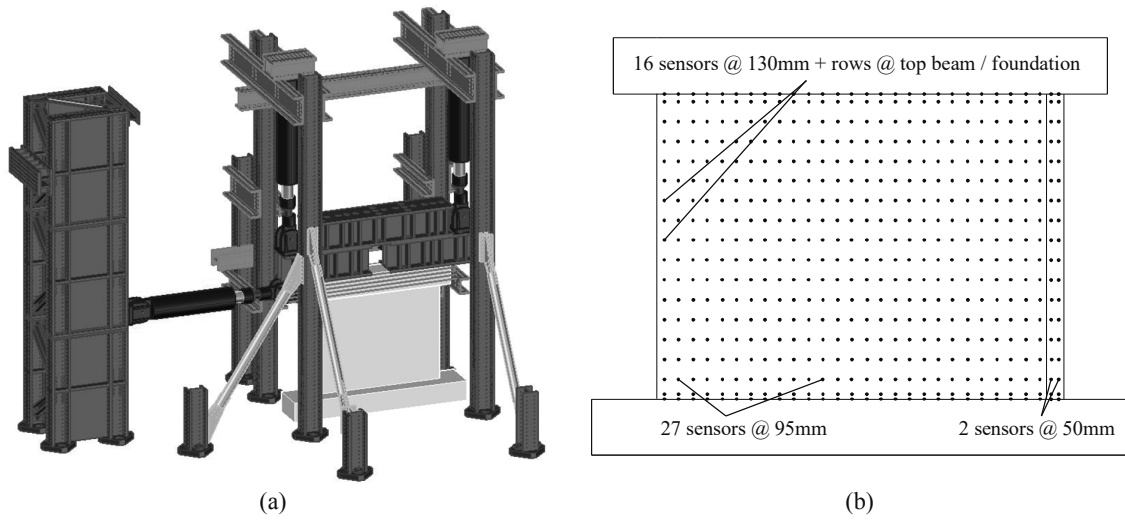


Figure 2.3: (a) View of the test setup; (b) LED grid used for the optical measurement system.

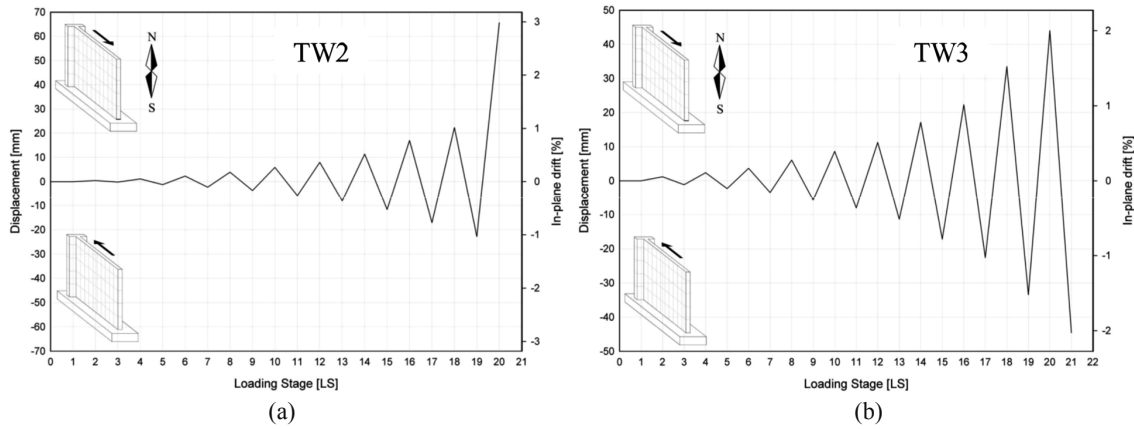


Figure 2.4: Drift protocols of the two quasi-static cyclic tests: (a) TW2; (b) TW3.

2.3.1 Hysteretic behaviour and influence of lap splices

The cyclic force-displacement responses of the test units TW2 and TW3 are depicted in Figure 2.5, which also includes the load stages at which different observable physical events took place. Crushing and splitting cracks were identified by the occurrence of vertical cracks, the former occurring in the compression edge of the test unit and the latter taking place in the tensile side signalling a local bond-slip failure. Table 2.3 summarises the applied load and drift ratio at the occurrence of these events. Cover spalling was not clearly observed when loading towards the flanged side (i.e., flange in compression). When loaded towards the edge without the perpendicular flange (i.e. flange in tension), the test unit TW2 presented a stable hysteretic response until a lateral drift of -0.75% (LS17). Along the same direction of loading, a loss of strength capacity of almost 50% occurred in the following cycle to -1% (LS18→LS19), determining the failure of the member. Failure is herein assumed as a 20% drop in the lateral capacity. As expected, the test unit showed a more ductile response towards the opposite direction (flange in compression), and only showed signs of degrading force capacity above drifts of 1.75% (LS19→LS20).

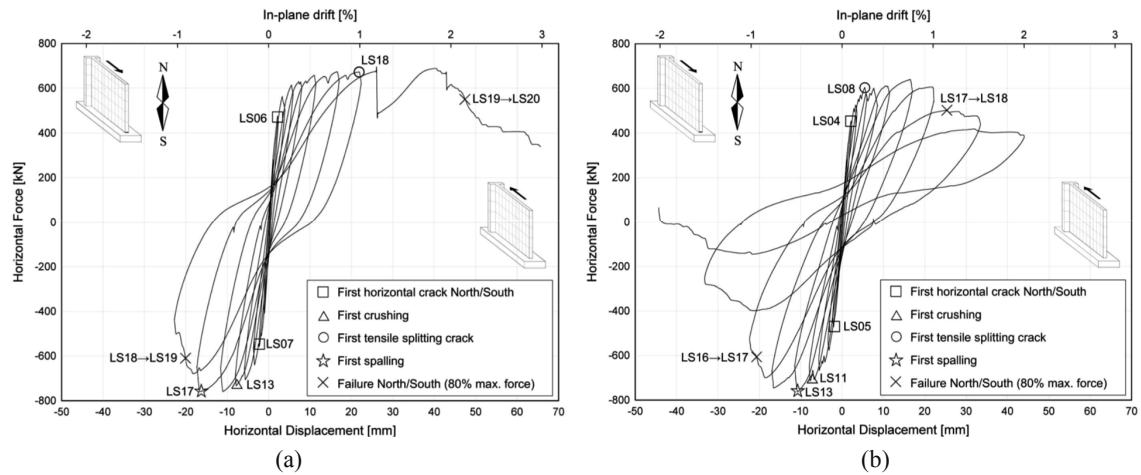


Figure 2.5: Hysteretic force-displacement response of test units: (a) TW2 (Note: the sudden drop occurring at a drift of around 1.25% was due to an emergency stop and it should be disregarded); (b) TW3.

Table 2.3: Summary of applied load and drift ratio at the occurrence of key events during the tests.

Specimen	Load direction	Horizontal Cracking		Spalling		Peak Load		Drift Capacity		Splitting Crack	Bar buckling	Bar fracture
		P [kN]	θ [%]	P [kN]	θ [%]	P [kN]	θ [%]	P [kN]	θ [%]	θ [%]	θ [%]	θ [%]
TW 2	North	475	0.10	-	-	688	1.84	538	2.16	1.00	-	1.84
	South	-559	-0.11	-759	-0.75	-759	-0.75	-607	-0.91	-	-	-
TW 3	North	455	0.10	-	-	640	0.75	501	1.15	0.25	-	1.00
	South	-471	-0.10	-763	-0.49	-763	-0.49	-610	-0.93	-	-0.49	-

θ : Lateral drift (ratio of horizontal displacement to height of application of horizontal load)

The member response of TW3 was similar to TW2 when the flange was in tension, as shown in Figure 2.5. Yet, when the flange was in compression, TW3 did not attain the same value of load capacity (7% less, as indicated in Table 2.3), and the strength degradation started at a smaller drift level (after a drift of 0.75%) resulting in a drift capacity reduction of almost 50%. The reason for this reduction is the presence of lap splices in TW3, which will be discussed in the following. For the loading cycles that tensioned the flange, the well distributed crack patterns on the two walls (near the flange side) were similar. Therefore, the following paragraphs will focus mainly on the distinct local member behaviour that occurred when compressing the flanged edge.

TW2 formed well distributed shear-flexure cracks in the lower half of the wall, see Figure 2.6 (a). As loading progressed the width of all cracks increased approximately evenly, which is a desirable type of plastic hinge behaviour. The first incipient signs of bond-slip degradation along the continuous vertical reinforcement showed up in LS18 (corresponding to a drift of 1.0%), through minor face-splitting vertical surface cracks at the edge without the flange. These cracks spread upwards and downwards (extending only for a couple of centimetres) from a few pre-existing horizontal cracks along the wall height. This is a major difference in comparison with TW3, as discussed subsequently. Figure 2.7 (a) shows the final condition of TW2 at the base of the non-flanged edge, which resulted from distributed concrete compression crushing above the base crack and rebar tensile fracture.

The behaviour of TW3 was governed by signs that highlighted the high stress demand on the concrete in the lap splice region: Figure 2.4 (b) indicates that the first face-splitting vertical cracks at the edge without flange appeared at the early loading stage LS08 (corresponding to a drift of 0.25%). This should be compared with the incipient splitting cracks that appeared at 1% drift for wall TW2, see Figure 2.5 (a). In TW3, at LS10 (0.35% drift), a clear side-splitting crack at the non-flanged edge extremity also showed up extending throughout approximately the height of the entire lap splice, see Figure 2.8 (a).

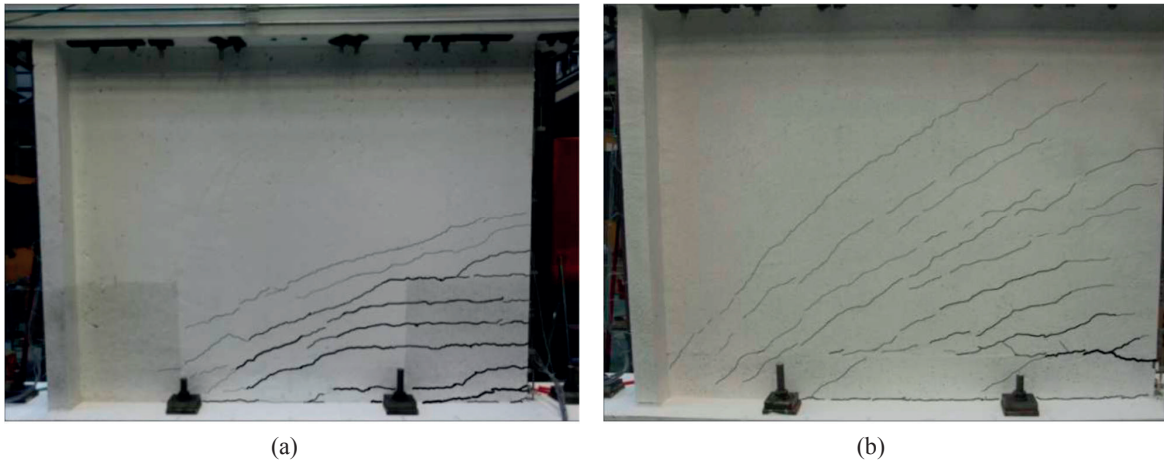


Figure 2.6: Crack pattern at 0.75% drift: (a) TW2; (b) TW3.

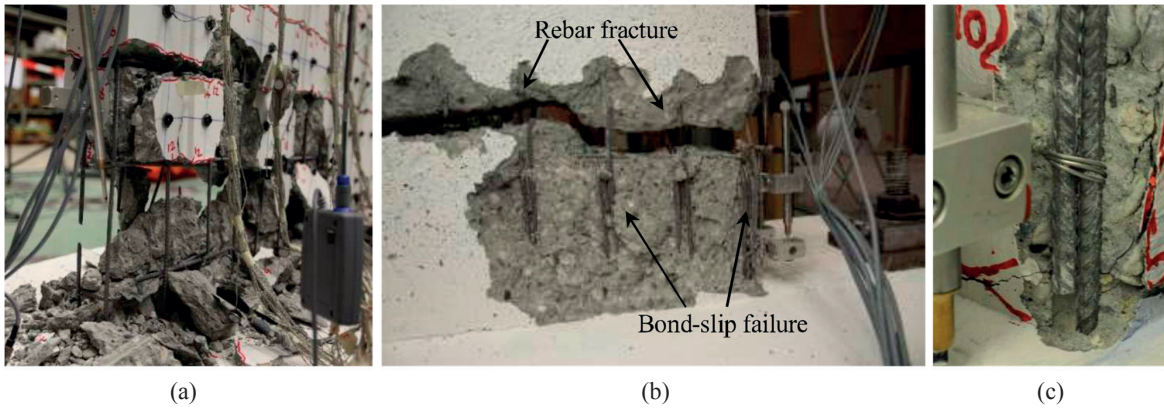


Figure 2.7: Base of the wall edge without flange in the last load stage: (a) TW2; (b) TW3; (c) Photographic evidence of bond slip failure in TW3 at LS16 (1% drift), after spalling of the corners.

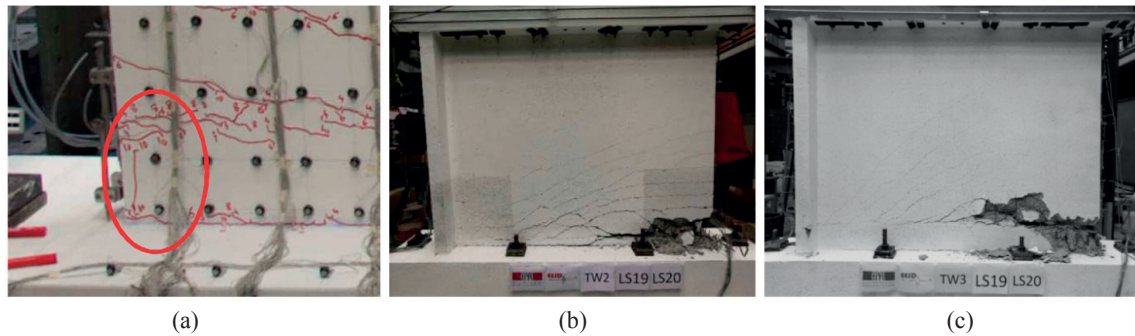


Figure 2.8: (a) Occurrence of side-splitting crack along the lap splice height for TW3, at LS10 (0.35% drift); Visual condition of the walls at last load stage before the end of the test, wherein both specimens were resisting approximately to 60% of the peak force: (b) TW2; (c) TW3.

From cycles LS11 and LS12 onwards (0.5% drift), deformations of TW3 started to concentrate in the horizontal crack just above the lap splice (at around 220 mm above the foundation). No new cracks formed, and the pre-existing ones above the lap splices progressively reduced their width. This redistribution of stresses within the member associated to the localization of deformations is a consequence of lap splice failure. Concrete crushing localized in that same crack when loading was reversed and the wall was pushed towards the edge without flange.

At LS16 (1% drift), following concrete cover spalling in the lap splice region, the large relative slip at the lower end of the splice could be observed visually, Figure 2.7 (c). Tensile failure of bars along the large crack above the lap splice involved a combination of rebar fracture and lap splice failure, Figure 2.7 (b). Bar rupture seems to have taken place when

loading from LS17→LS18 (1.5% drift), when consecutive sounds of rebar rupture could be heard. At this value of lateral displacement the wall had already lost 20% of its force capacity—see point of failure depicted in Figure 2.5 (b)—which further confirms that bond-slip was the triggering source of lateral load failure. Figure 2.7 provides evidence on the influence of lap splices at member failure: in the wall without lap splices (Figure 2.7 (a), TW2), damage (concrete crushing and rebar fracture) spreads along a height of around 300 mm, while in the wall with lap splices (Figure 2.7 (b), TW3) crushing initiates and concentrates at a single major crack above the web. Looking at the entire wall, Figure 2.8 (c) confirms that damage concentrated in the lap splice region, while the remaining part of the member remained largely intact, contrasting with the equivalent view of unit TW2 in Figure 2.8 (b).

2.4 Inelastic cyclic response of lap splices in walls loaded in plane

2.4.1 Influence of lap splices on cyclic wall performance from tests and field observations

Based on the experimental findings in literature and the new tests presented above, this section addresses the effect of wall lap splices with regard to: (i) the location of the critical section within the wall and the displacement capacity of the wall, (ii) failure modes of lap splice and the influence of a moment gradient, (iii) force-displacement response of walls with lap splices, and (iv) the axial load bearing capacity of walls after lap splice failure.

- (i) **Location of critical section and displacement capacity of the member.** Field observations showed that lap splices often shift the critical section resisting to overturning moments and concentrate inelastic response. This was evident in the reported collapse of the chimneys during the 1999 (Turkey) and 2007 (Japan) earthquakes, as well as in several buildings in Chile and New Zealand after the earthquakes of 2010 and 2011. These notes from field reports are backed up by conclusions from experimental tests (Table 2.2), which show that lap splices in walls reduce the displacement ductility relative to that of a wall with continuous reinforcement. In walls designed according to modern detailing rules, which will require appreciable confinement of the lap splice, the plastic hinge is forced to relocate to a section above the lap splice, where damage will concentrate (e.g., in the form of concrete crushing and rebar buckling/fracture), leaving the lap splice region largely undamaged [15]. Shifting the plastic hinge to a section above the lap splice reduces the member ductility (as already previously observed for columns [54] and also increases the shear demand on the wall.

For walls with lower horizontal reinforcement ratios ($\rho_h < 0.25\%$) or shorter lap splices ($l_s < 40\text{--}45 d_{bl}$), damage generally first manifests in the form of splitting cracks along the lap splice length. As the imposed member displacement demand further increases, such bar slippage reflects in the build-up of horizontal cracks forming at the top and bottom of the lap splice.

Finally, if the wall lap splice region is not adequately confined, a corresponding reduction of the splice deformation capacity is inevitable, and consequently the member flexural ductility capacity also diminishes. For cases of poor transverse reinforcement or short lap splices, the flexural yield member strength may not even be attained and a sudden brittle failure will occur.

- (ii) **Failure modes of lap splices and influence of a moment gradient.** Lap splices can fail in three modes, i.e. (i) tension failure, (ii) tension failure upon load reversal after concrete crushing in compression took place, and (iii) compression failure of the lap splice in conjunction with crushing of the concrete. The latter is uncommon in walls (compression failure tends to initiate in the crack above the lap splice) but the two first modes have both been observed. When walls are tested under cyclic loads, it is often difficult to distinguish between these two modes. During quasi-static cyclic tests, the onset of formation of splitting or crushing cracks indicates whether failure of the splice initiated when it was in tension or in compression, respectively.

It is noted that member failure due to lap splices does not imply that all rebars must fail through a bond slip mechanism. In fact, mix of bar fractures and splice failures were observed both in post-earthquake scenarios, such as in the *Alto Río* building in Chile [6], and in experimental tests, such as wall TW3 as depicted in Figure 2.7 (b).

The existence of a moment gradient (shear) over the lap splice length appears to be another fundamental aspect in the behaviour of walls. Although the presence of shear and therefore a gradient in tension force over the length of the lap splice is in principle beneficial to its performance (see discussion on factors affecting lap splice response in the next Section), it can lead to degradation of the lateral load capacity due to the occurrence of a single widening

flexural crack just outside the high moment end; hence, closely spaced confinement should be extended to the neighbouring region whenever possible in design.

- (iii) **Force-displacement response of walls with lap splices.** The analysis of the cyclic force-displacement responses of the wall specimens collected in the database, depicted in Figure 3.14 and Figure 3.15 of the next Chapter, indicate that the failure of the outermost layer of lap splices typically signals a marked specimen strength degradation and can be hence assumed as member failure. The displacement corresponding to this onset of degradation, as observed from the experimental tests (Δ_{deg}), is also indicated in the abovementioned figures. In Table 2.1 the corresponding drift (δ_{deg}), defined as the ratio between Δ_{deg} and the specimen height, is reported. Pinching of the hysteresis curves after such onset of lap splice strength degradation are also evident in many tests, indicating bond deterioration and slip along the lap length, which is a type of behaviour that had been also observed in beam tests [48]. Additionally, past experimental programs on columns showed the large sensitivity of the post-peak branch to variations of the loading history [12].
- (iv) **Axial load bearing capacity of walls after lap splice failure.** Lap splice failure originates a rocking type of response that does not necessarily result in overturning [6,24]. However, it is believed that such type of lap splice response in relatively thin RC walls is not reliable because it is uncertain whether the wall base can endure the impacts associated with rocking (which can cause concrete crushing) and because a lateral out-of-plane shift of the wall can occur due to ground motion components in the perpendicular direction or due to torsional effects. Song et al. [6] name the same causes for the collapse of the *Alto Río* building in Chile. Conversely, in bridge piers that are typically wider than walls, the rocking response after lap splice failure might be rather stable [57]. Finally, in walls with insufficient shear reinforcement, a premature lap splice failure might precede a shear failure [57]. Lap splices might therefore act as a “fuse”, which prevents the loss of the axial load bearing capacity entailing from shear failure.

2.4.2 Factors affecting lap splice strength and strain at degradation onset

With a view to contribute to seismic modelling tools, the three following quantities define the basic corner points of an equivalent uniaxial stress-strain curve for lap splices of longitudinal reinforcement in cyclically loaded walls:

- (i) **Strength.** Lap splice strength has been thoroughly addressed over the last decades and therefore its influencing factors are well known, particularly in the context of monotonic loading. Discussions and computation of lap splice strength are inseparable from the concept of bond stress, which plays a central role in most strength prediction models and code prescriptions. They are typically based on estimations of an *average* bond stress (averaged over bar lengths of at least 18 bar diameters). It is noted that *local* bond stresses, derived from measurements along shorter distances of one to three bar diameters [61] can be four to five times larger [40].
- (ii) **Strain at degradation onset.** Average strains within the splice length at the onset of degradation were seldom measured in past experimental tests. However, it is a fundamental quantity for the development of an equivalent constitutive model for lap splices. From analysis of experimental and numerical results (Chapter 3), it appears too conservative to assume that the strain corresponding to the onset of cyclic strength degradation corresponds to the lap splice strength divided by the steel Young’s Modulus. Despite its relevance for simulation purposes, only few expressions could be found in the literature to estimate the strain capacity of lap splices [24,31,32], of which only one provided an expression for the maximum tensile strain that the lap splice can sustain [32].
- (iii) **Residual strength and strain.** Upon the onset of lap splice degradation, the strength of most test units with lap splices dropped sharply while for two test units the loss of strength was more gradual (TW3 and VK2). Post-peak response modelling is a delicate task as it requires challenging procedures to match numerical and physical localization issues [33,62,63]. This applies in particular to brittle deformation mechanisms such as lap splices, which are often characterized by steep softening slopes. Both under monotonic and cyclic loads, some resistance is maintained even at large values of bar slip due to friction and interface shear [40], which is however difficult to quantify.

The derivation of expressions to estimate both lap splice strength and the strain at the onset of cyclic degradation relies on a correct identification of the corresponding governing factors. Many expressions are available in the literature to estimate the monotonic strength of lap splices since the corresponding influencing factors are well identified and there is sufficient experimental test data for calibration and statistical validation. It can be expected that most factors governing the monotonic strength also significantly influence the response under repeated or reversed cyclic loads. For what concerns the strain at the onset of degradation, scarcer experimental results are available. The governing parameters are therefore retrieved from regression analysis of the simulated wall database, which is detailed in Chapter 3. A summary of

the determined key factors influencing both lap splice strength and strain at the onset of degradation is given in the following.

2.4.2.1 Splice length

Design and assessment codes assume an average (constant) bond strength for concrete that is estimated based on a number of parameters [40]. The lap splice length is not among them, which is at odds with the established decades-long observation that there is a nonlinear relation between splice length and splice strength [64,65]. In fact, under monotonic loading the effectiveness of a splice reduces with the increase in length as the bond stress throughout the length progressively changes from an approximately constant distribution to one wherein stress concentrates at the splice extremities [3]. Further, it is also known that this bond stress concentration is more pronounced for smaller diameters, and hence the ratio between the lap splice length and the bar diameter should be the controlling parameter. As stated in Song et al. [6], who used data reported by the ACI [66] and Seliem et al. [67], the monotonic unit bond strength of unconfined deformed bars with relatively small cover shows a clear inverse proportionality with the previously noted ratio. Canbay and Frosch [3] analysed a database of 203 beam tests containing lap splices in constant moment regions with splitting failure and estimated that splice strength is proportional to the square root of the ratio lap splice length-bar diameter.

The extent to which the previous observations apply to cyclic response is still not clear. However, as discussed below, it is known that transverse confining reinforcement plays a fundamental role to ensure that longer lap splices perform well under cyclic loading. If an adequate confinement is not provided to prevent bond strength degradation, additional lap length is of little added value as yielding will quickly penetrate from one or both ends accompanied by progressive longitudinal splitting. Paulay [10] named this succession of events as an ‘unzipping phenomenon’.

Lap splice length is also strongly correlated to the average lap splice strain capacity. This effect can be also observed at the member level regarding the drift δ_{deg} at the onset of strength degradation, see Figure 2.9 (a). As discussed in the next sub-section, the abscissa coordinate depicts the ratio between the lap splice length and the shear span, but it is the former variable that relevantly affects this trend. In contrast, the statistical correlation for the lap splice strain capacity does not improve when the ratio between the splice length and the rebar diameter is considered.

2.4.2.2 Moment gradient

Most experimental tests to date have been carried out on lap splices in beam and column regions subjected to a constant moment [64]. When the effect of moment gradient was first studied under monotonic loading, some researchers proposed simple modifications for the splice strength to account for the ratio between the smaller and the larger stress at the two splice ends [65,68]. Others observed that, for tests below yield and from statistical analyses, the effect of moment gradient did not seem relevant enough to justify an inclusion in the developed expression for the bond strength [37].

As further experimental evidence accumulated, it became clear that a moment gradient along the lap splice was always unquestionably beneficial for splice performance. In fact, without shear (uniform moment), damage progresses from both ends of the splice potentiating its detrimental interaction. With increasing shear (and thus larger moment gradients), the failure initiates from the extremity with higher moment and the interaction between the two ends is reduced. The specimens with shear tested at *Cornell University* sustained unequivocally a larger number of cycles above 95% of yielding than the specimens under constant moment [8].

Because lap splice tests with varying moment are difficult to interpret and provide larger estimates of bond strength [3], most available expressions for the prediction of lap splice strength do not account explicitly for the effect of the moment gradient.

For RC walls with continuous longitudinal reinforcement, plasticity spreads along the member as the moment gradient decreases, enabling the member to achieve a larger ductility capacity. For many decades, most expressions for the plastic hinge length have thus reflected this effect, wherein the moment gradient is represented by the shear span [69]. As mentioned in the beginning of this sub-section, the moment gradient along the lap splice is also expected to influence its ductility. However, unlike for continuous longitudinal reinforcement, a larger moment gradient is now expected to increase the ductility capacity. This effect has been mentioned in recent wall tests with lap splices [13,14]. Because the member shear span only insufficiently reflects the effect of the moment gradient along the lap splice, the ratio between the lap splice length and the shear span should be considered instead, see Figure 3.12 of Chapter 3. At the member level, the influence of this ratio on the drift at degradation onset δ_{deg} is also apparent; see Figure 2.9 (a).

Finally, it is observed that this effect on lap splices in walls is expected to be possibly more detrimental than along column lap splices in ductile frames. In fact, whereas for the latter the shear span varies typically between half and the total storey height, the shear span at the wall base in a building with more than 4-5 storeys can be a multiple of the storey height, therefore inducing a close to uniform moment profile along the lap splice length.

2.4.2.3 Transverse reinforcement

Transverse (confining) reinforcement is the most critical factor in the response of lap splices, regarding both strength and strain at degradation onset. The effect of transverse reinforcement is particularly important after tensile splitting has taken place, since splitting planes inevitably cross layers of transverse reinforcement [31]. The tension stress in the hoops allows to transfer bond stresses between bars and concrete via a shear friction mechanism [31]. Transverse reinforcement delays yield penetration rate into the splice [8]. It has been shown experimentally that specimens with well-confined lap splices can sustain many cycles of repeated load up to a displacement ductility of at least two before failure [8,48].

However, a large amount of transverse reinforcement can bring undesired consequences. By limiting yield penetration into the splice region, the plastic hinge length may reduce significantly. The curvature ductility required to attain the imposed lateral displacement will therefore increase, resulting potentially in large steel strains, excessive strain hardening and possible fracture of longitudinal reinforcement [10]. Conversely, and alternatively, splices detailed according to modern codes can force wall damage to occur at the top of the splice, thus relocating the critical section and reducing the member drift capacity [15,54].

Based on tests of four columns subjected to monotonic tensile loading and four columns under severe load reversals, Aristizabal-Ochoa et al. [70] concluded from strain measurements in transverse reinforcement that hoops at the ends of the splice are more effective than interior hoops in confining the lap splice and that an insufficient amount can lead to a reduction in deformation capacity and strength. This observation is coherent with the previous comment regarding the concentration of bond stress at the extremities of long lap splices under monotonic behaviour. However, as discussed in ACI [40], the comprehensive research carried out at *Cornell University* [44,45] observed that the bursting forces tended to distribute uniformly along the lap splice as yield penetration progressed, concluding that uniform stirrup spacing provides the most effective confinement for cyclic loading, which confirmed the early studies by Muhlenbruch [71]. These observations seem to indicate that cyclic loading contributes to ‘smooth’ the rebar strain and stress demands along confined lap splices, hence supporting the use of an equivalent steel constitutive model for the entire region.

Figure 3.12 (b) in Chapter 3 shows that the average lap splice strain capacity correlates strongly with the confinement reinforcement. At the member level, the displacement at the onset of lap splice degradation is also clearly correlated with the confinement reinforcement ratio, as shown in Figure 2.9 (b). A possible justification is the increased significance of the shear friction component after splitting cracks have formed, enabling the transfer of forces between two spliced bars and a more efficient yield penetration along the lap splice without sudden strength degradation [31]. This comes in line with the consideration that the frictional mechanism in the post-yield range represents an important contribution. In particular, low levels of strains at degradation onset were observed for those specimens that presented no stirrup branches between the lap splices and the side or face surfaces (or both), i.e. when at least one splitting crack could freely develop from the rebars to the surface.

2.4.2.4 Concrete cover, longitudinal bar spacing and diameter

All the specimens summarised in Table 2.1 with lap splice degradation developed splitting cracks. The occurrence of this failure mode (instead of pull-out) can be mainly ascribed to the fact that all specimens had a concrete cover less than 2.5 bar diameters. In the presence of closely spaced stirrups, splitting brings about an increase in ductility and energy absorption, facilitating a redistribution of forces and a nearly constant bond stress along the splice [8,31].

Concrete cover, bar spacing and diameter are directly taken into account for the computation of the lap splice strength. However, they do not have a clear influence on the strain capacity at degradation onset, possibly because they vary within a narrow range for most of the walls in the database. Figure 2.9 (c) shows that, also at the member level, the drift at degradation onset δ_{deg} is not sensitive to the clear face cover of reinforcing bars.

2.4.2.5 Cyclic loading

The tests at *Cornell University* [8] showed that repeated loading and the number of load cycles have little effect on lap splice behaviour if the load level is below approximately 75% of the monotonic capacity. However, when not appropriately confined, the rate of bond deterioration in lap splices increases rapidly even for a few cycles close to yield, also

because excessive compressive strains will cause microcracks that will in turn reduce the tensile concrete strength [31]. To overcome this problem, Paulay [10] and Sivakumar et al. [47] proposed rules for adequate design of confining reinforcement, and demonstrated experimentally that they allow lap splices to safely sustain cycling up to 95% of its ideal flexural strength, and even to perform satisfactorily in the inelastic range for many cycles of low ductility demands.

It is also well known that fully reversed cyclic loads are significantly more unfavourable to lap splice performance than repeated unidirectional loads, which can be readily explained by the progression of physical damage induced by cyclic loads. The beam tests carried out by Sparling and Rezansoff [48] are exemplary illustrations of this effect: although a well-confined reference unit tested under monotonic loading reached 123% of the yield load at a displacement ductility of 4.37 and an identical beam loaded under repeated unidirectional loads sustained 579 cycles between 109% and 130% of the yield load up to a ductility of 3.91, the specimens that were subjected to reversed cycling at 109% of the yield load resisted only to 56-175 cycles failing at considerably smaller ductilities of 2.04-2.87.

The previous observations suggest that the error associated with using existing expressions for monotonic splice strength to estimate the capacity of specimens under seismic loading is acceptable. The comparison of the experimental data and the results of the numerical simulations in Chapter 3 confirms that, for the loading protocols imposed in the wall tests performed at *EPFL*, such hypothesis is valid and will thus be adopted.

2.4.2.6 Other factors

Bond strength before the development of splitting cracks is directly related to the tensile strength of concrete, which in turn is often expressed as a function of the compressive strength. The relatively small size of the wall database combined with the narrow range of concrete compressive strengths of the test units, depicted in Figure 2.1, did not allow to draw any conclusions with regard to the possible influence of this variable on the strain at degradation onset.

Other factors influencing lap splice behaviour [40] are not herein addressed due to space limitations and also because they fall outside the scope of the present study. Among them, the wall length appears to be of possible relevance since the regression analysis of computed strains at degradation onset showed that these values tend to be larger for longer walls. This dependency can perhaps be explained by an increasing relevance of the shear deformation mechanism for longer walls after flexural stiffness drop due to rebar yielding and progression of splitting cracks, which would thus delay the occurrence of strain degradation at lap splices. Nevertheless, as most of the members in the database have lengths in the reduced band of 1-1.5 m, it was preferred to neglect such parameter and thus to not extrapolate the relation for larger (more realistic) values of wall lengths. Other influencing factors on the lap splice strength and possibly on the strain at degradation onset include the relative rib area (namely smooth vs ribbed bar), casting position, concrete vibration, reduction of bond strength due to epoxy coating [72], type of concrete [17], corrosion level, presence of alkali-silica reactions, temperature, effect of steel or polymer fibres in concrete, etc.

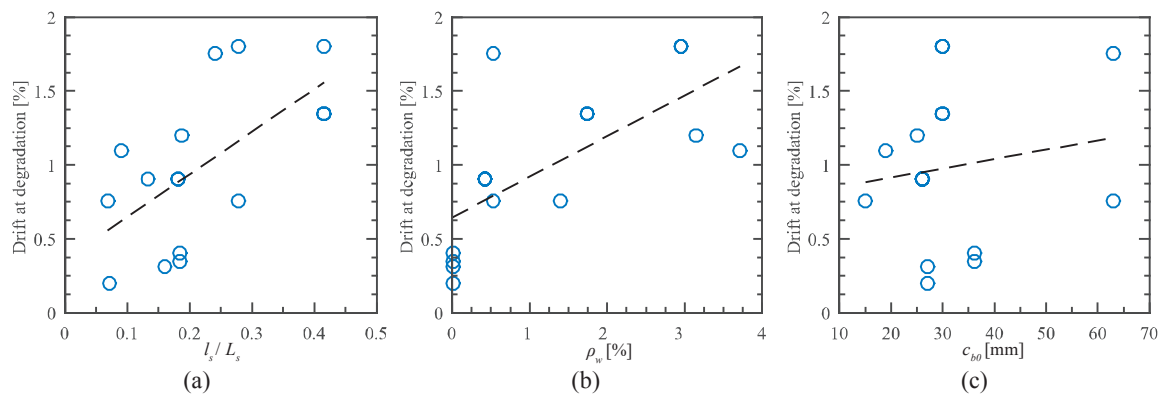


Figure 2.9: Linear regression of experimental data relating drift at onset of strength degradation with: (a) Ratio between lap splice length and shear span; (b) Confining reinforcement ratio; (c) Clear face cover of reinforcing bars.

2.5 Conclusions

Field evidence collected after recent earthquakes has shown that the cyclic inelastic response of many RC wall structures was adversely affected by the presence of lap splices, including cases in which such structures were designed according to modern codes. A number of experimental programmes were launched during the last years to better understand the full extent to which such constructional detail affects the inelastic cyclic performance of walls. The present Chapter collected and systematized the results of such tests, which are constituted by 16 walls with lap splices and 8 reference units with continuous reinforcement. They include a recent test campaign performed at the structural laboratory of *EPFL* involving two large-scale walls (one with and one without lap splices). The latter complement the existing tests by investigating a member with a large lap splice length to shear span ratio, which allowed to investigate the influence of the moment gradient on the lap splice performance.

The assembled database allowed for identification the factors that most crucially influence the displacement ductility of walls with lap splices. This aspect, of fundamental relevance in seismic engineering applications, has not been object of extensive studies in the past, which focused mainly on the determination of the strength of lap splices. The displacement ductility of members with lap splices was shown to be mainly affected by the confining reinforcement, moment gradient, lap splice length, and loading history. They are used in Chapter 3 to derive an expression to estimate the strain at the onset of splice degradation.

2.6 Acknowledgments

The financial support by the *Stiftung zur Förderung der Denkmalpflege* to the project “Erbeverhalten von bestehenden Stahlbetongebäuden mit dünnen Wänden” and by the *Swiss Federal Roads Office (OFROU)* to the project number AGB 2015/002, under which the present study was partly carried out, is acknowledged.

3 Equivalent Uniaxial Lap Splice Constitutive Law for the Simulation of Spliced RC Walls

This Chapter presents a uniaxial, equivalent steel constitutive law for lap splices, which can be used in shell element models to simulate the behaviour of spliced RC walls. It represents the post-print version of the article:

D. Tarquini, J.P. Almeida, O. K. Beyer, 2017. “Influence of lap-splices on the cyclic inelastic response of reinforced concrete walls. II: Shell element simulation and equivalent uniaxial model”, *ASCE Journal of Structural Engineering* 143 (12), DOI: [10.1061/\(ASCE\)ST.1943-541X.0001859](https://doi.org/10.1061/(ASCE)ST.1943-541X.0001859).

Figures and tables formatting, reference-, section-, and equation- numbering were adapted to the style of this document. The first author developed the model, carried out all the analyses and wrote the article under the supervision of the second and third author.

Abstract

Spliced longitudinal reinforcement may result in a reduction of both strength and displacement capacity of reinforced concrete (RC) members. This applies in particular if lap splices are located in regions where inelastic deformations concentrate, such as the plastic zone at the base of RC walls. The present Chapter introduces a simple numerical model suitable for engineering practice to simulate the force-displacement response of RC walls with lap splices. Based on experimental data from 16 test units, an equivalent uniaxial steel stress-strain law is proposed that represents the monotonic envelope of the cyclic response of spliced rebars in RC walls up to the onset of strength degradation. It allows to model lap splice response with finite element models while avoiding the use of complex interface bond-slip elements. A new semi-empirical expression for the strain at the onset of strength degradation is derived, which expresses the strain capacity of the lap splice as a function of the confining reinforcement ratio and the ratio of lap splice length to shear span of the wall. The proposed equivalent constitutive law was included in shell element models to predict the force-displacement response of the above set of RC walls. Results demonstrated the ability of this approach to adequately capture the peak strength and displacement capacity of the spliced units.

Keywords: Seismic effects; Reinforced concrete walls; Lap splice; Equivalent uniaxial model.

3.1 Introduction

Most performance-based assessment approaches are based on the comparison between the structural displacement capacity and the expected demand. In new reinforced concrete (RC) structures, the capacity design philosophy [69,73] ensures that the response is governed by a ductile flexural mechanism. Estimating the displacement capacity of existing structures is a more challenging task since a large number of failure modes and deformation components need to be considered [74]. In particular, the displacement capacity of a structural member can be substantially reduced by detailing deficiencies such as insufficient shear reinforcement, insufficient confinement of boundary elements or the presence of poorly detailed spliced longitudinal reinforcement.

This Chapter addresses the detrimental effect of lap splices in the cyclic behaviour of RC walls which may adversely affect the overall structural seismic response. While the force-capacity of lap splices has been extensively studied in the past, their deformation ductility was only addressed in a limited number of models. They were all developed in the framework of plastic hinge analysis and will be herein reviewed. The present work aims at complementing previous studies by proposing a new equivalent steel stress-strain relationship for the behaviour of spliced rebars in RC walls. It can be used in numerical simulations avoiding the need for complex interface bond-slip models in finite element analysis (typically required to account for the slip of the reinforcement with respect to the surrounding concrete), resulting thus in a suitable tool for engineering practice. The entailing monotonic constitutive model, intended to be an envelope of the cyclic response of lap splices up to the onset of strength degradation, is built from two defining points representing an equivalent yield and an ultimate condition. The yield point is related to the lap splice strength, for which the existing large number

of literature proposals are first reviewed and subsequently applied to the spliced RC walls of the database—16 walls with lap splices plus 8 reference units with continuous reinforcement—collected in Table 2.1. The ultimate strain capacity describes instead the point of strength degradation onset triggered by the presence of lap splices in the structural member and is obtained from regression analysis of the response of the 16 spliced units. Finally, the validation of the proposed equivalent constitutive law is carried out by combining it with shell element models to estimate the force-displacement response of the complete set of RC walls.

3.2 State-of-the-art models for lap splice behaviour

The majority of previous studies on lap splice response concentrated on lap splice strength rather than lap splice deformation capacity. The latter was mainly addressed by means of plastic hinge models, for which moment-curvature relationships were adapted to account for the reduction in deformation capacity due to this constructional detail.

Existing finite element simulations of the full monotonic or cyclic behaviour of members with lap splices typically employ local bond-slip laws that have been developed for isolated anchored rebars, which is an effort in progress since the initial thriving phase of the finite element method back in the late 60s / early 70s [75,76]. Currently, the most well-known and widely employed model to describe the hysteretic response between bond stress and slip in an anchored bar failing by pull-out is the one proposed by Eligehausen et al. [61]. Cyclic bond-slip models for splitting failure (i.e., for bars with small concrete cover, such as in RC walls) are scarcer [40], but a few recent proposals have addressed this gap [77–80].

3.2.1 Lap splice strength: literature review and application to wall database

Several expressions have been proposed to compute the bond strength of spliced bars. Most of the available models aim at predicting the strength of single lap splices under monotonic loading and are based on estimations of an average bond stress. They were obtained either from regression analyses of experimental test data [37,38,81–85] or, more recently, using physically-based principles of tension cracking of concrete [3,31]. Expressions derived from regression analysis of experimental tests under cyclic loading are also available in the literature, as those of Biskinis and Fardis [55] and Sakurada et al. [86]. In the following paragraphs a qualitative overview of the abovementioned models is presented.

The first proposal for the strength of tension lap splices, based on a nonlinear regression analysis of results from beam tests under monotonic loading, is the one by Orangun et al. [37]. This equation, which forms the basis for the bond requirements of the current ACI 318 Building Code [17], reflects the effect of splice length, cover, spacing, bar diameter, concrete strength, and amount of transverse reinforcement on the strength of anchored bars. A similar expression for compression lap splices under monotonic axial loading was proposed by Cairns [84]. The parameters that influence the behaviour of tensile lap splices play similar roles in compression splices but their relative importance changes. Namely, with respect to tension splices, the significance of transverse steel increases while the influence of concrete cover and bar size decreases. Sozen and Moehle [83] proposed a simple lower-bound equation for the maximum tensile unit bond strength of anchored and spliced bars. Besides concrete cover, bar spacing, amount of transverse reinforcement and concrete strength, the influence of casting position and epoxy coated bars was also taken into account. More recently, Esfahani and Rangan [87] also presented an expression for the estimation of the bond strength of tension lap splices for both normal and high-strength concrete. It was initially introduced for the unconfined case and later extended to account for transverse reinforcement [82]. One of the most commonly used predictive equation built on regression analysis of monotonic experimental data is the one provided by Zuo and Darwin [38], which forms the basis for bond recommendations given by the ACI committee 408 [88]. The latter expresses the splice strength of bottom cast uncoated bars as a function of member geometry, concrete strength, relative rib area, bar size, and confinement exerted by both concrete and transverse reinforcement. An improvement of this model was proposed by Ichinose et al. [81] whom, based on experimental data on pull-out and lap splice tests, modified the original equation to account for size effect. The revised expression suggest a large size effect for splices with small cover and short splice length—where brittle failure is expected—and a small size effect for splices with low rib-height bars and high confinement—where ductile failure is likely. Based on a semi-empirical approach, an alternative formulation for the bond strength of spliced bars—included in fib Model Code [89]—was proposed by Lettow and Eligehausen [85]. This category of methods consists in using numerical results (from experimentally validated models) to calibrate the proposed analytical equations.

To the author's knowledge there are only three models for lap splice strength currently available in the literature, based on statistical regression analyses, which are backed by an experimental database including cyclic loading tests: namely the one of Sakurada et al. [86], Cho and Pincheira [90] and Biskinis and Fardis [55]. The first, using results from sixteen beam specimens subjected to reversed cyclic loading tests, proposed an equation for the unit bond splitting strength depending on rebar diameter and spacing, amount of lateral reinforcement, and concrete strength. The second, using a database of 14 column tests under reversed cyclic loading, suggested a modification of the equation for lap splice strength available in FEMA 356 [91]. Finally the third, built on a semi-empirical approach and stemming from a large database composed of beams and columns, proposed an expression where the only parameters involved are the lap length, rebar diameter, and material strengths.

As mentioned in the first paragraph of the present section, models with a theoretical mechanical basis were also developed. The first one, introduced by Priestley et al. [31], estimates the strength of lap splices from considerations on the failure mechanisms and is applicable for circular and square beams and columns. The second, developed by Canbay and Frosch [3], is built on a physical model of tension cracking of concrete in the lap-spliced region. Two different types of failure modes are considered: horizontal splitting that develops at the level of the bars (side-splitting failure), and vertical splitting that develops along the bar on the face cover (face-splitting failure). The final equation of the lap splice strength includes also a term that accounts for the presence of confining reinforcement and it was validated against a database of beam tests with lap splices in the constant moment region, which were loaded monotonically.

Table 3.1 lists the results in terms of lap splice strength f_s obtained by the application of the most relevant models, among those described above, to the database of RC walls with lap splices. The diverse models produce sensibly different results, with a mean and maximum coefficient of variation for the computed lap splice strengths of 12.4% and 19.3% respectively. The table also indicates how the predicted values of f_s compare with the steel yield and ultimate stresses (f_y and f_u): when $f_s < f_y$, lap splice failure is expected before yielding of the longitudinal rebars. This feature should be accounted for in an equivalent steel stress strain model for the characterization of the lap splice behaviour.

Table 3.1: Lap splice strength predicted according to different models.

Test Unit	Orangun et al. (1977)		Priestley et al. (1996)		Zuo and Darwin (2000)		Canbay and Frosch (2005)		Eligehausen and Lettow (2007)		C.o.V
	f_s	$f_s > f_y$	f_s	$f_s > f_y$	f_s	$f_s > f_y$	f_s	$f_s > f_y$	f_s	$f_s > f_y$	
	[MPa]	[-]	[MPa]	[-]	[MPa]	[-]	[MPa]	[-]	[MPa]	[-]	
TW3	1026	✓	987	✓	1188	✓	669	✓	901	✓	17.8
VK2	774	✓	897	✓	700	✓	691	✓	627	✓	12.5
VK4	776	✓	900	✓	701	✓	692	✓	627	✓	12.6
VK5	736	✓	853	✓	678	✓	672	✓	611	✓	11.5
PW2	986	✓	838	✓	904	✓	1159	✓	820	✓	13.1
RWS A-A	895	✓	844	✓	1062	✓	815	✓	894	✓	9.5
RWS E-E	1240	✓	1092	✓	1181	✓	1189	✓	906	✓	10.5
W1/2	646	✓*	714	✓	526	✓*	544	✓*	505	✓*	13.6
CW2/3	343	✗	374	✗	428	✗	349	✗	393	✗	8.2
W-MC-60C	969	✓	891	✓	882	✓	968	✓	801	✓	6.9
W-MC-40C	681	✓	598	✓*	645	✓*	736	✓	655	✓*	6.8
W-MC-60N	1012	✓	930	✓	753	✓	817	✓	743	✓	12.3
W1*	277	✗	415	✗	393	✗	315	✗	480	✓*	19.2
W2*	274	✗	409	✗	390	✗	313	✗	477	✓*	19.3

f_s : computed lap splice strength; f_y : measured rebar yield strength; f_u : measured rebar ultimate stress;

✓: $f_s > f_u$ ✗: $f_s < f_u$ ✓*: $f_y < f_s < f_u$

12.4

3.2.2 Deformation capacity of lap splices

Although reliable estimations of the lap splice strength are required for structural assessment, the simulation of the available member ductility is a no less important parameter for seismic evaluation. When splices are short and unconfined, the yield strength of the lapped rebars cannot be achieved and premature failure is reached [50–53]. If an adequate lap splice length is adopted as indicated based on experimental observations, the yield strength may be reached but a non-ductile response is still expected if the level of confinement remains low [10]. Further, in this situation, repeated cyclic loads above 75% of the yield strength may likely lead to failure [8,48]. Finally, if splices are additionally well confined, not only the yield strength can be developed but also a degree of ductility is attainable [9,15]. Since splices mainly rely on force transfer by steel-concrete bond, which is an intrinsically brittle deformation mechanism that can be quickly exhausted, such displacement ductility capacity will be always lower than the ductility capacity of a continuous rebar, particularly under the effect of cyclic loads (as demonstrated in Chapter 2). Nevertheless, for the assessment of existing structures such contribution to the inelastic deformation can be relevant and should not be neglected (it will be subsequently shown that appreciable strains at the onset of degradation, in the order of 3.5%, can be reached).

3.2.3 Plastic hinge models for members with lap splices

Plastic hinge models are a common approach to predict the response of RC members. Several researchers have therefore proposed moment-curvature relationships to be used in conjunction with plastic hinge models that account for the presence of lap splices. Priestley et al. [31] modify the moment-curvature relationship of members without lap splices as follows: firstly it is checked whether the maximum equivalent tension stress in the rebar, derived from the computed lap splice strength, is less than the yield stress. In such case, a reduced moment capacity (M_s) is calculated, after which a post-peak branch begins. If the lap splice strength is sufficient to reach the nominal moment capacity (M_n), the latter is kept constant up to a curvature corresponding to a maximum fibre compression strain $\epsilon_c = 0.002$, which is then followed by a post-peak branch. The proposed softening branches for both cases are rather gradual, but the authors acknowledge the small database from which they were derived. The rationale behind the adoption of compression strain limits is related to the formation of longitudinal splitting cracks which reduce the concrete resistance in compression and, consequently, in tension. Hannewald [24], who also adopted compression strain limits in the context of plastic hinge analyses of three wall specimens with lap splices, observed that the previously mentioned value of $\epsilon_c = 0.002$ was a rather conservative bound. Instead, the strain at peak stress for confined concrete (ϵ_{cc}) suggested by Mander et al. [92] was seen to provide better results, after which a sudden strength drop was assumed. A model accounting for tension failure of lap splices was proposed by Biskinis and Fardis [32,93], who suggested steel tensile strain limits ($\epsilon_{su,l}$) for the outermost lap-spliced rebars. The strain limits were derived to fit the ultimate chord rotation (corresponding to a 20% drop in the member lateral resistance) as obtained from tests of columns and beams. Walls were not included in their database since most tests on walls with lap splices were carried out after the publication of the research. The moment-curvature ($M-\phi$) relationships of the abovementioned plastic hinge models accounting for the reduced deformation capacity of spliced RC members are qualitatively depicted in Figure 3.1.

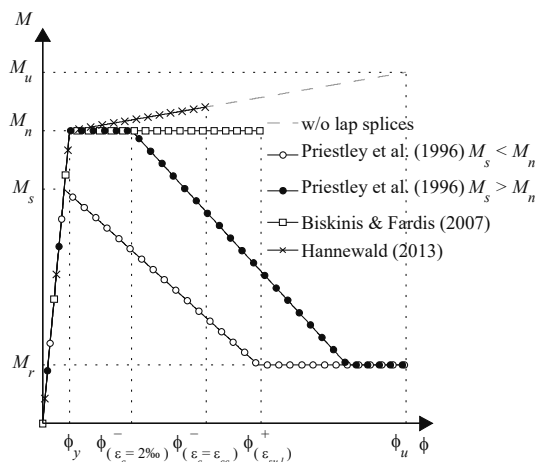


Figure 3.1: Existing proposals for the evaluation of the deformation capacity of spliced RC members (to be used with the corresponding plastic hinge model).

The estimation of the residual strength, intended as the force level that the lap splices can sustain without failing for large slip values, is comparatively more challenging and there are no dependable conclusions on this issue. Priestley et al. [31] suggest to compute a residual moment (M_r) from the maximum eccentricity of the normal force within the core concrete, while other sources propose residual bond strengths ranging between 0% and 40% of the maximum strength, depending on the provided confinement [89]. Following the experimental work by Bimschas [29] and Hannewald et al. [57], Hannewald [24] stated that it does not seem reasonable to assume a slow cyclic strength degradation in between the onset of splice failure and a larger ductility at which the residual capacity is reached, unlike what other researchers had suggested [31,32].

3.2.4 Finite element simulations of members with lap splices

This section summarises studies in which the behaviour of RC members with lap splices was addressed with finite element simulations. Within this framework the use of lumped plasticity models for lap splice lengths larger than 25-30 diameters may be debatable since it becomes challenging to decide on the longitudinal reinforcement ratio to be assigned to the plastic hinge (single or double, see subsection on “Modelling Lap Splices as Double Reinforcement” for further details) and because the location of the plastic hinge may not be straightforward (at the wall base or above the spliced region). However, for short lap splices ($l_s < 25 d_{bl}$), lumped plasticity models appear to be a valid modelling option. Cho and Pincheira [90] used rotational bond-slip springs combined with beam-column models to simulate the response of column members.

Xiao and Ma [94] proposed a numerical model to obtain the monotonic force-displacement response of columns taking into account the deformation due to bond-slip in lap-spliced longitudinal rebars. It corresponds to a modified plastic hinge analysis—wherein bond links are assumed for all the lap splices above the hinge length—involving iterations to achieve equilibrium between bond and tensile force. A constitutive bond-slip law based on a form of Popovics' equation [95] and accounting for the effects of confinement is assigned to the links. The same relation was adopted by Binici and Mosalam [96] to compute an effective steel stress taking into account bar slip, based on the assumption of a linear distribution of bond stresses along the lap splice length of both the starter and the spliced bar, and a decomposition of the total steel strain into slip strain and mechanical strain. These strain components are computed iteratively to satisfy equilibrium of stresses along the splice region and the bond stress-slip relationship. The same authors implemented the resulting model in a nonlinear analysis program with displacement-based frame elements with cross-sectional fibre discretization, which was later expanded to include cyclic lap splice behaviour as well as a hysteretic damage component [97].

The concept of strain decomposition, together with idealized bond stress-slip relationships, was applied by other authors to develop truss elements [98,99] or bars with additional degrees of freedom to express the relative slip between steel and concrete [100]. They were incorporated in refined finite element models to simulate the response of columns with lap splices. Finally, Chowdhury and Orakcal [101] included bond-slip behaviour in a fibre-based flexural macro-model to simulate the cyclic response of RC columns with lap splices.

3.3 Detailed finite element models for response of walls with lap splices

3.3.1 Description of nonlinear shell models

All 24 walls of the collected database were modelled using the nonlinear finite element software VecTor2 (V2) [102] developed at the University of Toronto, which is based on the Modified Compression Field Theory [103]. All the defined models, although different in geometry, materials, applied loads and reinforcement content, share the following features:

- The RC walls are modelled as cantilever walls; an incremental lateral displacement Δ is imposed (pushover) at the shear span height and, where present, a constant axial load N is applied. For the cases in which, due to the particular configuration of the test setup, the tested specimens represent only a portion of the actually imposed shear span (i.e. TW2, TW3, PW2, PW4, CW2, CW3), a fictitious stiff collar is introduced to bridge the remaining part of the shear span up to the point of application of the imposed displacement.
- Foundation and top loading beam belonging to the test setup were explicitly included in the models. Since no damage is expected in those regions, large tensile and compressive strengths (≈ 100 MPa) were assigned to the corresponding concrete material. In order to achieve a realistic simulation of the confinement effect provided by the foundation to

- the wall, the concrete elastic stiffness was, however, not enhanced (this model stiffness homogeneity also help promoting numerical convergence).
- Two different element types were employed for the structure discretization: plane stress rectangles and discrete truss bars. The former were used to simulate the joint behaviour of the concrete matrix and the horizontal reinforcement, using a smeared approach. The latter, instead, served to simulate the longitudinal reinforcement. The truss elements shared the same nodes as the RC elements. For walls with lap splices the effect of bond on the lap splice behaviour was included by employing an equivalent stress-strain law in the truss elements of the lapped region; this model is derived in the next section. Such an implicit way of accounting for the bond-slip effect avoids the use of specific bond-slip elements (e.g. link or interface elements), which would simultaneously increase the computational demand and decrease the numerical stability (e.g. convergence issues) of the FE model. Instead of using truss elements with perfect bond, the vertical reinforcement could have also been modelled as smeared reinforcement.
 - Default VecTor2 settings concerning material models were adopted, which included: Hognestad [104] and Modified Park-Kent [105] models for the pre-peak and post-peak concrete in compression respectively, linear elastic response before cracking with post-cracking tensile stress equal to zero for concrete in tension. Strength and ductility enhancement due to confining reinforcement was calculated according to a combination of the models proposed by Kupfer et al. [106] and Richart et al. [107]. The Mohr-Coulomb criterion is used to determine the failure shear stress, which is computed according to the Modified Compression Field Theory (MCFT) [103]. For the reinforcing steel the model proposed by Seckin [108] including the Bauschinger effect is employed. The following modifications were made to the default models: (i) tension stiffening and softening were disregarded since their use showed to provide, for all RC walls, stiffer and stronger responses with respect to the experimental force-displacement curves—as also observed by Almeida et al. [33]; (ii) the model proposed by Palermo and Vecchio [109,110] and suggested by Palermo and Vecchio [111] and Pugh [112] is used for the hysteretic behaviour of the RC elements. Although all the structures in the analyses were loaded monotonically up to failure, partial unloading and reloading may occur at the material level. It was observed that, when compared with simulations employing the default hysteretic model [113], the model by Palermo and Vecchio [109,110] lead to appreciable improvements in the global $F-\Delta$ predictions.

Figure 3.2 displays as an example the mesh discretization of the specimen TW3 tested at the structural laboratory of *EPFL*. As discussed above, the displacement is applied at the wall cantilever height (i.e. at the shear span height) which does not correspond necessarily to the height of the displacement imposed in the experiment. The truss bar elements in the lap splice zone are depicted within a black dashed line box in a lighter shade of grey; as later clarified, those are the elements to which the developed equivalent lap splice constitutive law will be assigned. For the entire set of test units, the material properties as well as the geometrical features and reinforcing layout are presented in Table 2.1 and Figure 2.1.

3.3.2 Local-level validation of the shell element model up to the onset of lap splice degradation

The finite element model presented herein for the simulation of the force-displacement response of spliced RC walls builds on the definition of an equivalent constitutive model for the lap splice behaviour up to the onset of structural strength degradation. In order to calibrate such a relation, information on local deformation quantities (namely vertical strains) from the collected database of members with lap splices is required. Due to the limited amount of available strain data (only 9 out of the 16 RC walls with lap splices were duly equipped to measure strains attributable to bond slip of lap splices), a semi-empirical approach was followed and the required local quantities were assembled as outcomes from advanced numerical models.

In order to justify the use of the abovementioned technique, the reliability of the strain predictions originating from the finite element models described in the previous sub-section need to be validated. To accomplish this goal, the vertical strains obtained from the numerical models are compared against the measured local experimental results from specimens TWs and VKs; the former were tested directly at *EPFL* while the latter were tested partly by Bimschas [29] and partly by Hannewald et al. [57]. In all these test series, experimental strains were derived from LED measurements. For each couple of companion walls (TW2 vs. TW3, VK1 vs. VK2, VK3 vs. VK4 and VK6 vs. VK5), the comparison between numerical and experimental strains was carried out up to a level of displacement that corresponded to the onset of strength degradation induced by the failure of the lap splices in the units that featured such constructional detail (TW3, VK2, VK4 and VK5). After the latter displacement level, softening of the force-displacement curve takes place, leading to complex phenomena of localized deformation. Since the equivalent model proposed in this work is not intended to simulate this post-peak range of response, the results beyond the onset of degradation are intentionally disregarded.

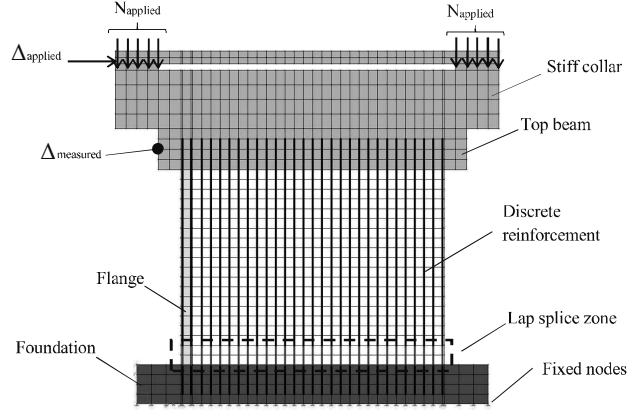


Figure 3.2: Representation of shell and truss element mesh of wall TW3 using FE software VecTor2 [102].

Figure 3.3 shows the strain maps derived from experimental measurements for test units TW2 and TW3 at a displacement level $\Delta = 16.5$ mm, which corresponds to the onset of strength degradation for wall TW3. The dimensions of the LED mesh employed to calculate the experimental strains were intentionally selected such that the bottom mesh layer included the main deformations resulting from bond-slip occurring in the lap splice region (i.e. the horizontal cracks developing immediately above or below lap splices were considered as well). This choice was driven by the fact that finer meshes would depict strain concentrations (where major cracks formed) that cannot be numerically simulated by a model that accounts simultaneously for both mechanical and bond-slip straining. Only the positive loading direction (towards the flange side) is considered for this validation procedure since this is the direction where lap splices failed in tension. The observed vertical strain distributions in both test units (TW2 and TW3) are similar throughout the wall surface. Namely, in the element rows that include the lap splice region (i.e. the bottom layer), negligible differences in the order of 5% can be observed between the two test units. This latter remark is of particular importance for the development of the proposed equivalent lap splice model, as it will be clarified later.

The shell element model of walls TW2 and TW3, labelled *V2 cont. reinf.*, assumes continuous vertical reinforcement with as-tested mechanical properties along the entire specimen height. This modelling choice does not account explicitly for the lap splices present in TW3. The hypothesis made in the present work and supported by the experimental evidences discussed in the previous paragraph (i.e. comparable strain demands between TW2 and TW3) is that the behaviour of a lap splice, until the onset of strength degradation, can be on average approximated by that of a single continuous rebar to which the unmodified stress-strain steel model is assigned. This is possible since the computed lap splice strength f_s is larger than the yield strength f_y of the rebars (see Table 3.1). For walls where the splice strength is smaller than the rebar yield strength, the assumption above is no longer valid and the proposed equivalent steel model will be adjusted accordingly in the next section. The strain distributions predicted by the abovementioned shell element models for the same displacement level at which the experimental strains were evaluated (onset of splice strength degradation) are displayed in Figure 3.4.

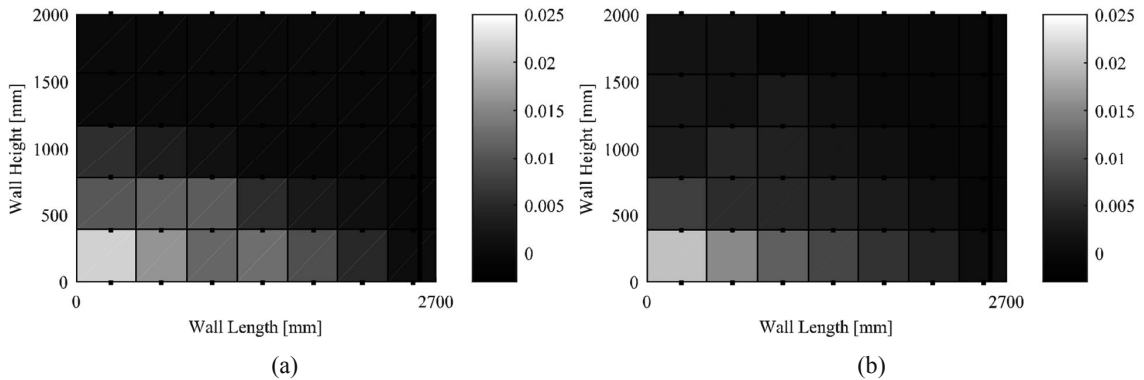


Figure 3.3: Vertical strain map from experimental measurements at $\Delta = 16.5$ mm: (a) RC wall TW2 (b) RC wall TW3.

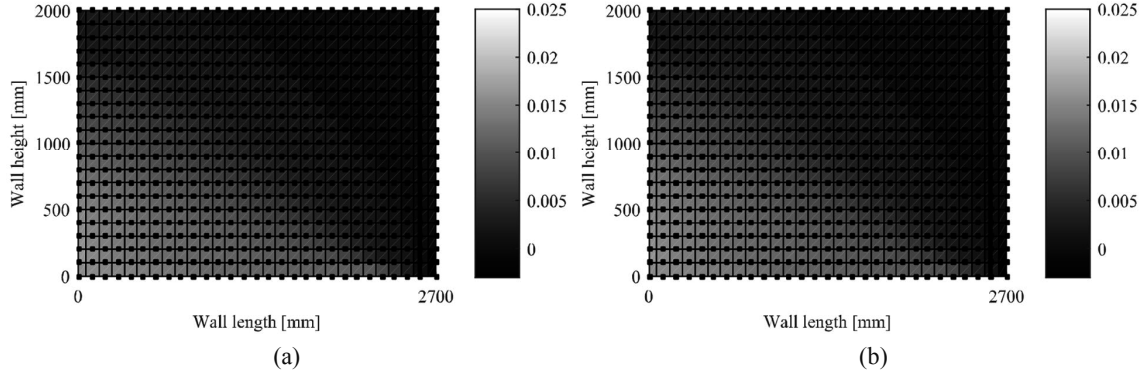


Figure 3.4: Vertical strains map from numerical simulations at $\Delta = 16.5$ mm: (a) RC wall TW2 (b) RC wall TW3.

The strain distributions obtained from the FE models at the onset of degradation satisfactorily approximate the experimental ones observed for both walls TW2 and TW3 in Figure 3.3. In fact, as discussed in Almeida et al. [33], differences of the order of several hundred percent can be obtained in the evaluation of strain quantities of a RC member for different modelling techniques, even if based on the same materials constitutive law. The numerical model proposed in this Chapter, as shown later, yields relative errors in strain prediction that are consistently smaller than 50% in the plastic hinge zone, with an agreement that tends to improve for regions of the wall that remain in the elastic domain.

Observations on the experimental tests of the selected database indicate that the global strength degradation of RC walls is typically triggered by the tensile failure of the outermost layer of lap splices. The ability of the numerical model to simulate the previous finding was checked by averaging the vertical strains in the left corner membrane elements of the models of Figure 3.4 along a total mesh length similar to the one used for the experimental results shown in Figure 3.3. The results in terms of relative error between the numerically predicted and the experimentally observed vertical strain for test units TW2 and TW3 are displayed in Figure 3.5 (b) and Figure 3.6 (b). This comparison was carried out for the displacement levels indicated in Figure 3.5 (a) and Figure 3.6 (a), which span from a nearly elastic response ($\Delta \approx 2$ mm) to the onset of wall strength degradation ($\Delta \approx 16.5$ mm). For both test units, the relative error in terms of vertical strains at the onset of strength degradation is about 30%. The average error along the entire displacement range up to strength degradation is of 40% and 20% for TW2 and TW3 respectively. In the next section (“Development of a simplified constitutive model for lap splices”) it is shown that such an error in strain prediction leads to errors in the displacement predictions of less than $\pm 20\%$. The good strain match in the elastic region of the wall explains the smaller errors obtained for member displacements.

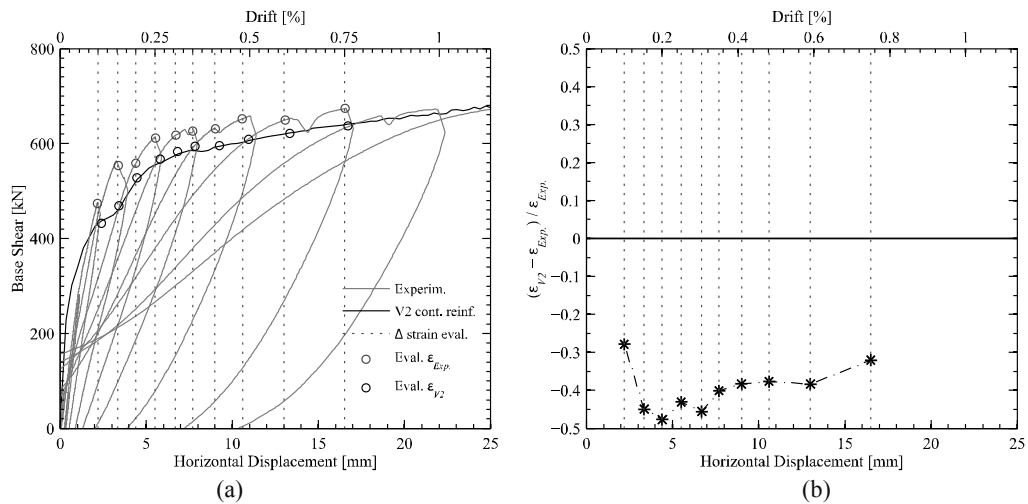


Figure 3.5: RC wall TW2: (a) points in the force-displacement curve at which the strains are evaluated; (b) relative error between experimental and numerical average strains at the outermost lap splice zone in tension.

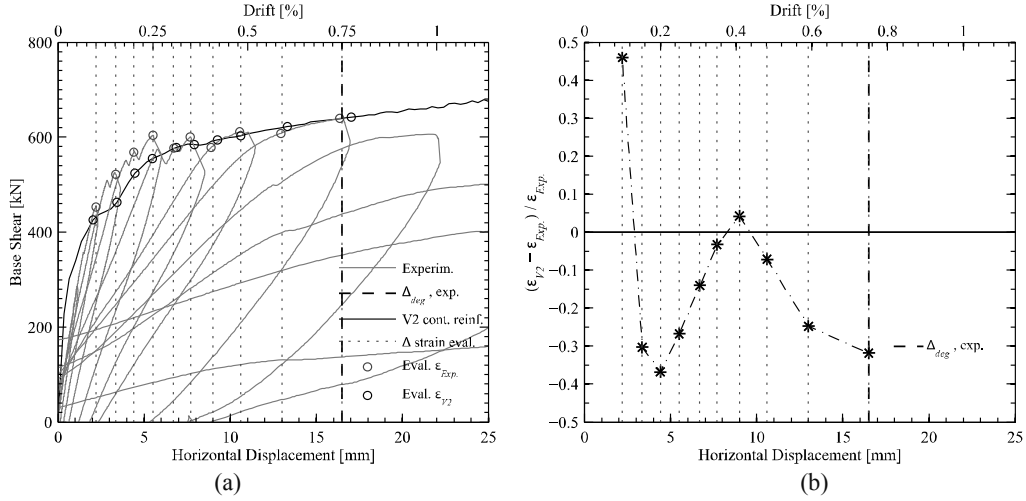


Figure 3.6: RC wall TW3: (a) points in the force-displacement curve at which the strains are evaluated; (b) relative error between experimental and numerical average strains at the outermost lap splice zone in tension.

In order to further validate the employed FE model, the same comparative evaluation procedure described above was adopted for the VK units as well, which were tested by Bimschas [29] and Hannewald et al. [57]. Due to space limitations, the strain maps of the VK units are not included. Figure 3.7 (a) and (b) depict the relative error between experimental and numerical strains in the outmost lap splice region in tension for the reference units (VK1, VK2, VK6) and the spliced units (VK2, VK4, VK5) respectively. With the exception of VK4, for which the average relative error is around 45%, relative errors in vertical strains at the onset of degradation smaller than 20% were obtained. The ability of the employed nonlinear shell model in predicting vertical strains in the plastic zone can hence be considered dependable and will be used for the semi-empirical approach discussed further down in the document.

3.3.3 Modelling lap splices as double reinforcement

When lap splices are long and well confined, the central region of both adjoining bars might be considered to effectively contribute to the lateral stiffness and resistance of the RC structural member. In such cases, doubling the flexural reinforcement in the lap splice zone could be considered to represent a suitable modelling option, which is assessed in the present sub-section.

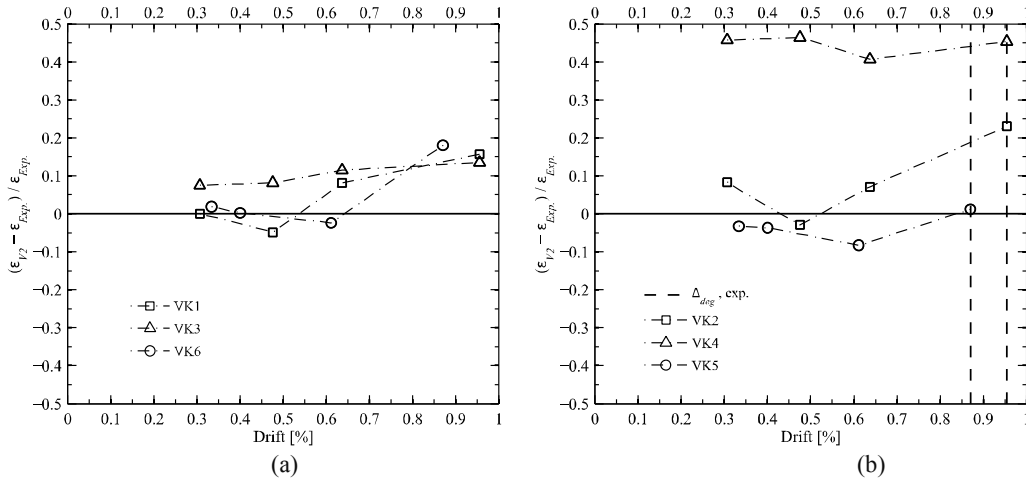


Figure 3.7: Relative error between experimental and numerical average strains at the outermost lap splice zone in tension: (a) Reference units VK1, VK3, VK6; (b) Walls with lap splices VK2, VK4, VK5.

A FE model with double reinforcement (labelled *V2 double reinf.*) was created, which is identical to the one described above (*V2 cont. reinf.*) apart from the fact that the steel area of both spliced bars are assigned to the vertical reinforcing elements in the lap splice zone. The comparison in terms of force-displacement response between the experimental results and the two abovementioned models (*V2 cont. reinf.*, *V2 double reinf.*) is shown in Figure 3.8 for three different RC walls, namely TW3, PW2 and W-60-C. While the first one presents a uniform lap splice length of about 35 diameters without seismic confinement detailing, the remaining two test units exhibit code-compliant confined boundary elements with lap splice lengths of 48 and 60 diameters respectively. As expected, doubling the longitudinal reinforcement leads to larger predictions in terms of lateral strength and initial stiffness with respect to the model *V2 cont. reinf.*, which better matches the experimental results in the three cases. However, while for TW3 and PW2 the model *V2 double reinf.* still yields reasonable predictions at the global level, it overestimates the actual force capacity of W-60-C by a factor of around two. This can be explained as follows: when modelling lap splices with double reinforcement, the yielding of the flexural reinforcement may occur within or above the spliced region and depends on the flexural demand-to-capacity ratio. If the flexural demand is constant along the member length (no or low moment gradient), inelastic deformations will occur above the lap splice zone, where single reinforcement is present. If, on the other hand, there is a sharp moment gradient and the lap splice is long, it is possible that the demand within the double reinforcement region overcomes the capacity of the doubled rebars before the attainment of the single-bar-capacity above the lap splice zone. The latter case is less common and did not apply to any of the walls analysed in this document. Whether the yielding of the flexural reinforcement above the spliced region has a significant effect on the global force-displacement response depends on the splice length to shear span ratio. TW3 and PW2 featured relatively small lap splice length to shear span ratios (6% and 9% respectively). On the other hand, the lap splice length to shear span ratio in W-60-C was larger than 40%; therefore shifting the plastic section above the lap splice (which was not observed in the experimental test) increased the global strength considerably. In particular, the rebars in the lap splice zone (modelled with double reinforcement) were able to exploit their full strength before the yielding (and then failure) of the reinforcing bars placed immediately above the lap splice zone. This is distinct from specimens TW3 and PW2, where the steel elements above the lap splice controlled the post-yielding branch of the member F-Δ response.

The numerical and experimental results were also compared at the local level for specimens TW3, VK2, VK4 and VK5. As an illustrative example, Figure 3.9 shows the vertical strain map obtained with the model *V2 double reinf.* for wall TW3 at the same displacement level discussed in the previous section. Due to the doubling of the longitudinal reinforcing area, the vertical strains recorded in the lap splice zone are considerably smaller than those obtained for the model *V2 cont. reinf.* shown in Figure 3.4 (b). Considering that the spliced region of wall TW3 was not sufficiently long and confined to develop the strength of doubled continuous rebars, and recalling the use of perfect bond between concrete and steel in the models, an underestimation of the average lap splice vertical tensile strains (with consequent loss in accuracy) is expected when comparing numerical and experimental results. This is confirmed by contrasting Figure 3.10 (a) with its counterpart Figure 3.6 (b): the relative error in the strain prediction at the onset of degradation increases from about 30% for the model *V2 cont. reinf.* to 60% for *V2 double reinf.* The same reasoning applies for walls VKs where, in all cases, doubling the reinforcement worsens the strain predictions at the onset of degradation, compare Figure 3.10 (b) with Figure 3.7 (b). However, it should be acknowledged that for walls subjected to low moment gradient and featuring sufficiently long and well confined splices, the use of double reinforcement may turn out to be the best modelling option. Nonetheless, for the wall dataset investigated in this study, modelling lap splices with double reinforcement leads to worse predictions of both global and local quantities.

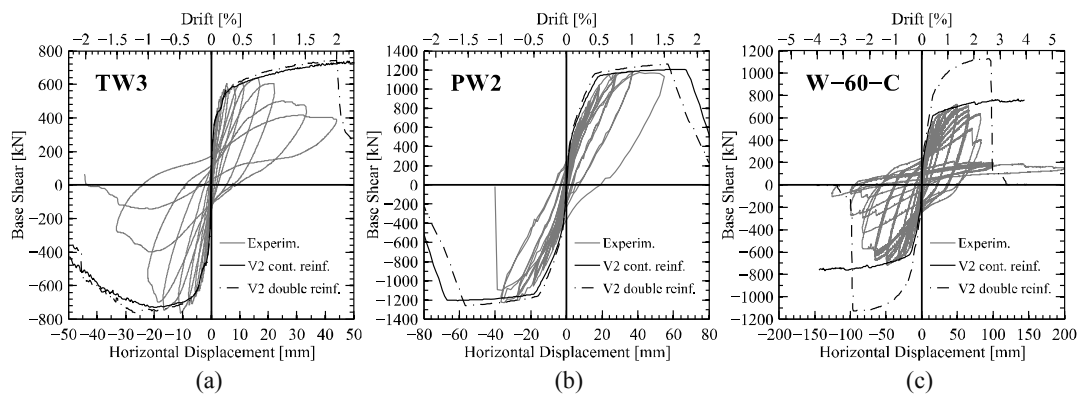


Figure 3.8: Force-displacement curves of FE model with single and double reinforcement in the lap splice region.

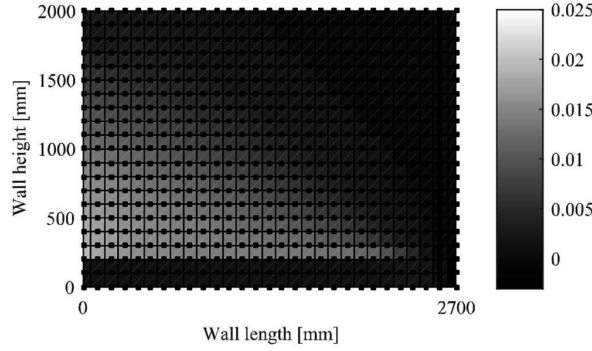


Figure 3.9: Vertical strains map from numerical simulations for wall TW3 with double reinforcement in the lap splice region at $\Delta = 16.5$ mm.

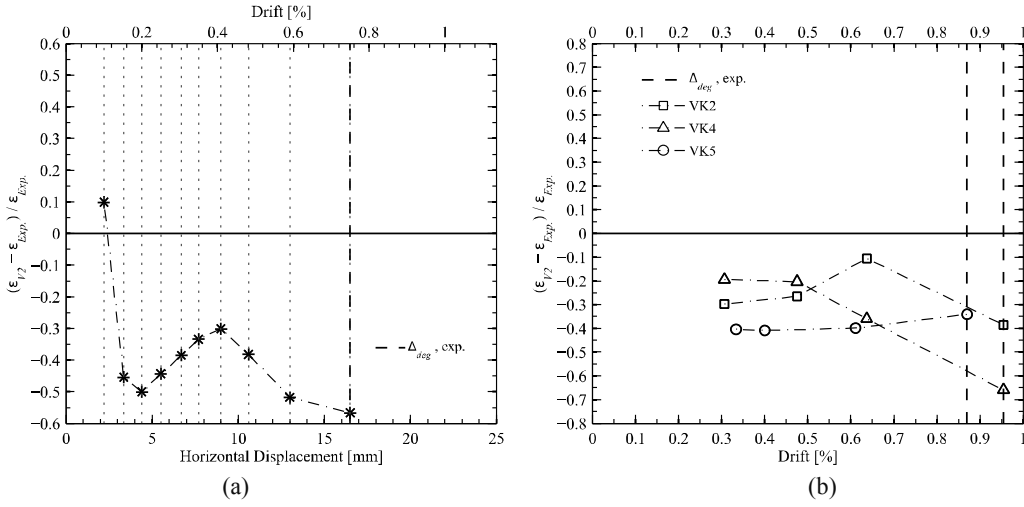


Figure 3.10: Relative errors between experimental and numerical average strains at the outermost lap splice zone in tension using double reinforcement in the lap splice region: (a) RC wall TW3; (b) RC walls VK2, VK4, VK5.

3.4 Development of a simplified constitutive model for lap splices

3.4.1 Background and assumptions for development of equivalent uniaxial steel model

Although several studies can be found in the literature describing the local bond-slip relationship under cyclic loading [61,77–80], to the author's knowledge no such relation is at present available for the global characterization of lap splice behaviour. As a consequence, when FE methods are used to simulate the response of RC members featuring lap splices, the bond-slip contribution to the total deformation is normally accounted for in addition to the reinforcing steel straining component (through ad hoc bond-slip elements) and needs to be numerically integrated along the lap splice length. The complexity both in terms of implementation and interpretation of the output renders these models currently beyond usual engineering practice, also because bond-slip elements are often not implemented in commonly available software.

The goal of the present Chapter is to introduce a simple equivalent uniaxial stress-strain model capable of representing the combined behaviour of the mechanically strained reinforcing steel and the bond-slip mechanism occurring within the lap splice. Such a model can easily be implemented in common finite element software and simulates with reasonable accuracy the detrimental effect of lap splices in the cyclic behaviour of RC walls at the global level.

As a first remark it is pointed out that the proposed equivalent average stress-average strain law for the splice element, although calibrated against cyclic tests on RC walls, is only applicable for monotonic loading, i.e. it will be a suitable tool for pushover analysis. However, since it was calibrated from data on cyclic tests, the effect of cyclic loading are indirectly included. The proposed stress-strain curve is composed of two parts (Figure 3.11): an elastic branch, up to an equivalent

yielding point $(\varepsilon_{y,ls}, f_{y,ls})$, and a post-yield region up to an ultimate point $(\varepsilon_{u,ls}, f_{u,ls})$. The definition of these two points will be addressed in the following two sub-sections, which characterize the equivalent yield strength $f_{y,ls}$ and the equivalent ultimate strain $\varepsilon_{u,ls}$. The latter is set as the maximum strain recorded at the outermost tension lap splice at the onset of member strength degradation and is from now on identified as ε_{deg} . Once these are determined, the corresponding counterparts (equivalent yield strain $\varepsilon_{y,ls}$ and ultimate stress $f_{u,ls}$) can be calculated straightforwardly. After the ultimate point, the equivalent stress is assumed to drop to a value of zero. This simplifying hypothesis will naturally affect the global force-displacement response of the FE models, which will hence present an abrupt and conservative decay in strength capacity at the onset of lap splice degradation (shown later in Figure 3.14 and Figure 3.15). The following considerations support this assumption: (i) the experimental responses after the attainment of the peak force are highly unreliable and difficult to predict. This applies in particular to brittle deformation mechanisms such as those of lap splices, which are characterized by steep softening slopes; (ii) from the numerical point of view, localization phenomena come into play rendering the outcomes of nonlinear FE analysis untrustworthy and mesh dependent [33,62].

3.4.2 Lap splice strength

The equivalent yield point is defined by the equivalent yield stress $f_{y,ls}$ and the equivalent yield strain $\varepsilon_{y,ls}$, which is simply obtained by dividing the former by the Young's modulus E_s of the reinforcing steel (Figure 3.11). It is thus assumed that, up to the equivalent yield point, the lap splice element acts as a single embedded continuous rebar.

The equivalent yield stress $f_{y,ls}$ is determined as the minimum between the steel yield stress f_y and the lap splice strength f_s . In short and poorly detailed splices the spliced rebars will not reach the yield strength. As soon as the first splitting crack forms and the surrounding concrete begins to loosen its clamping action, most of the lap splice deformation will come from relative bar slippage. No further stresses will thus accumulate in the spliced bars resulting in a diminished overall force capacity. This observation finds support in the comparison between experimental and numerical results shown in Figure 3.14 and Figure 3.15: for those walls featuring a splice strength f_s smaller than the steel yield strength f_y , the results obtained from the FE model employing continuous vertical reinforcement with as-tested mechanical properties (*V2 cont. reinf.*) lead to a considerable overestimation of the experimental member strength capacity. On the other hand, for well detailed lap splices (adequate splice length and confining reinforcement) the concrete matrix surrounding the adjoining bars will be able to transfer entirely the stress at yielding of the single rebar.

The model proposed by Canbay and Frosch [3] was chosen among the available formulations to compute the splice strength f_s for the following two reasons: (i) It is the most recent and more advanced within the available physical-based approaches, explicitly accounting for different lap splice failures, namely side- and face-splitting; and (ii) Due to the theoretical framework on which Canbay and Frosch's model [3] builds on, it is more suitable than statistical approaches to be extended outside the member dataset forming the domain of validation (RC beams and columns).

In the context of the present work, the main limitations of the expression proposed by Canbay and Frosch [3] are: (i) it was derived for strength evaluation of tension splices under monotonic loading; and (ii) it does not account for the beneficial effect of the moment gradient on lap splice strength. Following the discussion in Chapter 2, monotonic splice strength is herein accepted as an estimate of the splice capacity under cyclic loading.

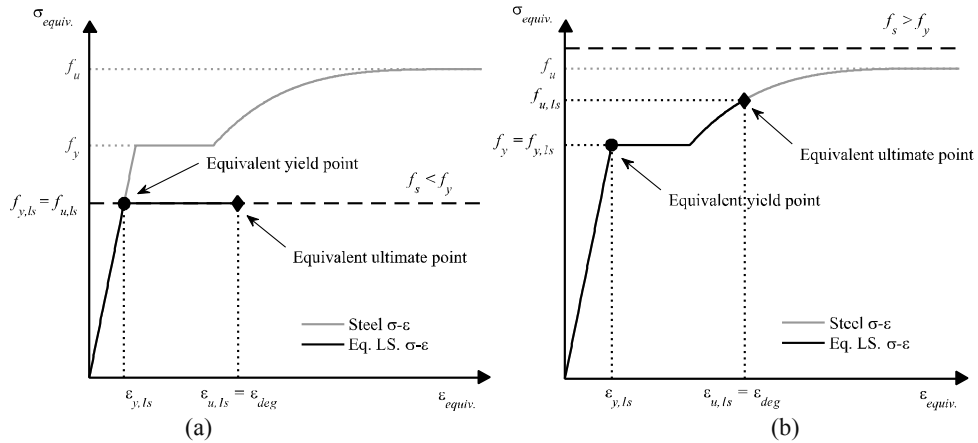


Figure 3.11: Equivalent lap splice stress strain law: (a) $f_s < f_y$; (b) $f_s > f_y$.

3.4.3 Strain at onset of strength degradation

A pivotal point in the definition of the equivalent stress-strain relationship for lap splices in RC walls is the identification of the ultimate strain limit $\varepsilon_{u,ls}$, which is defined as the strain at the onset of strength degradation ε_{deg} . As already pointed out, few propositions are currently available in the literature to determine analytically the lap splice strain capacity, which are all targeted to plastic hinge methods. The goal of the present section is to develop an estimate of the strain at the onset of degradation by means of a semi empirical approach, as described in the following paragraphs.

Firstly, the RC walls with lap splices included in the assembled database were modelled with the nonlinear FE software VecTor2 [102] as discussed in the previous section. Exception was made for specimens PW2 and RWS, which were disregarded for the following reasons: the first did not show any sign of strength degradation due to lap splices while the second, featuring four different types of longitudinal rebars and splice lengths, depicted a cyclic behaviour that was not amenable to be analytically simulated (the same applied to the companion unit with continuous longitudinal reinforcement, RWN). Single reinforcement is used along the entire height of the test units since, as previously remarked, this represents the best available modelling option both in terms of global and local level results. It is noted that, for those cases where the lap splice strength f_s is smaller than the steel yield stress f_y , an elasto-plastic stress-strain law was assigned to all the reinforcing elements simulating the lap splices. The latter is described in the next section representing the basis for the model $V2 w/f_s$.

Secondly, the maximum vertical tensile strains of the outermost steel elements located in the lap splice region are recorded for three different displacements: at the onset of strength degradation as observed from the experimental tests (Δ_{deg}), and at a lower and an upper bound of this value in a 20% interval ($\Delta_{LB} = \Delta_{deg} - 0.2 \times \Delta_{deg}$; $\Delta_{UB} = \Delta_{deg} + 0.2 \times \Delta_{deg}$). This procedure allows obtaining a range of variation for the strains around the onset of strength degradation, which are then useful to calibrate the predictive equation. The choice of considering the most strained lap splice in tension reflects the fact that, in all the selected experimental studies on RC walls with lap splices, failure of the outermost layer of lap splices signals a marked specimen strength degradation (as pointed out in Chapter 2). The maximum value of the vertical steel strain along the lap splice length was monitored due to the following considerations: (i) in the case of short splices, or long splices under small moment gradient, the strain distribution is rather constant along the splice length, (ii) for long splices under high moment gradient, strength degradation can start without splitting cracks developing along the entire splice length, especially if the lap splice is not well confined. The use of an average strain value along the splice length would thus lead to non-conservative estimates of the strain at strength degradation.

The results obtained for the strain at degradation onset $\varepsilon_{V2(Adeg)}$ are listed in Table 3.2 together with its lower and upper bounds, $\varepsilon_{V2(ALB)}$ and $\varepsilon_{V2(AUB)}$ respectively. The relative errors between these quantities and $\varepsilon_{V2(Adeg)}$ are also included in the table and it can be observed that they are on average larger than the error arising from the strain estimation by the employed refined FE model (around 30%, as shown in the previous section). The latter can therefore be considered to provide dependable results and the use of the semi-empirical approach is thus justified.

Before introducing the proposed predicting equation for the strain at the onset of degradation, the method used to select the governing parameters is described. Firstly an initial set of parameters deemed potentially relevant for the strain capacity of lap splices was singled out. Subsequently, their correlation with the strain at the onset of degradation was assessed through univariate regression analyses. Finally, the coefficient of determination was computed for each parameter, allowing to identify the most important ones, as discussed next.

Transverse (confining) reinforcement is undoubtedly the most critical factor controlling the strain at degradation onset because it enables the force transfer mechanism between spliced bars once splitting cracks have formed and because it allows for a more effective yield penetration, which prevents sudden strength degradation. Lap splice length, shear span (which accounts for the moment gradient), and loading history are the other fundamental quantities governing the lap splice deformation behaviour. Due to the difficulty in evaluating the effects of the loading history, they are only indirectly taken into account in the expression for the splice strain capacity in the measure that the RC walls in the database were subjected to cyclic loading histories.

Table 3.2: Strains at the onset of degradation with associated lower and upper bounds, values estimated with equation (3.1), and comparison.

RC Wall	$\epsilon_{V2(\Delta deg)}$	$\epsilon_{V2(\Delta LB)}$	$\epsilon_{V2(\Delta UB)}$	$\frac{\epsilon_{V2(\Delta LB)} - \epsilon_{V2(\Delta deg)}}{\epsilon_{V2(\Delta deg)}}$	$\frac{\epsilon_{V2(\Delta UB)} - \epsilon_{V2(\Delta deg)}}{\epsilon_{V2(\Delta deg)}}$	$\epsilon_{predicted}$	$\frac{\epsilon_{predicted}}{\epsilon_{V2(\Delta deg)}}$
	[‰]	[‰]	[‰]	[-]	[-]	[‰]	[-]
TW3	14.73	11.25	18.46	-24%	25%	13.44	0.912
VK2	18.81	10.39	31.75	-45%	69%	10.86	0.577
VK4	10.29	6.01	20.88	-42%	103%	10.86	1.055
VK5	6.64	4.01	10.69	-40%	61%	9.40	1.416
W1	11.94	10.74	14.14	-10%	18%	13.88	1.163
W2	14.25	12.18	17.10	-15%	20%	12.77	0.896
CW2	3.78	1.82	4.90	-52%	30%	3.90	1.032
CW3	6.46	3.20	9.85	-51%	52%	6.54	1.013
MC-60-C	30.31	25.30	35.40	-17%	17%	34.03	1.123
MC-40-C	29.69	24.63	35.85	-17%	21%	29.93	1.008
MC-60-N	24.62	20.17	27.07	-18%	10%	26.00	1.056
MC-60-N2	25.46	19.37	28.51	-24%	12%	26.04	1.023
W1-L	8.33	3.39	13.18	-59%	58%	7.11	0.854
W2-L	7.59	2.57	13.50	-66%	78%	7.10	0.936
mean				34%	41%		1.005
std							0.178

Once identified the abovementioned fundamental quantities, a final multivariate regression analysis yielded the following expression for ϵ_{deg} , valid for RC walls with mechanical and geometrical features within the range of the walls in the database:

$$\epsilon_{deg} = \epsilon_{y,ls} + 0.65 \cdot \rho_w + 0.03 \cdot \frac{l_s}{L_s} \quad (3.1)$$

where $\epsilon_{y,ls}$ represents the equivalent yield strain, l_s is the length of the outermost lap splice in tension, L_s is the shear span of the member, and ρ_w is the confining reinforcement ratio defined as:

$$\rho_w = \rho_x + \rho_y \quad (3.2)$$

$$\rho_x = A_{trx} \cdot \frac{n_{legs}}{s_x \cdot b} \quad (3.3)$$

$$\rho_y = \frac{A_{try}}{s_y \cdot (d_{bl} + c_{bo})} \quad (3.4)$$

where ρ_x and ρ_y are respectively the reinforcement ratios in the plane parallel and orthogonal to the plane of bending, A_{tr} is the area of the confining stirrups, s is the spacing, n_{legs} is the number of stirrup legs, d_{bl} is the diameter of the longitudinal bars, b is the section width, and c_{bo} is the clear face concrete cover.

It is important to point out that, if the transverse reinforcement cannot exert its confining action, either because there are no stirrups or because the shear reinforcement is not appropriately detailed at the wall edges (135° hooks or closed up), the value of ρ_w should be set equal to zero. In such cases, when the splitting cracks form, no additional force transfer mechanism between adjoining rebars is possible and strength degradation due to bond slip will occur. Within the assembled database of RC walls, this is the case of specimens CW2, CW3, W1* and W2*, tested by Elnady and Layssi and Mitchell [28,56].

The influence of the two parameters ρ_w and l_s/L_s on the strain at the onset of degradation $\epsilon_{V2(\Delta deg)}$ is presented in Figure 3.12 (a) and (b), evidencing a strong correlation. The last two columns of Table 3.2 report the strains at the onset of degradation predicted by equation (3.1), referred to as $\epsilon_{predicted}$, and the ratio with those from the nonlinear FE analyses, $\epsilon_{V2(\Delta deg)}$. The predicted values are very close to the ones given by the numerical model, with an average ratio $\epsilon_{predicted} / \epsilon_{V2(\Delta deg)}$ close to unity and a coefficient of variation smaller than 20%. In Figure 3.13 the goodness of fit of the predicted

strains is represented in the form of an error-bar plot. In all cases the values of $\varepsilon_{predicted}$ fall within the range of variation of $\varepsilon_{V2(AlB)}$, represented by the interval $[\varepsilon_{V2(AlB)}, \varepsilon_{V2(AUB)}]$ and the prediction is therefore judged satisfactory.

Once the strain at the onset of degradation ε_{deg} is estimated with equation (3.1)—it corresponds to the ultimate strain $\varepsilon_{u,ls}$ of the proposed equivalent lap splice constitutive law—the equivalent ultimate stress $f_{u,ls}$ can be determined accordingly (Figure 3.11):

- If the steel yield stress f_y is larger than the lap splice strength f_s , i.e. when $f_{y,ls} = f_s$: an elastic-perfectly plastic stress strain curve is assumed for the equivalent steel and hence $f_{u,ls} = f_{y,ls} = f_s$. It is noted that strains beyond $f_{y,ls}$ come from bond slip and not mechanical straining of the rebar.
- If the steel yield stress f_y is smaller than the lap splice strength f_s , i.e. when $f_{y,ls} = f_y$: the stress strain curve of the equivalent uniaxial material is assumed to be equal to the one of the reinforcing steel up to the value of $\varepsilon_{u,ls}$. Hence, when present, the yield plateau or hardening branch of the steel constitutive law should be considered. It should be noted that, in the particular case where $f_y < f_s < f_u$, the equivalent ultimate stress $f_{u,ls}$ may result larger than the predicted lap splice strength f_s . However, due to the unavoidable inaccuracy related to the evaluation of the lap splice strength f_s , a separate consideration of this scenario is not justified; additionally it is very uncommon and did not occur for any of the spliced walls included in the assembled database.

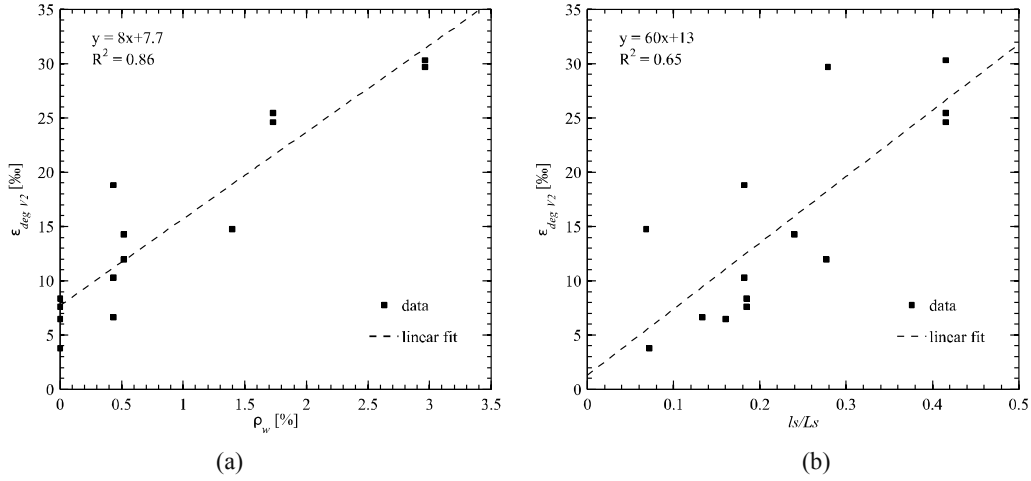


Figure 3.12: Strain at degradation onset predicted by the V2 models vs: (a) reinforcement ratio ρ_w , and (b) ratio between the lap-splice length and the shear span, l_s/L_s .

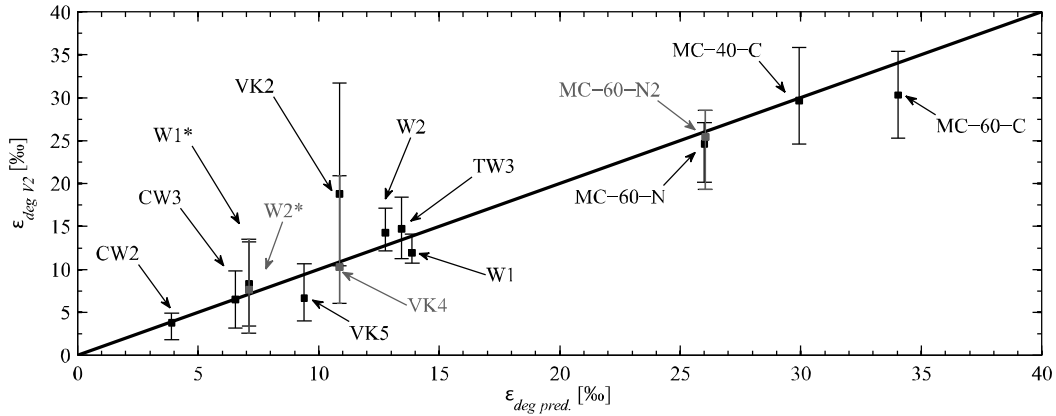


Figure 3.13: Comparison between the strains predicted by V2 and those computed according to equation (3.1).

3.5 Validation of model against wall database

Figure 3.14 and Figure 3.15 show the comparison between the experimentally measured force-displacement curves and the numerical simulations for all the RC walls in the database, which includes 16 specimens with lap splices and 8 with continuous reinforcement. The walls with continuous reinforcement along the entire height represent the reference units for 10 of the walls with spliced bars and are included for two main reasons: they serve as benchmark for the numerical models (e.g. if the FE model is not able to accurately predict the response of the reference wall, then the simulation results obtained for the companion spliced wall cannot be considered as reliable) and they put into evidence the premature failure of walls with lap splices.

The employed shell element models have all been implemented in the nonlinear FE software VecTor2 (their common features were listed in the sub-section “Description of Nonlinear Shell Models”):

- *Model with continuous reinforcement (V2 cont. reinf.)*: the vertical (flexural) reinforcement is modelled as continuous throughout the entire height of the wall specimen with the as-tested mechanical rebar properties. Whilst this is an appropriate approach for the reference unit walls, it does not account for the presence of lap splices.
- *Model accounting for lap splice strength (V2 w/ f_s)*: for all bar elements representing the longitudinal reinforcement in the lap splice zone, an equivalent elasto-plastic constitutive law accounting for the maximum splice bond strength f_s is used. The equivalent steel yield stress is set equal to the lap splice strength f_s —according to Canbay and Frosch [3]—while a large value ($>10\%$) is imposed for the equivalent steel ultimate strain ε_{su,f_s} . The purpose of this model is to show the reduction in the numerically predicted capacity for the test units where a prior-to-yielding lap splice failure was expected (walls W1*, W2*, CW2, CW3 in the database).
- *Proposed model (V2 w/ eq. LS)*: the uniaxial average stress-average strain law described in the previous section (Figure 3.11) is assigned to all the vertical steel elements within the lap splice zone. This model accounts for the limited lap splice strength and strain capacity.

In all plots of Figure 3.14 and Figure 3.15 horizontal displacements and drifts are indicated on the primary and secondary x-axis respectively. The reported displacements do not necessarily correspond to the ones imposed in the pushover analyses (this is true only for walls tested as cantilever). If a particular test setup is used in order to impose a bending moment at the top of the specimen (as for walls TW2, TW3, PW2, PW4, CW2, and CW3), the plotted displacements are the ones experimentally measured at the point of application of the lateral load. The lateral drift is calculated as the ratio between the measured displacements and the height above the foundation at which the measurement is taken. The base shear is shown on the y-axis. In order to ease the interpretation of the results, a dashed black line displays the experimentally observed displacement at the onset of strength degradation (Δ_{deg}). In the following paragraphs, the obtained results with the abovementioned models are discussed and compared.

The reference unit walls are discussed first. Up to the peak force of the experimental results, the FE model with continuous reinforcement is able to accurately predict the backbone curve of the cyclic responses. The only exception is given by wall RWN where, for negative drift values, the post-elastic stiffness degradation and the maximum force capacity are not well captured (error of about 20% in the prediction of the force at ultimate displacement). The non-symmetrical layout of the flexural reinforcement presented by this specimen, leading to a complex cyclic behaviour, can be the source of the model inability to effectively predict the experimental results. However, the analytical monotonic response is close to the one shown in the reference paper for this test [27], obtained through the use of a plastic hinge model. Regarding the displacement at which the peak force is attained, the numerical simulations provided noticeably good results as well. An exception is again the wall RWN but also PW4, for which the abovementioned displacement level is considerably over-estimated. Beyond the displacement at peak force the analytical response is subjected to numerical pathologies and it should not be considered as dependable. Therefore, no discussion will follow on the comparison between the numerical and experimental post peak responses.

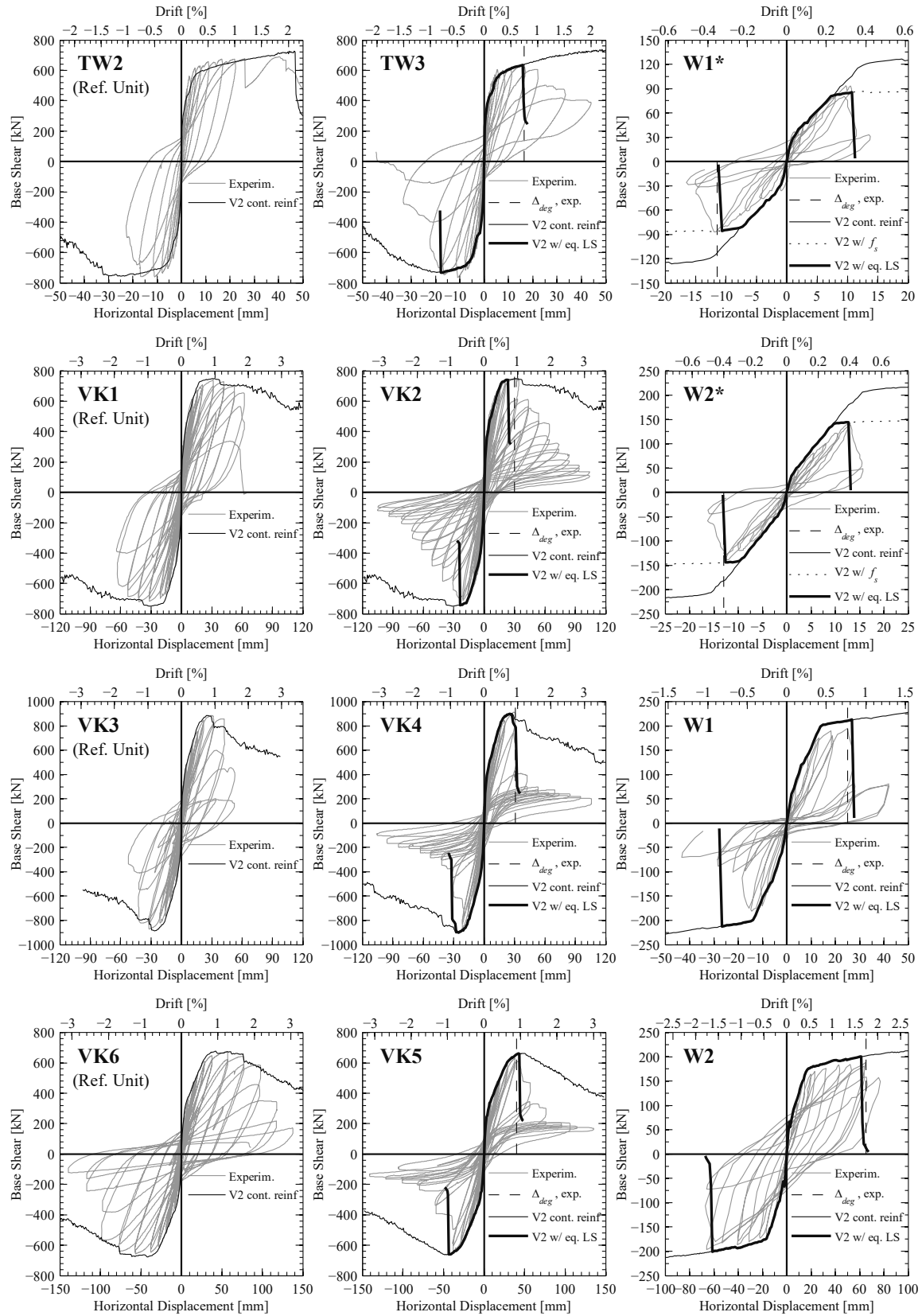


Figure 3.14: Comparison between experimental and numerical results.

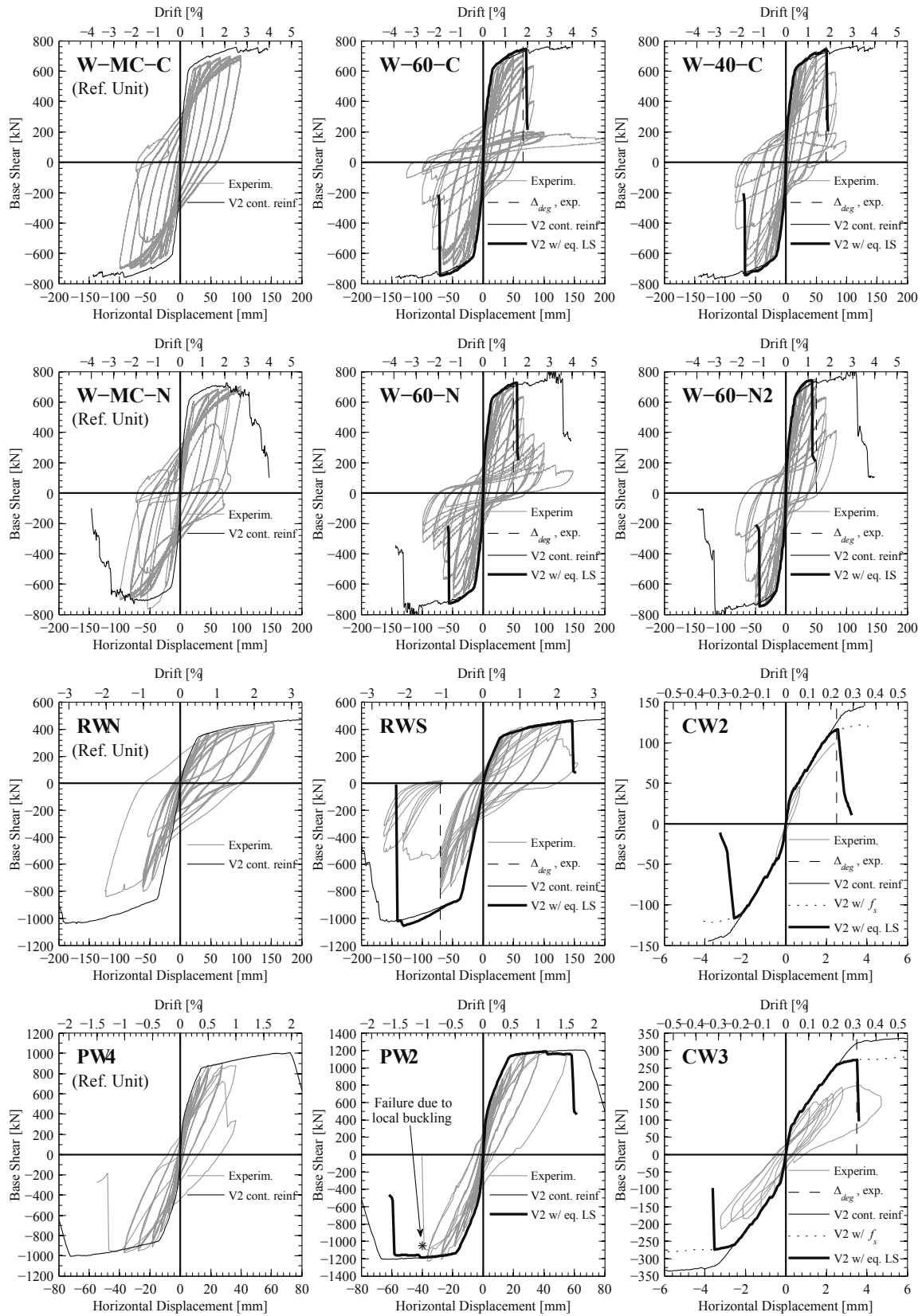


Figure 3.15: Comparison between experimental and numerical results (cont.).

The presence of lap splices in the region of RC walls where inelastic deformations are expected can lead to two detrimental effects: (i) reduction in the force capacity of the structural member and (ii) anticipation of the process of strength degradation due to bond deterioration occurring between adjoining bars. The first scenario is expected when the splice strength is not sufficient to transfer the rebar yielding force. In the selected database, and according to the chosen equation for the splice strength [3], this occurred in only four cases, namely for specimens W1*, W2*, CW2 and CW3. Obviously, for those test units, the model with continuous reinforcement largely overstates the experimental force capacity. A better estimate of the latter is obtained by employing the model $V2 w/f_s$ represented in the plots of Figure 3.14 and Figure 3.15 with a black dotted line. As it can be seen, the maximum base shear predicted by this model is in line with the experimental results for walls W1*, W2* and CW2, while for CW3 it overestimates the experimental results by almost 40%. The use of a smaller value of f_s with respect to Canbay and Frosch's proposal [3] in the equivalent constitutive law of wall CW3 would improve the predicted force capacity. However, none of the modelling approaches available in the literature provided a sufficiently low estimate of the splice strength (see Table 3.1).

The effect of lap splices on the displacement capacity of RC walls is not captured by any of the abovementioned models, neither $V2 cont. reinf.$ nor $V2 w/f_s$. However, for almost all the test units featuring lap splices, the model $V2 w/eq. LS$ correctly identifies the displacement at the onset of structural strength degradation entailed by the lap splices detrimental effect (Δ_{deg}). The only exception is represented by the wall RWS, where Δ_{deg} is overestimated. A particular case is also PW2, which, although featuring lap splices, did not show any evident sign of strength degradation. Rather, the specimen failed due to local buckling of the vertical rebars above the lap splice zone of the boundary elements. For this case Eq. (1) predicts a lap splice strain capacity $\epsilon_{u,ls}$ which is larger than the numerical strain recorded in the outermost rebar in tension at the ultimate displacement level $\epsilon_{u,V2}$ ($\epsilon_{u,ls} = 3\%$ vs $\epsilon_{u,V2} = 2\%$), which is hence consistent with the experimental results. Looking at the overall shape of the force-displacement curves from the model $V2 w/eq. LS$, one can notice the presence of a sudden drop in force at the level of the ultimate displacement. This corresponds to the attainment of the ultimate equivalent strain $\epsilon_{u,ls}$ in the longitudinal reinforcing elements within the lap splice zone. A residual strength to the modified steel constitutive law would have to be assigned in order to obtain a global non-abrupt descending branch. Further research would be required in order to dependably use the latter approach and to deal with the consequent numerical problems such as localization.

A final remark is due on the fact that the same database of RC walls is used for the validation procedure as well as for the determination of the equivalent uniaxial lap splice stress strain law. As a consequence, a good agreement between the analytical (model $V2 w/eq. LS$) and experimental results could in principle be expected. The reason behind the use of the same database lies in the limited number of spliced RC walls that were available. One alternative could have been to split the data set in two parts and using one for calibration and one for validation. This approach was investigated by performing a robustness analysis. The parameters of the predictive equation were determined with any combination of 8, 10 or 12 specimens out of the 14 test units with lap splices, showing a robust fit. The entire set of walls naturally provided the best match, from which the predictive equation was derived.

3.6 Conclusions

Lap splices are frequently found at the wall base of existing RC structures as well as recent ones that are not designed for a ductile response. The simulation of the behaviour of lap splices is a challenging task, as it is affected by many factors, the influence of which is mostly understood only from a qualitative viewpoint. This contrasts with the engineering need to have a simple but dependable model to account for lap splice response. The present Chapter proposes an equivalent uniaxial steel stress-strain model that represents the monotonic envelope of the cyclic response of lap-spliced rebars up to the onset of strength degradation. It is characterized by two points defining an equivalent yield state and an ultimate condition. A new expression is introduced to estimate the lap splice strain capacity, which was calibrated from a semi-empirical approach. It depends on the equivalent yield strain, confining reinforcement ratio and ratio of lap splice length to shear span, which turned out to be the parameters mostly influencing the ductility capacity of lap splices. The derived expression shows an average ratio of predicted *versus* semi-empirical strains close to unity and a mean coefficient of variation below 20%. The newly proposed equivalent steel stress-strain model was used in combination with nonlinear shell element models to simulate the response of all the RC walls in the database. A good accuracy in the evaluation of both member strength and displacement capacity was obtained: the numerical vs experimental average ratio resulted of 12 and 25% for the former and the latter, respectively. Beyond the point of strength degradation, the prediction of the member lateral resistance becomes non-dependable and it is not addressed.

3.7 Acknowledgments

The financial support by the *Stiftung zur Förderung der Denkmalpflege* of the project “Erbeverhalten von bestehenden Stahlbetongebäuden mit dünnen Wänden” and by the *Swiss Federal Roads Office (OFROU)* to the project number AGB 2015/002, under which the present study was partly carried out, is acknowledged.

4 An Enhanced Beam Element Model to Account for Tension Shift Effects in Reinforced Concrete

This Chapter presents a displacement-based beam element model in which axial equilibrium is strictly verified. Such element can be employed to better simulate the local level response of RC members, and namely to account for tension shift effects. The Chapter represents the post print version of the following paper:

D. Tarquini, J.P. Almeida, K. Beyer, 2017. “Axially equilibrated displacement-based beam element for simulating the cyclic inelastic behaviour of RC members”, *Earthquake Engineering and Structural Dynamics* 46 (9): 1471-1492, DOI: [10.1002/eqe.2865](https://doi.org/10.1002/eqe.2865).

Figures and tables formatting, reference-, section-, and equation- numbering were adapted to the style of this document. The first author developed, implemented and validated the beam element model under the supervision of the last two authors. The second author developed the finite element (FE) software SAGRES under which the element was initially implemented. The element was then also implemented by the first author in the open source FE software OpenSees. Further details on this matter can be found in Appendix 9.1, which is based on the conference paper:

Tarquini D., Almeida J.P., Beyer K., 2017. “Axially equilibrated displacement-based beam element: implementation in OpenSees and application to dynamic analysis of structures”. *6th International conference on Computational Methods in Structural Dynamics and Earthquake Engineering (COMPDYN 2017)*, Rhodes, Greece.

Abstract

Distributed plasticity beam elements are commonly used to evaluate limit state demands for performance based analysis of reinforced concrete (RC) structures. Strain limits are often preferred to drift limits since they directly relate to damage and are therefore less dependent on member geometry and boundary conditions. However, predicting accurately strain demands still represents a major simulation challenge. Tension shift effects, which induce a linear curvature profile in the plastic hinge region of RC columns and walls, are one of the main causes for the mismatch between experimental and numerical estimates of local level quantities obtained through force-based formulations. Classical displacement-based approaches are instead suitable to simulate such linear curvature profile. Unfortunately, they verify equilibrium only on an average sense due to the wrong assumption on the axial displacement field, leading to poor deformation and force predictions. This Chapter presents a displacement-based element in which axial equilibrium is strictly verified along the element length. The assumed transversal displacement field ensures a linear curvature profile, connecting accurately global displacement and local strain demands. The proposed finite element is validated against two sets of quasi-static cyclic tests on RC bridge piers and walls. The results show that curvature and strain profiles for increasing ductility demands are significantly improved when axially equilibrated rather than classical displacement-based or force-based elements are used to model the structural members.

Keywords: Beam Element; Axial Equilibrium; Displacement-based formulation; Distributed plasticity; Tension shift effects.

4.1 Introduction

Performance-based assessment of structures is based on the definition of clear limit states, which are not to be exceeded under different levels of ground motion. Limit states can be based on drift values or local quantities such as curvatures and strains, which are deemed to be a better indicator of structural damage [114]. In reinforced concrete (RC) structures, damage concentrates in plastic hinge regions, and therefore efficient models should accurately simulate the main sources of deformation associated to the plastic hinge development. The classical interpretation of such mechanism, at least for well detailed members, considers three main components, namely the moment gradient, tension shift, and anchorage slip (or strain penetration) effects [69].

Although several modelling approaches are available, the attractive compromise between accuracy and computational cost renders beam element models one of the most widely employed numerical tools in engineering practice, especially when complex and multi-member structures such as buildings or bridges are involved. Beam element models are typically divided into lumped and distributed plasticity approaches. The former are more performant from the computational view-point as they typically lump the three above mentioned components of the plastic hinge at pre-defined member locations. This is accomplished by using the concept of equivalent plastic hinge length, which therefore often features three terms [69]. On the contrary, each of those terms can be individuated in the so-called distributed plasticity elements. Anchorage slip can be accounted for by a zero-length element, such as that developed by Zhao and Sritharan [115] or any other appropriately calibrated relation [116,117]. The moment gradient is explicitly simulated since the development of plasticity is not restrained to a specific member location but can spread along several integration points (IPs) in which the finite element (FE) is typically discretized. Up to the present moment, tension shift effects due to inclined cracking caused by shear force—see Figure 4.1 (a)—have not been explicitly addressed in the pre-peak phase of the force-displacement member response, although their influence will necessarily affect the comparison between experimental and numerical results at the global (i.e., member displacement) level [118,119]. In the post-peak branch, the need to use a regularization length makes it possible to indirectly account for it [63,120]. This Chapter shows that models based on distributed plasticity elements and classical beam theory can also be adapted to directly incorporate tension shift effects whilst verifying strictly axial equilibrium, thus significantly strengthening the accuracy of these approaches at the local scale.

Put simply, distributed plasticity elements can be mainly subdivided in displacement-based (DB) and force-based (FB) formulations [33] depending on the type of the imposed independent fields. As their name suggest, displacement and force distributions along the element length are assigned in the former and latter case. The hypotheses governing the beam kinematics control the number of sectional deformations that arise. The current work considers only Euler-Bernoulli (EB) beam hypothesis since: (i) it is simple and allows to model most of the structural members in a RC structure; (ii) linear and nonlinear EB beam elements are available in roughly all the commonly used structural analysis software (e.g., [121,122]). Linear and Hermitian polynomial functions are employed in classical DB formulations to characterize axial and transversal displacement fields. These assumptions provide an exact solution only for linear elastic material and nodal loads. On the other hand, constant and linear shape functions are used to define axial force and bending moment distributions in FB formulations, which results in an exact solution regardless of the development of material nonlinear response. Additionally, in FB formulations equilibrium is strictly verified along the element length—see Figure 4.1 (d)—whereas in DB approaches equilibrium is only verified in an average sense [62]—see Figure 4.1 (f). As a consequence, while a single FB element usually suffices to simulate the nonlinear response of a structural member, member discretization in several FEs is required if DB elements are used—see Figure 4.1 (b).

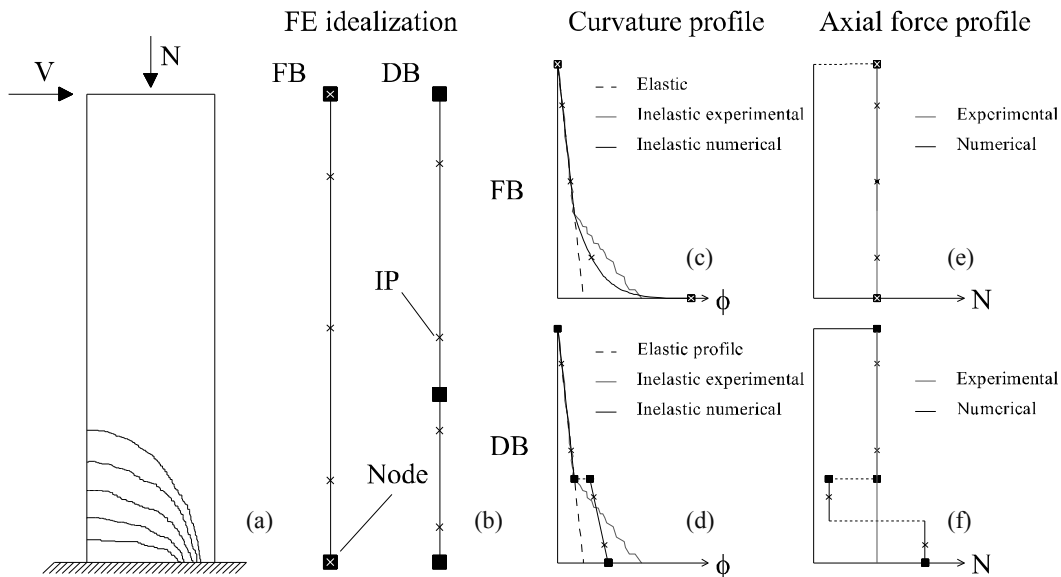


Figure 4.1: RC member subjected to top vertical and horizontal load: (a) Qualitative sketch of inclined cracks due to tension shift effects; (b) Structural discretization with FB and DB elements; Qualitative experimental vs numerical curvature and axial strain profiles: FB element models - (c) and (e); DB element models - (d) and (f).

The state determination of DB formulations is simpler and less computationally demanding than their FB counterpart as the element end forces and tangent stiffness matrix are directly obtained by integration of the sectional responses, hence avoiding the intra-element iterations needed for FB approaches. However, the superiority of the latter in terms of theoretical accuracy and significant size reduction of the resulting global structural stiffness matrix has led to a gradual reduction in the use of DB formulations over the past 15-20 years.

More recently, experimental measurements from accurate instrumentation systems [123] applied to nonlinearly responding RC members have confirmed important limitations of the FB formulations. Disregarding the effects of tension shift in the pre-peak phase, as stated above, was proven to be one of the most relevant. The latter cause a linear distribution of plastic curvatures inside the plastic zone of the structural member ([124–127], see Figure 4.1) and, as pointed out by Priestley *et al.* [69], it represents the first reason for the mismatch between the force-displacement response as obtained from a FB element (which verifies equilibrium in an exact form) and experimental results. Furthermore, the previously mentioned test campaign [123] has shown that the intersection between plastic and elastic curvature profiles occurs at an increasing height for larger ductility demands.

DB formulations offer a solution for the analytical simulation of the above physical phenomena and thus provide a bypass to the limitations brought about by FB approaches. In fact, the observed linear curvature profiles in the plastic hinge region of RC members can be simulated by imposing appropriate lateral displacement fields to the beam finite element, which is the natural framework of DB and not FB formulations—see Figure 4.1 (c) and (e). This Chapter represents a first step to reflect the discussed experimental findings in beam element models with a view to predict more confidently the performance of RC structures. To accomplish such goal, a fundamental drawback of the classical DB formulations is addressed beforehand. As already mentioned, the imposed linear axial displacement field implies that axial equilibrium is only verified in an average sense, which results in case of material nonlinearity in different values of the axial force for distinct integration sections. This leads to a misvaluation of the moment capacity of the structural member and therefore to a poor local and global performance of the finite element [62]. In this Chapter an enhanced DB element for the inelastic simulation of RC members is proposed in which the axial equilibrium is strictly verified (hence emulating the advantages of a FB formulation in this respect) through the use of an iterative procedure. It will be shown that the use of such an element, combined with a convenient structural discretization, lead to an important improvement in the simulation of global and, more importantly, local level quantities when compared with models employing classical DB or FB approaches.

The new element and its state determination are described in Section 4.2 along with an application example describing its main features and relative performance with respect to classical DB formulations. Section 4.3 benchmarks the performance of the new beam element against two sets of experimental tests on RC bridge piers and RC walls. Comparison at the global and local levels, namely curvature and strain profiles, are provided and limitations of the proposed formulations discussed. Conclusions are drawn in Section 4.4.

4.2 Axially equilibrated displacement-based element: formulation and state determination

The beam formulation herein proposed is a plane frame element, which implies that in the global reference system (X, Y) six components are required to characterize the vector of nodal forces (\mathbf{P}) and displacements (\mathbf{U}). Three components suffice instead to describe the basic forces and displacements ($\mathbf{p}^{bsc} = [p_1^{bsc}, p_2^{bsc}, p_3^{bsc}]^T$ and $\mathbf{u}^{bsc} = [u_1^{bsc}, u_2^{bsc}, u_3^{bsc}]^T$) in the member-bound reference system without rigid-body modes (x, y) , which are shown in Figure 4.2.

The concept of a displacement-based element satisfying axial equilibrium was originally proposed by Izzudin *et al.* [128] for nonlinear-elastic problems. No plasticity was considered in their work and explicit expressions were derived for both sectional forces and stiffness matrix. Further, shape functions were not defined for the axial displacement field while a quartic formulation was used for the transversal displacement field. The element end forces \mathbf{p}^{bsc} and tangent stiffness matrix \mathbf{K} were then obtained according to the principle of virtual work and by direct differentiation of each individual component respectively.

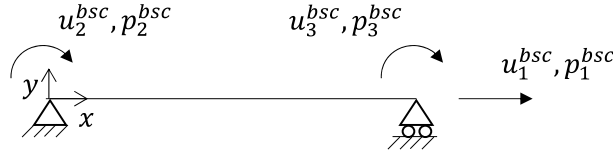


Figure 4.2: Element forces and displacements in the basic reference system.

The formulation presented in this manuscript features the following distinctive aspects with respect to the one above: (i) Material constitutive laws including plastic deformations and cyclic behaviour were considered in the derivation and validation phases; (ii) Hermitian polynomials for the transversal displacement field are used, which results in linear curvature profiles as in classical displacement-based approaches. This assumption, as already discussed, is sought in order to numerically account for tension shift effects; (iii) A variational approach is employed to determine the element end forces and the tangent stiffness matrix. In particular, differences were obtained with respect to [128] in the components of the tangent stiffness matrix referring to the derivatives of the basic axial force p_1^{bsc} with respect to the vector of basic displacements \mathbf{u}^{bsc} .

A similar procedure to the one proposed by Izzudin *et al.* [128] was used to achieve axial equilibrium of the element. The latter is discussed in subsection 4.2.1 while subsection 4.2.1 focuses on the state determination algorithm. Finally, in subsection 4.2.3, the main features of the proposed FE formulation are explored and the new beam element is compared against classical displacement-based formulations with the aid of an application example.

4.2.1 Axial equilibrium

In a beam subjected to nodal loads, equilibrium considerations impose the axial force $N(x)$ to be constant along the beam axis x and equal to the nodal axial basic force p_1^{bsc} . As discussed in Section 4.1, this is not the case for classical displacement-based elements employing nonlinear material constitutive laws. In fact, the linear shape function approximating the axial displacement field $u(x)$ ensures axial equilibrium only in an average sense, which yields different values of the axial force at distinct integration points (i.e., $N^{IP_j} \neq N^{IP_{j+1}}$).

The main idea behind the axial equilibrium procedure consists in correcting the set of sectional axial strains $\varepsilon_0^{IP_j}$ such that the value of the axial force is the same in all IPs ($N^{IP_j} = N^{IP_{j+1}}$). Given the intrinsic nonlinearity of the problem, an iterative procedure is required to attain this goal, which is discussed in the following paragraphs and schematically represented in the flowchart of Figure 4.3.

Consider a Newton-Raphson (NR) cycle n within an arbitrary load step l , for which a vector of displacement increments in the basic reference system $\Delta \mathbf{u}^{bsc}$ is imposed. The steps to be performed to go from the basic to the global reference system require classical structural analysis operations, i.e. the rotation of the coordinate system as well as the use of linear or nonlinear compatibility and equilibrium relations [129], and will thus be omitted in this work. Shape functions employed in classical DB formulations (linear and Hermitian polynomials for the axial and transversal displacement fields) are initially used to obtain, after differentiation, the corresponding increments of sectional deformations $\Delta \mathbf{e}^{IP_j}$ at all IPs along the element. The sectional deformations are calculated from the basic nodal displacements through pre-multiplication by the matrix $\mathbf{B}_{DB/c}$, where the subscript DB/c underlines that classical DB shape functions are considered. Once the sectional axial strain and curvature increments are known ($\Delta \varepsilon_0^{IP_j}$ and $\Delta \phi^{IP_j}$), the Euler-Bernoulli hypothesis and the sectional constitutive law enable to compute the generalized sectional forces \mathbf{s}^{IP_j} . The differences between the axial forces recorded in two successive IPs are then calculated. Axial equilibrium is considered to be satisfied if the cumulative sum of the absolute value of these differences throughout all pairs of IPs in the element is below a certain tolerance. It is noted that this convergence criterion is different from the one proposed by Izzudin *et al.* [128], where strain differences were checked. If such axial equilibrium is verified, the state determination proceeds as for the classical DB formulation, otherwise intra-element iterations (identified with the index m in Figure 4.3) on the increment of sectional axial strains at each IP ($\Delta \varepsilon_0^{IP_j}$) are performed, as explained below.

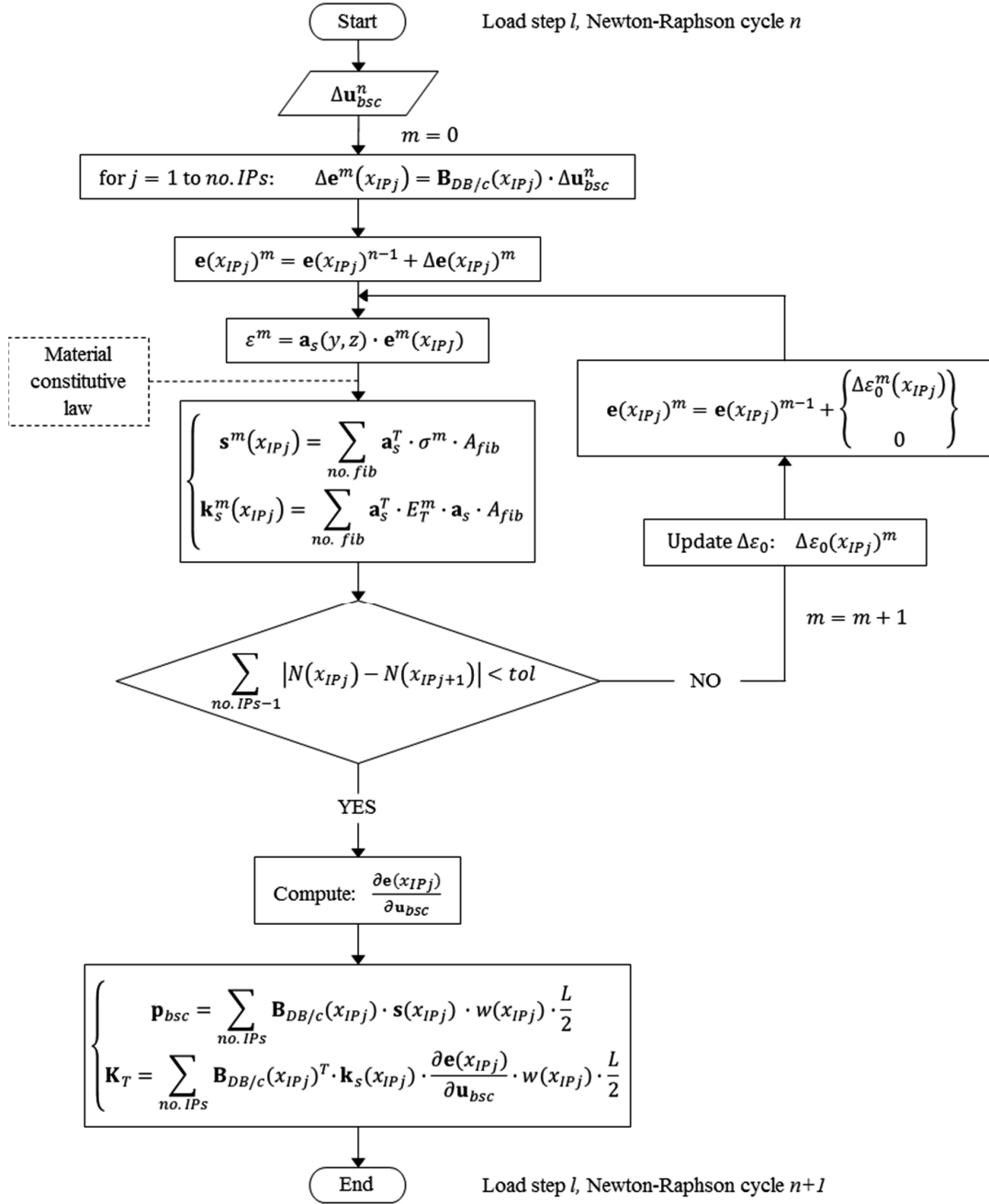


Figure 4.3: Flowchart for the element state determination of the axially equilibrated displacement-based element.

Two conditions need to be fulfilled: (i) The axial force should be equal in all IPs, and (ii) the integral of the axial strains along the element length must correspond to the basic axial displacement u_1^{bsc} . They are expressed in equations (4.1) and (4.2) respectively:

$$\begin{cases} N^{IPj} + k_{11}^{IPj} \cdot \Delta \varepsilon_0^{IPj} = N^{IPj+1} + k_{11}^{IPj+1} \cdot \Delta \varepsilon_0^{IPj+1} & \text{for } j = 1 \text{ to } no. \text{ IPs} - 1 \end{cases} \quad (4.1)$$

$$\begin{cases} \sum_{j=1}^{no. \text{ IPs}} \frac{w^{IPj} \cdot L}{2} \cdot (\varepsilon_0^{IPj} + \Delta \varepsilon_0^{IPj}) = u_1^{bsc} \end{cases} \quad (4.2)$$

where k_{11}^{IPj} is the first row-first column component of the sectional stiffness matrix evaluated at IP_j , w^{IPj} is the integration weight of the j^{th} integration point (it is assumed that the sum of the integration weights is equal to 2) and L is the element length. As it can be noticed, conditions (4.1) and (4.2) provide a linear system of equations; the number of equations corresponds to the number of IPs. The equations can be solved at each IP to obtain the axial strain increments $\Delta\varepsilon_0^{IPj}$ as function of the current set of axial forces. These relationships are provided in equations (4.3) and (4.4) for the first and the remaining IPs:

$$\Delta\varepsilon_0^{IP1} = \frac{\frac{2 \cdot u_1^{bsc}}{L} - \sum_{j=1}^{no. IPs} w^{IPj} \cdot \left(\varepsilon_0^{IPj} + \frac{N^{IP1} - N^{IPj}}{k_{11}^{IPj}} \right)}{\sum_{j=1}^{no. IPs} w^{IPj} \cdot \frac{k_{11}^{IP1}}{k_{11}^{IPj}}} \quad (4.3)$$

$$\Delta\varepsilon_0^{IPj} = \frac{(N^{IP1} - N^{IPj}) + k_{11}^{IP1} \cdot \Delta\varepsilon_0^{IP1}}{k_{11}^{IPj}} \quad (4.4)$$

The so computed strain increments $\Delta\varepsilon_0^{IPj}$ are used to update the total axial strains ε_0^{IPj} from the previous intra-element iteration and new sectional forces are computed. As shown in Figure 4.3, the procedure is repeated until the resulting axial forces N^{IPj} are equilibrated. In other words, this internal iterative procedure corrects the constant axial strain profile as obtained from the classical DB approach to ensure the same value of the axial force along the element. Note that the curvature profile remains linear as imposed in classical DB formulations.

4.2.2 Element state determination

The present subsection discusses the state determination for the axially equilibrated DB element, which consists in the evaluation of the element end forces \mathbf{p}^{bsc} and tangent stiffness matrix \mathbf{K}^{bsc} for a given increment of basic displacements $\Delta\mathbf{u}^{bsc}$. Once the axial force is equilibrated according to the method previously discussed, the generalized deformations \mathbf{e}^{IPj} at a generic integration point can be decomposed as:

$$\mathbf{e}^{IPj} = \mathbf{B}_{DB/c}^{IPj} \cdot \mathbf{u}^{bsc} + \mathbf{e}_{AE}^{IPj} \quad \text{with} \quad \mathbf{e}_{AE}^{IPj} = \begin{Bmatrix} \varepsilon_{0,AE}^{IPj} \\ 0 \end{Bmatrix} \quad (4.5)$$

where the first term $\mathbf{B}_{DB/c}^{IPj} \cdot \mathbf{u}^{bsc}$ represents the contribution associated to the classical displacement-based shape functions while the second \mathbf{e}_{AE}^{IPj} corresponds to the sum of the incremental corrections of the sectional axial strain computed during the internal iterative process, identified as $\varepsilon_{0,AE}^{IPj}$ in equation (4.5).

The element end forces are determined by application of the principle of virtual displacements (PVD), which can be written as follows:

$$[\delta\mathbf{u}^{bsc}]^T \mathbf{p}^{bsc} = \int_L [\delta\mathbf{e}(x)]^T \cdot \mathbf{s}(x) dx \quad (4.6)$$

The numerical integration of the expression above over the total number of IPs yields:

$$[\delta\mathbf{u}^{bsc}]^T \mathbf{p}^{bsc} = \sum_{no. IPs} [\delta\mathbf{e}^{IPj}]^T \cdot \mathbf{s}^{IPj} \cdot w^{IPj} \cdot \frac{L}{2} \quad (4.7)$$

For the axially equilibrated DB element, the PVD can be specialized by using equations (4.5) and (4.7):

$$[\delta \mathbf{u}^{bsc}]^T \mathbf{p}^{bsc} = [\delta \mathbf{u}^{bsc}]^T \cdot \sum_{no. IPs} [\mathbf{B}_{DB/c}^{IP_j}]^T \cdot \mathbf{s}^{IP_j} \cdot w^{IP_j} \cdot \frac{L}{2} + \sum_{no. IPs} [\delta \mathbf{e}_{AE}^{IP_j}]^T \cdot \mathbf{s}^{IP_j} \cdot w^{IP_j} \cdot \frac{L}{2} \quad (4.8)$$

The previous equations should be valid for any virtual increment δ , which results in the following system of two equations that have to be satisfied simultaneously:

$$\left\{ \begin{array}{l} \mathbf{p}^{bsc} = \sum_{no. IPs} [\mathbf{B}_{DB/c}^{IP_j}]^T \cdot \mathbf{s}^{IP_j} \cdot w^{IP_j} \cdot \frac{L}{2} \\ \sum_{no. IPs} [\delta \mathbf{e}_{AE}^{IP_j}]^T \cdot \mathbf{s}^{IP_j} \cdot w^{IP_j} \cdot \frac{L}{2} = 0 \end{array} \right. \quad (4.9)$$

$$\sum_{no. IPs} [\delta \mathbf{e}_{AE}^{IP_j}]^T \cdot \mathbf{s}^{IP_j} \cdot w^{IP_j} \cdot \frac{L}{2} = 0 \quad (4.10)$$

The verification of equation (4.2) directly demonstrates equation (4.10) for any $\delta \mathbf{e}_{AE}^{IP_j}$, while equation (4.9) shows that the basic end forces \mathbf{p}^{bsc} are computed from the internal section forces $\mathbf{s}(x)$ as in classical DB formulations.

The element tangent stiffness matrix \mathbf{K}^{bsc} is then straightforwardly obtained by deriving the element end forces \mathbf{p}^{bsc} with respect to the element basic displacements \mathbf{u}^{bsc} . With the aid of the chain rule of derivation and considering that the matrix $\mathbf{B}_{DB/c}$ does not depend on \mathbf{u}^{bsc} the following equation is derived:

$$\mathbf{K}^{bsc} = \frac{\partial \mathbf{p}^{bsc}}{\partial \mathbf{u}^{bsc}} = \sum_{no. IPs} [\mathbf{B}_{DB/c}^{IP_j}]^T \cdot \frac{\partial \mathbf{s}^{IP_j}}{\partial \mathbf{e}^{IP_j}} \cdot \frac{\partial \mathbf{e}^{IP_j}}{\partial \mathbf{u}^{bsc}} \cdot w^{IP_j} \cdot \frac{L}{2} \quad (4.11)$$

where the partial derivatives of the sectional forces with respect to generalized strains $\partial \mathbf{s}^{IP_j} / \partial \mathbf{e}^{IP_j}$ correspond, by definition, to the sectional stiffness matrix \mathbf{k} . The partial derivatives $\partial \varepsilon_0^{IP_j} / \partial \mathbf{u}^{bsc}$ at each integration point can be calculated from equations (4.3) and (4.4), making additional use of the conditions expressed in (4.1) and (4.2):

$$\frac{\partial \varepsilon_0^{IP_1}}{\partial u_k^{bsc}} = \frac{\frac{\partial}{\partial u_k^{bsc}} \left(\frac{2 \cdot u_1^{bsc}}{L} \right) - \sum_{j=1}^{no. IPs} w^{IP_j} \cdot \left(\frac{k_{12}^{IP_1} \cdot \frac{\partial \phi^{IP_1}}{\partial u_k^{bsc}} - k_{12}^{IP_j} \cdot \frac{\partial \phi^{IP_j}}{\partial u_k^{bsc}}}{k_{11}^{IP_j}} \right)}{\sum_{j=1}^{no. IPs} w^{IP_j} \cdot \frac{k_{11}^{IP_1}}{k_{11}^{IP_j}}} \quad (4.12)$$

$$\frac{\partial \varepsilon_0^{IP_j}}{\partial u_k^{bsc}} = \frac{\left(k_{12}^{IP_1} \cdot \frac{\partial \phi^{IP_1}}{\partial u_k^{bsc}} - k_{12}^{IP_j} \cdot \frac{\partial \phi^{IP_j}}{\partial u_k^{bsc}} \right) + k_{11}^{IP_1} \cdot \frac{\partial \varepsilon_0^{IP_1}}{\partial u_k^{bsc}}}{k_{11}^{IP_j}} \quad (4.13)$$

where the subscript k is used to indicate the component of \mathbf{u}^{bsc} with respect to which the derivation is performed. The derivatives of the curvatures are not presented here because they are similar to those obtained from classical DB approaches. The state determination procedure summarised in the flowchart of Figure 4.3 depicts the application of the expressions presented in the current subsection.

4.2.3 Axially equilibrated vs classical DB element

The axially equilibrated displacement-based (DB/ae) formulation was implemented in the finite element software SAGRES (Software for Analysis of GRAdient Effects in Structures), which also includes in its library classical displacement-based (DB/c) and force-based (FB) elements [130]. In this subsection the main features of the proposed FE are presented resorting to an application example. Namely, models using DB/ae and DB/c elements are compared both at the global and local level in order to highlight their relative advantages and drawbacks.

A 3 m RC cantilever column, subjected to an axial load ratio of about 1.25% and an incremental lateral displacement Δ , served as reference structure. The RC section was 300 mm large, 400 mm deep (bending direction), and 20 mm concrete

cover was assumed in both directions. The longitudinal reinforcement was formed by 16 Ø10 mm steel bars, corresponding roughly to a reinforcement ratio of about 1%. A schematic representation of the reference structure as well as of the sectional discretization used in all FE models herein considered is shown in Figure 4.4 (a). The mathematical relation proposed by Popovics [95] was used for both confined and unconfined concrete ($E_c=30$ GPa, $f'_c=37$ MPa, $\varepsilon_c=0.002$, $f'_{cc}=42$ MPa, $\varepsilon_{cc}=0.003$) while a bilinear constitutive law was assigned to the longitudinal reinforcement ($E_s=200$ GPa, $f_y=480$ MPa, $b=0.005$).

The influence of mesh refinement on the global-level response is investigated in Figure 4.4 (b), which displays pushover curves, in the form of a dimensionless lateral resisting force $V_N=(V \times L_s)/(N \times h)$ versus horizontal drift Δ/L_s . Models employing one, two and three DB elements (both DB/ae and DB/c), as well as a single FB element were considered. DB elements featured two Gauss-Legendre integration points (IPs) while five Gauss-Lobatto IPs were used for the FB element model. As discussed in Calabrese *et al.* [62], FB elements are sensitive to the element discretization and a minimum number of four IPs is generally required for good-accuracy solutions. DB/c element models, on the other hand, are only sensitive to the structural discretization and hence it is not justifiable to use more than two integration points per element. For comparison purposes the same number of IPs are used as well for DB/ae elements, even though, as discussed below with respect to Figure 4.4 (c), a larger number would be required for a closer-to-objective response.

The model with a single DB/c element shows, as expected, the strongest and stiffest response due to the constraints imposed in both the axial and transversal displacement fields. By removing the constraint on the axial displacement field through the iterative procedure introduced in subsection 4.2.1, the model using one DB/ae element provides a considerably softer response, causing a reduction in the simulated lateral strength. However, it can be noted that the latter is still overestimated when compared to the solution provided by the FB formulation, where no displacement fields are assigned and exact equilibrium is satisfied. By increasing the mesh refinement, both DB formulations tend to the FB solution, although the DB/ae element model converges much faster than the one using classical displacement shape functions (e.g., the response with one DB/ae element is superior to the one provided by two DB/c elements).

The impact of the number of integration points on the force-displacement response of the DB/ae element is shown in Figure 4.4 (c). Different combinations of integration points and schemes (Gauss-Legendre/Gauss-Lobatto) were considered using a single FE to discretize the structural member. The figure shows that the pushover curves tend to a unique, objective solution—represented by the highly refined nine IPs Gauss-Lobatto model—as the number of IPs increase. Further, a relatively low number of IPs, e.g. three Gauss-Legendre or four Gauss-Lobatto IPs, suffice to provide a satisfactory response. Even if two Gauss-Legendre or three Gauss-Lobatto are used, a relatively small numerical error of about 10% at peak response is observed for this example. Figure 4.4 (c) also shows a further particular feature: while FB and DB formulations always provide an upper and lower bound for the strain energy respectively, the proposed formulation does not offer a bound for this quantity. This relates to the exact verification of equilibrium, which is only achieved throughout the element for the axial force but not for the bending moment. Finally, the issue of localisation for softening sectional behaviour will not be addressed in the present document, although such pathology should occur for this formulation as it occurs for DB/c and FB approaches [33].

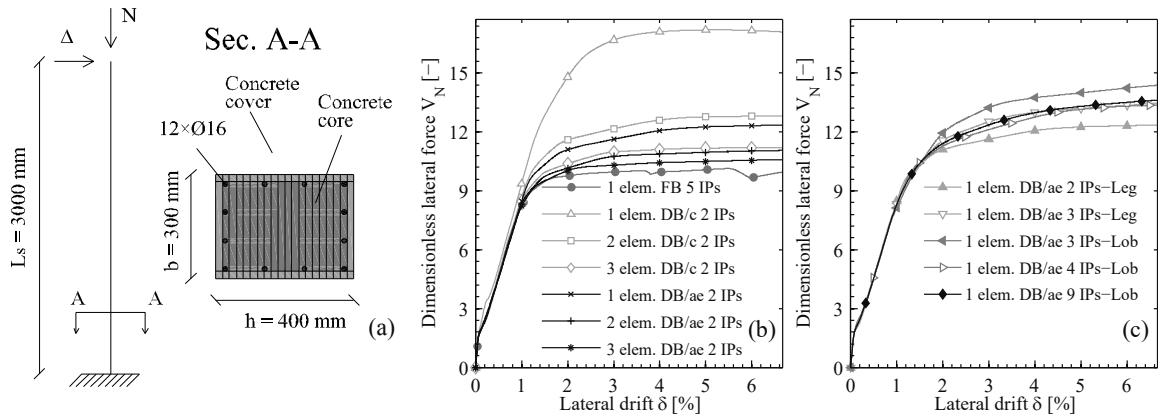


Figure 4.4: Application example: (a) Structural representation and sectional discretization. Global-level response of DB/ae models: (b) Influence of mesh refinement; (c) Influence of element discretization.

The local-level performance of models with a single DB/ae element (four Gauss-Lobatto IPs) and one DB/c element (two Gauss-Legendre IPs) is compared in the following. Figure 4.5 (a) starts by showing, for three different values of lateral drift, that curvatures profiles are linear irrespectively of the employed DB formulation. This is unsurprising since Hermitian shape functions are employed in both DB/ae and DB/c approaches to define the element transversal displacement field. Note, however, that the curvature profiles of the DB/ae element are not quantitatively equal to those of a DB/c element. In fact, although both DB/c and DB/ae elements are constrained to curvature linearity, the DB/ae formulation verifies the principle of virtual work—as expressed by eq. (4.9)—under a constant member axial force while the DB/c approach satisfies it by assuming a constant axial strain profile. This is shown in Figure 4.5 (b) and, as expected, on account of the shifting of the neutral axis towards the compression side of the section, positive strain values (tension), which increase with drift demands, are observed. The figure also depicts the strain profiles for the DB/ae element, which evidence different values for distinct integration sections resulting from the iterative procedure to obtain a constant axial force along the column. The highest tensile average strain is recorded at the bottom IP while at the element top, in correspondence of the inversion in sign of the curvature profile that takes place for large inelastic demands, small unrealistic tensile axial strains can be perceived. The constraint on the curvature profile is responsible for this effect. Overall, the DB/ae element better adheres to reality than the DB/c element as the shifting of the neutral axis is expected to occur at the cantilever base where the bending moment is largest. Finally, Figure 4.5 (c) shows the evolution of the axial force at distinct IPs with lateral drift. After an initial elastic phase, different IP axial forces occur in the DB/c element, which are symmetric around the value of the imposed axial load ($N^{IP_j} = N \pm \Delta N$). This conservation of average equilibrium, which was noted elsewhere [33,62], leads to an incorrect estimation of the flexural capacity of the structural member. This bias is not introduced by the DB/ae element, wherein the axial force in the four IPs is constant and equal to the external applied axial load.

The numerical performance of DB/ae and DB/c formulations is analysed in Figure 4.6 (a) by comparing the number of Newton-Raphson (NR) iterations required to attain convergence. Two models providing similar accuracy at the global level response, as shown in Figure 4.4, were selected: a single DB/ae element with four Gauss-Lobatto IPs and two DB/c elements with two Gauss-Legendre IPs per element. Two to four iterations were typically necessary for both models, with the DB/ae converging faster on average. This observation is corroborated by the fact that a total of about 2700 and 3400 NR iterations were needed for the DB/ae and DB/c model respectively, see Figure 4.6 (c). Although this could be expectable since only one DB/ae element is used, it is an encouraging indicator of the dependability of the element tangent stiffness matrix derived in eq. (4.11). The DB/ae total and average number of internal axial equilibrium iterations per NR cycle at each load step are displayed in Figure 4.6 (b) with black crosses and a grey line respectively. An average of 2.5 iterations per NR cycle is required throughout the entire simulation, which represents an acceptable increase in computational time. However, as the classical DB formulations do not require this iterative procedure they remain comparatively more performant time-wise, see Figure 4.6 (c).

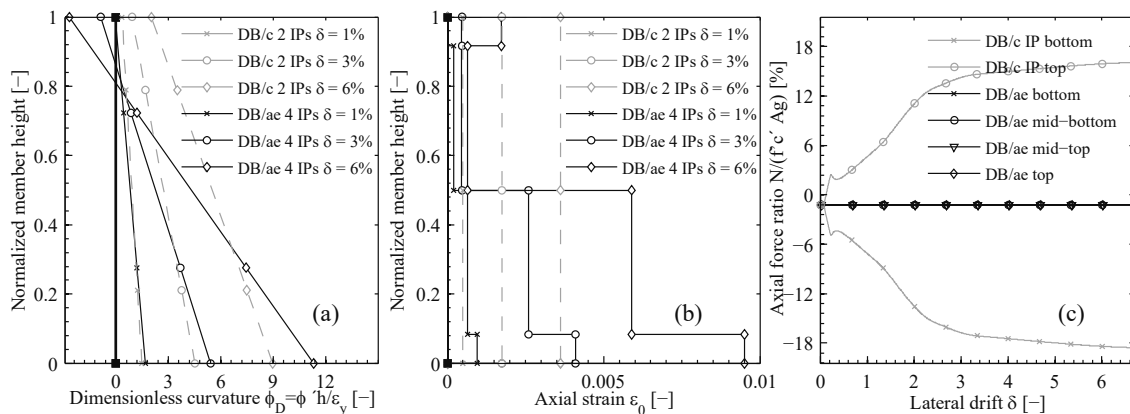


Figure 4.5: Comparison between DB/ae and DB/c element models at the local level: (a) Curvature profiles; (b) Vertical strain profiles; (c) Axial force history in different IPs.

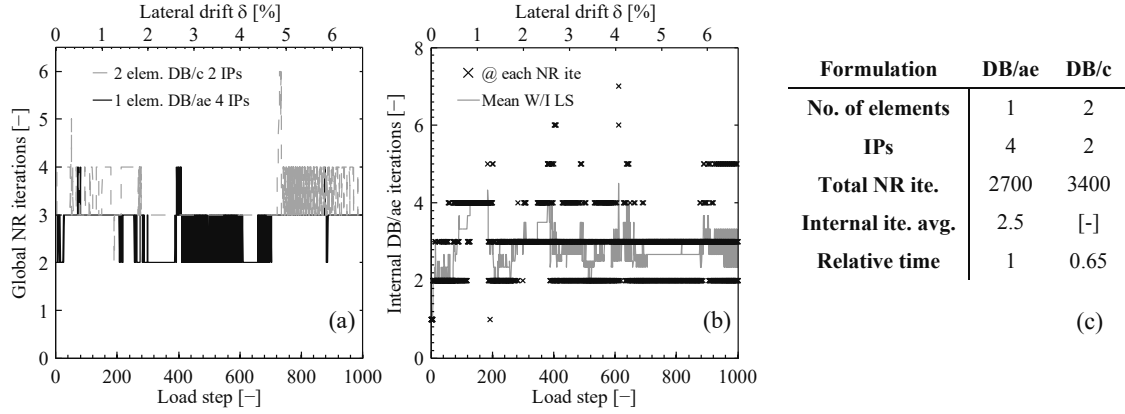


Figure 4.6: Numerical performance of the DB/ae formulation: (a) DB/ae vs DB/c-Global NR iterations; (b) Intra element iterations; (c) Summary of results.

4.3 Validation examples

The accuracy of the DB/ae formulation is herein benchmarked against experimental data from two series of quasi-static cyclic tests on RC bridge piers (subsection 4.3.1) and RC walls (subsection 4.3.2). Models employing DB/c and FB elements are included in the comparison in order to point out the strengths and weaknesses of the proposed approach. The numerical results are compared against the experimental results with regard to global and local quantities.

4.3.1 Tests on RC bridge piers

The ability of the DB/ae element to predict the nonlinear response of RC members is validated against a selection of quasi-static cyclic tests on circular RC bridge piers performed by Goodnight *et al.* [131]. The test units, which are listed in Table 4.1, were selected to be representative of the largest possible spectrum of shear spans $L_s/D \in [4, 8.67]$ and axial load ratios $N/(f'_c \times A_g) \in [5\%, 20\%]$. The longitudinal and lateral reinforcement layout was common to all the specimens and consisted of 10 #6 rebars ($\approx \emptyset 19$ mm) and a #3 ($\approx \emptyset 10$ mm) spiral at 2 inches (≈ 50 mm) pitch, corresponding to vertical and lateral reinforcement ratios that ranged between $\rho_l \in [1.6\%, 1.7\%]$ and $\rho_w \in [1\%, 1.3\%]$. A qualitative sketch of one of the test units, labelled as T9, is given in Figure 4.7 (a).

Table 4.1: Test matrix used for the validation of the proposed formulation (taken from [127]).

Test	D [mm]	L_s/D [-]	Longitudinal reinforcement (ρ_l)	Confining reinforcement (ρ_w)	$N/(f'_c \times A_g)$ [-]
T9	610	4	16 $\emptyset 19$ (1.6%)	$\emptyset 10$ @50 mm (1%)	5.5%
T19	457*	5.33	16 $\emptyset 19$ (1.7%)	$\emptyset 10$ @50 mm (1.3%)	10%
T20	457*	5.33	16 $\emptyset 19$ (1.7%)	$\emptyset 10$ @50 mm (1.3%)	5%
T23	457*	8.67	16 $\emptyset 19$ (1.7%)	$\emptyset 10$ @50 mm (1.3%)	5%
T24	457*	8.67	16 $\emptyset 19$ (1.7%)	$\emptyset 10$ @50 mm (1.3%)	10%
T27	610*	4	16 $\emptyset 19$ (1.6%)	$\emptyset 10$ @50 mm (1%)	10%
T28	457*	5.33	16 $\emptyset 19$ (1.7%)	$\emptyset 10$ @50 mm (1.3%)	15%
T29	457*	5.33	16 $\emptyset 19$ (1.7%)	$\emptyset 10$ @50 mm (1.3%)	20%

D : Column diameter, L_s : Shear span, *Nominal diameter, not accounting for the fact that cover concrete was not present in the instrumented region.

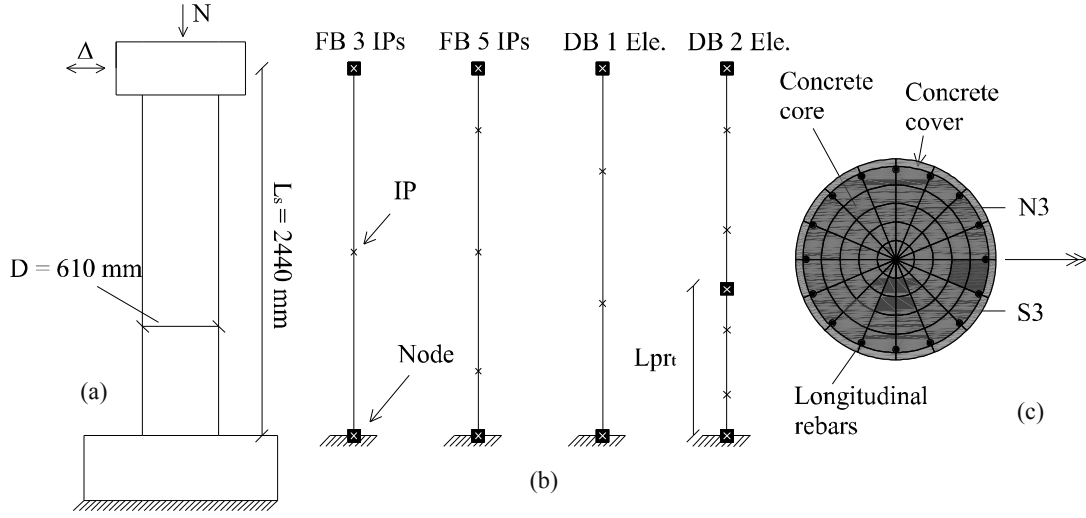


Figure 4.7: Test series by Goodnight et al. [131]: (a) Sketch of test unit T9; (b) Element formulation and discretization; (c) Sectional discretization of test unit T9.

All columns were subjected to a standard cyclic loading protocol with three cycles at each displacement amplitude. Target markers attached to the longitudinal rebars in the plastic hinge region tracked the displacements during the test and allowed to isolate the main deformation contributions to the total lateral displacement, namely base rotation and flexural displacements. Due to the relatively large shear span ratio of the considered test units, the impact of shear deformations was negligible.

The whole set of test units described in Table 4.2 was simulated with models employing DB/ae, DB/c and FB elements, following the four schemes depicted in Figure 4.7 (b). Two models used a single FB element with three and five Gauss-Lobatto integration sections. The former represents the minimum number of IPs to simulate the linear response with a FB beam column element without under-integration [132]. However, not less than four IPs are recommended to simulate the nonlinear hardening response of structural members [133]. Despite such consideration, a discretization with three IPs was selected as it ensured for the studied specimens an influence length of the bottom integration point similar to the measured extent of plasticity as discussed below. The fulfilment of this condition is recommended to optimize the agreement between the numerical results for FB elements and the experimental measurements at the local level [33]. For what concerns DB/c and DB/ae, models featuring one and two finite elements per structural member were selected. Four Gauss-Lobatto IPs were used within each DB element for two reasons: (i) the Gauss-Lobatto quadrature rule allows to have an integration section at the element ends, which is useful if base curvatures are to be compared; (ii) although the DB/c formulation is insensitive to element discretization [62], this is not the case for DB/ae elements, which requires around four IPs as shown in Figure 4.4. For the cases where the structural member is discretized with two finite elements, the length of the base element is selected as the upper bound of the measured extent of plasticity— L_{pr} in Figure 4.7 (b), which is given by the following equation [134]:

$$L_{pr} = 2kL_s + 0.75D \quad (4.14)$$

where $k = 0.2 \times f_u / f_y - 1 < 0.08$ is the factor accounting for the moment gradient as suggested by [69], L_s is the shear span, and D is the column diameter. The same sectional discretization consisting of 80 confined concrete and 10 steel fibres is used to model the columns. They had no cover concrete in the plastic hinge region and therefore no unconfined concrete fibres were defined. The exception was specimen T9, for which 16 unconfined concrete fibers had to be included as well for the sectional discretization as represented in Figure 4.7 (c). The relationship proposed by Popovics-Mander [95] and Mene-gotto-Pinto [135] were used for the mechanical characterization of concrete and steel. The enhancement in concrete strength and strain at peak strength due to confinement were computed according to Mander's model [136]. The main material parameters used to characterize the concrete and steel stress-strain laws were derived from the actual material tests reported by Goodnight *et al.* [131], which differed for each tested specimen. Table 4.2 reports the parameters used to model unit T9. Due to space constraints, the comparison between the numerical and experimental results shown in the next figures refer to this specimen alone.

Table 4.2: Main material parameters used in the numerical models of test T9.

Concrete					Reinforcing steel			
f'_c	ε_c	E_c	f'_{cc}	ε_{cc}	f_y	f_u	E_s	b
[MPa]	[‰]	[GPa]	[MPa]	[‰]	[MPa]	[MPa]	[GPa]	[‰]
46.9	2	34.3	62.6	5.3	470	640	199.8	7.3

The force-displacement F- Δ response for all the models discussed above is depicted in Figure 4.8 and compared with the experimental measurements. A different graph is provided for each type of element formulation. Flexural displacements are reported on the bottom x-axis. These correspond to the total displacements of the numerical model; the experimental flexural displacements are computed by subtracting the displacement due to base rotation from the total displacement. The lateral displacement ductilities corresponding to the imposed demands of the cyclic loading protocol are shown in the top x-axis. The following observations can be made: (i) The FB models match satisfactorily the experimental data, with the model FB 3IPs slightly underestimating the actual response, which is typical for the bottom-up type of convergence of FB formulations [62]; (ii) Both DB models using a single element overestimate the experimental F- Δ curve, although the error associated to the DB/ae is sensibly lower; (iii) A good match of the experimental F- Δ curve is obtained by using two DB elements per member, both for the DB/c and the DB/ae approaches.

The DB/c and DB/ae with two elements per member and the FB element with five IPs (FB 5IP) are seen to perform better at the global level, which is the reason why they are chosen for the following comparison at the local level. The experimental and numerical curvature profiles for different levels of displacement ductility are shown in Figure 4.9. Taking into account the symmetry of the system, only the curvature profiles in the positive direction of loading were analysed. Increasing displacement ductility levels from yielding ($\mu_A=1$) up to $\mu_A=8$ were considered. Within each element, the obtained curvatures at the successive IPs are connected with a straight line. For DB elements, where the linearity of curvatures is imposed, this representation of the curvature profiles is exact; for FB elements, it corresponds instead to a slight overestimation of the real curvature distribution along the element. The better match of the DB/ae formulation is apparent: (a) The model FB 5IPs tends to overestimate the base curvature, and markedly so for large drift levels. As an example, the relative error¹ corresponding to the base curvature ($\eta_{\phi b}$) for a ductility demand $\mu_A=8$ is approximately 110%; (b) The opposite trend applies to the DB/c model, which underestimates the experimental base curvature ($\eta_{\phi b}=50\%$ for $\mu_A=8$). Moreover, when such elements are employed, it is worthy to notice how the numerical curvature profiles are not continuous along the member length, which originates from the non-strict verification of equilibrium along each finite element; (c) The match between observed and calculated curvature profiles is remarkably improved when DB/ae are used, showing a relative error for the base curvature at $\mu_A=8$ smaller than 5%. The agreement between analytical and experimental base curvature appears to decrease with the attained ductility level, with a maximum relative error of 35% for $\mu_A=2$. This can be attributed to the use of a constant bottom element length, which does not reflect the experimentally observed decrease on the extent of plasticity with ductility demand [127]. Finally, observe that the strict verification of axial equilibrium almost completely eliminates the discontinuity in curvatures between the bottom and upper elements.

¹ relative error: $\eta_v = \left| 1 - \frac{v_{exp}}{v_{num}} \right|$

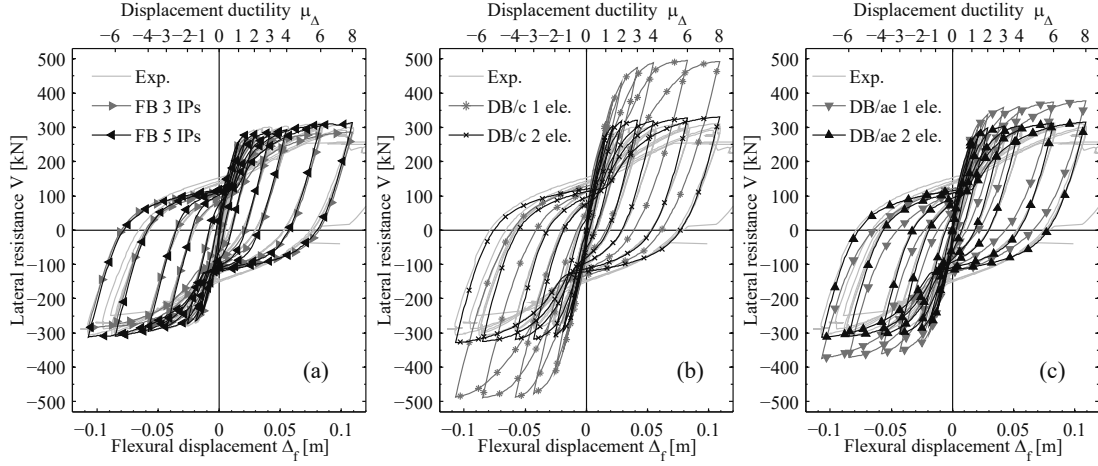


Figure 4.8: Experimental vs numerical force-displacement response for test T9: (a) FB, (b) DB/c and (c) DB/ae models.

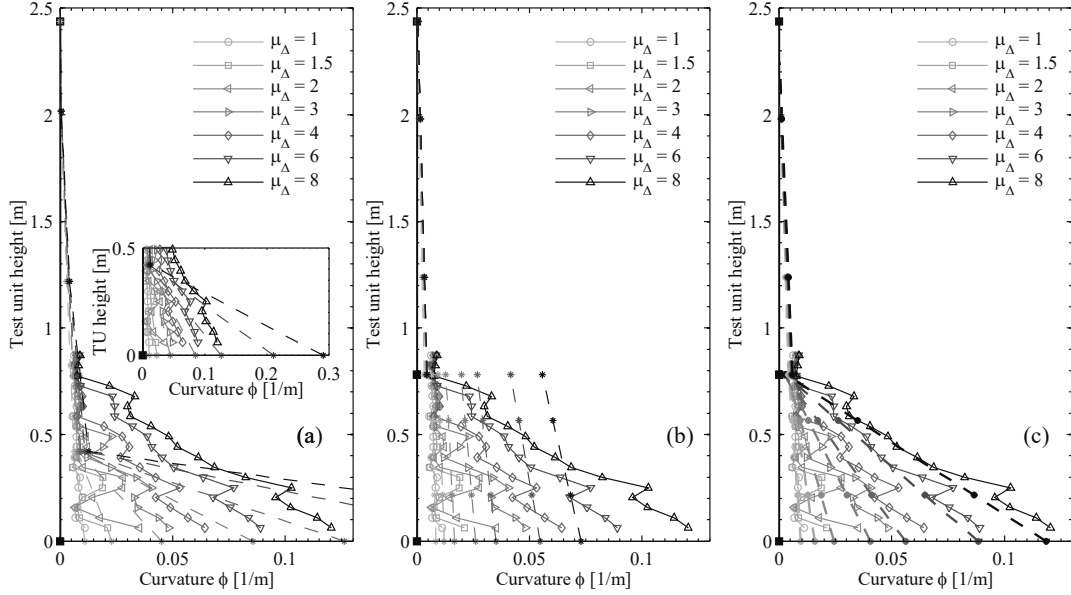


Figure 4.9: Experimental vs numerical curvature profiles for test T9 at positive ductility levels: (a) FB 5 IPs, (b) two elements DB/c and (c) two elements DB/ae models.

The vertical strains are depicted in Figure 4.10 and Figure 4.11 for the two outmost rebars in tension (N3) and compression (S3), which are indicated in Figure 4.7 (c). Once again, for both cases the DB/ae provides improved strain predictions with respect to DB/c and FB elements models, which tend to underestimate and overestimate respectively the maximum experimental strains. If base strains are averaged over all ductility levels, the following relative errors are obtained: $\eta_{\varepsilon_b}^{N3}=75\%$ and $\eta_{\varepsilon_b}^{S3}=65\%$ for FB, $\eta_{\varepsilon_b}^{N3}=44\%$ and $\eta_{\varepsilon_b}^{S3}=37\%$ for DB/c, $\eta_{\varepsilon_b}^{N3}=9\%$ and $\eta_{\varepsilon_b}^{S3}=25\%$ for DB/ae models. The errors for DB/ae reduce to $\eta_{\varepsilon_b}^{N3}=2\%$ and $\eta_{\varepsilon_b}^{S3}=18\%$ if only large ductility levels are considered ($\mu_{\Delta}=6$ and $\mu_{\Delta}=8$). The discrepancy between numerical and experimental strains obtained for the rebar in compression with respect to the one in tension is due to the following reasons: (i) compression strain profiles are not as linear as their counterpart in tension as they are more influenced by phenomena occurring at the micro-level; (ii) the height at which compression strains deviate from linearity is smaller than the extent of plasticity (L_{pr}) used to discretize the structural member. A different (shorter) length of the bottom DB/ae element would therefore be needed to improve the simulation of compressive strain profiles. For this reason, in the framework of plastic hinge models, Goodnight *et al.* [134] proposed a different plastic hinge length L_{pr_c} (to be used in conjunction with a bilinear curvature profile) to reliably evaluate limit state displacements based on compression strains. Nevertheless, changing the length of the base DB/ae element would then inevitably lead to a poorer prediction of both the curvatures and tensile strains. The latter have a more clear influence on the measured curvatures since, for the same level of top displacement, they are in absolute value considerably larger than compression strains.

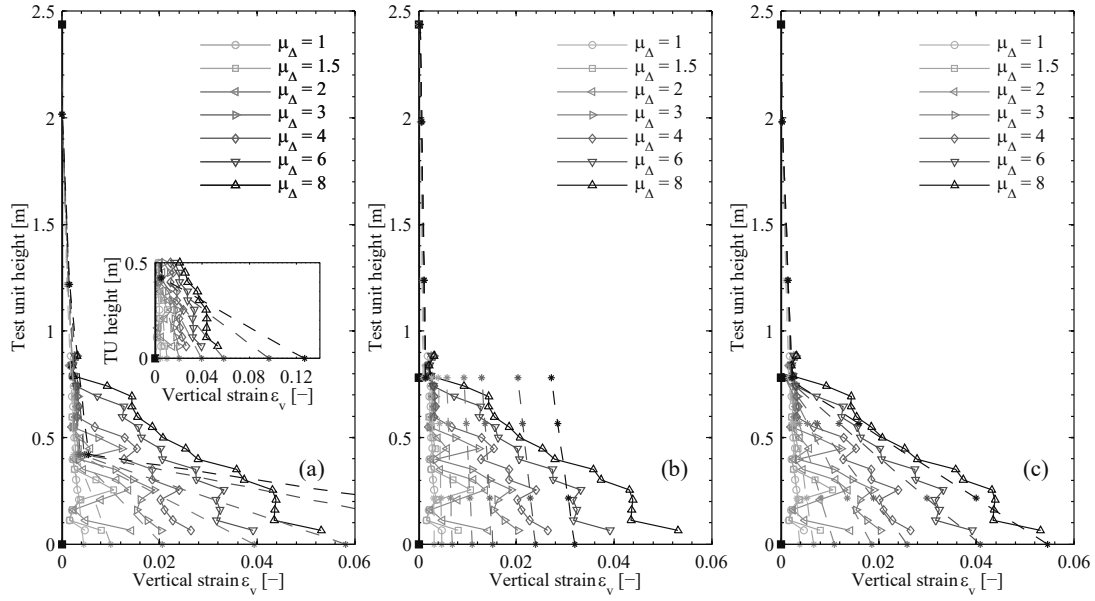


Figure 4.10: Experimental vs numerical vertical strain profiles of rebar N3 for test T9 at positive ductility levels: (a) FB 5 IPs, (b) two elements DB/c and (c) two elements DB/ae models.

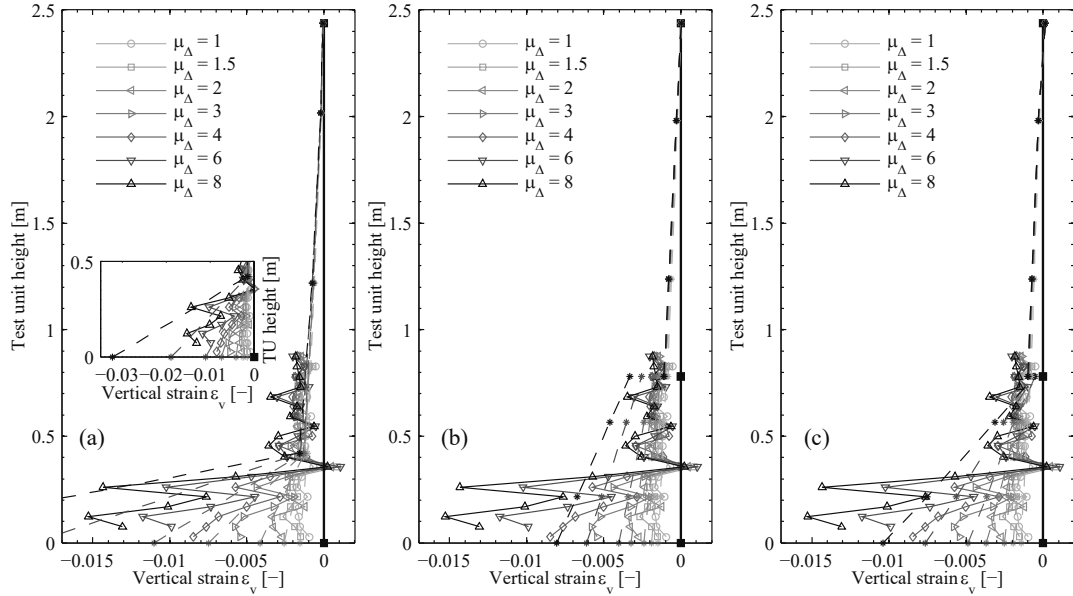


Figure 4.11: Experimental vs numerical vertical strain profiles of rebar S3 for test T9 at positive ductility levels: (a) FB 5 IPs, (b) two elements DB/c and (c) two elements DB/ae models.

As a further local level investigation, the comparison between the experimental vertical strains of rebar N3 monitored at the bottom of the RC column, and the numerical ones (measured at the bottom IP), are shown in Figure 4.12. Again, the DB/ae model offers the best agreement between simulation and test data, especially regarding the tensile peak strain levels. An underestimation of the residual strains at zero displacement level is instead common to all three models, indicating that the accumulation of plastic reinforcement strains over multiple cycles is not well captured. However, this issue is not directly related to the element formulation and could arguably be addressed with more advanced steel and concrete constitutive relationships for cyclic response.

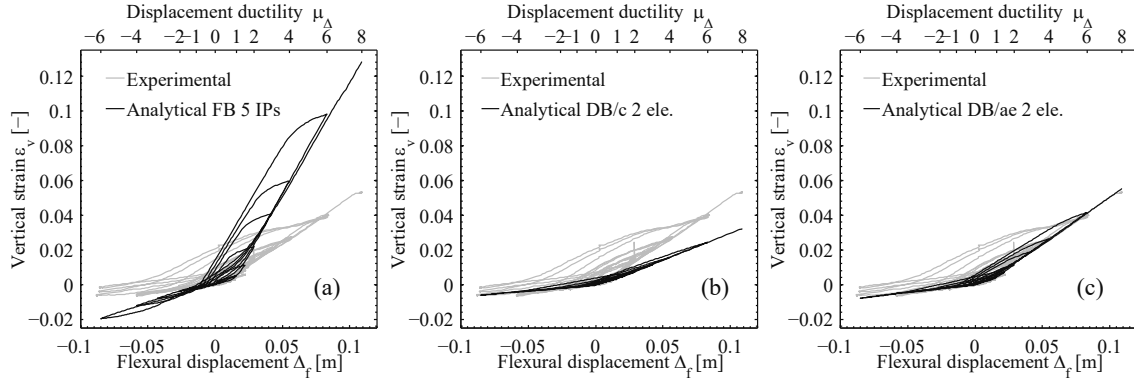


Figure 4.12: Experimental vs numerical vertical strain history of rebar N3 measured at the base section of test T9 for positive ductility levels: (a) FB 5 IPs, (b) two elements DB/c and (c) two elements DB/ae models.

Table 4.3: Numerical error in the calculation of the base curvature for all the models and selected test units tested by Goodnight et al. [131] at different ductility levels.

Test	Ductility Level (μ_Δ)	Base curvature average relative error: $\eta_{\phi b}^{avg} = \frac{1}{2} \left(\left 1 - \frac{(\phi_{b,an}^+)}{\phi_{b,exp}^+} \right + \left 1 - \frac{(\phi_{b,an}^-)}{\phi_{b,exp}^-} \right \right)$					
		FB 3IPs	FB 5IPs	DB/c 1 ele.	DB/c 2 ele.	DB/ae 1 ele.	DB/ae 2 ele.
T9	$\mu_\Delta = \pm 2$	43.6%	18.3%	65.1%	55.5%	59.9%	35.6%
	$\mu_\Delta = \pm 4$	28.3%	92.7%	61.2%	47.2%	54.6%	15.6%
	$\mu_\Delta = \pm 6$	19.5%	124.8%	58.1%	41.8%	50.0%	5.8%
T19	$\mu_\Delta = \pm 2$	45.2%	5.9%	64.6%	53.9%	61.4%	35.1%
	$\mu_\Delta = \pm 4$	37.6%	53.9%	64.1%	49.7%	60.2%	22.5%
	$\mu_\Delta = \pm 6$	32.7%	68.5%	62.3%	46.1%	57.7%	16.1%
T20	$\mu_\Delta = \pm 2$	49.0%	6.3%	67.4%	58.0%	63.6%	38.5%
	$\mu_\Delta = \pm 4$	33.6%	58.7%	62.6%	48.1%	57.5%	17.6%
	$\mu_\Delta = \pm 6$	33.1%	46.8%	62.9%	48.4%	57.7%	16.8%
T23	$\mu_\Delta = \pm 2$	52.1%	5.6%	69.4%	56.0%	65.8%	34.9%
	$\mu_\Delta = \pm 4$	39.0%	45.9%	65.5%	45.0%	60.9%	11.2%
	$\mu_\Delta = \pm 6$	35.6%	26.2%	64.7%	42.7%	59.6%	4.2%
T24	$\mu_\Delta = \pm 2$	51.0%	5.4%	68.2%	54.2%	65.2%	34.8%
	$\mu_\Delta = \pm 4$	40.1%	47.5%	65.5%	44.5%	61.7%	12.9%
	$\mu_\Delta = \pm 6$	38.1%	55.9%	65.4%	42.4%	61.1%	8.4%
T27	$\mu_\Delta = \pm 2$	32.4%	44.2%	58.1%	47.3%	53.9%	23.4%
	$\mu_\Delta = \pm 4$	17.7%	111.6%	53.8%	38.9%	48.3%	5.9%
	$\mu_\Delta = \pm 6$	16.5%	119.7%	54.2%	38.3%	47.9%	5.0%
T28	$\mu_\Delta = \pm 2$	35.0%	34.0%	58.5%	45.3%	55.7%	21.9%
	$\mu_\Delta = \pm 4$	30.8%	79.9%	59.8%	44.1%	56.5%	13.7%
	$\mu_\Delta = \pm 6$	30.0%	88.5%	60.3%	43.4%	56.4%	12.3%
T29	$\mu_\Delta = \pm 2$	37.0%	31.7%	59.2%	45.8%	57.4%	24.8%
	$\mu_\Delta = \pm 4$	31.6%	78.7%	59.3%	43.5%	57.2%	14.7%
	$\mu_\Delta = \pm 6$	30.2%	90.8%	59.3%	42.3%	56.7%	12.5%

Finally, Table 4.3 compares the experimental base curvatures of the entire dataset units with all the employed models for three distinct values of displacement ductility ($\mu_\Delta=2$, $\mu_\Delta=4$ and $\mu_\Delta=6$). The comparison is made in terms of average relative error ($\eta_{\phi b}^{avg}$), which is defined as the mean of the relative base curvatures errors for the positive and negative directions of loading. For each test unit and ductility level, the minimum value of $\eta_{\phi b}^{avg}$ is highlighted in bold in Table 4.3. For most cases, the model composed of two DB/ae elements per structural member provides the best simulation of base

curvatures. The $\eta_{\phi b}^{avg}$ predicted by such model results generally smaller than 20% and tends to decrease for increasing inelastic demands. Values of $\eta_{\phi b}^{avg}$ larger than 30% are obtained only for $\mu_\Delta=2$ in tests T9, T19, T20, T23 and T24, in which cases the model FB 5 IPs leads to the best predictions. For larger values of μ_Δ the experimental base curvatures are consistently and largely overestimated by the model FB 5 IPs, as confirmed by Figure 4.9.

4.3.2 Tests on RC structural walls

Five out of the six RC walls (labelled WSH1 to WSH6) from the experimental campaign carried out by Dazio *et al.* [137] are used in this subsection for validation purposes. Wall WSH1 was disregarded due to the poor ductility properties of the longitudinal reinforcement which led the specimen to fail at a low level of inelasticity. Moreover only manual measurements were employed to evaluate local level quantities of WSH1, which were judged less reliable than those of all the other tests where hard wired instruments were used.

The main geometrical and loading characteristics of the test specimens are shown in Table 4.4. A constant vertical load was applied at the top of the specimens, which were then subjected to a standard cyclic loading protocol [138]. The test units differed mainly with regard to the layout and content of both longitudinal and horizontal reinforcement, as well as to the applied axial load ratio.

Local deformations were obtained from linear variable differential transformers (LVDTs) and Demec measurements, allowing to isolate the different contributions to the total lateral displacement, namely due to flexure, base rotation and shear. The latter played a non-negligible role (up to a maximum of around 10% of the total deformation) due to the small shear span ratios and thus could not be disregarded. In the framework of Euler-Bernoulli beam theory, shear deformations are not considered and therefore, in order to compare consistently numerical and experimental results, their contribution had to be removed from the total lateral displacement. However, this does not represent a limitation to the present validation example since: (i) the proposed formulation can be extended to a more general one accounting for shear deformations, e.g. Timoshenko beam theory; (ii) shear deformation can be included separately as a ratio of the flexural displacement [69,139–141].

The same models described in the previous subsection 4.3.1—i.e. FB 5 IPs, FB 3 IPs, 1 and 2 elements DB/c, 1 and 2 elements DB/ae—are employed to simulate the set of chosen RC walls. Due to space constraints, only test unit WSH6 is used in the following paragraphs to show and discuss the comparison between numerical and experimental results, both at the global and local level. The summary of the response of the entire set of RC walls is included in a table provided at the end of the present subsection.

The geometry and cross sectional reinforcement layout of wall WSH6 are depicted in Figure 4.13 (a) and (b). Well confined boundary elements were present to increase the flexural capacity of the structural member. The longitudinal reinforcement consisted of 22 Ø8 mm and 6 Ø12 mm bars for the web ($\rho_w=0.54\%$) and boundary elements ($\rho_b=1.54\%$). The shear reinforcement was composed of Ø6 mm bars spaced 150 mm while Ø6mm and Ø4.2 mm hoops at 50 mm were employed to properly confine the wall edges. The fibre sectional discretization used in the numerical models is displayed in Figure 4.13 (c). As in the previous subsection, the material models proposed by Popovics-Mander [95] and Menegotto-Pinto [135] were adopted to characterize the concrete and steel stress-strain laws. Different confinement factors were computed according to the model by Mander *et al.* [136] for the core concrete in the web and in the boundary elements. The main material parameters are given in Table 4.5. When two elements were employed to discretize the structural member (DB/c and DB/ae), the length of the one at the bottom was taken as the height of the plastic zone L_{pz} , which is defined by Dazio *et al.* [137] as the height at which the plastic curvature profile is equal to the yield curvature.

The experimental and numerical force-displacement responses of wall WSH6 are contrasted in Figure 4.14. On the bottom x-axis, flexural displacements Δ_f were calculated by subtracting the displacements due to base rotation and shear deformations from the total lateral displacements. Displacement ductility μ_Δ and lateral resisting force V are instead represented on the top x-axis and vertical y-axis. The two DB models using two elements per structural member satisfactorily reproduce the experimental results. Namely, the force capacity at all displacement reversals is adequately captured, with relative errors $\eta_V < 5\%$. FB models are slightly less accurate, underestimating the resisting force at loading reversals (η_V up to 12%). As expected, the DB models using a single FE overestimate the strength capacity of the structural member, although this effect is significantly less pronounced for the DB/ae model.

Table 4.4: Main properties of test units by Dazio et al. [137] used for validation of the DB/ae formulation.

Test unit	L_s [mm]	h [mm]	L_s/h [-]	t [mm]	$N/(f'_c \times A_g)$ [%]	$\rho_{l,bound}$ [%]	$\rho_{l,web}$ [%]	ρ_h [%]	Conf. BE ¹ [-]
WSH2	4560	2000	2.28	150	5.7	1.32	0.30	0.25	✓
WSH3	4560	2000	2.28	150	5.8	1.54	0.54	0.25	✓
WSH4	4560	2000	2.28	150	5.7	1.54	0.54	0.25	✗
WSH5	4560	2000	2.28	150	12.8	0.67	0.24	0.25	✓
WSH6	4520	2000	2.20	150	10.8	1.54	0.54	0.25	✓

L_s : shear span, h : wall length, t : wall thickness, $N/(f'_c \times A_g)$: axial load ratio, $\rho_{l,bound}$: boundary elements longitudinal reinforcement ratio $\rho_{l,web}$: web longitudinal reinforcement ratio ρ_h : horizontal reinforcement ratio **Conf. BE¹**: additional confining and stabilizing reinforcement in the boundary elements (hoops and ties)

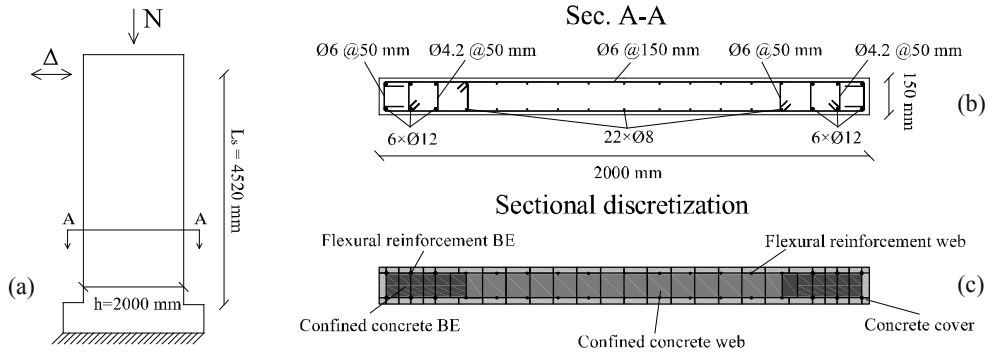


Figure 4.13: Test unit WSH6: (a) Sketch of geometry and applied loading; (b) reinforcement layout and (c) sectional discretization.

Table 4.5: Main material parameters used in the numerical models of test WSH6, derived from the properties reported by Dazio et al. [137].

	Concrete						Reinforcing steel			
	f'_c [MPa]	ε_c [‰]	E_c [GPa]	f'_{cc} [MPa]	ε_{cc} [‰]		f_y [MPa]	f_u [MPa]	E_s [GPa]	b [‰]
Web	45.6	2	36.9	48.4	2.6	Ø8 mm	576	675	200	9.3
Boundary	45.6	2	36.9	53.5	5.1	Ø12 mm	583	714	200	8.4

At the local scale of analysis, the numerical *versus* the experimental curvature and strain profiles of corner rebars are displayed in Figure 4.15 and Figure 4.16. Only the models yielding the best match at the global level are included in the comparison, i.e. FB 5IPs, DB/c and DB/ae with two elements per structural member. Several displacement ductility demands are considered, each one corresponding to a point of reversal in the hysteretic force-displacement response of Figure 4.14. Due to the symmetry of both specimen cross-section and loading protocol, only curvature and strain profiles relative to positive top displacements are shown.

The DB/ae element model best matches the experimental curvatures, with $\eta_{\phi b} < 10\%$ for all ductility levels. For large values of μ_A , the base curvatures are greatly underestimated by the DB/c model (e.g., $\eta_{\phi b} > 40\%$ for $\mu_A = 8$) and overestimated by the FB 5IPs model (e.g., $\eta_{\phi b} > 120\%$ for $\mu_A = 8$). Similar comments apply regarding the tensile strain profiles of Figure 4.16. Strain profiles in compression are instead best captured by the model FB 5IPs. Although the DB/ae model performs slightly better than the DB/c, both underestimate the recorded maximum compressive strain. As discussed in subsection 4.3.1, this is a direct consequence of the assumed FE discretization of the structural member. A smaller length for the base element would have improved the comparison at the price of worsening both the simulated curvatures and tensile strains. The good fit from the model FB 5IPs is however not a general rule, as confirmed by the results obtained in the previous subsection (Figure 4.11).

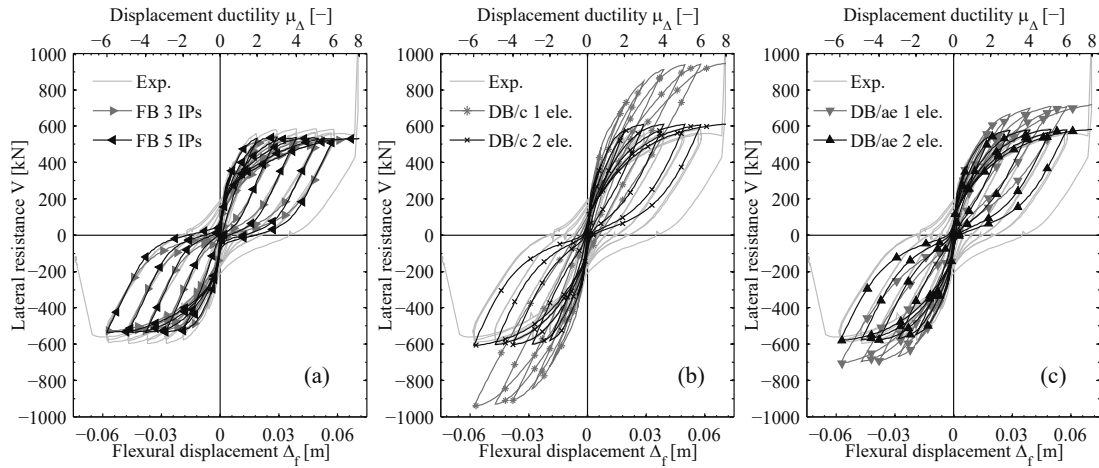


Figure 4.14: Experimental vs numerical force-displacement response for test WSH6: (a) FB, (b) DB/c and (c) DB/ae models.

Finally, numerical and experimental base curvatures for the entire set of employed models and selected RC walls are compared in Table 4.6 in terms of the average relative error ($\eta_{\phi b}^{avg}$), which is calculated at three distinct ductility levels. Similar to the results of the previous subsection (Table 4.3), the DB/ae model with two elements per structural member generally leads to the highest precision. Once again, the worst results are obtained at the lowest ductility level ($\mu_{\Delta}=2$), reaching a value of $\eta_{\phi b}^{avg}$ around 30%. This is sensibly smaller than the relative errors obtained with any of the other models, where the maximum $\eta_{\phi b}^{avg}$ ranged from 50% to 120%.

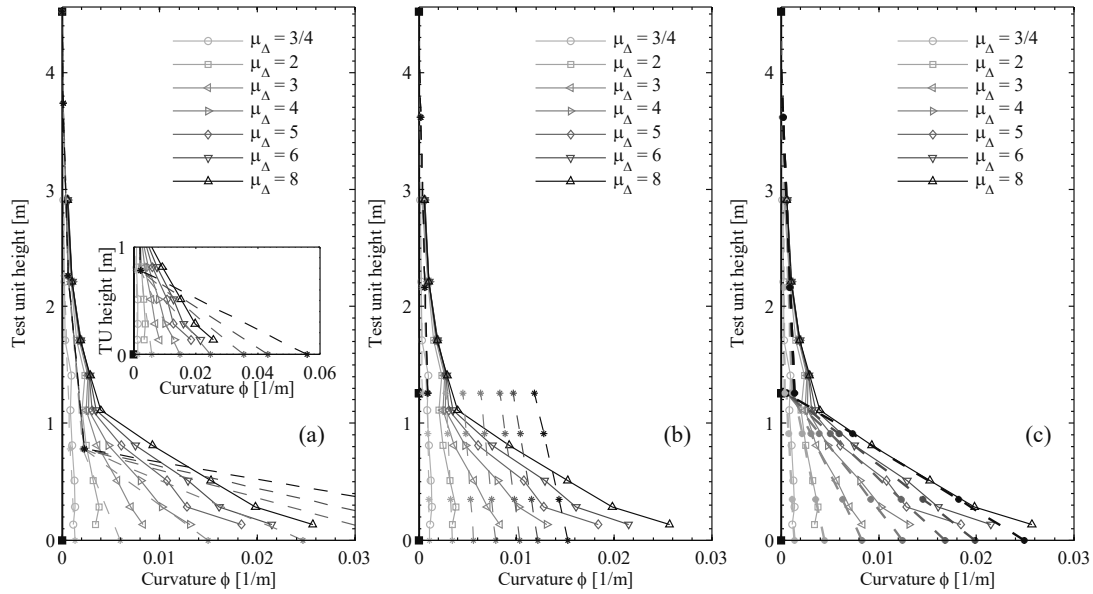


Figure 4.15: Experimental vs numerical curvature profiles for test WSH6 at positive ductility levels: (a) FB 5 IPs, (b) two elements DB/c and (c) two elements DB/ae models.

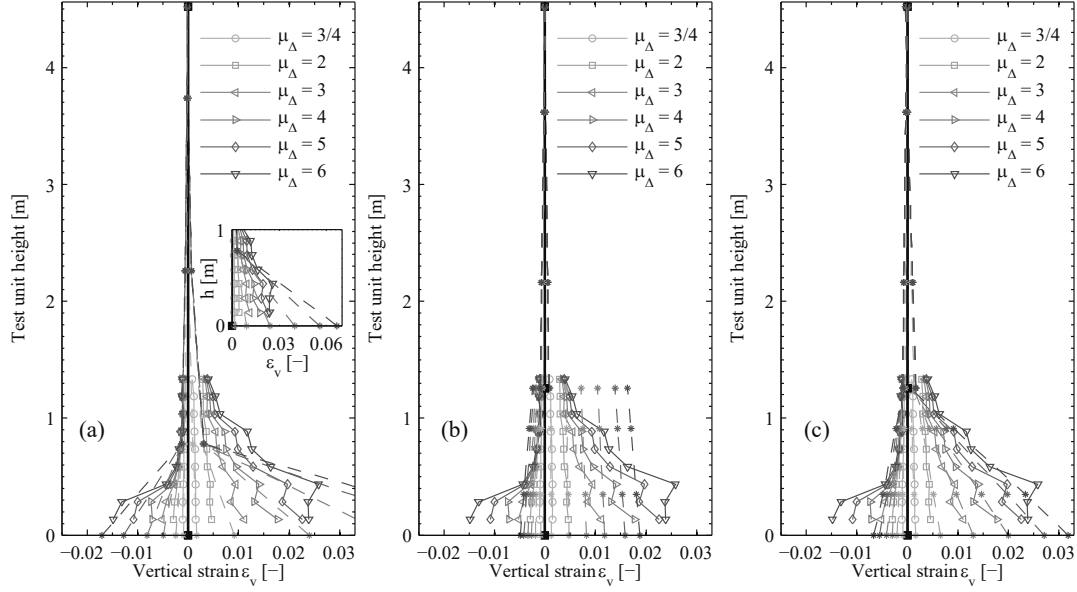


Figure 4.16: Experimental vs numerical vertical strain profiles of corner rebars for test WSH6 at positive ductility levels: (a) FB 5 IPs, (b) two elements DB/c and (c) two elements DB/ae models.

Table 4.6: Numerical error in the calculation of the base curvature for all the models and selected test units tested by Dazio et al. [137] at different ductility levels.

Test	Ductility Level (μ_Δ)	Base curvature average relative error: $\eta_{\phi b}^{avg} = \frac{1}{2} \left(\left 1 - \frac{(\phi_{b,an}^+)}{\phi_{b,exp}^+} \right + \left 1 - \frac{(\phi_{b,an}^-)}{\phi_{b,exp}^-} \right \right)$					
		FB 3IPs	FB 5IPs	DB/c 1 ele.	DB/c 2 ele.	DB/ae 1 ele.	DB/ae 2 ele.
WSH2	$\mu_\Delta = \pm 2$	17.1%	16.8%	55.1%	7.7%	40.0%	0.2%
	$\mu_\Delta = \pm 4$	34.1%	58.3%	68.3%	27.4%	58.1%	10.1%
	$\mu_\Delta = \pm 6$	56.4%	15.7%	80.0%	52.2%	73.2%	22.7%
WSH3	$\mu_\Delta = \pm 2$	29.8%	76.1%	28.0%	25.8%	23.1%	30.9%
	$\mu_\Delta = \pm 4$	24.5%	89.7%	61.0%	44.2%	51.2%	8.8%
	$\mu_\Delta = \pm 6$	35.1%	79.5%	68.1%	53.2%	59.6%	22.2%
WSH4	$\mu_\Delta = \pm 2$	20.4%	37.2%	52.8%	27.4%	41.7%	3.0%
	$\mu_\Delta = \pm 4$	35.2%	70.2%	67.0%	44.4%	58.5%	15.0%
	$\mu_\Delta = \pm 6$	N/A	N/A	N/A	N/A	N/A	N/A
WSH5	$\mu_\Delta = \pm 2$	14.9%	20.7%	27.8%	12.2%	23.0%	30.3%
	$\mu_\Delta = \pm 4$	20.9%	36.9%	59.2%	20.6%	49.8%	13.4%
	$\mu_\Delta = \pm 6$	38.8%	57.5%	70.8%	36.4%	62.7%	6.8%
WSH6	$\mu_\Delta = \pm 2$	12.1%	63.0%	34.4%	9.2%	21.7%	17.9%
	$\mu_\Delta = \pm 4$	25.0%	86.2%	60.9%	40.9%	53.0%	6.1%
	$\mu_\Delta = \pm 6$	19.4%	124.8%	59.1%	36.6%	50.9%	10.7%

4.3.3 Limitations

The validation examples presented in the previous sub-sections have shown that the DB/ae formulation can be effectively used in the simulation of the cyclic-nonlinear response of RC members with an encouraging match occurring also at the local strain level. Namely, it was shown that the linear curvature profile that develops in the plastic hinge region of a member in single bending due to tension shift effects can be captured by employing two DB/ae elements, and assigning a length for the bottom element equal to the extent of plasticity. This quantity is not usually available for engineering practice applications, and further research is yet required on the subject. A first approximation to estimate the extent of

plasticity, which appears to be reasonably accurate for the present case studies, can be obtained by multiplying the ‘equivalent plastic hinge length’ as proposed by Priestley *et al.* [69] by a factor of two. This factor intends to account for the fact that the curvature profile is not constant but rather approximately linear within the inelastic region.

Additionally, as observed by Goodnight *et al.* [134], the length of plastification increases for increasing ductility demands, which is not accounted for in the present formulation. This contributes to a worse agreement between numerical and experimental local quantities for small ductility levels. Another limitation is that different lengths should be assigned to the bottom DB/ae element in order to optimally simulate tensile or compressive strain demand profiles. Because tension shift effects do not play a relevant role for compressive strains, a shorter length than the extent of plasticity would be required. However, this modelling issue is not specific to the present formulation as discussed by Goodnight *et al.* [134] in the context of plastic hinge analysis. Finally, it is noted that the entire set of test units used for validation showed a hardening behaviour of the structural member. Further research is required to investigate the softening response of the proposed DB/ae model.

4.4 Conclusions

Recent experimental tests on cantilever RC piers have confirmed that tension shift effects play an important role in the distribution of local level quantities such as strains and curvature profiles. Namely, linear curvatures are generated in the plastic hinge region due to inclined shear cracks, which intersect the elastic curvature profile at a certain height above the member foundation. These effects cannot be captured by current force-based formulations that satisfy equilibrium exactly, which consider only the effect of the moment gradient. Displacement-based formulations provide the natural framework to account additionally for tension shift effects as the linear plastic curvature distribution observed within the plastic region can be reproduced by imposing appropriate transversal displacement fields to the beam element.

However, the linear axial displacement profile used in classical displacement-based elements is a fundamental limitation to the accuracy of this approach when inelastic material behaviour is considered. The resulting axial forces are equilibrated only in an average sense, resulting in poor simulations of the experimental force-displacement response, as well as curvature and strain profiles.

In view of the above, this Chapter presents a displacement-based element that strictly satisfies axial equilibrium. An intra-element iterative scheme that automatically adjusts the axial strain profile is implemented to attain constant axial forces in all integration points, and equal to the applied axial load. The curvature profiles are instead kept linear as in classical displacement-based elements, although they result quantitatively different on account of the axial equilibrating procedure. The principle of virtual work is employed to obtain the element basic forces and a consistent stiffness matrix.

The axially equilibrated displacement-based element is validated against two sets of cyclic tests on RC cantilever piers and walls. Assuming an appropriate member discretization, it provides accurate results in terms of global and local scale response. Namely, the simulation of experimental curvatures and strains show a significant improvement when compared with models using classical force-based or displacement-based elements. As an example, when base curvatures over different ductility levels are considered, the model using the proposed formulation provides the best estimation in about 80% of the cases. Nevertheless, due to the different length of the plastic region over which tensile and compressive strains develop, different levels of accuracy are obtained for these quantities. The improved predictions come at the cost of slightly increased computational time with respect to the classical displacement-based formulation.

4.5 Acknowledgements

The research presented in this Chapter is part of a project funded by the Swiss Federal Roads Office (FEDRO) under project number AGB 2015/002. Additionally, the insightful suggestions and inspiring comments of Dr. Michele Godio and Dr. Nuno Pereira are acknowledged.

5 Uniaxial Cyclic Tests on RC Wall Boundary Elements with Lap Splices

This Chapter presents an experimental programme consisting of 24 RC members tested under uniaxial cyclic loading. The units are used as proxy of RC wall boundary elements, of which 22 featured lap splices above the foundation level and two were reference units with continuous reinforcement. The Chapter represents the post-print version of the data paper:

D. Tarquini, J.P. Almeida, K. Beyer, 2018. “Uniaxial cyclic tests on reinforced concrete members with lap splices”, *Earthquake Spectra*, published online, DOI: [10.1193/041418EQS091DP](https://doi.org/10.1193/041418EQS091DP).

Figures and tables formatting, reference-, section-, and equation- numbering were adapted to the style of this document. The experimental programme was designed and carried out by the first author at the structural laboratory of EPFL under the supervision of the other two. The first author was also responsible for collecting, processing and analysing the experimental data.

Abstract

This Chapter presents the quasi-static uniaxial cyclic tests of 24 RC members, of which 22 feature lap splices and two are reference units with continuous reinforcement. The objective of the experimental programme is to investigate the influence of lap splice length, confining reinforcement and loading history on the behaviour of lap splices. Particular attention is placed on the measurement of local deformation quantities such as lap splice strains and rebar-concrete slip. Details on the geometry and reinforcement layout of the specimens as well as on the employed test setup, instrumentation and loading protocols are provided. The global behaviour of the test units including the observed crack pattern and failure modes are discussed. The organization of the experimental data, which are made available for public use under DOI: 10.5281/zenodo.1205887, is outlined in detail.

Keywords: Experimental tests; Reinforced concrete; Lap splices; Uniaxial cyclic loading.

5.1 Introduction

The strength and ductility capacity of reinforced concrete (RC) members may be considerably reduced by the presence of lap splices, particularly if located in regions where the inelastic deformations are largest, such as plastic hinges. Several experimental programmes can be found in the literature on spliced RC members, the majority of which aimed at investigating the lap splice strength under monotonic (e.g. [1,64]) and cyclic (e.g. [8,9]) loading. A complete review of past experimental tests is available in Chapter 2. Research on the displacement capacity of lap splices is instead scarcer and it was only recently addressed by Biskinis and Fardis [32], Hannewald [24], and Tarquini et al. [142] (corresponding to Chapter 3 of the present document), who proposed limit strains defining the lap splice failure. However, the latter were based on semi-empirical approaches or limited experimental databases of members subjected to flexural loads wherein only global displacements were typically measured. Therefore, broader and more detailed test data are required in order to better characterize the full hysteretic response of lap splices as a function of the main influencing parameters.

This Chapter presents quasi-static tension-compression cyclic tests on 24 half-scale RC wall boundary elements carried out at the *Earthquake Engineering and Structural Dynamics (EESD) Laboratory* of the *École Polytechnique Fédérale de Lausanne (EPFL)*. The test units, of which 22 with lap splices and two reference units with continuous reinforcement, were designed based on the RC walls tested by Bimschas [29] and Hannewald [57]. Details on the prototype structure, which represent a typical Swiss bridge pier, as well as on the scaling procedure can be found in Bimschas [29]. The tests of the boundary elements have as objectives to study the influence of lap splice length, confining reinforcement and loading history on the behaviour of lap splices. These parameters were singled out in Chapters 2 and 3 as those that influence the ductility of spliced RC walls most.

The document is organized as follows: the geometry of the test units, the reinforcement layout and the mechanical features of the employed materials are first introduced. The test setup, loading protocol and the utilized instrumentation are then

described. Next, the behaviour of the specimens in terms of crack patterns and failure modes is addressed. A section is dedicated to the organization of the raw and post-processed test data, which are shared online and free for download. Finally, few example plots that can be obtained from the processed experimental data are provided.

5.2 Description of the test units

5.2.1 Geometry and reinforcement layout

The entire set of test units (TUs) are listed in Table 5.1, together with the main geometrical and reinforcement layout characteristics. As an example, a 3D representation as well as the vertical and cross-sectional views of specimen LAP-P1 are displayed in Figure 5.1.

All TUs share the same geometry with a column height $h = 1260$ mm and a square cross-section of side dimension $b = 200$ mm. A $550 \times 550 \times 310$ mm foundation and top beam were casted at the member extremities, in order to allow for the anchorage of the longitudinal rebars and to clamp the specimens to the testing machine.

Table 5.1: Main geometrical features and reinforcement details of the specimens

Label	h [mm]	b [mm]	l_s [mm]	$A_l (\rho_l)$ [mm]	$A_t (\rho_t)$ [mm]	LH [-]
LAP-P1	1260	200	560 (40 \varnothing_l)	4 \times $\varnothing 14$ (~1.5%)	$\varnothing 6@100$ (~0.3%)	C1
LAP-P2	1260	200	560 (40 \varnothing_l)	4 \times $\varnothing 14$ (~1.5%)	$\varnothing 6@300$ (~0.1%)	C1
LAP-P3	1260	200	560 (40 \varnothing_l)	4 \times $\varnothing 14$ (~1.5%)	$\varnothing 6@200$ (~0.15%)	C1
LAP-P4	1260	200	350 (25 \varnothing_l)	4 \times $\varnothing 14$ (~1.5%)	$\varnothing 6@100$ (~0.3%)	C1
LAP-P5	1260	200	840 (60 \varnothing_l)	4 \times $\varnothing 14$ (~1.5%)	$\varnothing 6@300$ (~0.1%)	C1
LAP-P6	1260	200	560 (40 \varnothing_l)	4 \times $\varnothing 14$ (~1.5%)	$\varnothing 6@200$ (~0.15%)	M
LAP-P7	1260	200	560 (40 \varnothing_l)	4 \times $\varnothing 14$ (~1.5%)	$\varnothing 6@200$ (~0.15%)	C1
LAP-P8	1260	200	560 (40 \varnothing_l)	4 \times $\varnothing 14$ (~1.5%)	$\varnothing 6@200$ (~0.15%)	M
LAP-P9	1260	200	560 (40 \varnothing_l)	4 \times $\varnothing 14$ (~1.5%)	$\varnothing 6@200$ (~0.15%)	C2
LAP-P10	1260	200	840 (60 \varnothing_l)	4 \times $\varnothing 14$ (~1.5%)	$\varnothing 6@100$ (~0.3%)	C1
LAP-P11	1260	200	350 (25 \varnothing_l)	4 \times $\varnothing 14$ (~1.5%)	$\varnothing 6@200$ (~0.15%)	C1
LAP-P12	1260	200	350 (25 \varnothing_l)	4 \times $\varnothing 14$ (~1.5%)	$\varnothing 6@300$ (~0.1%)	C1
LAP-P13	1260	200	840 (60 \varnothing_l)	4 \times $\varnothing 14$ (~1.5%)	$\varnothing 6@200$ (~0.15%)	C1
LAP-P14	1260	200	840 (60 \varnothing_l)	4 \times $\varnothing 14$ (~1.5%)	[-] (~0%)	C1
LAP-P15	1260	200	560 (40 \varnothing_l)	4 \times $\varnothing 14$ (~1.5%)	[-] (~0%)	C1
LAP-P16	1260	200	560 (40 \varnothing_l)	4 \times $\varnothing 14$ (~1.5%)	$\varnothing 6@150$ (~0.2%)	C1
LAP-P17	1260	200	560 (40 \varnothing_l)	4 \times $\varnothing 14$ (~1.5%)	$\varnothing 6@120$ (~0.25%)	C1
LAP-P18	1260	200	700 (50 \varnothing_l)	4 \times $\varnothing 14$ (~1.5%)	$\varnothing 6@200$ (~0.15%)	C1
LAP-P19	1260	200	560 (40 \varnothing_l)	4 \times $\varnothing 14$ (~1.5%)	$\varnothing 6@120$ (~0.25%)	M
LAP-P20	1260	200	560 (40 \varnothing_l)	4 \times $\varnothing 14$ (~1.5%)	$\varnothing 6@120$ (~0.25%)	C1
LAP-P21	1260	200	560 (40 \varnothing_l)	4 \times $\varnothing 14$ (~1.5%)	$\varnothing 6@120$ (~0.25%)	C3
LAP-P22	1260	200	560 (40 \varnothing_l)	4 \times $\varnothing 14$ (~1.5%)	$\varnothing 6@120$ (~0.25%)	C4
LAP-C1	1260	200	[-]	4 \times $\varnothing 14$ (~1.5%)	$\varnothing 6@200$ (~0.15%)	C1
LAP-C2	1260	200	[-]	4 \times $\varnothing 14$ (~1.5%)	$\varnothing 6@100$ (~0.3%)	C1

h : specimen height; b : cross-section width; l_s : lap splice length; \varnothing_l : longitudinal bar diameter; A_l : longitudinal reinforcement content; ρ_l : longitudinal reinforcement ratio; A_t : confining reinforcement content; ρ_t : confining reinforcement ratio; LH : loading history type.

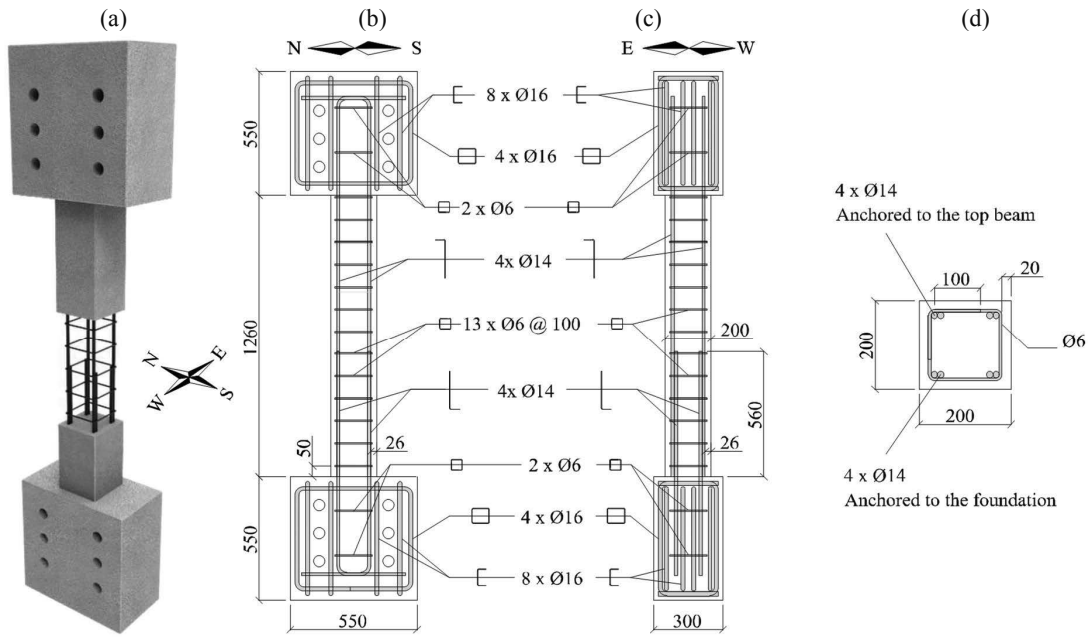


Figure 5.1: Main geometrical and reinforcement features of specimen LAP-P1: (a) 3D representation; (b) and (c) Vertical sections along E-W and N-S directions; (d) Cross-section.

The longitudinal reinforcement was composed of four diameter (\varnothing) 14 mm rebars which, in 22 out of the 24 test units (identified with the label LAP-P(i) in Table 5.1), were spliced above the column-foundation interface. The top anchored rebar was always placed on the outside with respect to the one anchored to the foundation—see Figure 5.1 (d). The lap splice length (l_s) was a variable parameter of the experimental programme and ranged from 25 to 60 times the longitudinal rebar diameter \varnothing_l . Two TUs featured continuous reinforcement and were labelled LAP-C(i). Transverse (confining) reinforcement was provided by $\varnothing 6$ mm hoops with 90-degree hooks, as representative of 60s and 70s central European construction practice (Figure 5.1 (d)). The confining reinforcement ratio (ρ_t) was the second variable parameter of the test programme and was bounded between 0 and 0.3%. Both ranges of l_s and ρ_t were defined in order to investigate pre-seismic [53,56] as well as code compliant [18,19] detailing configurations. A clear concrete cover $c = 20$ mm, measured from the outer edge of the stirrups, was adopted.

For instrumentation purposes, specifically-designed plastic pieces, removed after casting, were used to create 20×30 mm holes in the concrete cover and allow the spliced bars to be visible at pre-defined locations. More details on the dimensions and locations of these constructive details can be found in subsection 5.3.3.2, titled ‘Optical Triangulation Measurements’.

5.2.2 Material properties

The TUs were cast horizontally, four at a time. Concrete strength was assessed for each casting series by testing three 160×320 mm concrete cylinders according to SIA [143]. The average concrete cylinder strength (f'_c) and the units of the corresponding batch are displayed in Table 5.2.

All the rebars composing the longitudinal reinforcement ($\varnothing_l = 14$ mm) were obtained from the same production batch as well as those used for the transverse reinforcement ($\varnothing_t = 6$ mm). The main steel properties were derived from uniaxial tension tests [143] and are reported in Table 5.3; it is noted that, differently from the hot-rolled steel used for the longitudinal reinforcement, the cold-formed transverse steel did not present any yield plateau. The test results as well as the full steel stress-strain curves are part of the shared data, as discussed in section 5.5, titled ‘Organization of test data’.

Table 5.2: Mean concrete cylinder strength

TU LAP-	P1, P2, P3, C1	P4, P5, P7, P9	P6, P8, P10, C2	P11, P12, P13, P14	P15, P16, P17, P18	P19, P20, P21, P22
f_c [MPa]	31.7	30.4	31.6	33.1	34.4	33.5

f_c : concrete cylinder compressive strength, determined from three tests per casting series.

Table 5.3: Mechanical characterization of the reinforcing bars (average of six tests per diameter)

Reinforcement	f_y [MPa]	f_u [MPa]	ϵ_y [%]	ϵ_h [%]	ϵ_u [%]
Longitudinal (Ø14 mm)	510	635	0.25	0.95	9.3
Transverse (Ø6 mm)	475	625	0.25	0.25	9.8

f_y : steel yield strength; f_u : steel ultimate tensile strength; ϵ_y : steel yield strain; ϵ_h : steel strain at hardening onset; ϵ_u : steel strain at ultimate strength.

5.3 Test Setup, loading protocol and instrumentation

5.3.1 Test setup

The test setup used for all the specimens is depicted in Figure 5.2. The TUs are clamped, both at the foundation and the top beam level, to two T-shaped steel profiles. The latter are in turn pre-stressed to the testing machine which is composed of a mobile bottom hydraulic piston and a fixed top. The actuator has a capacity of 2.5 MN in tension and 10 MN in compression, and a stroke of 250 mm.

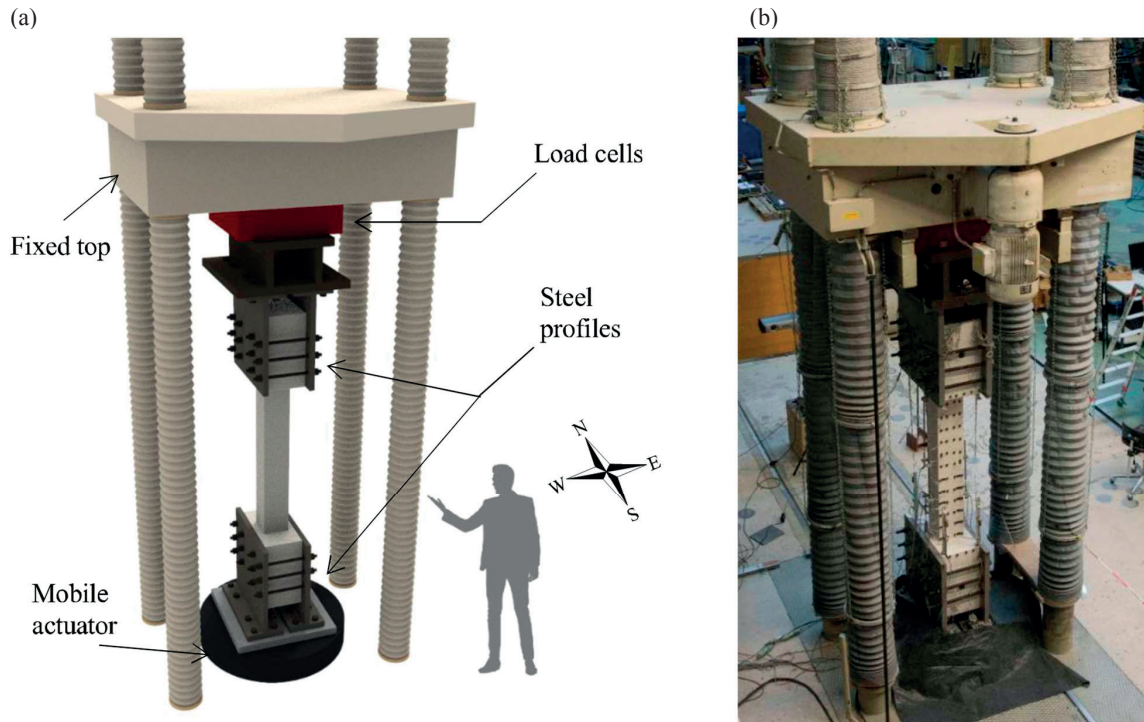


Figure 5.2: Test setup: (a) CAD rendering; (b) Bird's-eye view.

5.3.2 Loading protocol

The tests were performed under quasi-static loading conditions and displacement control. Five different protocols, including four cyclic and one monotonic, were defined in order to investigate the impact of the loading history on the behaviour of lap splices. The four cyclic loading protocols differed with regard to the ratio of tension and compression displacements that were applied within one cycle. This ratio was chosen as a test parameter because damage inferred by compression strains can affect the force-displacement response of lap splices under tension. In the following, the various loading protocols are described. The protocol that was applied to each TU is reported in the loading history (*LH*) column of Table 5.1.

- *Reference cyclic LH (C1)*: It consists in the application of increasing vertical displacements (Δ_v) with a 10:1 ratio between tension and compression. This ratio was determined based on the strain proportion observed along the lap splice region of the walls tested by Bimschas [29] and Hannewald [57] at the onset of splice failure. Each peak displacement is referred to as load step (*LS*); a cycle is composed of two *LS* (tension and compression) and two cycles are performed at each displacement amplitude, as shown in Figure 5.3 (a). Average vertical strains (ϵ_v), obtained as the ratio of the applied vertical displacements (Δ_v) and the specimen height (h) are indicated on the right y-axis. After the first three displacement levels at $\Delta_v = 1, 2$ and 3 mm ($\epsilon_v \approx 0.08, 0.16$ and 0.24%), which correspond to the pre-yield phase, 3 mm increments were considered for the following amplitudes ($\Delta_v = 6, 9, 12 \dots$ or $\epsilon_v \approx 0.48, 0.71, 0.95\%$) until specimen failure. The latter is defined to occur when the structural member has lost more than 20% of its maximum recorded axial force, either in tension or compression. The test is then concluded with a final pulling cycle until a large level of displacement deemed close to compromising the member integrity.
- *Double compression LH (C2)*: Similar to the reference protocol (*C1*) except that the imposed compression levels were twice as large, i.e., tension to compression ratio of 10:2, see Figure 5.3 (b).
- *Repeated cyclic LH (C3)*: No negative displacements are applied. On each *LS* following a tensile displacement, the TUs are unloaded to zero displacement—Figure 5.3 (c).
- *Fixed high compression force LH (C4)*: A value of approximately 90% of the axial load ratio ($ALR = N/f'_c \cdot A_g$) is applied at each compression *LS*, see Figure 5.3 (d).
- *Tensile monotonic LH (M)*: The column is subjected to a monotonically increasing tensile displacement until failure of the four lap splices.

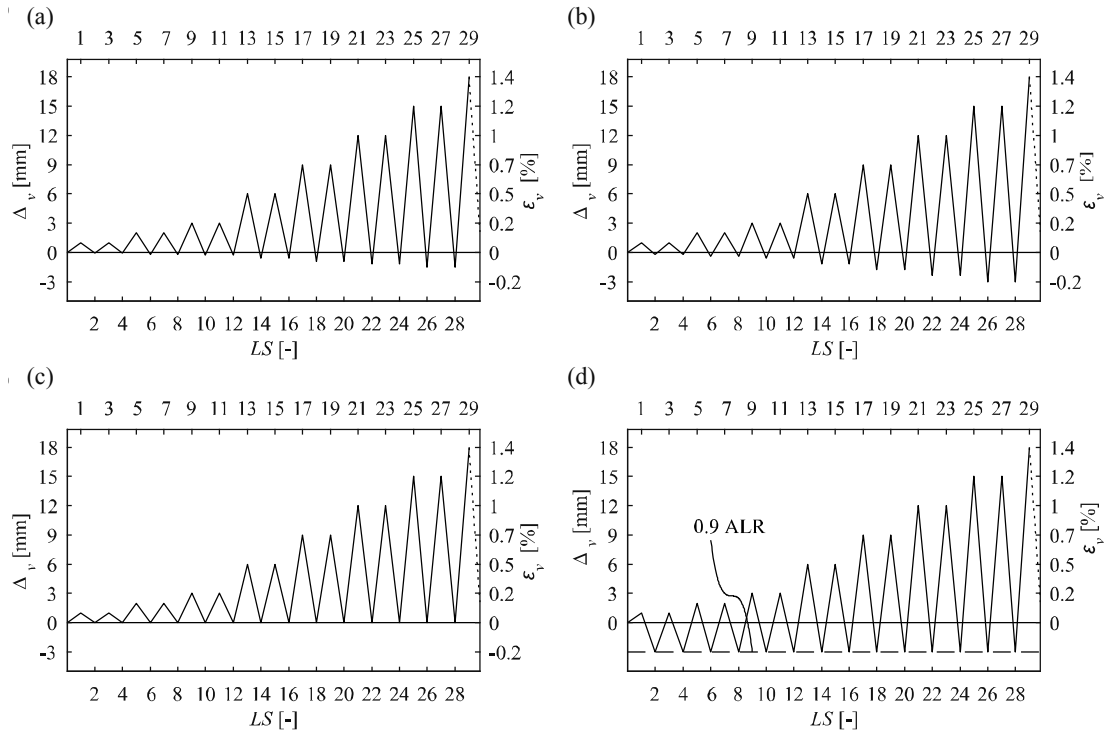


Figure 5.3: Cyclic loading protocols used in the experimental program: (a) Reference cyclic-C1; (b) Double compression-C2; (c) Repeated cyclic-C3; (d) Fixed high compression force-C4.

It has to be pointed out that the actual applied protocols slightly differed from the intended ones described above as the actuator was stopped manually at each load step. The real displacement history imposed during each test is reported in the individual TU reports that are discussed in section 5.5.

5.3.3 Instrumentation

The test units were instrumented using conventional measurements and optical triangulation systems. Crack widths were measured manually. Moreover, at each *LS*, photos were taken and videos recorded.

5.3.3.1 Conventional Measurements

The same conventional instrumentation was used in all the tests of the experimental programme. A total of 33 channels were recorded with the available data acquisition software [144], of which 18 were directly measured and 15 computed. Displacements were evaluated by means of linear variable differential transformers (LVDTs), while load cells were employed to monitor forces.

Four LVDTs (100 mm stroke) were installed with a plumb line system at the column corners, from the top beam to the foundation interface, see Figure 5.4 (a) and (b). They were used to pilot the testing machine as they indicated the applied net column deformation. Three LVDTs in series (with different strokes) were also placed on both the east and west specimen faces, as shown in Figure 5.4 (a) and (b). Their base-lengths varied from test to test with the main objective of having a back-up measure of the strains in the lap splice region, besides the one obtainable from the optical triangulation system discussed below. A supplementary LVDT was connected to the bottom mobile actuator of the testing machine to monitor that the deformations due to the test setup remained relatively small. Four load cells to measure the axial force, with a total capacity of ± 2000 kN, were located below the fixed top of the testing machine, as depicted in Figure 5.2 (a). Additionally, an internal load cell back-calculated the imposed force from the hydraulic pressure of the machine actuator. Detailed information on the conventional measurements can be found in the individual TU reports, as discussed in section 5.5.

5.3.3.2 Optical Triangulation Measurements

The north and south column faces were instrumented with a dense mesh of light-emitting diodes (LEDs). The three-dimensional displacement of each LED was tracked by two cameras, one per TU side, and each featuring three digital optical sensors. The hardware and software provided by the commercial system NDI Optotrak Certus HD [145] was used.

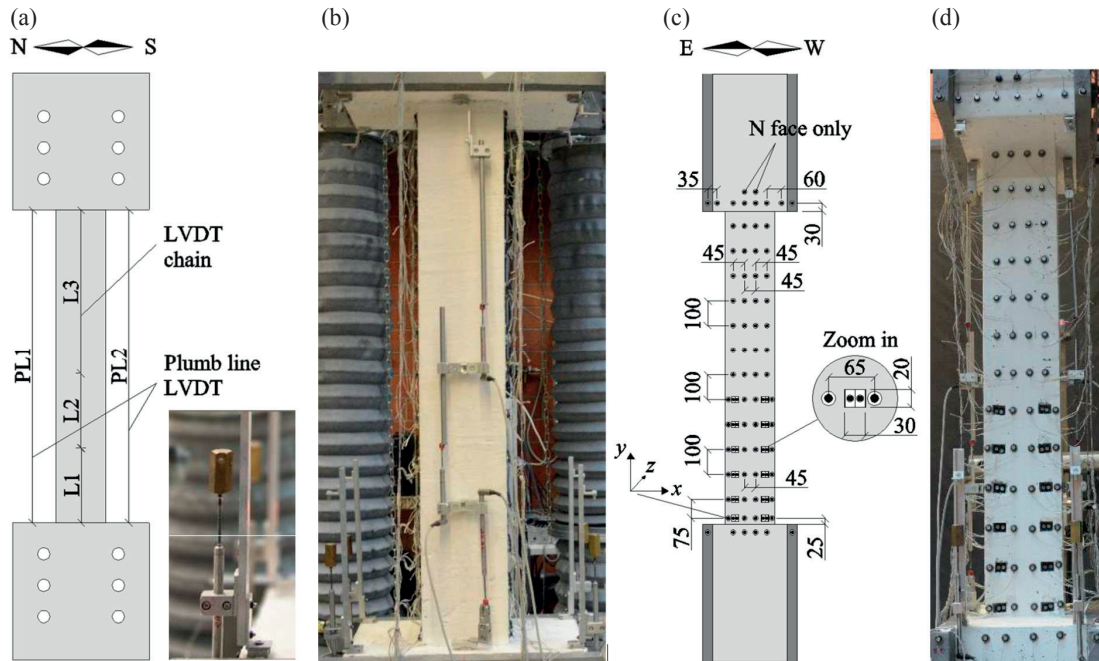


Figure 5.4: Instrumentation installed on the TU: (a) Sketch of the LVDTs pattern and close-up of the plumb-line LVDT system; (b) Photo of the prior-to-test east face of LAP-P1; (c) LEDs distribution for specimens with a lap splice length $l_s=40\phi$; (d) Photo of the prior-to-test north face of LAP-P1.

The LED mesh on the column concrete surfaces was designed as a function of the lap splice length; it was therefore unit-specific but it normally followed gridlines spaced 100 mm in the vertical and 50 mm in the horizontal direction, as shown in Figure 5.4 (c) and (d). Furthermore, LED pairs were also glued at a regular vertical spacing of 100 mm to the spliced adjacent rebars, as depicted in the close-up of Figure 5.4 (c), in the concrete holes left during the casting phase. Such disposition permitted to track the relative slip between the spliced bars as well as between each bar and the surrounding concrete. Finally, on both north and south sides, two LED rows were attached to the foundation and top beam, as well as single markers glued on the steel profiles.

The LED data were recorded during loading and, for a short time period, at each *LS*. The latter aimed at registering stable (constant) values of the imposed vertical displacements. In the data post-processing phase, the initial random numbering of the LEDs was ordered and their coordinates were transformed to the following spatial reference system: the *x* and *z* axes refer to the horizontal directions (positive from east to west and from north to south respectively) while the *y*-axis to the vertical direction (positive from bottom to top). The origin of the coordinate system is defined as the LED located at the column north-east bottom corner, see Figure 5.4 (c). The specific LED grid for each TU and their numbering upon post-processing can be found in the individual test reports, see section 5.5.

5.3.3.3 Crack Widths, Photos and Videos

Crack widths were measured by means of crack width meters at different locations along the specimen height and for most tensile load steps. They were successively recorded in the specific TU lab books, which are part of the publically available material (refer to section 5.5 for more details). Photos were taken at several *LS*, and always when a new tensile displacement level was attained. In such occasions, one photo per column side was taken, as well as of relevant signs of damage (horizontal and splitting cracks, concrete crushing, spalling, rebar buckling and rupture, etc). Finally, videos were recorded during all loading phases (i.e. between successive *LS*) on the north and south column faces. Only for monotonic tests, videos were taken on all four-unit sides.

5.4 Test observations

The present section summarises the behaviour of all the TUs. The pre-failure phase and the observed failure modes are addressed in the next two subsections. Specimen-specific observations are reported in Table 5.4. The force-displacement responses are shown in Figure 5.5 and Figure 5.6, where the vertical axial force *N* is given on the *y*-axis and the vertical displacement (Δ_v) and average strain (ε_v) are reported on the bottom and top *x*-axes respectively. The vertical force *N* is computed by summing up the forces of the four load cells located below the fixed top while Δ_v is the average displacement measured by the four plumb line LVDTs. The occurrence of splice failure, maximum tension level prior to the onset of reinforcement buckling, rebar rupture and/or concrete crushing are signalled by the presence of markers while a dashed line indicates the overall specimen failure.

5.4.1 Pre-failure behaviour

All the specimens with lap splices behaved rather similarly until the occurrence of one of the three following events: failure of one or more lap splices, rebar rupture or core concrete crushing. The strain at which failure occurred depended, however, strongly on the test unit configuration; this is shown in the next subsection. The behaviour of members with continuous reinforcement was governed by a uniform crack pattern and a failure in compression:

- *TUs with lap splices (LAP-P1 to LAP-P22)*: upon application of the first tensile loading ($\Delta_v = 1$ mm, $\varepsilon_v \approx 0.08\%$), six to ten cracks usually formed along the column height, while two opened at the foundation and top beam interfaces. Not all cracks normally run along the entire column perimeter, particularly within the spliced region. They were spaced apart about 150 to 200 mm, with an approximately constant crack width $w \approx 0.1$ mm. Horizontal crack development (i.e. opening of the last cracks or extension and widening of existing ones) continued for the next two tensile amplitudes ($\Delta_v = 2$ mm and $\Delta_v = 3$ mm). At this stage, the width (*w*) of the cracks located above and within the lap splice region started to differentiate; $w \approx 0.2$ - 0.3 mm for the former and $w \approx 0.1$ mm for the latter. At $\Delta_v = 3$ mm ($\varepsilon_v \approx 0.24\%$) the first vertical splitting cracks also appeared, though small and localized at the splice ends. During compression cycles, crack closure was observed. At the first *LS* to $\Delta_v = 6$ mm ($\varepsilon_v \approx 0.48\%$), the TUs began to show specimen-specific behaviour. Rebar yielding occurred at $\Delta_v \approx 4$ mm ($\varepsilon_v \approx 0.32\%$), after which several lap splice configurations failed (see Table 5.4). Only specimens LAP-P11 and LAP-P12, featuring the shortest lap splice length and medium to low confinement reinforcement ratios ($l_s = 25 \varnothing_l$, $\rho_l = 0.15\%$ and 0.1% , respectively), did not reach the yield strength.

For tensile displacements larger than $\Delta_v = 6$ mm, the horizontal cracks located outside the spliced region progressively widened; on the other hand, their width remained approximately constant ($w \approx 0.1$ mm) within the lap splice zone—see Figure 5.7 (a). The largest crack typically occurred at the top of the splices, followed by the one at the foundation interface. Vertical splitting cracks extended from the bottom and top lap splice extremities towards the middle. Regarding the behaviour of the TUs in compression, crack closure with no damage was observed until an average vertical strain $\epsilon_v \approx -0.15\%$, corresponding to a total displacement $\Delta_v \approx -1.8$ mm. At such compression level, concrete spalling at major crack locations and development of vertical crushing cracks (usually extending pre-existing tension splitting cracks) started to take place. Whenever larger compression amplitudes were reached, extensive spalling formed above the spliced region followed by rebar buckling and eventually crushing of the concrete core.

- *TUs with continuous reinforcement (LAP-C1 and LAP-C2)*: Differently from the units with lap splices, the crack width was approximately constant along the member height, at all displacement levels. Vertical cracks formed only due to compression loading and were typically located between two horizontal cracks. Failure occurred due to concrete core crushing after buckling of longitudinal reinforcement.

5.4.2 Observed failure modes

The occurrence of lap splice failure depended on several factors, among which lap splice length, amount of confining reinforcement, loading history, location of the stirrup hooks and top casting face. A thorough discussion on the influence of these parameters and a new predictive model for the strain capacity of lap splices is addressed in Chapter 6. Two distinct lap-splice failure modes were observed: splitting-unzipping and splitting-explosive. Both of them consisted in the opening of vertical splitting cracks along the entire splice length—see Figure 5.7 (b), which allowed the slippage of the rebars and resulted in a loss of tensile load carrying capacity. However, in a splitting-unzipping failure, vertical cracks formed gradually along the splice length; they originated at the lap splice extremities, where rebar strains are maximum, and extended towards the middle. This relatively slow, pseudo-ductile crack forming process was enabled by the presence of transverse reinforcement, which prevented a sudden crack propagation. Before failure, vertical cracks typically spread along the entire lap splice length. At failure, they opened up with a non-loud, low-pitched unzipping sound and the relative rebar slip took place. Concrete friction then became the only available force transfer mechanism; a residual force of around 20% of the rebar yield strength was typically observed. As for the splitting-explosive mode, no extensive vertical cracking was visible before failure, which was loud (comparable to a rebar rupture) and fragile. No residual force was available after failure.

Rebar rupture always occurred after specimen failure, i.e., after the axial force had dropped below 80% of its maximum attained value (see subsection 5.3.2). When a specific lap splice did not fail, rupture of the top anchored rebar took place above the spliced region where the largest crack formed, see Figure 5.7 (e). If large compression levels were reached, rebar rupture was preceded by buckling and core concrete crushing, as shown in Figure 5.7 (c) and (d). The latter was normally associated with a strength loss of around 80%.

Table 5.4: Description of the specific behaviour of the test units and observed failure modes

Specific Comments	FM
LAP-P1: At the first cycle to $\Delta_v = 24$ mm ($\varepsilon_v \approx 1.9\%$), a clear relative slip between the spliced bars on the east side (NE and SE corners) of the column was observed. During the second cycle to the same amplitude, at $\Delta_v \approx 16$ mm ($\varepsilon_v \approx 1.3\%$), splitting-unzipping failure of these splices occurred with a loss of almost 35% of the column load carrying capacity. The third lap splice (NW corner) failed during the last cycle at $\Delta_v \approx 18$ mm ($\varepsilon_v \approx 1.4\%$), according to the same failure mode. Finally, rebar rupture occurred for the top-anchored bar of the SW corner lap splice at $\Delta_v \approx 32$ mm ($\varepsilon_v \approx 2.5\%$). The rupture took place above the lap splice, where the largest crack was located.	M
LAP-P2: While loading to $\Delta_v = 6$ mm, upon rebar yielding ($\Delta_v \approx 4.5$ mm, $\varepsilon_v \approx 0.36\%$), splitting-unzipping failure of the two splices on the west side occurred. A drop in force of around 30% was observed. The remaining two splices failed simultaneously during the last cycle, at an applied displacement of $\Delta_v \approx 10$ mm ($\varepsilon_v \approx 0.8\%$), according to a splitting-explosive failure mode.	M
LAP-P3: The lap splice on the NE corner failed (splitting-unzipping) during the first loading to $\Delta_v = 9$ mm, at an applied displacement $\Delta_v \approx 7.5$ mm ($\varepsilon_v \approx 0.6\%$). A strength loss of 10% was recorded. The same failure mode was observed for the remaining lap splices: NW and SE corners failed simultaneously at $\Delta_v \approx 9$ mm ($\varepsilon_v \approx 0.7\%$), on the first cycle $\Delta_v = 12$ mm. At this stage the column resisting force was reduced by 50%. The last lap splice (SW) failed at $\Delta_v \approx 19$ mm ($\varepsilon_v \approx 1.5\%$).	S-U
LAP-P4: Simultaneous splitting-unzipping failure of the four lap splices occurred during the first loading to $\Delta_v = 6$ mm, at an applied displacement $\Delta_v \approx 4$ mm ($\varepsilon_v \approx 0.3\%$), corresponding to the onset of rebar yielding. The residual axial force was $N \approx 50$ kN, approximately 15 % of the column yielding force N_y .	S-U
LAP-P5: On the first cycle to $\Delta_v = 18$ mm, splitting-unzipping failure of the NE corner splice occurred at a displacement $\Delta_v \approx 17$ mm ($\varepsilon_v \approx 1.35\%$). A drop of 15% of axial force was observed. Upon load reversal, buckling of the bars above the NE and SE lap splice region took place. At the second cycle to $\Delta_v = 18$ mm, the resisting axial force N was around 75% of the peak strength. On the last tensile cycle, the SE splice failed at $\Delta_v \approx 20$ mm ($\varepsilon_v \approx 1.6\%$), again according to a splitting-unzipping failure type. Both the splices on the west column side showed instead a splitting-explosive failure, occurring at $\Delta_v \approx 35$ mm ($\varepsilon_v \approx 2.8\%$).	M
LAP-P6: The two lap splices on the west column side failed at an applied displacement level $\Delta_v \approx 4.5$ mm ($\varepsilon_v \approx 0.36\%$), immediately after rebar yielding. The lap splices located on the SE and NE column corners failed at $\Delta_v \approx 9$ mm ($\varepsilon_v \approx 0.7\%$) and $\Delta_v \approx 15$ mm ($\varepsilon_v \approx 1.2\%$), respectively.	S-U
LAP-P7: Both splices on the west column side failed after rebar yielding ($\Delta_v \approx 4.5$ mm, $\varepsilon_v \approx 0.36\%$), while loading to $\Delta_v = 6$ mm. A force drop of around 20-25% was observed. The two splices on the east side failed simultaneously at $\Delta_v \approx 7.5$ mm ($\varepsilon_v \approx 0.6\%$).	S-U
LAP-P8: Splitting-unzipping failure of the two splices on the west side occurred at a displacement level $\Delta_v \approx 12$ mm ($\varepsilon_v \approx 0.95\%$). The same failure mode was observed for the splices on the SE and NE column corners, which failed at $\Delta_v \approx 15$ mm ($\varepsilon_v \approx 1.2\%$) and $\Delta_v \approx 18$ mm ($\varepsilon_v \approx 1.4\%$), respectively.	S-U
LAP-P9: Behaviour similar to specimen LAP-P7. The two splices on the west column side failed at a displacement level of $\Delta_v \approx 4$ mm ($\varepsilon_v \approx 0.3\%$) while those on the east side at $\Delta_v \approx 10$ mm ($\varepsilon_v \approx 0.8\%$).	S-U
LAP-P10: Deformations concentrated on the horizontal crack located about the splice top. At a displacement level $\Delta_v = -2.4$ mm ($\varepsilon_v \approx -0.19\%$), concrete spalling was observed in the same region, promoting rebar buckling in the following compression cycles. The maximum tension displacement attained prior to first observation of reinforcement buckling was $\Delta_v = 24$ mm ($\varepsilon_v \approx 1.9\%$). Concrete core crushing occurred on the first cycle to $\Delta_v = -2.7$ mm ($\varepsilon_v \approx -0.21\%$), with a reduction of the compression load capacity of almost 75%. On the second loading cycle to $\Delta_v = 27$ mm ($\varepsilon_v \approx 2.15\%$), the NW top-anchored bar fractured where it had previously buckled. Similarly, the NE top-anchored bar ruptured on the final cycle, at an applied displacement $\Delta_v \approx 20$ mm ($\varepsilon_v \approx 1.6\%$).	C-C
LAP-P11: Splitting-unzipping failure of the four lap splices occurred simultaneously before reaching rebar yielding, during the first cycle to $\Delta_v = 6$ mm. A maximum vertical force $N = 260$ kN was attained at an imposed displacement of $\Delta_v \approx 3.5$ mm ($\varepsilon_v \approx 0.28\%$), corresponding to 80% of the column yielding force ($N_y \approx 320$ kN). The final residual force was $N \approx 80$ kN.	S-U
LAP-P12: Similar behaviour as LAP-P11. Failure occurred before rebar yielding, at a displacement $\Delta_v \approx 3.5$ mm ($\varepsilon_v \approx 0.28\%$) and a force $N = 260$ kN. The residual force was $N \approx 80$ kN.	S-U

LAP-P13: Similar behaviour as LAP-P10. Rebar buckling was first observed at a level of compression of $\Delta_v = -1.8$ mm ($\varepsilon_v \approx -0.14\%$); the last tension displacement prior to first observation of reinforcement buckling was $\Delta_v = 15$ mm ($\varepsilon_v \approx 1.2\%$). Concrete crushing occurred at the first cycle to $\Delta_v = -2.1$ mm ($\varepsilon_v \approx -0.17\%$) with a drop of force of roughly 75%. On the last tensile cycle, the NE and SW top anchored bars fractured at the buckling locations (above the lap splice region) at $\Delta_v \approx 32$ mm ($\varepsilon_v \approx 2.5\%$) and $\Delta_v \approx 35$ mm ($\varepsilon_v \approx 2.8\%$), respectively. At this same displacement level, a splitting-explosive failure mode was instead observed for the SE lap splice.	C-C
LAP-P14: Before reaching $\Delta_v = 9$ mm ($\varepsilon_v \approx 0.7\%$), the SE corner splice failed with a loud noise. A loss of force capacity of about 20% was observed. During the cycles at the following amplitude level ($\Delta_v = 12$ mm), vertical cracking extended in the three remaining splices. They failed during the final cycle, at $\Delta_v \approx 10$ mm ($\varepsilon_v \approx 0.8\%$) and $\Delta_v \approx 17$ mm ($\varepsilon_v \approx 1.35\%$) for the SW and both north face splices, respectively. At the end, the specimen showed no tensile residual force capacity.	S-E
LAP-P15: All splices failed according to a splitting-explosive failure mode. The lap splices on the east side of the column failed before reaching $\Delta_v \approx 6$ mm ($\varepsilon_v \approx 0.48\%$), on the first loading to such displacement amplitude. The SW and NW lap splices failed on the final cycle, at $\Delta_v \approx 9$ mm ($\varepsilon_v \approx 0.7\%$) and $\Delta_v \approx 13$ mm ($\varepsilon_v \approx 1\%$). The test concluded with no residual tensile force.	S-E
LAP-P16: Splitting-unzipping failure of the east side splices occurred on the first loading to $\Delta_v = 12$ mm, at $\Delta_v \approx 9$ mm ($\varepsilon_v \approx 0.7\%$). A strength loss of almost 30% was observed. The splices on the west side failed at $\Delta_v \approx 13$ mm ($\varepsilon_v \approx 1\%$), during the last loading cycle.	S-U
LAP-P17: The NE corner splice failed while loading to $\Delta_v = 15$ mm ($\varepsilon_v \approx 1.2\%$), shortly before reaching the target displacement. The SE splice failed during the second cycle at the same amplitude. The splices located on the west column side failed on the last tensile cycle, again approximately at $\Delta_v \approx 15$ mm.	S-U
LAP-P18: Splitting-unzipping failure of both SW and NW splices occurred during the first loading to $\Delta_v = 18$ mm, at $\Delta_v \approx 13$ mm ($\varepsilon_v \approx 1\%$) and $\Delta_v \approx 15$ mm ($\varepsilon_v \approx 1.2\%$), respectively. The remaining two splices failed on the last tensile cycle: at $\Delta_v \approx 30$ mm ($\varepsilon_v \approx 2.4\%$) splitting-unzipping failure of the NE lap splice shortly preceded the splitting-explosive failure of the NW one.	S-U
LAP-P19: The lap splices on the NE, SE and NW column corners exhibited a splitting-unzipping type of failure at $\Delta_v \approx 12$ mm ($\varepsilon_v \approx 0.95\%$), $\Delta_v \approx 17$ mm ($\varepsilon_v \approx 1.35\%$) and $\Delta_v \approx 22$ mm ($\varepsilon_v \approx 1.75\%$). On the other hand, the top-beam anchored rebar of the SW corner splice ruptured at $\Delta_v \approx 50$ mm ($\varepsilon_v \approx 4\%$).	M
LAP-P20: The first lap splice (SW corner) failed at $\Delta_v \approx 12$ mm ($\varepsilon_v \approx 0.95\%$), on the second cycle to this amplitude. The NW splice failed at the first loading to $\Delta_v = 15$ mm ($\Delta_v \approx 13$ mm, $\varepsilon_v \approx 1\%$). The NE and SE corner splices failed at the last tensile cycle at $\Delta_v \approx 20$ mm ($\varepsilon_v \approx 1.6\%$) and $\Delta_v \approx 35$ mm ($\varepsilon_v \approx 2.8\%$).	S-U
LAP-P21: Splitting failure of both east side splices occurred on the second cycle to $\Delta_v = 21$ mm ($\varepsilon_v \approx 1.7\%$), just before the target displacement. The NW splice failed during the last cycle at $\Delta_v \approx 28$ mm ($\varepsilon_v \approx 2.2\%$) while the SW top anchored bar fractured at about $\Delta_v \approx 40$ mm ($\varepsilon_v \approx 3.2\%$).	M
LAP-P22: The SE corner splice failed right before reaching $\Delta_v = 6$ mm ($\varepsilon_v \approx 0.48\%$), on the first cycle to this displacement amplitude. The NE corner splice failed on the first cycle to $\Delta_v = 12$ mm, at a displacement $\Delta_v \approx 9.5$ mm ($\varepsilon_v \approx 0.75\%$). Both the west corner splices failed at around $\Delta_v \approx 12$ mm ($\varepsilon_v \approx 0.95\%$). The loading was continued until $\Delta_v \approx 20$ mm ($\varepsilon_v \approx 1.6\%$); the residual force was around 80 kN.	S-U
LAP-C1: Core concrete crushing occurred while loading to $\Delta_v = -4.2$ mm ($\varepsilon_v \approx -0.33\%$), leading to a force drop of about 85%. Spalling between the main horizontal cracks, located at the centre of the column, had taken place on the previous cycle to $\Delta_v = -3.9$ mm ($\varepsilon_v \approx -0.31\%$), followed by rebar buckling upon load reversal. On the last tensile cycle, rupture of the SW, SE and NW rebars was observed at the respective buckling locations, for $\Delta_v \approx 35$ mm ($\varepsilon_v \approx 2.8\%$), $\Delta_v \approx 70$ mm ($\varepsilon_v \approx 5.6\%$) and $\Delta_v \approx 90$ mm ($\varepsilon_v \approx 7.1\%$).	C-C
LAP-C2: Similar to the behaviour of LAP-C1. Concrete crushing occurred on the first loading to $\Delta_v = -3.9$ mm ($\varepsilon_v \approx -0.31\%$), with a force loss of about 85%. On the last cycle, at approximately $\Delta_v \approx 40$ mm ($\varepsilon_v \approx 3.2\%$), the NW corner rebar ruptured at the buckling location.	C-C
FM: Failure mode; S-U: splitting-unzipping failure of all lap splices; S-E: splitting-explosive failure of all lap splices; C-C: concrete crushing followed by rebar rupture; M: mixed rebar rupture / lap splice failures.	

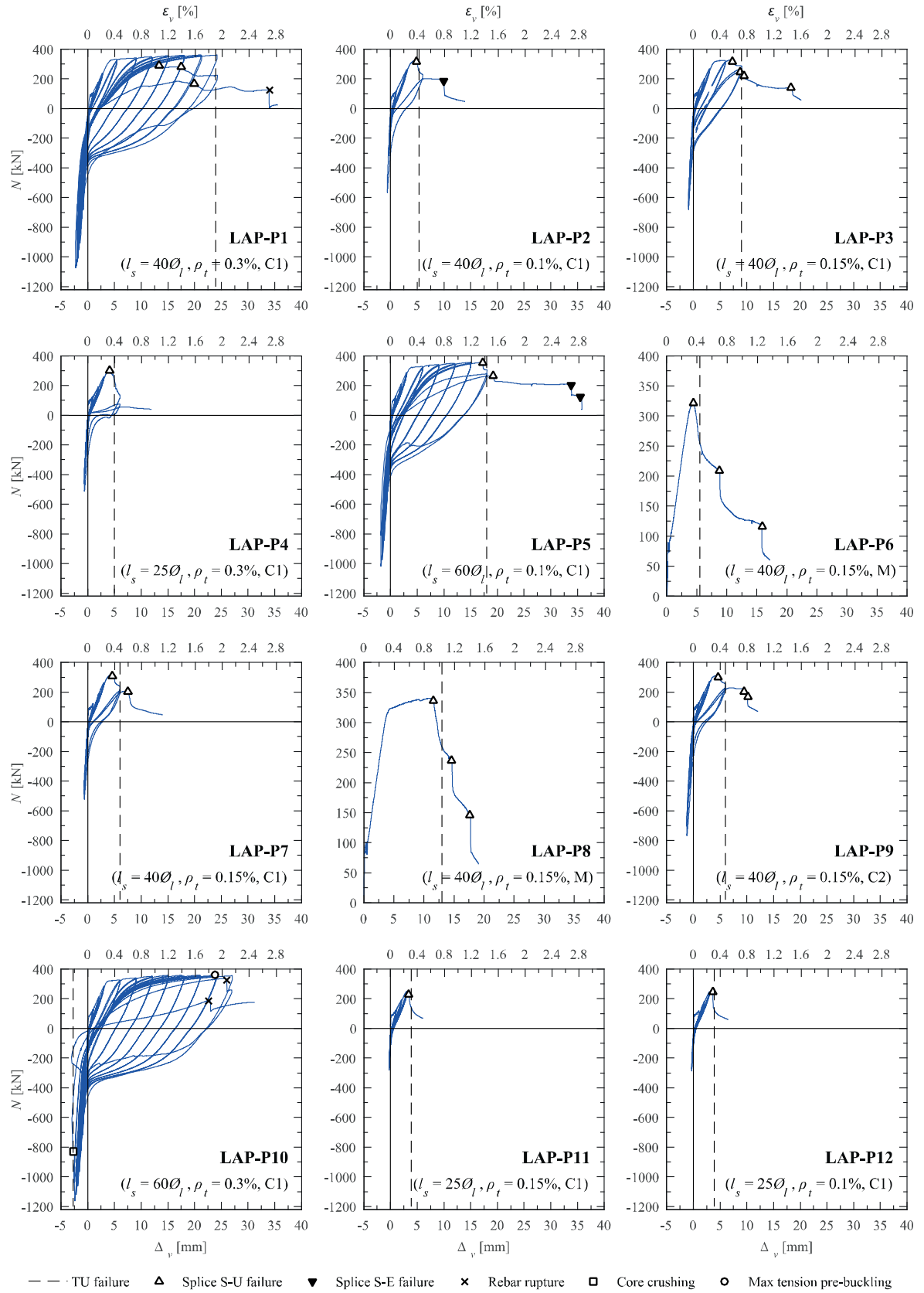


Figure 5.5: Cyclic response of specimens LAP-P1 to LAP-P12.

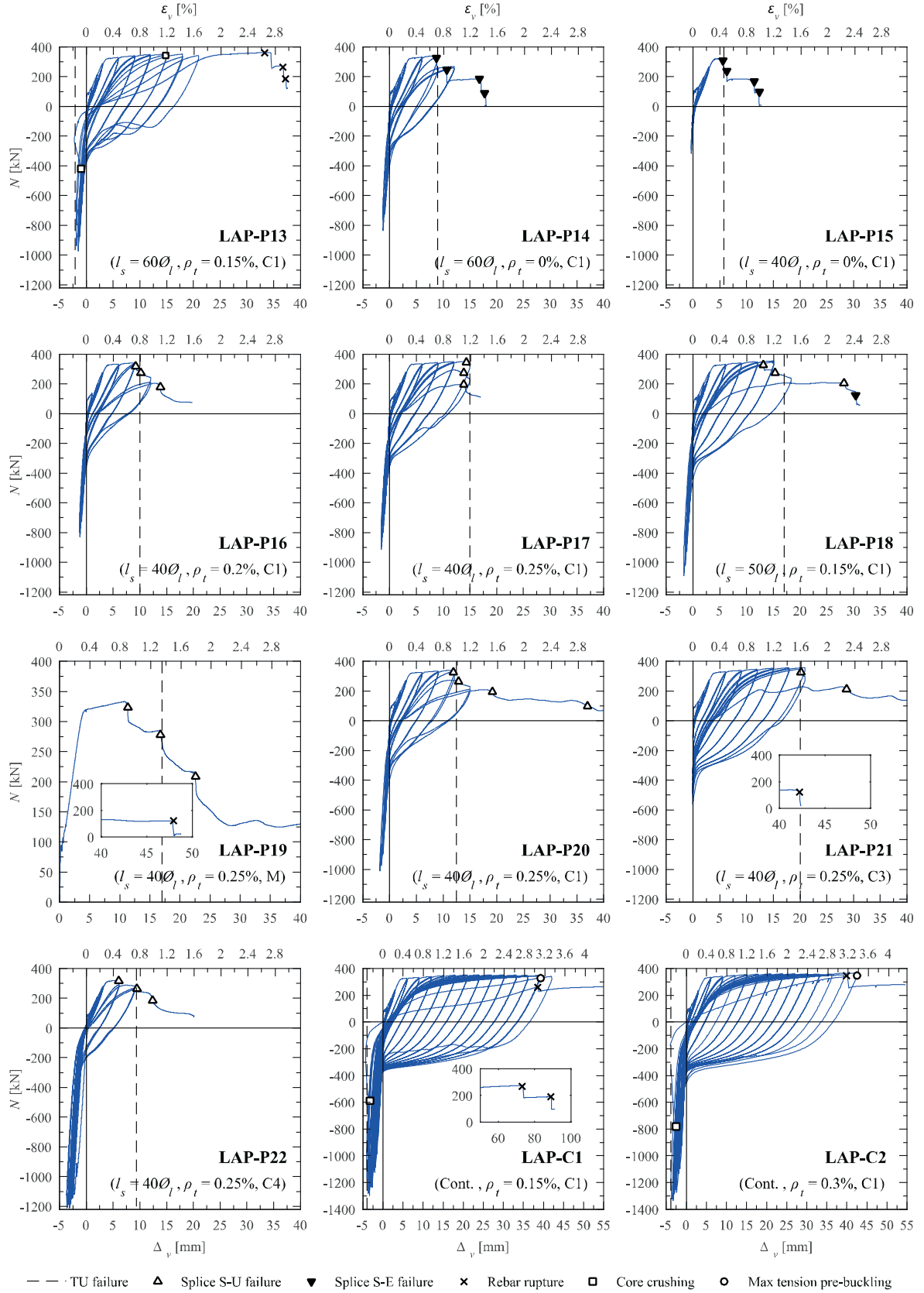


Figure 5.6: Cyclic response of specimens LAP-P13 to LAP-P22, LAP-C1 and LAP-C2.

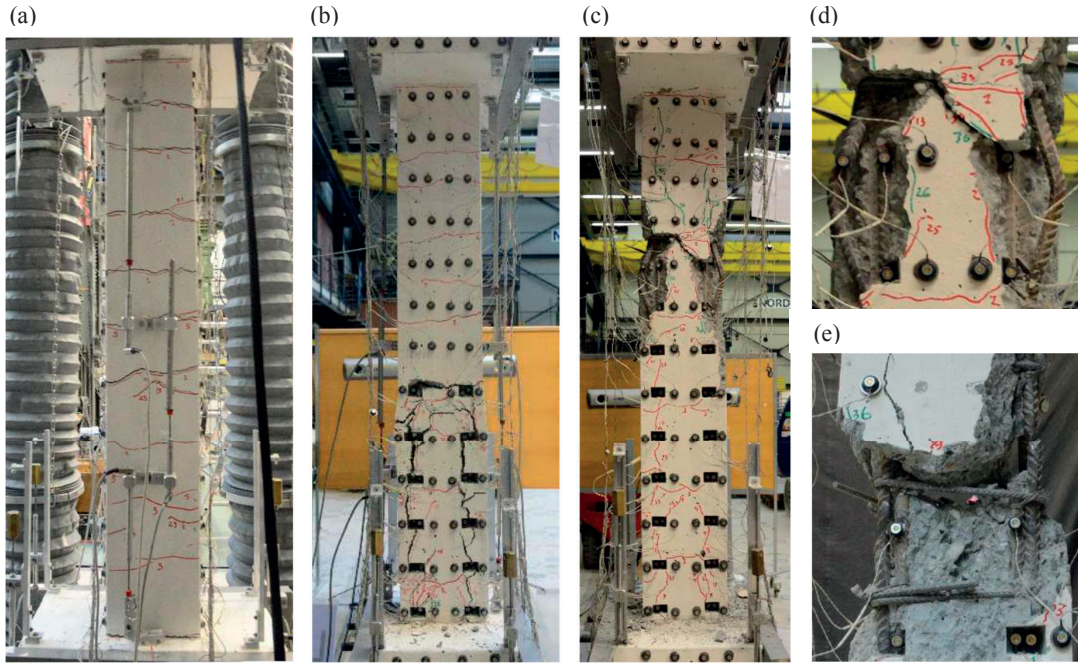


Figure 5.7: Photos of: (a) Crack pattern before failure of LAP-P21, $\Delta_v = 21$ mm ($\epsilon_v \approx 1.7\%$), east face; (b) Splitting-unzipping failure of LAP-P7, $\Delta_v = 15$ mm ($\epsilon_v \approx 1.2\%$), south side; (c) Failure in compression of LAP-P13, $\Delta_v = -2.1$ mm ($\epsilon_v \approx -0.17\%$), south face; (d) Close-up of core crushing and rebar buckling above the spliced region of LAP-P13; (e) Rebar rupture after buckling, NW top anchored rebar, $\Delta_v = 27$ mm ($\epsilon_v \approx 2.15\%$), LAP-P10.

5.5 Organization of test data

The test data are publically available and free to download from the platform Zenodo, at the following DOI: 10.5281/zenodo.1205887. The structure of the data organization is illustrated in the flowchart of Figure 5.8. A separate folder (e.g., ‘LAP_C(i)’, ‘LAP_P(i)’) is uploaded for each TU, the content of which is described in the next subsection.

5.5.1 LAP_P(i)/Lap_C(i) folders

An informative file and four main folders are made available for each test unit:

- ‘LAP_P(i)/LAP_C(i)_Specimen_description’ file: these files include the unit-specific reinforcement layout, LEDs pattern and numbering upon post-processing, LVDTs base-lengths, actual applied displacement history and force-displacement response. Moreover, a detailed description of the measured, computed and post-processed conventional channels is provided.
- ‘01_Material_tests’ folder: Two subfolders contain the results of the concrete and reinforcement material tests. A ‘.pdf’ file is provided for the concrete cylinder compression tests while a ‘.xls’ file for each rebar diameter is available for the steel. The latter contains the experimental data (stress-strain curves) as well as mean values of the main quantities to be used for modelling purposes. It is noted that since the reinforcement came from the same production batch for all TUs, the corresponding material test files do not change from one specimen to the other.
- ‘02_Experimental_level’ folder: It includes the ‘.xls’ lab book file and two folders, labelled ‘Photos’ and ‘Videos’. The lab book reports the main facts relative to the tests as well as live observations on the behaviour of the TUs. Other useful information can be found such as date and time at which every *LS* was performed, LVDTs base-lengths, non-connected LEDs in their original numbering, and attained vertical forces (*N*) and displacements (Δ_v) at each *LS*. The folder ‘Photos’ contains a selection of photos taken at different *LS* during the test. Where available, photos of the four column sides at the beginning of the test (*LS00*), at the last *LS* before failure, at the first *LS* after failure and after significant localized damage are included. Similarly, the folder ‘Videos’ contains trimmed videos of the most important moments of the test, such as splice failures, rebar ruptures or concrete crushing.

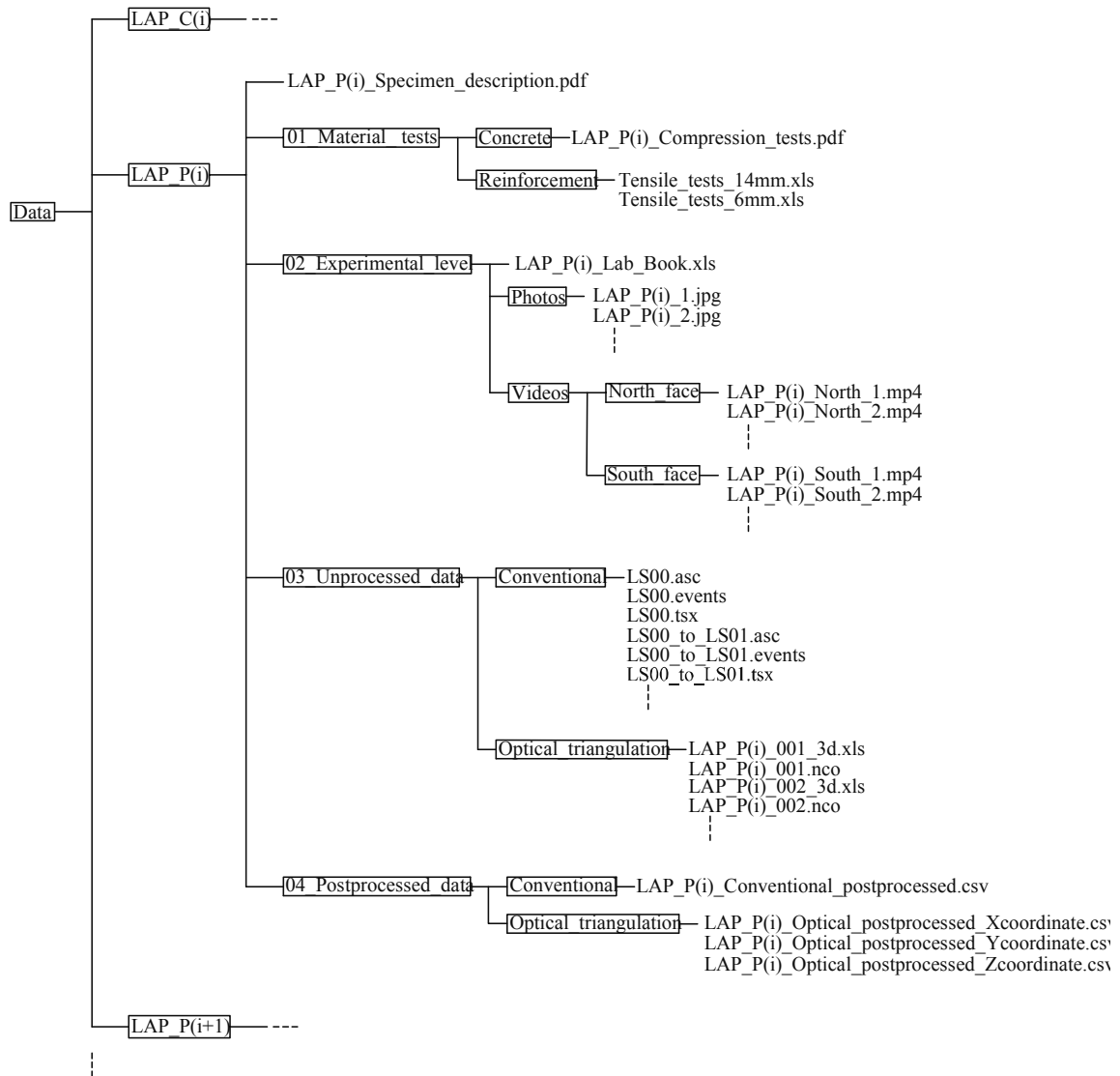


Figure 5.8: Organization of the data.

- ‘03_Unprocessed_data’ folder: The as-recorded data belong to this folder. They were differentiated between conventional data and data obtained from the optical triangulation system. The relationship between the load steps and the corresponding data files is straightforward for the conventional data, while it is reported in the lab book for the LED data. A more detailed description of the conventional data, including the definition of the different channels and their numbering can be found in the specific specimen description file. As for the optical triangulation data, the ‘.xls’ extension files contain the recording of the 3D displacement field of all LEDs, organized in columns. Non connected or non-visible LEDs result in empty columns for the x, y and z coordinates. In the NDI-specific-format files (‘.ncs’ extension) the camera sensor settings are stored. It is recalled that at the unprocessed data level the LEDs numbering is unorganized and that the origin of the reference system is given by the centre of the master sensor. Furthermore, at this level the LED data and the data gained from the conventional measurement system are not synchronised. The synchronization between the conventional and optical measurement systems is performed during the post-processing of the data through the LED conventional channel, which reports when the optical system is recording (see the TU description files for more details). The LED system was therefore always switched on after the conventional system and off before the conventional system.
- ‘04_Postprocessed_data’ folder: The data was post-processed in order to synchronize the conventional and optical measurement systems, to discard data recorded prior or after loading and to remove any bias or data that is not linked

to the behaviour of the TUs (e.g., LEDs falling off). Two subfolders contain the post-processed conventional and optical triangulation data. In the ‘Conventional’ folder, a ‘.csv’ extension file reports the conventional data organized in 41 columns; the first 33 involve measured and computed channels while the last 8 concern quantities added in the post-processing phase. The correspondence between columns and channels, as well as the definition of the post-processed quantities, is provided in the TUs description files. The ‘Optical triangulation’ folder features three ‘.csv’ files corresponding to the x , y and z LED coordinates, after renumbering and transformation into the new reference system presented in subsection 5.3.3.2. Each column corresponds to a single LED. The LEDs numbering after post-processing is illustrated in the TUs specific description files.

5.6 Post-processed data and example plots

By using the post-processed experimental data, several plots can be produced. As an example, the force-displacement responses of Figure 5.5 and Figure 5.6 were obtained by using the forces N and vertical displacements Δ_v from the post-processed conventional measurements (channels 35 and 20 respectively). Global displacements can also be derived from the post-processed optical triangulation measurements, as the vertical displacement difference between markers glued on the top beam and foundation RC blocks. However, LEDs data may also be employed to evaluate local deformations: Figure 5.9 (a) displays the force *vs* average lap splice strain (ϵ_{ls}) envelopes, where ϵ_{ls} is determined using the LEDs immediately above and below the spliced region. The history of ϵ_{ls} throughout all loading protocol is represented in Figure 5.9 (b) while the same quantity is shown in Figure 5.9 (c), at four different load steps.

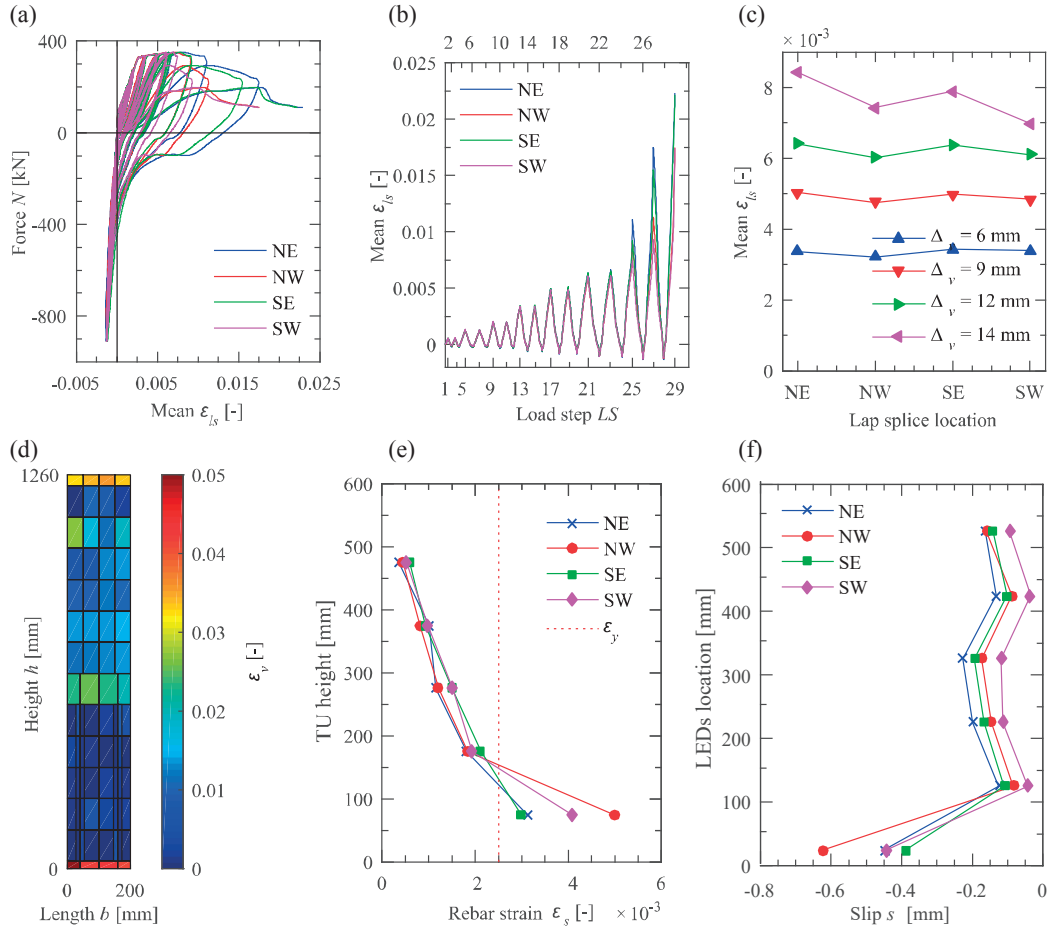


Figure 5.9: Example plots of local-level deformation quantities on test unit LAP-P17: (a) Hysteretic curves of force *vs* average strain over the lap splice length; (b) Average lap splice strain histories; (c) Average lap splice strains at different displacement levels; (d) North face strain map at $\Delta_v \approx 14$ mm ($\epsilon_v \approx 1.1$ %), corresponding to the onset of lap splice failure; (e) Rebar axial strain of the bottom anchored rebars at the displacement amplitude before failure, $\Delta_v = 12$ mm ($\epsilon_v \approx 0.95$ %); (f) Rebar *vs* concrete slip of the bottom anchored rebars at $\Delta_v = 12$ mm ($\epsilon_v \approx 0.95$ %).

As it can be observed, the strain increases for increasing applied vertical displacements and it is rather constant between the four splices. The vertical strain distribution of LAP-P17 at the onset of lap splice failure is illustrated in Figure 5.9 (d). Note how the vertical strains are concentrated in the crack located right above the lap splice region and at the interfaces to the foundation and top beam. Moreover, the vertical strains computed within the lap splice region are smaller than those in the region above. Finally, Figure 5.9 (e) and Figure 5.9 (f) depict the axial strain of the foundation anchored rebar and the relative slip between the same rebar and the concrete, respectively. Both quantities were evaluated at the *LS* preceding the splice failure. The slip is obtained by subtracting the displacement recorded by the markers glued on the concrete from the adjacent LEDs glued on the rebars. As expected, both the slip and the rebar strain are larger at the bottom, where the bar is anchored and the deformations are maximum.

5.7 Summary

Twenty four RC members, of which 22 with lap splices and 2 reference units with continuous reinforcement, were tested at the *Earthquake Engineering and Structural Dynamics (EESD) Laboratory* of the *École Polytechnique Fédérale de Lausanne (EPFL)*. This Chapter presents the main features of the experimental programme, including a description of the specimens, the test setup, the imposed loading protocols and instrumentation. Test observations as well as the organization of the obtained data are described.

All the units featured the same geometry and were tested under uniaxial quasi-static tension-compression cyclic loading. The goal was to study the influence of splice length, confining reinforcement and loading history on the behaviour of lap splices. Four different lap splice lengths ranging from 25 to 60 times the longitudinal rebar diameter were considered, as well as five distinct confining reinforcement ratios, from $\rho_t = 0\%$ to $\rho_t = 0.3\%$. In total, five loading protocols were imposed, four cyclic and one monotonic.

The test units were all equipped with conventional instrumentation and an optical measurement system. The latter was composed of a fine mesh of LEDs glued on both the north and south column faces, on the concrete surface as well as on the spliced rebars. This arrangement allowed to compute several local deformation quantities, such as concrete strains, lap splice strains and rebar-concrete slip. The raw and processed experimental data are made publically accessible through the Zenodo platform under the DOI: 10.5281/zenodo.1205887.

All the spliced units behaved similarly until the onset of failure, which occurred due to the opening of vertical splitting cracks along the lap splice length. Depending on the amount of provided confining reinforcement, a splitting-unzipping or splitting-explosive failure mode could be observed. The lap splice failures occurred, however, at very different strain demands, which depended on the lap splice length, the confining reinforcement and to a lesser extent on the loading history. For very long splice that were well-confined, the splices did not fail and the rupture of the top anchored rebar occurred. This happened after the specimen failed in compression due to core concrete crushing.

5.8 Acknowledgments

The financial support by the *Swiss Federal Roads Office (FEDRO)* to the project number AGB 2015/002, under which the present study is carried out, is acknowledged. Moreover, the author would like to thank Tiago Nico Pereira and Maria Katsidoniotaki for the precious help in the laboratory and Massimo Fermani for the assistance in producing some figures.

6 Evaluating the Ultimate Deformation Capacity of Lap Splices under Cyclic Loading

Based on the results from the experimental programme described in the previous Chapter, this Chapter investigates in detail the deformation capacity of lap splices. An expression for the quantification of the ultimate average lap splice strain is proposed. The Chapter represents the pre-print version of the paper:

D. Tarquini, J.P. Almeida, K. Beyer, 2018. “Experimental investigation on the deformation capacity of lap splices under cyclic loading”, submitted to *Bulletin of Earthquake Engineering* (under review).

Figures and tables formatting, reference-, section-, and equation- numbering were adapted to the style of this document. The analysis of the experimental data as well as the calibration of the equation for the deformation capacity of lap splices were carried out by the first author under the supervision of the other two.

Abstract

Correct detailing and positioning of lap splices is essential in order to prevent premature failure of reinforced concrete structural members. Especially before the introduction of capacity design guidelines, lap splices were often placed in member regions that undergo inelastic deformations under seismic loading. When assessing the seismic performance of such members, not only the lap splice strength, which was assessed in previous studies, but also information on the deformation capacity of lap splices is required. This Chapter analyses the results of a recently concluded experimental programme on spliced RC wall boundary elements tested under uniaxial tension-compression cyclic loading. The study aimed at investigating the influence of lap splice length, confining reinforcement and loading history on the deformation capacity of lap splices. The latter is defined as the average strain, at the onset of splice failure, ascribed to deformations originating from the lap splice zone. Analysis of the test results showed that the deformation capacity of lap splices: (i) increases with lap splice length; (ii) increases with confining reinforcement but the effectiveness of the confining reinforcement is dependent on the lap splice length; (iii) decreases with larger imposed compression levels; (iv) is larger for bottom-casted with respect to top-casted lap splices. Finally, an empirical model is proposed to estimate the strain capacity of lap splices, which provides a good fit with the experimental results.

Keywords: Uniaxial cyclic tension compression tests; Lap splices; Deformation capacity; Lap splice length; Confining reinforcement; Loading history.

6.1 Introduction

Splicing of longitudinal reinforcement is unavoidable in reinforced concrete (RC) structures and it can be found in all types of structural members such as beams, columns and walls. If not appropriately detailed and/or located in regions where inelastic deformations are expected, the presence of the lap splices may lead to a significant reduction of the strength and/or displacement capacity of the structural member. As reviewed in the following section, past research mainly focused on the evaluation of the strength capacity of lap splices, mostly through monotonic tests on beams spliced in the constant moment region. Tests on RC columns or walls are scarcer as well as tests performed under cyclic loading. On the contrary, to the author’s knowledge, no experimental programme was conducted aiming at the characterization of the deformation capacity of lap splices; and so despite its relevance in the context of performance-based design and assessment of structures, where displacement capacity rather than forces are compared with the seismic demand.

To address this gap, the present Chapter outlines the result of a recently concluded experimental programme focusing on the deformation capacity of lap splices. 24 test units, of which 22 with lap splices, designed to represent the boundary elements of spliced RC walls, were tested under uniaxial tension-compression cyclic loading. The specimens differed in terms of lap splice length, confining reinforcement, and loading history, as these are among the parameters most influencing the deformation capacity of lap splices (previously identified in Chapters 2 and 3). All specimens were instrumented to continuously monitor several displacement quantities as well as the applied forces. In particular a dense mesh of optical sensors allowed to identify and isolate the lap splice deformation contribution from the total imposed displacement.

The present Chapter is organized as follows. Past experimental tests on RC members with lap splices are described in Section 6.2, which is then complemented with the summary of the recently concluded experimental programme in Section 6.3. Section 6.4 discusses the influence of the main investigated experimental parameters on the deformation capacity of lap splices. In Section 6.5, based on experimental data, an empirical model for predicting the strain at failure of lap splices is proposed and validated. Conclusions are drawn in Section 6.6.

6.2 Experimental tests on RC members with lap splices: literature review

Early investigations on spliced RC members were conducted on beams with lap splices in the constant moment region, loaded monotonically up to failure [1,64,146,147]. The objective was to improve the understanding of the observed (splitting) failure modes as well as to quantify the strength of lap splices. The presence and amount of confining reinforcement, longitudinal rebar diameter, spacing and length of the splices, concrete cover and concrete strength were considered among the variable parameters. Additional experimental work on the strength of lap splices was done by Ferguson and Briceno [65], Ferguson and Krishnaswamy [68] and Thompson et al. [148], who used constant section beams to simulate spliced retaining walls: longitudinal rebars of large diameters, staggered splices and splices in both regions of constant and non-constant moment were tested. Based on a regression analysis of the results obtained from a selection of the above mentioned beam monotonic tests, Orangun et al. [37] proposed an equation for the bond strength of lap splices, which is to date a major reference for estimating this quantity.

The first experimental study on the cyclic inelastic behaviour of lap splices was carried out at Cornell University [8,9] at the beginning of the '80s. Cyclic tests were motivated by the fact that, due to the scarcity of information on performance of lap splices subjected to cyclic loading, most seismic codes of that time did not allow such details at locations of inelastic deformation, or else specified highly conservative design procedures. 68 large beams and 24 columns were tested and confining reinforcement and loading history (repeated and reversed cyclic loading) were varied between the test units. It was observed that adequate confining reinforcement was more effective for cyclic rather than monotonic loading and that reversed cyclic loading led to earlier splice failure than repeated loading. The influence of a moment gradient along the lap splice was also investigated and its beneficial effect on the splices performance was recognized. Further experimental programmes on spliced RC beams were performed by Rezaianoff et al. [49,149,150], Sakurada et al. [86], and Sparling and Rezaianoff [48], who studied the influence of confining reinforcement on the cyclic bond strength of lap splices; it was observed that adequately confined lap splices were sufficiently ductile to withstand a limited number of load reversals. Aristizabal-Ochoa [4] carried out inelastic cyclic tests on spliced RC columns under reversed axial loads and observed a reduction in the attained maximum ductility with the number of cycles. The author also noticed that proper placement of transverse reinforcement is crucial in order to avoid brittle failure. Paulay [10] proposed a simple design procedure to ensure that splices can sustain several cycles in the inelastic range; 8 RC columns subjected to lateral static loading were tested for validation purposes. Specific investigation on the behaviour of non-contact tension splices was carried out by Sagan et al. [151] and Hamad and Mansour [152], who conducted tests on 47 flat plate and 17 slab specimens, respectively. They concluded that the spacing between spliced rebars influences the ultimate load carrying capacity of the structural member as well as the number of resisted inelastic tensile load cycles.

An equation for the strength of lap splices in compression based on monotonic axial column tests by Cairns and Arthur [153] and Pfister and Mattock [154] was proposed for the first time by Cairns [84]. It was claimed that the strength of tension and compression lap splices is influenced by the same factors (spliced length, confining reinforcement, longitudinal rebar diameter and concrete cover), although their relative importance is different. Cyclic tests on three columns and four beams under repeated compression loading were carried out by Panahshahi et al. [2] who concluded that compression lap splices can be designed to sustain several cycles of inelastic loading. More recently, Chun et al. [155,156] investigated the monotonic behaviour of compression splices in normal and high strength concrete while Askar [157] studied the influence of splice length, transverse reinforcement and end bearing conditions on spliced RC columns loaded monotonically up to failure.

In the last three decades, following major earthquakes in California (e.g. San Fernando 1971 or Loma Prieta 1989) that emphasized the vulnerability of spliced RC piers and columns, several experimental programmes were carried out focusing on strengthening techniques of such structural members. Chai et al. [51] and Aboutaha et al. [50] evaluated the effectiveness of steel jackets to improve the strength and ductility of piers and columns with short lap splices. Several retrofitting techniques such as welding of spliced bars, confining the splice region with steel angles or providing additional reinforcing bar ties were investigated by Valluvan et al. [52] while seismic retrofit using prefabricated composite jacketing

was carried out by Xiao and Ma [94]. Cyclic tests on non-retrofitted RC columns with details typical of pre mid-1970 US construction practice and subjected to increasing lateral load can instead be found in the works by Lynn et al. [11] and Melek et al. [12]. Strengthening of non-ductile RC columns with carbon fiber reinforced polymers (CFRP) was explored by several authors, e.g. [158,159], and compared with the use of additional internal steel ties [160].

A large experimental program comprising 83 spliced beam specimens and aimed at determining the influence on bond strength of relative rib area and bar diameter was carried out by Darwin et al. [161]. Conventional and experimental deformation patterns for the rebars were evaluated. The continuation of the test series, with additional 64 beam tests, is reported in Zuo and Darwin [38] where the obtained data are used to determine an empirical relation for the bond strength of lap splices. The latter is expressed as function of concrete strength, relative rib area, bar size, and confinement provided by both concrete and transverse reinforcement. A modification to the above equation was proposed by Ichinose et al. [81] in order to better capture the size-effect in the bond strength observed in their own experimental programme.

Epoxy coated reinforcing bars are used whenever corrosion protection represents a principal design requirement for RC members. In the 1990s, a multitude of studies on the splice strength of epoxy coated reinforcing bars were carried out on beam monotonic tests [72,162–165]. It was concluded that epoxy coating significantly reduces the bond strength of lap splices and that, if used, a modification factor for the splice length should be adopted. Starting from the mid-1990s, research effort was also put in investigating the bond strength of lap splices in high-strength Concrete (HSC) [166–171] and fibre reinforced concrete [172–174] beams. Finally, as smooth bars are regularly encountered in historical structures, several test series on RC members featuring spliced plain bars can also be found in the literature (e.g. [175–178]).

Tests on RC wall elements with lap splices are scarce and relatively recent if compared to those on columns and beams [13,15,27–30,56,57,59]. The units were typically subjected to a constant axial load and increasing cyclic lateral displacement. A detailed review of these tests on spliced RC walls, including observations on the main failure modes, is carried out in Chapter 2.

6.3 New experimental programme on RC members with lap splices

6.3.1 Test setup, units, and loading

A total of 24 RC members, 22 of which with lap splices and two reference units with continuous reinforcement, were tested under uniaxial tension-compression cyclic loading at the structural laboratory of the *École Polytechnique Fédérale de Lausanne* (EPFL). The experimental programme, as well as some relevant experimental observations, are herein summarized. A detailed description of the tests is available in Chapter 5, which also outlines the organization of the available experimental data, free to download from the Zenodo platform at the DOI: 10.5281/zenodo.1205887.

The test units (TUs) represent spliced RC wall boundary elements and were designed based on the tests carried out by Bimschas [29] and Hannewald et al. [57]. The geometry was common to all specimens and consisted of a column height $h = 1260$ mm and a square 200×200 mm cross section, as illustrated in Figure 6.1. Foundation and top beam blocks of dimensions $550 \times 550 \times 300$ mm were included to connect the TUs to the uniaxial testing machine (with ± 125 mm stroke and $\pm 2.5/10$ MN force capacity) via four T-shaped steel profiles. The longitudinal reinforcement was formed by four 14 mm diameter rebars (corresponding to a longitudinal reinforcement ratio $A_l \approx 1.5\%$) which, except for the units with continuous reinforcement, were spliced above the foundation. Four different lap splice lengths were considered, spanning from 25 to 60 times the longitudinal bar diameter (ϕ_l). The confining reinforcement was composed of 6 mm diameter stirrups and 90° hooks, with confining reinforcement ratios ranging from 0 to 0.3%. Such ranges were chosen as representative of both pre-seismic and code-compliant central European construction practice. The longitudinal reinforcement was made of hot-rolled steel ($f_y = 510$ MPa, $\varepsilon_{sh} = 0.95\%$, $f_u = 635$ MPa, $\varepsilon_u = 9.3\%$) while cold formed steel was used for the transverse reinforcement ($f_y = 510$ MPa, $f_u = 635$ MPa, $\varepsilon_u = 9.3\%$). The TUs were casted horizontally four at a time and the 28-day concrete compressive strength, obtained from cylinder tests, remained between 30 and 35 MPa.

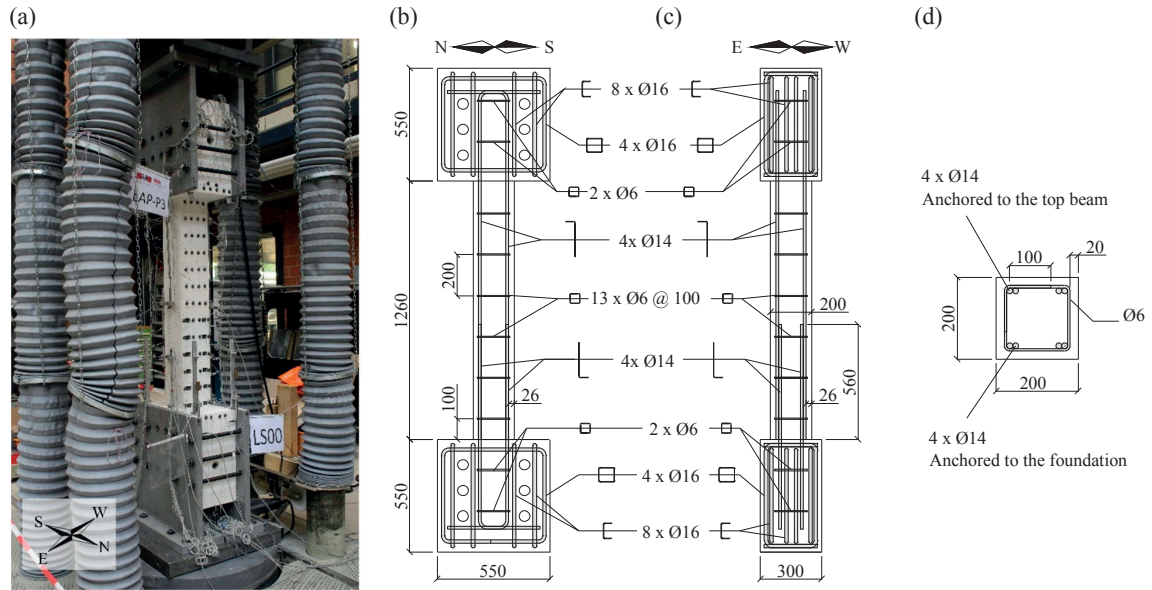


Figure 6.1: Test setup, geometry and reinforcement layout of the unit LAP-P3: (a) Photo of the TU before the test; (b) reinforcement content in the N-S direction; (c) reinforcement content in the E-W direction; (d) cross section.

Table 6.1: Test matrix.

TU	l_s [mm]	l_s [$\times \phi_l$]	A_t [mm]	ρ_t [%]	LH	TC face	FM	N_{max} [kN]	N_{min} [kN]	Δ_f [mm]
LAP-P1	560	40	Ø6@100	~0.3	C1	E	M	362	-1074	24
LAP-P2	560	40	Ø6@300	~0.1	C1	W	M	323	-568	5.3
LAP-P3	560	40	Ø6@200	~0.15	C1	E	S-U	326	-682	9
LAP-P4	350	25	Ø6@100	~0.3	C1	W	S-U	301	-513	5
LAP-P5	840	60	Ø6@300	~0.1	C1	E	M	357	-1018	18
LAP-P6	560	40	Ø6@200	~0.15	M	W	S-U	321	[-]	5.5
LAP-P7	560	40	Ø6@200	~0.15	C1	W	S-U	319	-523	6
LAP-P8	560	40	Ø6@200	~0.15	M	W	S-U	340	[-]	13
LAP-P9	560	40	Ø6@200	~0.15	C2	W	S-U	311	-766	6
LAP-P10	840	60	Ø6@100	~0.3	C1	E	C-C	359	-1163	-2.7
LAP-P11	350	25	Ø6@200	~0.15	C1	E	S-U	252	-281	3.9
LAP-P12	350	25	Ø6@300	~0.1	C1	E	S-U	254	-286	3.9
LAP-P13	840	60	Ø6@200	~0.15	C1	W	C-C	363	-973	-2.1
LAP-P14	840	60	[-]	0	C1	E	S-E	342	-835	9
LAP-P15	560	40	[-]	0	C1	E	S-E	322	-315	5.8
LAP-P16	560	40	Ø6@150	~0.2	C1	E	S-U	340	-832	10
LAP-P17	560	40	Ø6@120	~0.25	C1	E	S-U	351	-911	15
LAP-P18	700	60	Ø6@200	~0.15	C1	W	M	355	-1091	17
LAP-P19	560	40	Ø6@120	~0.25	M	E	M	333	[-]	17
LAP-P20	560	40	Ø6@120	~0.25	C1	W	S-U	342	-1011	12.5
LAP-P21	560	40	Ø6@120	~0.25	C3	E	M	358	-563	20
LAP-P22	560	40	Ø6@120	~0.25	C4	E	S-U	318	-1211	9.4
LAP-C1	[-]	[-]	Ø6@200	~0.15	C1	E	C-C	353	-1304	-4
LAP-C2	[-]	[-]	Ø6@100	~0.3	C1	E	C-C	366	-1342	-3.9

TU: test unit; l_s : lap splice length; ϕ_l : longitudinal bar diameter; A_t : confining reinforcement content; ρ_t : confining reinforcement ratio; LH: loading history type (see text description); TC face: location of top casted face; FM: failure mode (see Table 5.4); N_{max} : maximum applied (tensile) force; N_{min} : minimum applied (compression) force; Δ_f : global displacement at specimen failure.

Five different uniaxial loading protocols were considered, one monotonic (M) and four cyclic (C1 to C4). The cyclic histories featured increasing applied tension levels, with two cycles performed at each displacement amplitude. The attained compression levels differentiated the different protocols: a 10:1 ratio between the imposed tension and compression displacements was used in the main loading protocol, labelled C1. A 10:2 ratio characterized protocol C2, whereas C3 corresponded to a repeated cyclic loading history, i.e. the specimen was brought back to zero displacement after each applied tensile displacement amplitude. Finally, in protocol C4 an approximate axial load ratio (*ALR*) of 90% was applied at each compression load step.

The complete matrix of the tests is listed in Table 6.1. Unit-specific parameters such as lap splice length, confining reinforcement, loading history and location of the top-casted face are reported along with some important test results including the observed failure mode (discussed in subsection 6.3.2), maximum forces attained both in tension and compression, and the displacement at specimen failure. The latter was defined as the displacement corresponding to 20% loss of force capacity, either in tension or in compression.

Load cells were used to monitor the applied axial forces, whereas both hard-wired and optical instrumentation systems were employed to evaluate global and local displacements. Namely: (i) four linear variable differential transducers (LVDTs) were installed at the column corners by means of a plumb line system; (ii) six LVDTs arranged in two chains were located on the east and west unit faces; and (iii) light-emitting diodes (LEDs) were glued to the north and south column sides, both on the concrete and on the spliced steel bars (through holes prepared during casting), according to a regular mesh.

6.3.2 Experimental observations

The cracking behaviour of the TUs and the observed failure modes are briefly discussed in the following two subsections and framed into general categories. For a more detailed and unit-specific description of the TUs behaviour, as well as to consult their hysteretic response, the reader is referred to the Chapter 5, which shares all experimental data in digital form.

6.3.2.1 Cracking behaviour

Up until the failure of one of the splices or the occurrence of severe damage in compression such as concrete spalling or rebar buckling, all the specimens with spliced longitudinal reinforcement behaved in a similar way. At the application of the first tensile loading ($\Delta_v = 1$ mm), six to ten horizontal cracks opened along the unit height while two formed at the top beam and foundation interfaces. Due to the sudden stiffness change owing to the different longitudinal reinforcement content, two of these cracks were always located at the lap splice extremities (the bottom one therefore coinciding with the foundation interface crack). The cracks were roughly equally spaced along the entire length of the member and had a constant width ($w \approx 0.1$ mm). Yielding of the longitudinal reinforcement occurred at an imposed displacement of about $\Delta_v \approx 4$ mm. In the previous tensile cycles (i.e., at $\Delta_v = 2$ mm and $\Delta_v = 3$ mm), a distinct crack width evolution was observed between the spliced region and the zone above the splices. In particular, crack widths within the spliced region remained rather constant ($w \approx 0.1$ mm) while the others increased with the imposed tensile displacement (up to $w \approx 0.3$ mm for $\Delta_v = 3$ mm). At $\Delta_v = 3$ mm, the first vertical splitting cracks appeared at the splice loaded ends, leading to the start of the steel-concrete debonding action. During the following loading cycle to $\Delta_v = 6$ mm, yielding of the longitudinal rebars took place, and the specimen behaviour started to be unit-specific. Specimens with short lap splices ($l_s = 25 \times \phi_l$) failed before reaching the yield force with vertical cracks opening along the entire lapped length and causing the almost total loss of the member force capacity. For the other specimens with longer lap splices, increasing the imposed tensile displacement beyond yielding produced a continuation of the widening of the horizontal cracks outside the lap splice region while crack opening remained approximately constant within the spliced zone (Figure 6.2 (a) and (b)). Vertical cracks extended from the lap ends towards the centre with failure occurring when the debonded length equalized the lap splice length. No extension of the vertical (tension-produced) splitting cracks was observed in compression until average compression strains in the order of $\varepsilon_v \approx -1.5\%$ ($\Delta_v = -1.8$ mm) were applied. At this stage vertical crushing cracks appeared, as well as minor concrete spalling. Whenever larger compression deformations were reached, extensive spalling developed above the spliced region followed by rebar buckling and eventually concrete core crushing.

Specimens with continuous reinforcement showed an approximately uniform crack distribution along their height, with horizontal cracks spaced about 150 to 200 mm, see Figure 6.2 (c). The crack width was rather constant, increasing with the imposed tensile displacement, as shown in Figure 6.2 (d). Upon load reversals, crack closure with no damage was observed up to high imposed compression strain levels ($\varepsilon_v \approx -2\%$). At this point, vertical cracks formed between the main

horizontal cracks, preceding longitudinal rebar buckling and concrete crushing. The latter was the governing failure mode for these benchmark units (with continuous reinforcement), leading to a loss of almost 80% of their load carrying capacity. Rebar rupture was attained in the last pulling cycle, i.e. performed after specimen failure in compression.

6.3.2.2 Failure modes

The failure modes observed for each TU are listed in Table 6.1. Specimen failure, intended as a 20% loss of the maximum tension or compression force attained during each test (i.e., the TU capacity), was caused either by failure of one or more lap splices or by core concrete crushing. Two different lap splice failures could be distinguished: splitting-unzipping and splitting-explosive. The former was characterized by vertical splitting cracks, which, originating at the lap loaded ends gradually extended along the entire splice length. The progression of the crack opening depended on the confining reinforcement, with lower confinement ratios leading to a faster crack development. Lap splice failure occurred when the vertical cracks from the lap ends joined about the centre of the splice (Figure 6.3 (a)), causing a strength loss of around 80% of the rebar yield strength. When little or no confinement reinforcement was provided ($\rho_t < 0.1\%$), almost no vertical cracks could be observed before a sudden and loud lap splice failure occurred. No residual splice force was available for these failing splices and, upon load reversal, complete spalling of the cover concrete was typically observed (Figure 6.3 (b)). The term 'mixed' failure mode is used to identify the few cases in which lap splices of the same unit failed according to different failure modes.

Finally, core concrete crushing occurred when lap splices were long and well confined ($l_s = 60\phi$, $\rho_t > 0.15\%$) and for the reference units with continuous reinforcement. It was always preceded by extensive concrete spalling and rebar buckling which, for spliced members, took place right above the lap splice region (Figure 6.3 (d) and (e)). Rebar rupture was never the primary failure mode for any of the TUs and it was always attained after specimen failure, during the last tensile pulling cycle.

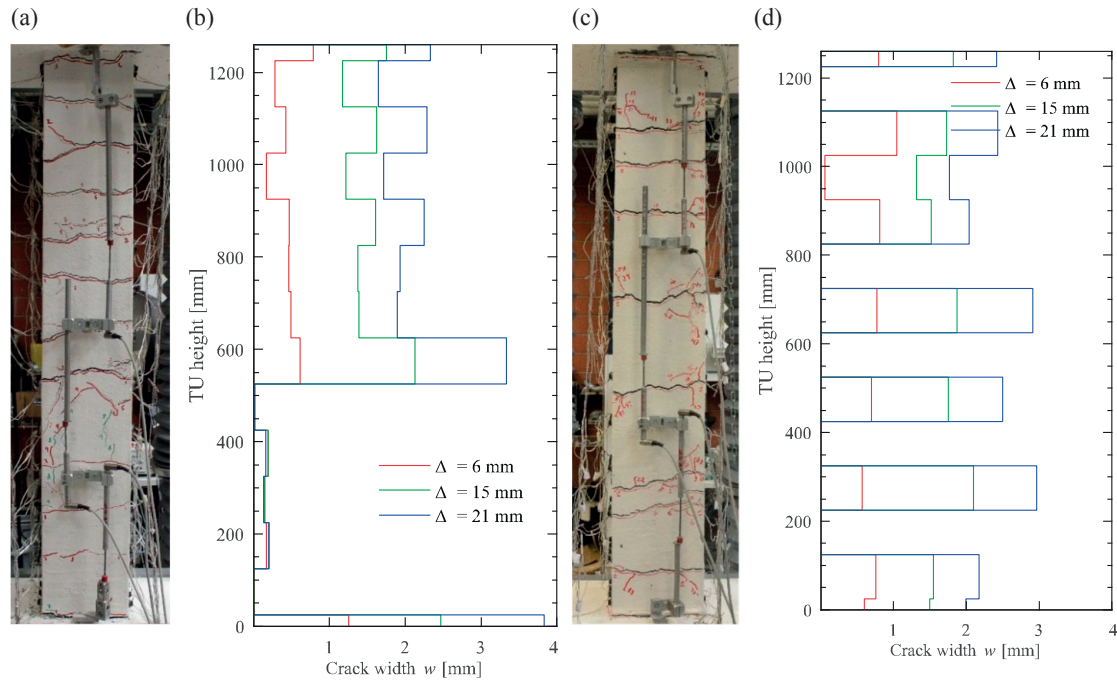


Figure 6.2: Crack distribution and width along the specimen height. LAP-P1: (a) crack distribution; (b) crack widths for three distinct levels of tensile displacement; LAP-C1: (c) crack distribution; (d) crack widths for three distinct levels of tensile displacement.

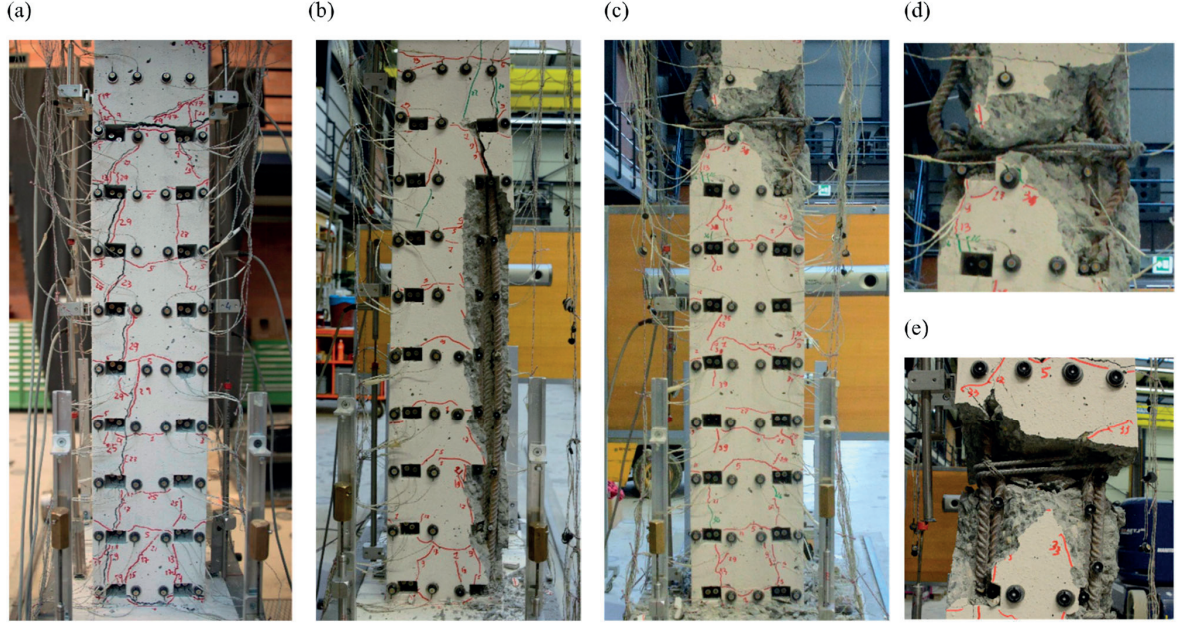


Figure 6.3: Failure modes: (a) splitting-unzipping failure of the NE splice of LAP-P5; (b) splitting-explosive failure of the SE splice of LAP-P14; (c) concrete crushing of LAP-P10 ; (d) close-up of concrete crushing of LAP-P10; (e) close-up of rebar rupture of LAP-P21.

6.4 Discussion of the experimental results

As discussed in Section 6.1, the main objective of this Chapter is to assess the deformation capacity of lap splices as function of the test-series variables, i.e. lap splice length, confining reinforcement, and loading history. The quantity used to characterize the deformation capacity of lap splices as well as the method employed for its calculation from experimental measurements are described in the next subsection 6.4.1 whilst the influence of each variable is separately assessed in subsection 6.4.2.

6.4.1 Definition of the average lap splice strain capacity

The average lap splice strain capacity (ϵ_{ls}) is defined as the average deformation, at the onset of failure, owing exclusively to deformations occurring within the lap splice region. Deformation contributions external to the lapped zone are not accounted for, such as the strain penetration of the rebar anchored into the foundation or the slip between the concrete and the rebar developed above the splices. In view of the available displacement measures in the spliced TUs (see Figure 6.4 (b)), the following steps were required to compute ϵ_{ls} :

- (i) Identify the load step at the onset of lap splice failure (LS_f , see Figure 6.4 (a));
- (ii) Compute at LS_f the lap splice displacement including the contribution of the two major cracks forming at the top and bottom lap splice ends ($\Delta_{ls,out}$). Referring to Figure 6.4 (b), $\Delta_{ls,out}$ is calculated as:

$$\Delta_{ls,out} = \Delta_F - \Delta_T \quad (6.1)$$

where Δ_F is the vertical displacement of foundation marker F and Δ_T is the vertical displacement of top marker T. Note that positive displacement values are downwards (the piston is attached to the foundation) as the reference system in Figure 6.4 (b) indicates.

- (iii) Calculate the width of the top and bottom end cracks (w_{TOP} and w_{BOT} , respectively):

$$w_{TOP} = \Delta_{T'} - \Delta_T \quad (6.2)$$

$$w_{BOT} = \Delta_F - \Delta_{F'} \quad (6.3)$$

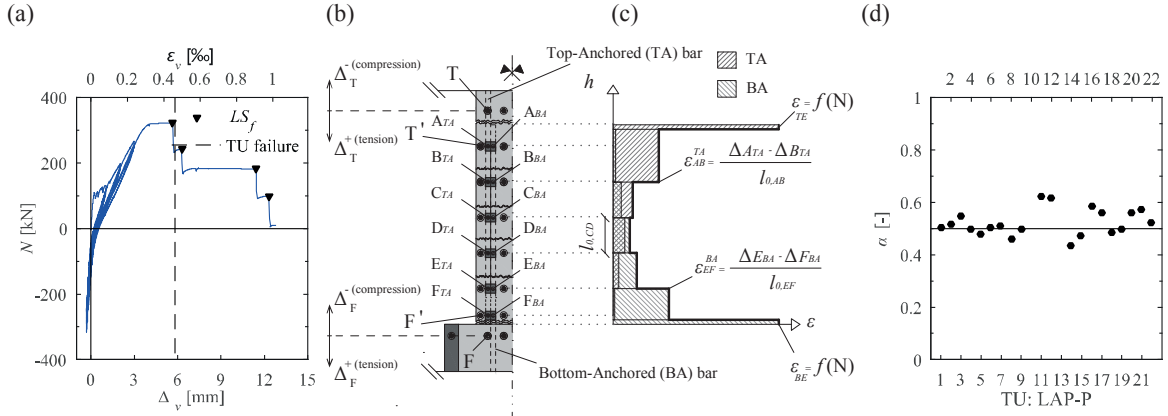


Figure 6.4: Auxiliary plots and sketches for definition of lap splice strain capacity ε_{ls} : (a) Identification of the four load steps at splice failure LS_f for TU LAP-P15; (b) Location of optical markers around the lap splice region; (c) Strain distribution for the pair of spliced bars; (d) Validation of the assumption on the parameter α ($\alpha_1 \approx \alpha_2 \approx 0.5$).

- (iv) Subtract the portion of w_{TOP} and w_{BOT} related to deformations occurring outside the lap splice region; namely, the part of the crack width due to the slip between the bar and the concrete above the lapped zone ($\alpha_1 \cdot w_{TOP}$) and the part of the crack width caused by strain penetration in the foundation-anchored rebar ($\alpha_2 \cdot w_{BOT}$). The processed lap splice displacement (Δ_{proc}) can therefore be expressed as:

$$\Delta_{proc} = \Delta_{ls,out} - \alpha_1 \cdot w_{TOP} - \alpha_2 \cdot w_{BOT} \quad (6.4)$$

- (v) Finally, the average lap splice strain capacity ε_{ls} is the ratio between Δ_{proc} and the nominal lap splice length l_s :

$$\varepsilon_{ls} = \frac{\Delta_{proc}}{l_s} \quad (6.5)$$

The calibration of the parameters α_1 and α_2 was carried out by comparing the displacement $\Delta_{ls,out}$ and the splice-end-crack widths w_{TOP} and w_{BOT} with the displacement Δ_{int} obtained by integrating, along the lap splice length, the envelope of the top and bottom anchored rebar strains (Figure 6.4 (c)). The parameter α (assuming $\alpha_1 = \alpha_2$) was computed as follows:

$$\alpha = (\Delta_{ls,out} - \Delta_{int}) / (w_{TOP} + w_{BOT}) \quad (6.6)$$

The comparison is represented in Figure 6.4 (d), which shows that $\alpha_1 = \alpha_2 = 0.5$ provided a good assumption for the present series of TUs. Further details on the calibration procedure as well as a mechanical interpretation of the obtained values for α_1 and α_2 are provided in Appendix 9.2.

6.4.2 Influence of variable test parameters on the average strain capacity of lap splices

6.4.2.1 Lap Splice Length

Three groups of TUs were selected in order to investigate the influence of splice length (l_s) on the deformation capacity of lap splices (ε_{ls}). The units within each group varied only with regard to l_s and featured the same confining reinforcement ratio (ρ_t) and imposed loading history (LH). The latter was common to all three groups and corresponded to C1.

The force-displacement responses of the selected TUs are displayed in Figure 6.5 (a). The total applied axial force N is given on the vertical y-axis while the global column vertical displacement Δ_v and strain ε_v are reported on the bottom and top x-axes. A separate plot is provided for each combination of l_s and ρ_t , where units belonging to the same group are represented with the same line colour. Namely blue, green and red are used for reinforcement ratios $\rho_t = 0.1\%$, $\rho_t = 0.15\%$ and $\rho_t = 0.3\%$ respectively. Results of longer and more confined lap splices can be found in the downward and rightward directions. Separate markers are used to indicate the onset of each lap splice failure, with distinct shape and fill depending on the observed failure type. A black dashed line identifies the overall specimen failure (corresponding to a loss of around 20% of the specimen load capacity) whereas rebar rupture, which always occurred after specimen failure, is displayed with a black cross. A black circle specifies lap splices considered as outliers, which are characterized by a displacement capacity far larger than the one observed in all other lap splices of the same TU. This larger ductility of specific lap splices

is related to the increased confining action provided by the stirrups, which, after failure of the first three splices, start to tilt with respect to their original horizontal position (see Figure 6.3 (e)). Such inclination introduces a compressive axial force component in the confining reinforcement contributing to restraining the pair of spliced rebars. However, since this effect is unit-specific and may not occur for different cross sectional geometries or reinforcement layouts, such outliers will not be considered in the analysis of the deformation capacity of lap splices.

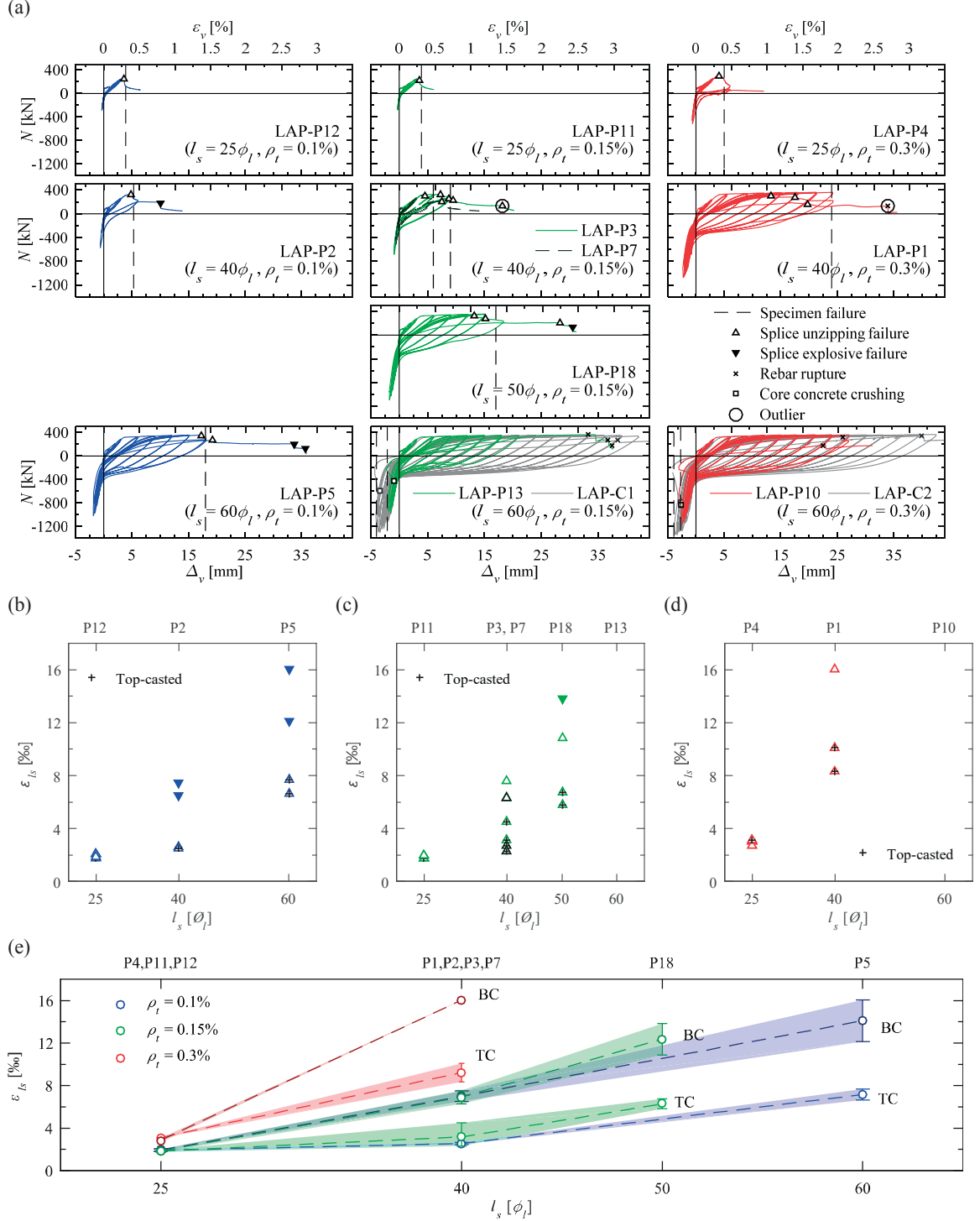


Figure 6.5: Influence of l_s on the behaviour of lap splices: (a) Force-displacement responses; (b), (c), (d) Lap splice strain capacity for fixed confining reinforcement ($\rho_t = 0.1\%$, $\rho_t = 0.15\%$, $\rho_t = 0.3\%$); (e) Lap splice strain capacity as function of l_s (TC: top-casted rebar, BC: bottom-casted rebar).

The hysteretic curves of Figure 6.5 (a) show that the displacement capacity of spliced members increases with l_s (i.e., the black dashed line consistently moves to larger displacements for longer splices). Except for $l_s = 60\phi_l$ and $\rho_t > 0.15\%$, where the lap splices did not fail but concrete crushing was the predominant failure mode, specimen failure was always caused by the failure of at least one lap splice. For short splices ($l_s = 25\phi_l$), simultaneous failure of the four lap splices took place before reaching the yielding of the longitudinal rebars. In all other cases, lap splice failure was observed after yielding of the longitudinal reinforcement and typically two splices failed clearly before the remaining two. The casting position is responsible for this difference as the increased porosity and water content reduces the concrete strength in top-casted splices [179]; this issue will be addressed more in detail in the following paragraph. The responses of the two reference units with continuous reinforcement are plotted in grey. It can be observed that, although specimens featuring long and well confined splices ($l_s = 60\phi_l$ and $\rho_t > 0.15\%$) did not fail, they nonetheless showed a significantly reduced deformation capacity with respect to the reference units. This is explained by the fact that, in spliced members, the deformation concentrates outside the lap splice region while cracks remain very small within the lapped zone.

The strain capacity of the single lap splices is plotted separately, for the three groups of TUs, in Figure 6.5 (b), (c) and (d). Outliers (namely, the last-holding splices of LAP-P1 and LAP-P3) and splices failing after crushing of the specimen were discarded. An additional marker (“+” symbol) is used to identify top-casted splices. The three plots show that ε_{ls} increases almost linearly with l_s , regardless of the provided confining reinforcement. Moreover, it is possible to distinguish the detrimental effect of top casting on the lap splice performance. In fact, except for short splices ($l_s = 25\phi_l$) where the four failed simultaneously, lap splices located on the top casted face showed considerably reduced ε_{ls} compared to those located on the bottom-casted face. However, it is important to point out that the determination of ε_{ls} is less reliable for bottom-casted than top-casted splices as the specimen is in a more damaged state. In fact, after the failure of the first splice, the bottom and top crack width begin to differ and no redundant measure is available to double check the computed value of ε_{ls} (Δ_{int} is not available, as discussed in Section 6.4.1).

Strains ε_{ls} for all the selected TUs are showed altogether in Figure 6.5 (e) under the form of error-bar plot. Strains belonging to top-casted (TC) and bottom-casted (BC) splices are again differentiated. The shaded regions represent the scatter for strains corresponding to a certain combination of l_s , ρ_t , and casting position. Again it is possible to observe the direct and almost-linear proportionality between ε_{ls} and l_s . Also, it is apparent that the scatter in the experimentally-determined strains increases with l_s and when passing from top- to bottom-casted splices (i.e. with the imposed displacement demand and therefore with the damage state of the specimen). Please note that only one value of ε_{ls} is available for the bottom-casted splices of specimen LAP-P1 ($l_s = 40\phi_l$ and $\rho_t = 0.3\%$), which explains the zero data scatter.

6.4.2.2 Confining reinforcement

The influence of the confining reinforcement on the behaviour of lap splices is illustrated in Figure 6.6, which contains similar plots to Figure 6.5. The selected TUs were subjected to the same loading protocol (C1) and subdivided in three groups, each one referring to a fixed value of l_s . Blue, green, and red line colours identify $l_s = 25\phi_l$, $l_s = 40\phi_l$, and $l_s = 60\phi_l$ respectively.

Figure 6.6 (a) shows that an increase in ρ_t does not necessarily correspond to a larger specimen ductility, especially for short lap splice lengths. In fact, the three TUs with $l_s = 25\phi_l$ depicted very similar hysteretic response and displacement at failure, although ρ_t varied from 0.1% to 0.3%. On the other hand, for long lap splices ($l_s = 60\phi_l$), a direct proportionality between ρ_t and the displacement capacity of the TUs can be observed. It is noted that for specimens LAP-P13 and LAP-P10, the provided ρ_t was sufficient to promote a change in failure mode, from lap splice failure to concrete crushing. As for medium length lap splices ($l_s = 40\phi_l$), an increase in ρ_t resulted in larger member ductility only for $\rho_t > 0.15\%$. In fact, all units with $\rho_t < 0.15\%$ (LAP-P15, LAP-P2, LAP-P3 and LAP-P7) showed a similar hysteretic response and displacement capacity; on the contrary, the latter increased for larger values of ρ_t in units with $\rho_t > 0.15\%$ (LAP-P16, LAP-P17, LAP-P20 and LAP-P1). Similar considerations to those above apply to the relation between ρ_t and ε_{ls} , as displayed in Figure 6.6 (b), (c), and (d): ε_{ls} is approximately constant in Figure 6.6 (b) (note the scale of the vertical axis), monotonically increasing in Figure 6.6 (d), and approximately bilinear (constant for $\rho_t < 0.15\%$, and increasing for $\rho_t > 0.15\%$) in Figure 6.6 (c). Again, except for the case of short lap lengths ($l_s = 25\phi_l$), within the same unit the top-casted splices always failed before the bottom-casted. An overall picture of the relationship between ρ_t and ε_{ls} is given in Figure 6.6 (e), which also confirms that data dispersion increases with the imposed displacement demand.

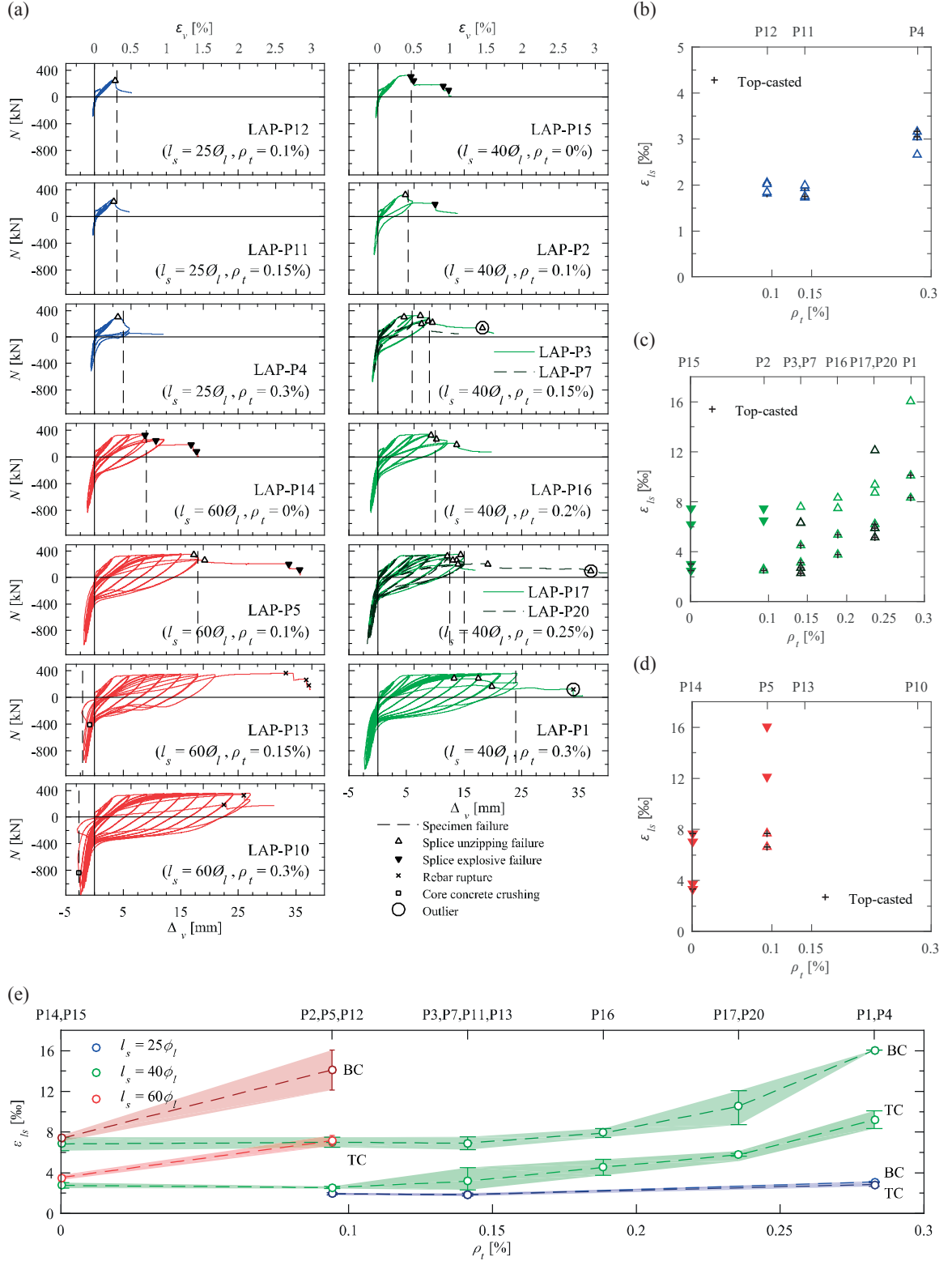


Figure 6.6: Influence of ρ_t on the behaviour of lap splices: (a) Force-displacement responses; (b), (c), (d) Lap splice strain capacity for fixed lap splice length ($l_s = 25\phi_l$, $l_s = 40\phi_l$, $l_s = 60\phi_l$); (e) Lap splice strain capacity as function of ρ_t .

6.4.2.3 Loading History

Two set of TUs having as only variable parameter the imposed loading history (LH) were characterized by: $l_s = 40\phi_l$ and $\rho_t = 0.15\%$ —depicted with a blue colour line in Figure 6.7—and $l_s = 40\phi_l$ and $\rho_t = 0.25\%$ —identified by a green colour

line. Each group was composed by five TUs and included the reference cyclic (C1) and the monotonic (M) loading protocols. Tests on units with same configuration and applied loading histories (LAP-P6/P8, LAP-P3/P7, and LAP-P17/P20) were performed in order to assess the repeatability of the test results.

Figure 6.7 (a) shows a comparable displacement capacity of the TUs of the first set ($l_s = 40\phi_l$ and $\rho_t = 0.15\%$), indicating that the imposed loading protocol did not play a significant role. Failure was in all cases triggered by splitting unzipping of the lap splices, occurring relatively soon after yielding of the longitudinal rebars. The smallest ductility is displayed by specimen LAP-P9, subjected to a loading protocol (C2) in which the compression levels were doubled with respect to those of C1. The two monotonic tests showed a significant aleatory difference in the attained displacement capacity, one failing right after yielding of the longitudinal reinforcement (LAP-P6, $\Delta_v \approx 6\text{mm}$) and the other reaching $\Delta_v \approx 12\text{mm}$. This scatter reduces slightly when ε_{ls} is considered—see Figure 6.7 (b) and (d), as the largest part of the member deformation occurs outside the lap splice region; recall that the crack width in the lapped zone remains relatively constant and small. Finally, the displacement and lap splice strain capacities of the two specimens tested under $LH = C1$ (i.e., LAP-P3 and LAP-P7) are in between the bounds obtained from the monotonic tests.

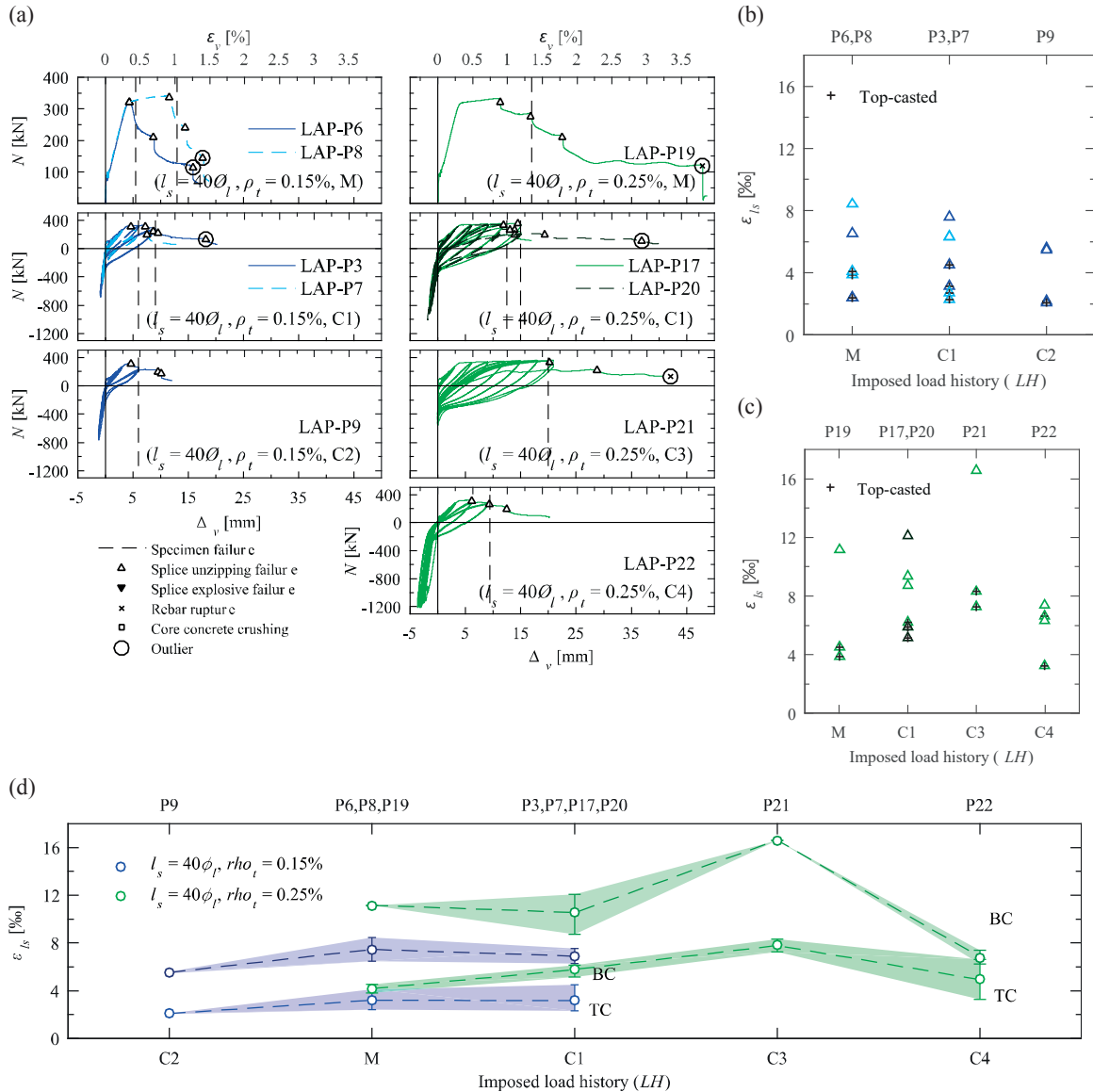


Figure 6.7: Influence of LH on the behaviour of lap splices: (a) Force-displacement responses; (b), (c) Lap splice strain capacity for fixed lap splice length and confining reinforcement ($l_s = 40\phi_l$ and $\rho_t = 0.15\%$, $l_s = 40\phi_l$ and $\rho_t = 0.15\%$); (d) Lap splice strain capacity as function of LH .

The impact of LH on the displacement capacity of the TUs is more clear for the second group ($l_s = 40\phi_l$ and $\rho_t = 0.25\%$). It stands out that, in a cyclic loading, larger imposed compression levels reduce the deformation capacity of lap splices (Figure 6.7 (a)). In fact, the displacement at failure of LAP-P21 ($LH = C3$, repeated cyclic loading) is larger than that of LAP-P17 and LAP-P20 ($LH = C1$), which in turn are larger than the one of LAP-P22 ($LH = C4$, fixed compression level $N \approx 0.9$ ALR). A similar trend applies when comparing values of ε_{ls} , as displayed in Figure 6.7 (c) and (d). For this configuration of TUs, a single test was performed under monotonic loading (LAP-P19), which attained a strain capacity in between those of tests with protocols C1 and C3.

While the available test results allow such qualitative comments regarding the influence of the loading history on the deformation capacity of lap splices, further testing is required for an appropriate quantitative characterization. Moreover, it was observed that, among the considered parameters, LH was the one with lowest impact on the lap splice strain capacity. Therefore, in the expression to estimate ε_{ls} proposed in the next section, the effect of LH will be disregarded.

6.5 Prediction of the lap splice strain capacity

Based on the experimental results discussed above, a predictive equation for ε_{ls} is proposed in this section, which builds on the following observations: (i) ε_{ls} increases with l_s , regardless of the provided ρ_t ; (ii) the influence of ρ_t on ε_{ls} depends on l_s . In particular, for short lap splices ($l_s = 25\phi_l$), ε_{ls} is not affected by variations in ρ_t ; on the other hand, for long lap splices ($l_s = 60\phi_l$), a small change from $\rho_t = 0$ to $\rho_t \approx 0.1\%$ produces a significant increase of ε_{ls} ; finally, for medium lap lengths ($l_s = 40\phi_l$) an increase of ε_{ls} is observed only for provided $\rho_t > 0.15\%$; (iii) loading history is the least influential among the considered variable parameters and further testing is required for an appropriate quantification; (iv) casting position plays a significant role in the displacement capacity of lap splices, with lower ε_{ls} associated to bottom-casted splices.

The expression for ε_{ls} is defined in the two-variable space l_s and ρ_t , with $25\phi_l < l_s < 60\phi_l$ and $0 < \rho_t < 0.3\%$. Stemming from the above consideration (ii), two regions were defined in this $[l_s, \rho_t]$ domain: one in which an increase in ρ_t causes an increase in ε_{ls} (labelled subdomain A) and another where the strain capacity does not depend on the confining reinforcement (subdomain B). The separation between the two regions is specified by the following equation:

$$\frac{l_s}{\phi_l} + \frac{60 - 25}{0.3} \cdot \rho_t - 60 = 0 \quad (6.7)$$

where ρ_t is defined in percentage [%]. The previous expression represents the line passing through the points with coordinates $[l_s, \rho_t] = [60\phi_l, 0\%]$ and $[25\phi_l, 0.3\%]$. All combinations of $[l_s, \rho_t]$ leading to positive values for equation (6.7) fall into subdomain A while those resulting in negative values belong to subdomain B. Moreover, since for $l_s = 60\phi_l$ and $\rho_t > 0.15\%$ no lap splice failure was observed, the equation should not be used in that subrange. A linear equation in the two variables l_s and ρ_t is then fitted, for each subdomain, through the experimental ε_{ls} values. The following two systems of equations, for top- and bottom-casted lap splices, were respectively obtained:

$$\begin{cases} \varepsilon_{ls}^{TC} = -23 + 50 \cdot \rho_t + 0.44 \cdot \frac{l_s}{\phi_l} & \rightarrow [l_s, \rho_t] \in \text{subdomain A} \end{cases} \quad (6.8)$$

$$\begin{cases} \varepsilon_{ls}^{TC} = 1.2 + 0.04 \cdot \frac{l_s}{\phi_l} & \rightarrow [l_s, \rho_t] \in \text{subdomain B} \end{cases} \quad (6.9)$$

$$\begin{cases} \varepsilon_{ls}^{BC} = -36 + 70 \cdot \rho_t + 0.76 \cdot \frac{l_s}{\phi_l} & \rightarrow [l_s, \rho_t] \in \text{subdomain A} \end{cases} \quad (6.10)$$

$$\begin{cases} \varepsilon_{ls}^{BC} = -2.1 + 0.2 \cdot \frac{l_s}{\phi_l} & \rightarrow [l_s, \rho_t] \in \text{subdomain B} \end{cases} \quad (6.11)$$

where ε_{ls} is expressed in permille [‰]. From a geometrical viewpoint, equations (6.8) to (6.11) represent two planes in the $[l_s, \rho_t]$ space. The two planes of each system intersect on a line whose projection on the plane $\varepsilon_{ls} = 0$ is given by equation (6.7). The fit between the experimental and predicted values of ε_{ls} is displayed, for top- and bottom-casted splices, in Figure 6.8 (a) and (b) as 3D plots. Residual plots are instead given in Figure 6.8 (c) and (d). The predictive equation captures rather well the trend of the experimental data as well as the coupling between l_s and ρ_t . The effect of the different loading protocols shows up in the relatively large scatter observable at combinations $[l_s = 40\phi_l; \rho_t = 0.15\%]$ and $[l_s = 40\phi_l; \rho_t = 0.25\%]$. All values of experimental (ε_{ls}^{exp}) and predicted (ε_{ls}^{pred}) lap splice strain capacities are listed in Table 6.2 together with the associated model error v , defined as:

$$v = \left| 1 - \frac{\varepsilon_{ls}^{pred}}{\varepsilon_{ls}^{exp}} \right| \quad (6.12)$$

LAP-P13 and LAP-P10 are not included in the table since no lap failure was observed. The good match between the predicted and experimental ε_{ls} is confirmed by an average error of 20% and 26% for top- and bottom-casted splices, which drops to 13% and 20% if only TUs tested under the main loading protocol (C1) are considered.

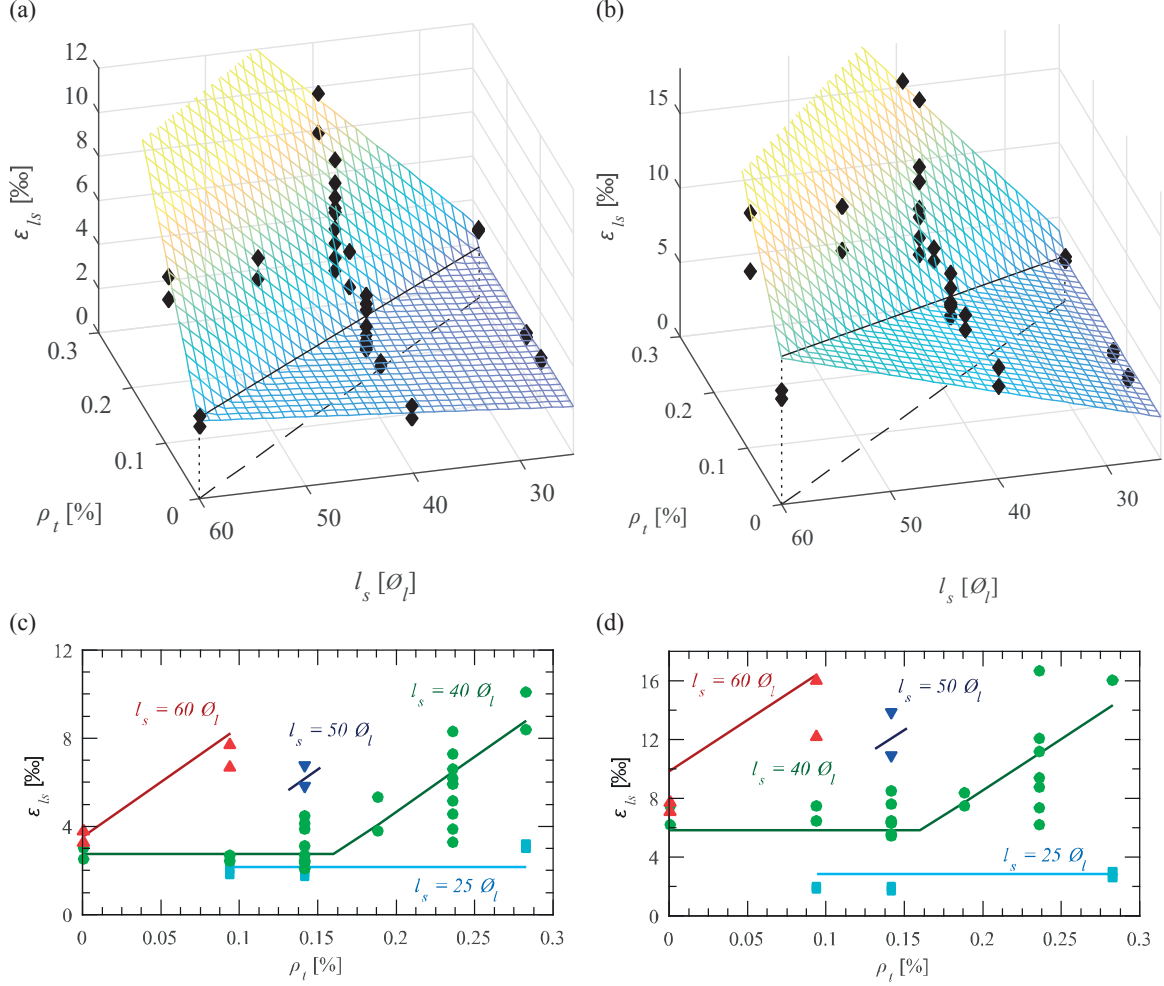


Figure 6.8: Predictive equation for ε_{ls} vs experimental results. Spatial representation for: (a) top-casted and (b) bottom-casted lap splices; Residual plot for: (c) top-casted and (d) bottom-casted lap splices.

Table 6.2: Experimental and predicted values of lap splice strain capacity, ϵ_{ls} .

TU	Top-casted splices					Bottom-casted splices				
	<i>Location</i> *	Δ_{proc} [mm]	ϵ_{ls}^{exp} [‰]	ϵ_{ls}^{pred} [‰]	<i>error</i> [%]	<i>Location</i>	Δ_{proc} [mm]	ϵ_{ls}^{exp} [‰]	ϵ_{ls}^{pred} [‰]	<i>error</i> [%]
LAP-P1	SE	4.68	8.36	8.74	4.5	NW	8.99	16.05	14.19	11.6
	NE	5.65	10.09		13.4	SW ^a	n/a	n/a		n/a
LAP-P2	NW	1.48	2.64	2.80	5.9	NE	4.19	7.49	5.90	21.2
	SW	1.37	2.45		14.5	SE	3.64	6.50		9.2
LAP-P3	NE	1.75	3.12	2.80	10.1	NW	4.22	7.54	5.90	21.7
	SE	2.52	4.50		37.8	SW ^a	n/a	n/a		n/a
LAP-P4	NW	1.07	3.06	2.20	28.0	NE	1.06	3.04	2.90	4.7
	SW	1.11	3.16		30.3	SE	0.93	2.67		8.6
LAP-P5	NE	6.45	7.67	8.11	5.7	NW	10.2	12.14	16.20	33.4
	SE	5.58	6.64		22.1	SW	13.5	16.07		0.8
LAP-P6	NW	1.35	2.41	2.80	16.1	NE ^a	n/a	n/a	5.90	n/a
	SW	1.36	2.43		15.3	SE	3.62	6.46		8.7
LAP-P7	NW	1.55	2.72	2.80	2.8	NE	3.54	6.32	5.90	6.7
	SW	1.30	2.31		21.1	SE	3.50	6.26		5.7
LAP-P8	NW	2.17	3.88	2.80	27.7	NE ^a	n/a	n/a	5.90	n/a
	SW	2.31	4.13		32.1	SE	4.74	8.46		30.3
LAP-P9	NW	1.19	2.13	2.80	31.8	NE	3.13	5.60	5.90	5.4
	SW	1.15	2.05		36.3	SE	3.06	5.46		8.0
LAP-P11	NE	0.68	1.93	2.20	14.1	NW	0.6	1.71	2.90	69.2
	SE	0.62	1.76		25.2	SW	0.7	2.00		45.0
LAP-P12	NE	0.72	2.04	2.20	7.7	NW	0.71	2.03	2.90	43.0
	SE	0.63	1.80		22.2	SW	0.64	1.84		57.4
LAP-P14	NE	6.44	7.67	3.60	53.0	NW	5.94	7.07	9.90	40.0
	SE	2.76	3.29		9.6	SW	3.17	3.77		162.3
LAP-P15	NE	1.69	3.02	2.80	7.2	NW	4.2	7.50	5.90	21.3
	SE	1.4	2.50		12.0	SW	3.45	6.17		4.4
LAP-P16	NE	2.99	5.33	4.02	24.5	NW	4.67	8.34	7.59	8.9
	SE	2.1	3.75		7.3	SW	4.19	7.48		1.5
LAP-P17	NE	3.32	5.92	6.38	7.8	NW	5.22	9.33	10.89	16.8
	SE	3.44	6.14		3.9	SW	4.88	8.71		25.0
LAP-P18	NW	4.73	6.76	6.07	10.2	NE	7.62	10.89	11.90	9.3
	SW	4.07	5.81		4.4	SE	9.7	13.86		14.2
LAP-P19	NE	2.15	3.83	6.38	66.6	NW	6.25	11.16	10.89	2.4
	SE	2.54	4.54		40.7	SW ^a	n/a	n/a		n/a
LAP-P20	NW	3.3	5.89	6.38	8.3	NE	6.76	12.08	10.89	9.8
	SW	2.88	5.14		24.1	SE ^a	NaN	n/a		n/a
LAP-P21	NE	4.66	8.32	6.38	23.3	NW	9.3	16.61	10.89	34.4
	SE	4.06	7.25		12.0	SW ^a	NaN	n/a		n/a
LAP-P22	NE	3.7	6.61	6.38	3.4	NW	3.5	6.25	10.89	74.3
	SE	1.825	3.26		95.8	SW	4.13	7.38		47.5
Error Avg: 20.9%						Error Avg: 26.1%				

*: Corner of the specimen where the considered splice was located during the testing

^a: Outlier data (see explanation in text)

6.6 Conclusions

Past experimental investigation on spliced RC members was mainly directed towards the characterization of their strength rather than their deformation capacity. The vast majority of tests included beams under monotonic loading with lap splices in the constant moment region typically designed to fail before yielding of the longitudinal reinforcement. No experimental studies focusing on the deformation capacity of lap splices, particularly beyond yielding, are currently available in the literature. This represents a limitation to the application of performance-based design and assessment philosophies, where displacements rather than forces are compared with the seismic demand.

This study analyses the results of an experimental programme on spliced RC members. The 24 test units represent the boundary elements of RC walls typical of both pre-seismic and code-compliant central European construction practice. They were tested under uniaxial tension-compression cyclic loading. The aim of the test series was to investigate the influence of lap splice length, confining reinforcement, and loading history on the deformation capacity of lap splices. A total of four lap splice lengths, from 25 to 60 times the longitudinal diameter, five confining reinforcement ratios, from 0 to 0.3%, and five loading protocols, 4 cyclic and one monotonic, were considered. Two reference test units with continuous reinforcement were also tested. Extensive instrumentation, including optical sensors glued directly on the spliced pairs or rebars, continuously monitored displacements of a comprehensive grid of points on the specimen faces.

The experimental data are used to derive an expression for predicting the deformation capacity of lap splices, which is defined as the average strain, at the onset of splice failure, owing exclusively to deformation contributions from the lapped region. Anchorage slip due to strain penetration or rebar slip from member locations outside the lap splice region were thus removed. With this approach, a strain limit for each of the four lap splices of each test unit was determined. The equation for the lap splice deformation capacity accounts for the confining reinforcement ratio, the lap splice length (as function of the bar diameter) and the position of the bar during casting. Larger deformation capacities were reached by bottom-casted splices with respect to top-casted, underlining the importance of concrete quality. Compared to these three parameters, the loading history was found to have only a minor influence and the data basis insufficient to quantify it. However, it was clear that larger imposed compression levels lead to a decrease in the splice failure strain.

The deformation capacity of lap splices increases with the splice length, irrespectively of the provided confining reinforcement. The effectiveness of the confining reinforcement depends instead on the lap splice length. Namely, the deformation capacity of short lap splices ($l_s = 25\phi_l$) is insensitive to the confining reinforcement ratio; on the other extreme, even very low levels of confining reinforcement are sufficient to increase the deformation capacity of long lap splices ($l_s = 60\phi_l$); for intermediate lap-splice lengths the splice deformation capacity increases only beyond a certain confining reinforcement ratio ($\rho_t > 0.15\%$). To account for this observation, two sets of equations are derived: the first one is applicable to long, well confined splices (referred to as subdomain A) and the second one to shorter, less confined or unconfined lap splices (subdomain B). Coefficients are determined for top- and bottom-casted splices yielding an average model error of about 20 and 26% for the former and the latter, respectively.

6.7 Acknowledgments

The financial support by the Swiss Federal Roads Office (FEDRO) to the project number AGB 2015/002, under which the present study is carried out, is acknowledged. Moreover, the author would like to thank Tiago Nico Pereira and Maria Katsidoniotaki for the precious help in the laboratory, and Dr. Michele Godio for the help in the design of some figures.

7 Mechanical Model for the Simulation of RC Wall Boundary Elements with Lap Splices

This Chapter presents a mechanical model to assess the behaviour of RC wall boundary elements with lap splices. The model predicts the crack width along the member as well as the steel and concrete stress/strain distributions. The ultimate displacement is derived from the lap splice strain equation presented in the previous chapter. The Chapter represents the pre-print version of the article:

D. Tarquini, J.P. Almeida, K. Beyer, 2019. “Extended tension chord model for boundary elements of RC walls accounting for anchorage slip and lap splices presence”, under submission.

Figures and tables formatting, reference-, section-, and equation- numbering were adapted to the style of this document. The mechanical model was developed by the first author under the supervision of the other two.

Abstract

This Chapter presents a mechanical model for the simulation of RC wall boundary elements with lap splices. It builds on the tension chord model from which it maintains the hypothesis on the material and bond slip relationships. The model is composed of an assembly of components, each one accounting for a different source of deformation. Namely: (i) an anchorage-slip element accounting for the strain penetration of the longitudinal reinforcement into the foundation; (ii) a basic tension chord element evaluating the member response outside the lap splice zone; and (iii) a lap splice element describing the behaviour within the lap splice region. For an imposed global displacement, the model provides the steel and concrete stress and strain distributions, the crack distribution and opening, and the global resisting axial force. For spliced members, the ultimate displacement is computed through a semi-empirical relationship providing the average lap splice strain at failure. Validation is carried out against a series of uniaxial cyclic tests on RC wall boundary elements featuring both continuous and spliced reinforcement; different lap splice lengths and confining reinforcement are considered. Overall, a good match is obtained between numerical and experimental results in terms of crack width, rebar strain distribution along the splices and ultimate displacement.

Keywords: Tension chord, Lap splices, Mechanical model, Crack width, Boundary element, RC walls.

List of symbols

A_c	Concrete area
A_s	Longitudinal reinforcement area
A_t	Total sectional area
E_c	Concrete elastic stiffness
E_s	Steel elastic stiffness
E_{sh}	Steel plastic stiffness
EA/L	Axial stiffness of the uncracked tension chord
f_{ct}	Concrete tensile strength
f'_c	Concrete compressive cylinder strength
f_y	Steel yield strength
f_u	Steel ultimate strength
h	Test units height
L_0	Total length of the RC wall boundary element (or of the tension chord)
l_0	Straight length of the anchored rebar
l_{ac}	Length required to develop the steel strain at crack (ϵ_{ac})
$l_{ac,p}$	Length required to develop the plastic portion of the steel strain at crack ($\epsilon_{ac} - \epsilon_y$)
l_{anc}	Anchorage length
l_b	Development length required to pass from a pre-crack to a post-crack steel stress state
l_p	Length required to develop the total rebar plastic strain ($\epsilon_{ult} - \epsilon_y$)
l_s	Lap splice length
l_y	Development length required to achieve rebar yielding
$l_{y,eqF}$	Distance between the yield point and the first point in which ϵ_{eqF} is reached

l_{ult}	Development length required to achieve rebar rupture
N	Imposed axial force
N_c	Concrete force
N_{cs}	Force required to attain crack stabilization
$N_{c,max}$	Maximum force carried by the concrete (at $srm/2$) with reinforcement remaining elastic
$N_{c,max,p}$	Maximum force carried by the concrete (at $srm/2$) with reinforcement that has yielded
N_s	Steel force
N_{fc}	Force required to attain first cracking
$N_{fc,lap}$	Force required to attain first cracking within the lap splice region
srm	Crack spacing
u_s	Steel displacement
u_c	Concrete displacement
w	Crack width
δ	Relative steel-concrete slip
Δ	Imposed axial displacement
Δ_{anc}	Slip of the anchored rebar at the interface
Δ_{comput}	Total displacement of the boundary element computed internally (integral of ϵ_s)
Δ_{ls}	Total displacement of a lap splice element
Δ_{TC}	Total displacement of a basic tension chord element
Δ_{tot}	Total imposed displacement to the RC wall boundary element
ϵ_{ac}	Steel strain at crack location
ϵ_c	Concrete strain
ϵ_{cs}	Minimum steel strain required to have crack stabilization
$\epsilon_{c,srm/2}$	Concrete strain at midway between two cracks ($srm/2$)
$\epsilon_{c,y}$	Steel strain at the point corresponding to steel yielding ($\epsilon_s = \epsilon_y$)
ϵ_{eqF}	Steel strain at the point where steel and concrete stresses are equal within the lap splice zone
ϵ_p	Steel plastic strain ($\epsilon_p = \epsilon_s - \epsilon_y$)
ϵ_s	Steel strain
$\epsilon_{srm/2}$	Steel strain at midway between two cracks ($srm/2$)
ϵ_y	Steel yield strain
ϵ_{ult}	Ultimate steel strain
\emptyset_l	Longitudinal rebar diameter
η	Relative error between numerical and experimental quantities
$\eta_{\Delta u}$	Relative error on the ultimate displacement of the RC wall boundary element
$\eta_{w,out}$	Relative error on the average crack width outside the lap splice region
$\eta_{w,lap}$	Relative error on the average crack width within the lap splice region
ρ_l	Longitudinal reinforcement ratio
ρ_t	Transverse reinforcement ratio
σ_c	Concrete stress
$\sigma_{c,max,p}$	Maximum concrete stress between cracks (at $srm/2$) when the steel is in a post-yield state
σ_s	Steel stress
$\sigma_{s,B}$	Concrete stress before crack
$\sigma_{s,C}$	Concrete stress after crack
τ_b	Bond stress
τ_{b0}	Elastic bond stress: the reinforcing steel is elastic ($\sigma_s < f_y$)
τ_{b1}	Plastic bond stress: the reinforcing steel has yielded ($\sigma_s > f_y$)
v_{num}	Generic numerical quantity
v_{exp}	Generic experimental quantity

7.1 Introduction

Experimental tests on RC walls (Chapter 2) have shown that the presence of lap splices may lead to a significant reduction of the member strength and ductility capacity. The behaviour of lap splices is influenced by several factors, among which lap splice length (l_s) and confining reinforcement play a dominant role. Namely, short and poorly confined lap splices located in regions where inelastic deformations are largest (i.e. plastic hinges) may induce failure of the RC wall prior to yielding of the longitudinal reinforcement. Longer and more confined lap splices may allow the wall to develop its flexural strength, however a decrease in the deformation capacity of the structural member is often still observed. Finally, long

and adequately confined lap splices will relocate the plastic hinge above the spliced zone, where buckling and rupture of the longitudinal rebars will occur. For the previous cases, damage typically starts at the wall edges (boundary elements) where the deformation demand is highest (as discussed in Chapter 3), which are also the regions first attaining failure.

Although several studies have been carried out in order to assess the strength of lap splices, significantly less research is available concerning their deformation capacity. In Chapter 6, based on an experimental programme on RC wall boundary elements, an expression to estimate the average strain at failure of lap splices as function of the lap splice length, confining reinforcement, and casting position was proposed. Such expression can be used to estimate the deformation capacity of RC wall boundary elements with lap splices.

Past mechanical models for lap splices mainly aimed at the characterization of their strength capacity [3,31]. To the author's knowledge, the analytical model proposed by Tastani et al. [35] is the only available in the literature describing the state of bond along spliced rebars, which can be used to predict the force-displacement response of lap splices. However, their approach is limited to steel elastic response and therefore only applicable to very short lap splice lengths.

The present work proposes a mechanical model for the simulation of RC wall boundary elements with lap splices. It represents an extension of the tension chord model [36], reviewed in Section 7.2, of which adopts the fundamental hypothesis on the constitutive materials (steel and concrete) and bond-slip laws. The model is constituted by an assembly of components, connected in series, discretizing the structural member. The three components, described in Section 7.3 are: (i) the anchorage-slip element; (ii) the basic tension chord element; and (iii) the lap splice element. The solution procedure allows to obtain for an imposed global displacement: the steel and concrete stress and strain distributions along the boundary element, crack location and width, and the total applied axial force. Moreover, the equation proposed in Chapter 6 for the lap splice deformation capacity can be directly employed in order to determine the failure of the spliced RC boundary element. The validation of the proposed model is carried out in Section 7.4 in terms of force-displacement, crack widths, and spliced rebar strains. Conclusions are drawn in Section 7.5.

7.2 Tension chord model

The tension chord model was originally developed as a simplified method for the determination of the rotation capacity of flexural plastic hinges in reinforced concrete girders [180,181]. Although it was successively extended to plane stress analysis problems [182,183] and to investigate the deformation capacity of prestressed and non-prestressed RC members [184], it was mainly applied to problems of cracking, tension stiffening, and minimum reinforcement in RC members subjected to uniaxial loading [36]. In the following paragraphs, the main assumptions and theoretical aspects underlying the tension chord model are briefly summarized.

Considering the tension chord element of Figure 7.1 (a), the equilibrium equations for an infinitesimal length dx of concrete and steel volumes can be written as (see Figure 7.1 (b)):

$$\frac{d\sigma_c}{dx} = -\frac{\tau_b \cdot \pi \cdot \phi_l}{A_t \cdot (1 - \rho_l)} \quad (7.1)$$

$$\frac{d\sigma_s}{dx} = \frac{4 \cdot \tau_b}{\phi_l} \quad (7.2)$$

where σ_c and σ_s are the concrete and steel stresses, τ_b is the bond stress, ϕ_l is the longitudinal rebar diameter, A_t is the gross sectional area, and $\rho_l = A_s/A_t$ is the longitudinal reinforcement ratio, where $A_s = \pi\phi_l^2/4$ is the steel area.

Strain-displacement relations provide $\varepsilon_s = du_s/dx$ and $\varepsilon_c = du_c/dx$, where u_s and u_c are the steel and concrete displacements, as shown Figure 7.1 (c), and ε_s and ε_c are the corresponding strains. From compatibility considerations (Figure 7.1 (c)), the steel-concrete slip δ can be expressed as the difference between the steel and concrete displacements:

$$\delta = u_s - u_c \quad (7.3)$$

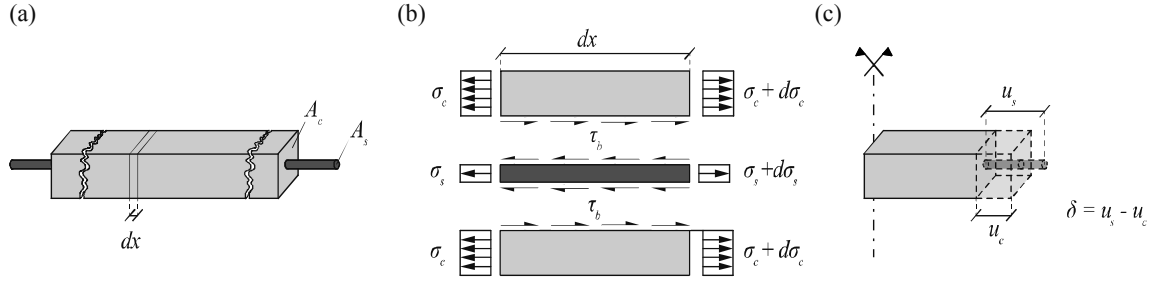


Figure 7.1: (a) Sketch of a basic tension chord element, i.e. the portion of tension chord between two cracks; (b) Concrete and steel equilibrium for an infinitesimal length dx ; (c) Compatibility requirements.

Assuming a linear and bilinear stress-strain law for the concrete and steel in tension (Figure 7.2 (a) and (b)), the following second order differential equation is obtained by combining the previous equations and using the chain rule of differentiation:

$$\frac{d^2 \delta}{dx^2} = \frac{4 \cdot \tau_b}{d\sigma_s/dx \cdot \phi_l} + \frac{\tau_b \cdot \pi \cdot \phi_l}{A_t \cdot E_c \cdot (1 - \rho_l)} \quad (7.4)$$

where $d\sigma_s/dx$ and E_c are the steel and concrete tangent stiffness. Before steel yielding $d\sigma_s/dx = E_s$, while after yielding $d\sigma_s/dx = E_{sh}$, which stands for the post-yield steel stiffness.

Equation (7.4) can be integrated if the bond-slip (τ_b - δ) relationship is known. In the tension chord model, the latter is assumed to be stepped, rigid-perfectly-plastic (Figure 7.2 (c)): the bond stress is constant (τ_{b0}) up to reinforcement yielding, after which it halves ($\tau_{bl} = \tau_{b0}/2$). This assumption for the τ_b - δ law is particularly convenient as it allows the uncoupling of the bond stress from the slip of the reinforcing bar. In the portion between two consecutive cracks of the tension chord (herein referred as basic tension chord element), the steel stress distribution can thus be derived from the equilibrium conditions alone, i.e. without the need to resort to complex numerical integration of the above second order differential equation. As a consequence, the concrete stress, concrete strain, and steel strain distributions can also be obtained, allowing the determination of the crack width and basic tension chord elongation. In the present work, as suggested by Marti et al. [36], it is assumed $\tau_{b0} = 2f_{ct}$ and $\tau_{bl} = f_{ct}$, where f_{ct} is the tensile concrete strength. The latter can be computed as a fraction of the concrete cylinder strength f'_c ; the calculations presented herein assume $f_{ct} = 0.3 \cdot f'_c{}^{2/3}$ [180,181].

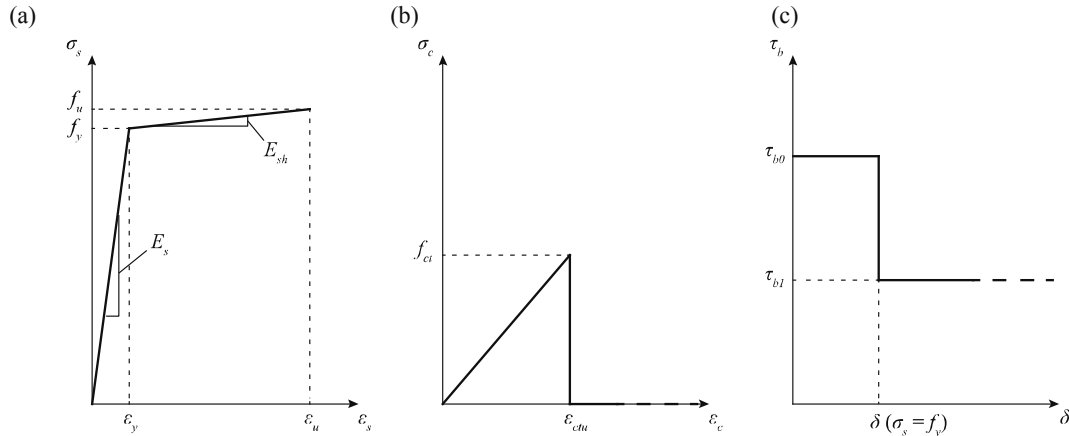


Figure 7.2: Constitutive relations employed in the extended tension chord model: (a) Bilinear steel stress-strain law; (b) Concrete tensile stress-strain behaviour; (c) Steel-concrete bond-slip relationship.

7.2.1 Evolution of deformation in a tension chord subjected to increasing displacement

Consider a tension chord of total length L_0 (Figure 7.3 (a)) subjected to an increasing imposed tensile displacement Δ . A qualitative force-displacement response is depicted in Figure 7.3 (b). Before first cracking, no relative slip occurs between the longitudinal steel and concrete, which thus share the same state of deformation, corresponding to state A in Figure 7.3. The equivalent member axial stiffness is computed as the sum of the stiffness of the two materials:

$$\frac{(EA)_{equiv.}}{L_0} = \frac{(E_c \cdot A_c + E_s \cdot A_s)}{L_0} \quad (7.5)$$

where $A_c = A_t - A_s$ is the concrete area. The first crack occurs when the concrete reaches the tensile strength f_{ct} (state B in Figure 7.3), which takes place at the following applied force:

$$N_{fc} = \frac{(EA)_{equiv.} \cdot f_{ct}}{E_c} \quad (7.6)$$

At the first forming crack the concrete stress and strain are null (state C in Figure 7.3). All the applied force is taken by the longitudinal reinforcement and the steel stress passes from a pre-crack to a post-crack stress state, respectively $\sigma_{s,B}$ and $\sigma_{s,C}$. Assuming that the rebar remains elastic, which is typically the case for common ranges of longitudinal reinforcement ratios, they are computed as [185]:

$$\sigma_{s,B} = \frac{E_s \cdot f_{ct}}{E_c} \quad (7.7)$$

$$\sigma_{s,C} = \frac{N_{fc}}{A_s} \quad (7.8)$$

For larger imposed deformations, cracks will open one after the other along the tension chord (state D in Figure 7.3 refers to the opening of the second crack) up until crack stabilization. The latter corresponds to the situation in which an increase in the imposed deformation results in simple opening of existing cracks; i.e. no new cracks are forming as shown by states E, F and G in Figure 7.3. The crack distance srn is bounded by $l_b < srn < 2l_b$, where l_b is the development length required to transfer, through bond action, the difference between steel forces in the pre- and post-crack states (see Figure 7.3 (a)):

$$l_b = \frac{\phi_l \cdot (\sigma_{s,C} - \sigma_{s,B})}{4 \cdot \tau_{b0}} = \frac{\phi_l \cdot f_{ct} \cdot (1 - \rho_l)}{4 \cdot \rho_l \cdot \tau_{b0}} \quad (7.9)$$

If two contiguous cracks open at a distance greater than $2l_b$, a region exists between these cracks where the concrete stress is equal to the material tensile strength f_{ct} , in which the formation of further cracks is still possible. On the other hand, if $srn < l_b$ the concrete stress in-between cracks is smaller than f_{ct} , preventing the formation of new cracks. Although several expressions have been proposed in the literature to evaluate the average crack spacing srn [18,89,186,187], in this Chapter the intermediate value of $srn = 1.5 \cdot l_b$ is assumed.

The maximum force carried by the concrete, $N_{c,max}$, depends on the value of srn and can be computed as:

$$N_{c,max} = \frac{srn}{2} \cdot \tau_{b0} \cdot \phi_l \cdot \pi \quad (7.10)$$

In between two cracks, the steel and concrete stress and strain distributions can be obtained by solving analytically equation (7.4). The crack width w is then calculated as the integral along srn of the difference between the steel and concrete strains—equation (7.11)—while the integral of the steel strains gives the total elongation of the basic tension chord—equation (7.12).

$$w = \int_{-\frac{srn}{2}}^{\frac{srn}{2}} \varepsilon_s - \varepsilon_c \, dx \quad (7.11)$$

$$\Delta_{TC} = \int_{-\frac{srn}{2}}^{\frac{srn}{2}} \varepsilon_s \, dx \quad (7.12)$$

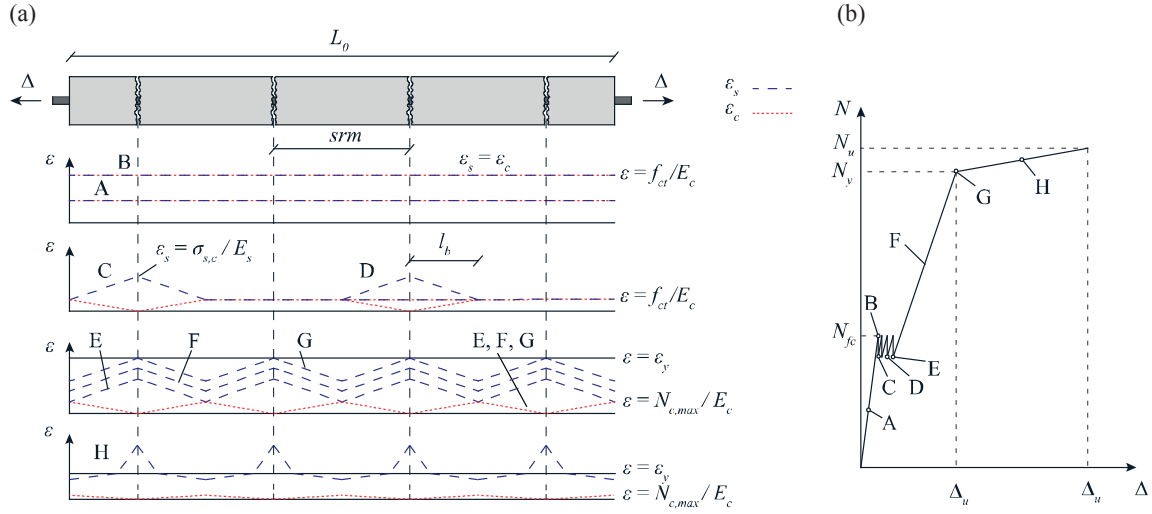


Figure 7.3 (adapted from [185]) : Tension chord subjected to increasing imposed displacements: (a) Force-displacement response; (b) Qualitative steel and concrete strain distributions.

For the assumed material and bond-slip relationships, in-between cracks the steel and concrete stress and strain distributions remain linear up to yielding of the longitudinal reinforcement (state G in Figure 7.3). After yielding, the reduction of the steel tangent stiffness (from E_s to E_{sh}) and bond stress (from τ_{b0} to τ_{b1}) causes the shift from linear to bilinear stress and strain distributions, as represented in state H of Figure 7.3 (a).

7.3 Mechanical model for boundary elements of RC walls with lap splices

The mechanical model proposed in the following is developed to simulate the response of RC wall boundary elements with lap splices subjected to uniaxial tensile loading. It is an extension of the classical tension chord model [36] described in the previous section, with which it shares the assumptions on the material and bond-slip relationships. The basic tension chord element is used in series with an anchorage-slip element and a newly developed lap-splice element; they are described separately in the next three subsections 7.3.1 to 7.3.3. Subsection 7.3.4 deals instead with the iterative procedure employed to obtain local deformations and forces for an imposed global displacement.

7.3.1 Anchorage-slip element

The deformation of RC walls due to strain penetration of the anchored reinforcement in the foundation can represent an important contribution to the total member displacement [115,188]. The anchorage-slip element presented herein allows to estimate the anchorage-slip displacement Δ_{anc} as well as to determine the steel and concrete stress and strain distributions along the anchorage length l_{anc} . The input parameter is the steel strain at the loaded end, ϵ_{ac} , where the subscript *ac* stands for ‘at crack’ as it corresponds to the location of the RC wall-foundation interface crack. Under the hypothesis that concrete strains are null within the foundation, Δ_{anc} can be computed as:

$$\Delta_{anc} = \int_{l_{anc}} \epsilon_s dx \quad (7.13)$$

Building on the material and bond assumptions described in the previous section, analytical expressions for Δ_{anc} can be derived, which depend on the anchorage type (straight or bent rebars), anchorage length, and imposed free-end deformation ϵ_{ac} . For a review of the different cases, the reader is referred to Feng and Xu [189], where a full description of the equations for the calculation of Δ_{anc} can be found. The current work only considers the anchorage configuration of the test units used to carry out the model validation in Section 7.4; i.e., rebars bent inside the foundation and an anchorage length l_{anc} longer than the development length required to achieve the ultimate steel stress (l_{ult}). For bent rebars, l_{anc} can be evaluated as function of the straight portion of the anchored length l_0 [190]:

$$l_{anc} = l_0 + 5 \cdot \phi_l \quad (7.14)$$

while l_{ult} , composed by elastic and plastic components (l_y and l_p respectively), can be computed as:

$$l_{ult} = l_y + l_p = \frac{f_y \cdot \phi_l}{4 \cdot \tau_{b0}} + \frac{(f_u - f_y) \cdot \phi_l}{4 \cdot \tau_{b1}} \quad (7.15)$$

where f_y and f_u are the steel yield and ultimate strength. The analytical expression to calculate the slip Δ_{anc} in case of $l_{anc} > l_{ult}$ is given by the following equation:

$$\Delta_{anc} = \begin{cases} \frac{\varepsilon_{ac}}{2} \cdot l_{ac} & \text{for } \varepsilon_{ac} < \varepsilon_y \\ \frac{\varepsilon_y}{2} \cdot l_y + \frac{\varepsilon_y + \varepsilon_{ac}}{2} \cdot (l_{ac} - l_y) & \text{for } \varepsilon_{ac} > \varepsilon_y \end{cases} \quad (7.16)$$

where l_{ac} is the development rebar length required to attain the strain at crack ε_{ac} , and is computed as:

$$l_{ac} = \begin{cases} \frac{\varepsilon_{ac} \cdot E_s \cdot \phi_l}{4 \cdot \tau_{b0}} & \text{for } \varepsilon_{ac} < \varepsilon_y \\ \frac{f_y \cdot \phi_l}{4 \cdot \tau_{b0}} + \frac{(\varepsilon_{ac} - \varepsilon_y) \cdot E_{sh} \cdot \phi_l}{4 \cdot \tau_{b1}} & \text{for } \varepsilon_{ac} > \varepsilon_y \end{cases} \quad (7.17)$$

The previous expressions underline that pre- and post-yielding cases are distinguished; for each situation, a sketch of the qualitative steel stress and strain distributions is included in Figure 7.4.

The upper and lower domain boundaries of applicability for equations (7.16) and (7.17) are defined by the minimum steel strain required to have crack stabilization (ε_{cs} , see subsection 7.3.4 for its calculation) and the ultimate steel strain (ε_{ult}), respectively. In fact, for $\varepsilon_{ac} < \varepsilon_{cs}$ the RC wall boundary element remains uncracked, implying $\Delta_{anc} = 0$. On the other hand, steel rupture will occur for $\varepsilon_{ac} > \varepsilon_{ult}$, thus resulting in the total loss of the member axial load capacity ($N = 0$).

7.3.2 Basic tension chord element

As introduced in the previous section, the basic tension chord element represents the portion of a tension chord enclosed between two consecutive cracks (spaced srm apart). For an arbitrary value of $\varepsilon_{cs} < \varepsilon_{ac} < \varepsilon_{ult}$, where ε_{ac} is the steel strain at crack, the steel and concrete stress and strain distributions can be determined by equilibrium considerations; as a result, the crack width as well as the total chord elongation are obtained by applying equations (7.11) and (7.12), respectively. Three cases can be distinguished: (i) $\varepsilon_{ac} < \varepsilon_y$; (ii) $\varepsilon_{ac} > \varepsilon_y$ and $l_{ac,p} < srm/2$; and (iii) $\varepsilon_{ac} > \varepsilon_y$ and $l_{ac,p} > srm/2$, where $l_{ac,p}$ is the length required to develop the plastic strain $\varepsilon_p = \varepsilon_{ac} - \varepsilon_y$, computed as:

$$l_{ac,p} = \frac{A_s \cdot E_{sh} \cdot (\varepsilon_{ac} - \varepsilon_y)}{\tau_{b1} \cdot \pi \cdot \phi_l} \quad (7.18)$$

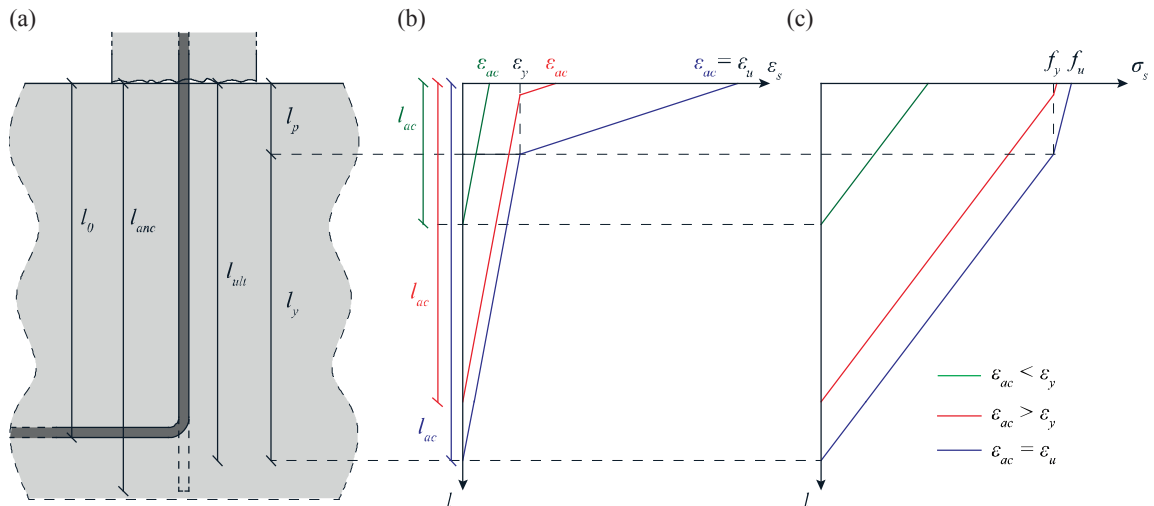


Figure 7.4: Anchorage-slip element for bent anchored bars with $l_{anc} > l_{ult}$: (a) Sketch of the anchorage detail; (b) Qualitative steel strain profiles; (c) Qualitative steel stress profiles.

For each scenario, the material stress and strain distribution is depicted in Figure 7.5, while the expression for calculating the basic chord elongation Δ_{TC} and the crack width w are provided by equations (7.19) and (7.20), obtained by solving equations (7.11) and (7.12):

$$\Delta_{TC} = \begin{cases} \left(\varepsilon_{ac} - \frac{N_{c,max}}{2 \cdot A_s \cdot E_s} \right) \cdot srm & \text{for case (i)} \\ \varepsilon_{ac} \cdot l_{ac,p} + \varepsilon_y \cdot \frac{srm}{2} + \frac{\varepsilon_{srm}}{2} \cdot \left(\frac{srm}{2} - l_{ac,p} \right) & \text{for case (ii)} \\ \left(\varepsilon_{ac} - \frac{N_{c,max,p}}{2 \cdot A_s \cdot E_{sh}} \right) \cdot srm & \text{for case (iii)} \end{cases} \quad (7.19)$$

$$w = \begin{cases} \left(\varepsilon_{ac} - \frac{N_{c,max}}{2 \cdot A_s \cdot E_s} - \frac{N_{c,max}}{2 \cdot A_c \cdot E_c} \right) \cdot srm & \text{for case (i)} \\ \Delta_{TC}^{case(ii)} - \varepsilon_{c,y} \cdot \frac{srm}{2} - \varepsilon_{c,srm/2} \cdot \left(\frac{srm}{2} - l_{ac,p} \right) & \text{for case (ii)} \\ \left(\varepsilon_{ac} - \frac{N_{c,max,p}}{2 \cdot A_s \cdot E_{sh}} - \frac{N_{c,max,p}}{2 \cdot A_c \cdot E_c} \right) \cdot srm & \text{for case (iii)} \end{cases} \quad (7.20)$$

where $\varepsilon_{srm/2}$ and $\varepsilon_{c,srm/2}$ are the steel and concrete strains evaluated at $srm/2$, equations (7.21) and (7.22); $\varepsilon_{c,y}$ is the concrete strain in correspondence of the steel yield point, equation (7.23); and $N_{c,max,p}$ is the maximum concrete force occurring at $srm/2$ when the steel is in the post-yield state, equation (7.24).

$$\varepsilon_{srm/2} = \varepsilon_y - \frac{\tau_{b0} \cdot \pi \cdot \phi_l \cdot \left(\frac{srm}{2} - l_{ac,p} \right)}{A_s \cdot E_s} \quad (7.21)$$

$$\varepsilon_{c,srm/2} = \varepsilon_{c,y} + \frac{\tau_{b0} \cdot \pi \cdot \phi_l \cdot \left(\frac{srm}{2} - l_{ac,p} \right)}{A_c \cdot E_c} \quad (7.22)$$

$$\varepsilon_{c,y} = \frac{\tau_{b1} \cdot \pi \cdot \phi_l \cdot l_{ac,p}}{A_c \cdot E_c} \quad (7.23)$$

$$N_{c,max,p} = \sigma_{c,max,p} \cdot A_c = \frac{srm}{2} \cdot \tau_{b1} \cdot \phi_l \cdot \pi \quad (7.24)$$

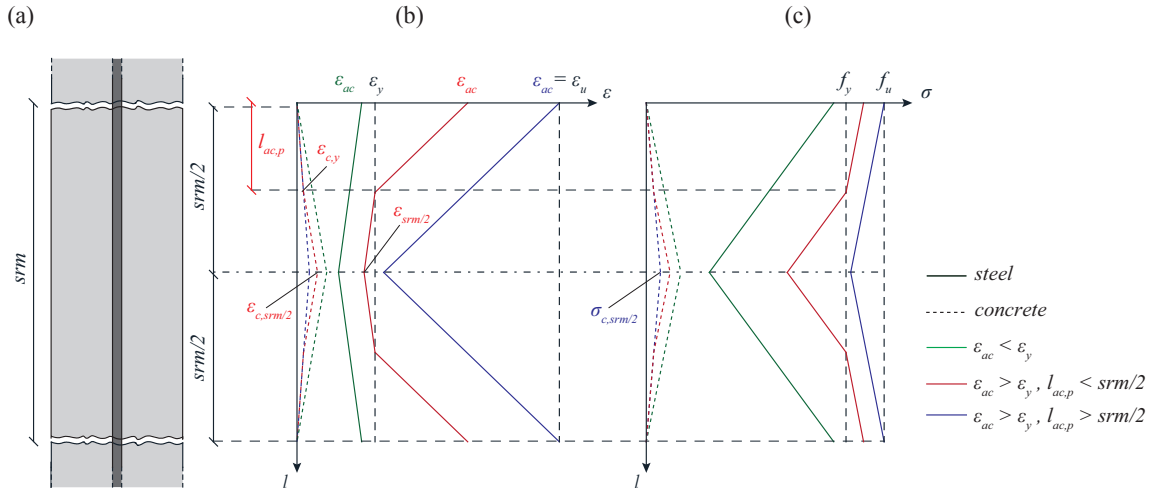


Figure 7.5: Basic tension chord element: (a) Sketch; (b) Qualitative steel and concrete strain profile; (c) Qualitative steel and concrete stress profile.

7.3.3 Lap-splice element

As discussed in Chapter 2 and 3, the strength and/or deformation capacity of RC walls may be sensibly reduced by the presence of poorly designed lap splices above the foundation level, where the seismic demand is maximum. Adequate detailing, i.e. providing appropriate lap-splice length and confining reinforcement, is crucial in order to attain the desired member ductility. The component presented in this subsection allows to account for the presence of lap splices in RC wall boundary elements and to estimate: (i) the steel strain distribution in the pair of spliced rebars; (ii) the crack width along the lap-splice length as well as the width contribution to the splice-end cracks originating from lap-splice deformation; (iii) the total lap-splice displacement and the failure point.

This component builds on the same hypothesis regarding material and bond behaviour assumed for the tension chord model described in Section 7.2. Once crack stabilization is attained along the lap-splice length (Figure 7.6 (a)), the resisting force is transferred from the anchored to the free end (unloaded) rebar through concrete bond. It is herein assumed that the concrete remains undeformed while transferring the force from one bar to another. Although the applied tensile load is partly resisted by the concrete, causing the formation of splitting cracks, the previous simplification represents a reasonable approximation up to the point of lap splice failure. In fact, as pointed out by Tastani et al. [35], neglecting the concrete strain contribution does not result in large model errors since the maximum tensile strain carried by normal strength-concrete up to tensile failure is less than 5% of the yield strain of the reinforcement. Nevertheless, this hypothesis implies a slight overestimation of the crack width as the latter is computed from the steel deformations alone, i.e. the tension stiffening effect due to concrete strains is ignored. A qualitative sketch of the steel stress and strain distribution for the couple of spliced rebars is represented in Figure 7.6 (b) and (c) for two different levels of strain at the interface crack ε_{ac} (pre- and post-yielding). From the top interface crack downwards, the steel stress is progressively transferred from the top-anchored to the bottom-anchored rebar. The stress transfer stops when equilibrium is reached with the two rebars attaining the same force level. An analogous if mirrored physical phenomenon occurs on the bottom half of the lap splice.

The crack spacing s_{rm} within the lap-splice zone is assumed the same as outside, which is supported by experimental observations. The width of the cracks located within the lap-splice region (for instance $w_{lap,1}$ and $w_{lap,2}$ in Figure 7.6 (a)) is computed by integrating, along the corresponding influence length (e.g. l_1 and l_2 in Figure 7.6 (a)), the envelope (i.e., the maximum) of the strains along the spliced rebars. For a given crack, the influence length is taken as the sum of the two half distances from the contiguous upper and lower cracks. Similarly, the integral of the strain envelopes along l_{top} and l_{bot} (see Figure 7.6 (a)) provide the portion of the top and bottom interface crack widths due to deformations originating within the lap splice region. The total width of these cracks is then obtained by summing up the contributions due to deformations occurring within and outside the lap splice region (the next subsection provides further details). The steel strain envelope is considered for the calculation of the crack width because, along the lapped zone, the spliced rebars are in general not equally stressed; the more stressed bar will induce a larger crack width (i.e., a larger strain integral) which, due to compatibility requirements, the less stressed rebar is forced to accommodate [35]. Closed-form expressions for the calculation of the splice-internal crack widths and the contribution to the interface cracks given by deformations within the lap-splice region are relatively complicated to obtain as they depend on a large number of variables. Therefore, in the present study these widths are computed numerically.

The total lap splice displacement (Δ_{ls}) is calculated as the integral of the steel strain envelopes along the entire lap splice length: the expressions for both the elastic ($\varepsilon_{ac} < \varepsilon_y$) and post-yield ($\varepsilon_{ac} > \varepsilon_y$) cases are as follows:

$$\Delta_{ls} = \begin{cases} \frac{1}{4} \varepsilon_{ac} (2 \cdot l_s - l_{ac}) & \varepsilon_{ac} < \varepsilon_y \\ (\varepsilon_{ac} - \varepsilon_y) \cdot l_{ac,p} + (\varepsilon_y + \varepsilon_{eqF}) \cdot l_{y,eqF} + 2 \cdot \varepsilon_{eqF} \cdot \left(\frac{l_s}{2} - l_{ac,p} - l_{y,eqF} \right) & \varepsilon_{ac} > \varepsilon_y \end{cases} \quad (7.25)$$

where ε_{eqF} , equation (7.26), is the strain of both top and bottom anchored rebars when they share the same force, and $l_{y,eqF}$ is the distance between the yield point and the first point in which ε_{eqF} is reached, see Figure 7.6 (b).

$$\varepsilon_{eqF} = \frac{E_{sh} \cdot (\varepsilon_{ac} - \varepsilon_y) + E_s \cdot \varepsilon_y}{2 \cdot E_s} \quad (7.26)$$

$$l_{y,eqF} = \frac{A_s \cdot (E_s \cdot \varepsilon_y - E_{sh} \cdot (\varepsilon_{ac} - \varepsilon_y))}{2 \cdot \tau_{b0} \cdot \pi \cdot \phi_l} \quad (7.27)$$

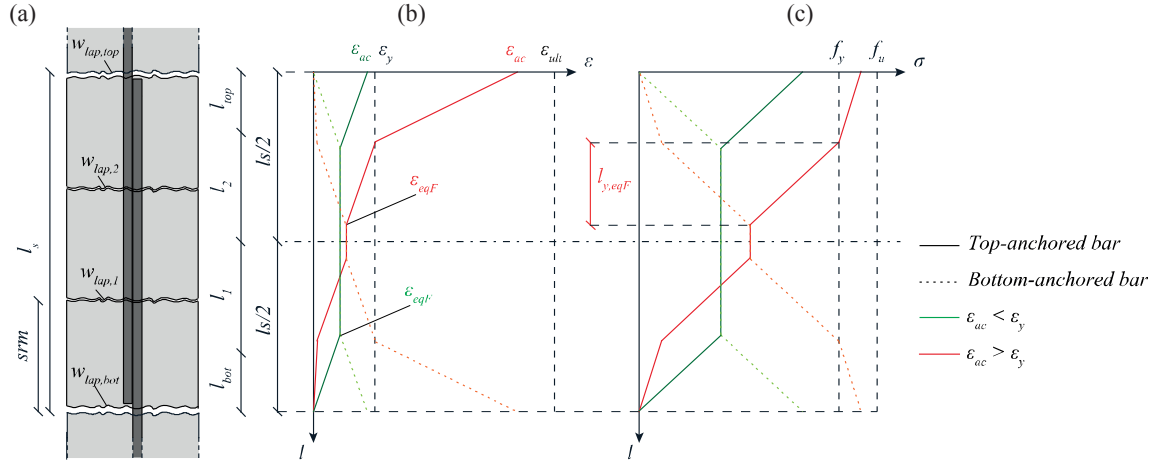


Figure 7.6: Lap-splice element: (a) Sketch; (b) Qualitative steel strain profile; (c) Qualitative steel stress profile.

Based on experimental data on uniaxial cyclic tests on spliced RC members, an expression for the average strain at lap splices failure (ϵ_{ls}) was determined in Chapter 6—equations (6.8) to (6.11). The latter, which depends on lap splice length, amount of confinement reinforcement and casting position, is used in the proposed model to define the deformation capacity of lap splices. The ultimate lap-splice displacement ($\Delta_{ls,ult}$) is therefore straightforwardly obtained by multiplying ϵ_{ls} by the nominal lap-splice length l_s ; failure of the lap-splice element is assumed to take place at this point, with the complete loss of the axial load capacity. It is worth noticing that the above-mentioned failure criterion typically precedes the attainment of non-zero stress values at the lap splice free ends ($l_{ac} > l_s$). In such a case, pull-out rather than lap splice failure might be expected.

7.3.4 Model implementation: iterative procedure and failure criteria

The components described in the three previous subsections can be connected in series in order to simulate the response of RC wall boundary elements with lap splices subjected to increasing tensile loading. Figure 7.7 (a) illustrates the assembly of an anchorage, lap splice, and several basic tension chord elements, to which a global top displacement Δ_{tot} is imposed. Given the steel and concrete material properties, outputs of the model are the resisting axial force, crack spacing and widths (inside and outside the lap-splice region), steel and concrete strain distributions, and the ultimate displacement. Iterations are required to solve the nonlinear problem, unless global forces are imposed, wherein a straightforward non-iterative solution is available. A flowchart depicting the steps involved in the iterative procedure is illustrated in Figure 7.7 (b) and discussed in the following paragraph.

Up to first cracking, perfect bond exists between steel and concrete, which therefore share the same strain:

$$\epsilon_s = \epsilon_c = \frac{\Delta_{tot}}{L_0} \quad (7.28)$$

where L_0 represents the total length of the boundary element (see Figure 7.7 (a)). First cracking occurs at a displacement level $\Delta_{tot} = (f_{ct}/E_c) \cdot L_0$ and at a force level N_{fc} given by equation (7.6). Between first cracking and crack stabilization (identified by the subscript 'cs'), cracks open one after the other with the axial force that is assumed constant and equal to $N = N_{fc}$. In reality, small force drops occur due to the stiffness reduction caused by each crack opening, as shown in Figure 7.3. The displacement at crack stabilization Δ_{cs} is identified by a steel strain at crack equal to:

$$\epsilon_{cs} = \frac{N_{fc}}{E_s \cdot A_s} \quad (7.29)$$

The above does not apply to cracks located within the lap-splice region where the steel area contributing to the axial stiffness is double. Such cracks open at an imposed axial force $N_{fc,lap} > N_{fc}$; however, for common longitudinal reinforcement ratios the difference between the two forces is relatively small and can be neglected (e.g., for the case-study of section 7.4, $N_{fc,lap} = 140$ kN while $N_{fc} = 130$ kN).

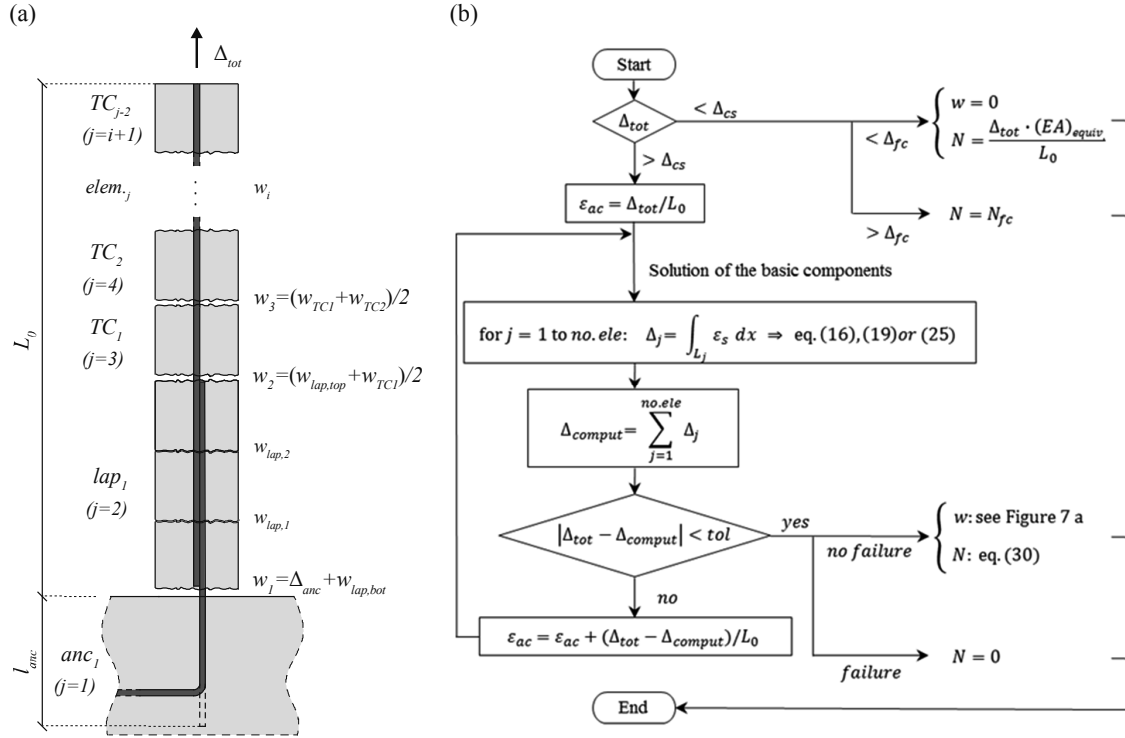


Figure 7.7: RC boundary element model: (a) Assembly of the components for a RC member featuring lap splice, anchorage, and multiple basic ten-sion chord (TCi) elements; (b) Flowchart of the iterative procedure.

For imposed displacements larger than Δ_{cs} , each component of the boundary element (anchorage, lap splice, and basic tension chord) can be solved separately for a given strain at crack ε_{ac} . This quantity is initially estimated as $\varepsilon_{ac} = \Delta_{tot}/L_0$ which is then used to compute the resulting total boundary element displacement. The latter, identified as Δ_{comput} , is obtained by summing up the resulting displacement of each element, evaluated through equations (7.16), (7.19), and (7.25). The computed displacement Δ_{comput} is then compared to the externally imposed Δ_{tot} : if their difference is smaller than a user-defined tolerance (in the following applications $tol = \Delta_{tot}/1000$ is used), convergence is attained, otherwise an updated estimate of ε_{ac} is calculated (see Figure 7.7 (b)) and a new iteration is performed. At convergence, the steel/concrete stress/strain distributions can be retrieved from each element, as well as the crack widths (see Figure 7.7 (a)). Finally, the total imposed axial force is calculated as:

$$\begin{cases} N = \varepsilon_{ac} \cdot E_s \cdot A_s & \varepsilon_{ac} < \varepsilon_y \\ N = \varepsilon_y \cdot E_s \cdot A_s + (\varepsilon_{ac} - \varepsilon_y) \cdot E_{sh} \cdot A_s & \varepsilon_{ac} > \varepsilon_y \end{cases} \quad (7.30)$$

Without a specific criterion defining the failure of the boundary element, the procedure above can be performed for any imposed displacement Δ_{tot} up to a strain at crack equal to the ultimate steel strain ($\varepsilon_{ac} = \varepsilon_{ult}$). The latter represents a reasonable failure criterion only in case of continuous reinforcement and monotonic tensile loading. In case of cyclic loading and continuous reinforcement, the ultimate steel strain will result in an overestimation of the member displacement capacity and a value of $\varepsilon_s = 0.6 \varepsilon_{ult}$ can be used [69]. In case inadequately detailed lap splices are also present, the attainment of the aforementioned ultimate displacement of the lap splice element, $\Delta_{ls,ult}$, signals the member failure, which consists in the total and sudden loss of the axial load carrying capacity.

7.4 Validation of the proposed model

Results from a recently concluded experimental programme on RC wall boundary elements with lap splices (described in the previous two Chapters) are used to validate the proposed mechanical model. The 24 test units (TUs), of which 22 with lap splices and two reference units with continuous reinforcement, shared the same geometry, illustrated in Figure 7.8. They differed in terms of lap-splice length, confining reinforcement and loading history, which constituted the variable parameters of the test programme. The testing machine was a uniaxial press with a fixed top and a mobile bottom actuator to which the TUs were connected by means of rigid steel profiles. The instrumentation included load-cells as well as

LVDTs and LED grids to evaluate global and local displacement values. Namely, LEDs were also directly glued on the pair of spliced rebars, allowing a direct monitoring of rebar strains.

The same reinforcing steel was used for all the TUs. Although different castings were performed, the concrete showed a limited variability in the cylinder compressive strength f'_c . All details regarding material properties can be found in Chapter 5; Table 7.1 reports the material parameters relevant to the mechanical model that were used to run the analyses shown in the next two subsections.

7.4.1 TU with continuous reinforcement

The mechanical model is compared in this section with the test unit LAP-C1 with continuous longitudinal reinforcement and a confinement reinforcement ratio $\rho_t \approx 0.3\%$. The experimental vs numerical force-displacement curves are shown in Figure 7.9 a with grey and black solid lines, respectively. The applied axial force N is reported on the vertical axis while the total vertical displacement Δ is given on the horizontal axis. A black dashed line indicates the experimental specimen failure, defined as the displacement at which a loss of axial load capacity of about 20% was observed. For LAP-C1, this occurred in compression, due to core concrete crushing. As it can be observed, the numerical pushover curve reproduces satisfactorily the tensile experimental backbone curve. Namely, the stiffness evolution as well as the maximum force are well predicted. Due to the failure in compression of the specimen, no failure criterion was defined for the mechanical model, which thus does not show decay in strength. Three coloured dots identify post-cracking ($\Delta = 3\text{mm}$), plastic ($\Delta = 15\text{mm}$), and pre-failure ($\Delta = 35\text{mm}$) states, which are used in the following plots to compare local-level quantities.

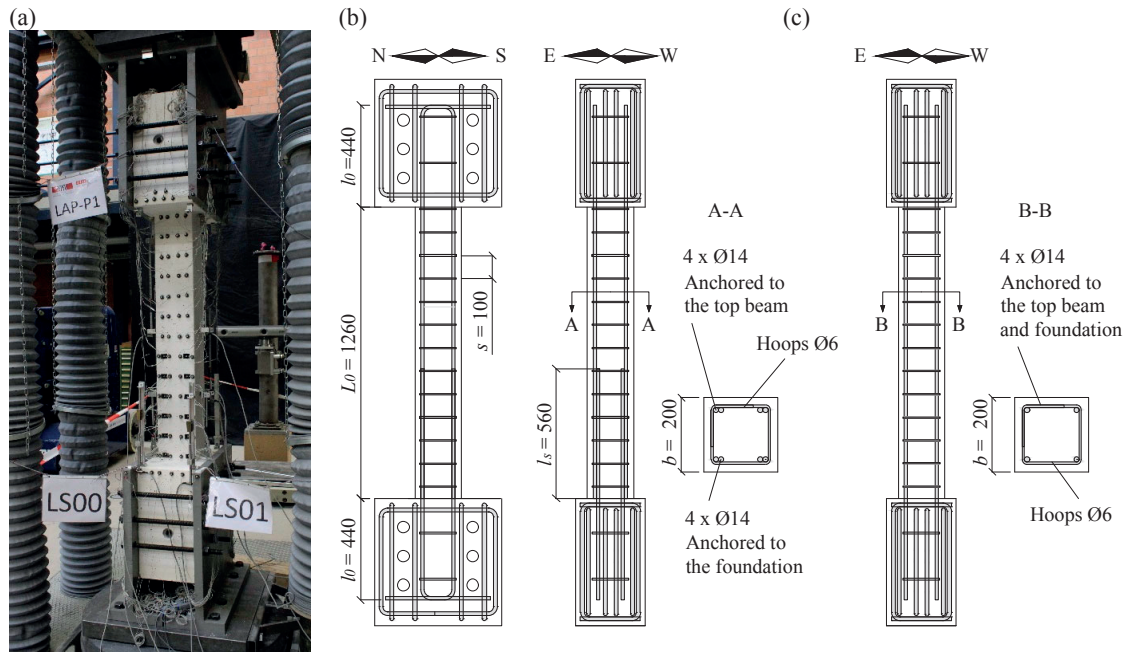


Figure 7.8: Experimental programme used for model validation ([193], i.e. Chapter 5): (a) Photo of LAP-P1 before the test; Reinforcement layout of (b) TU with lap splices (LAP-P1); and (c) TU with continuous reinforcement (LAP-C1).

Table 7.1: Material parameters used in the simulation

Material property	f'_c [MPa]	f_y [MPa]	f_u [MPa]	E_s [MPa]	E_{sh} [MPa]	ϵ_{ult} [%]
	32	510	635	204000	1430	9

Simulated steel and concrete strain distributions along the boundary element are depicted in Figure 7.9 (b) with solid and dashed lines, respectively. Steel strains were not directly measured in TUs with continuous reinforcement and therefore a comparison between numerical and experimental data is not possible. It can be observed that steel strains are maximum at crack locations, minimum midway between cracks, and increase from the post-cracked state A to the pre-failure state C. A similar trend can be observed for the steel force distribution (N_s) illustrated in Figure 7.9 (c); on the other hand, concrete forces (N_c) show an opposite behaviour with $N_c = 0$ at crack and $N_c = N_{c,max}$ midway between cracks. Furthermore, due to the reduction in bond strength after the occurrence of reinforcement yielding, N_c decreases with the spread of inelasticity. It is worth noticing that, due to equilibrium requirements, the sum of the concrete and steel forces at all coordinates along the boundary element is constant and equal to the externally applied axial force.

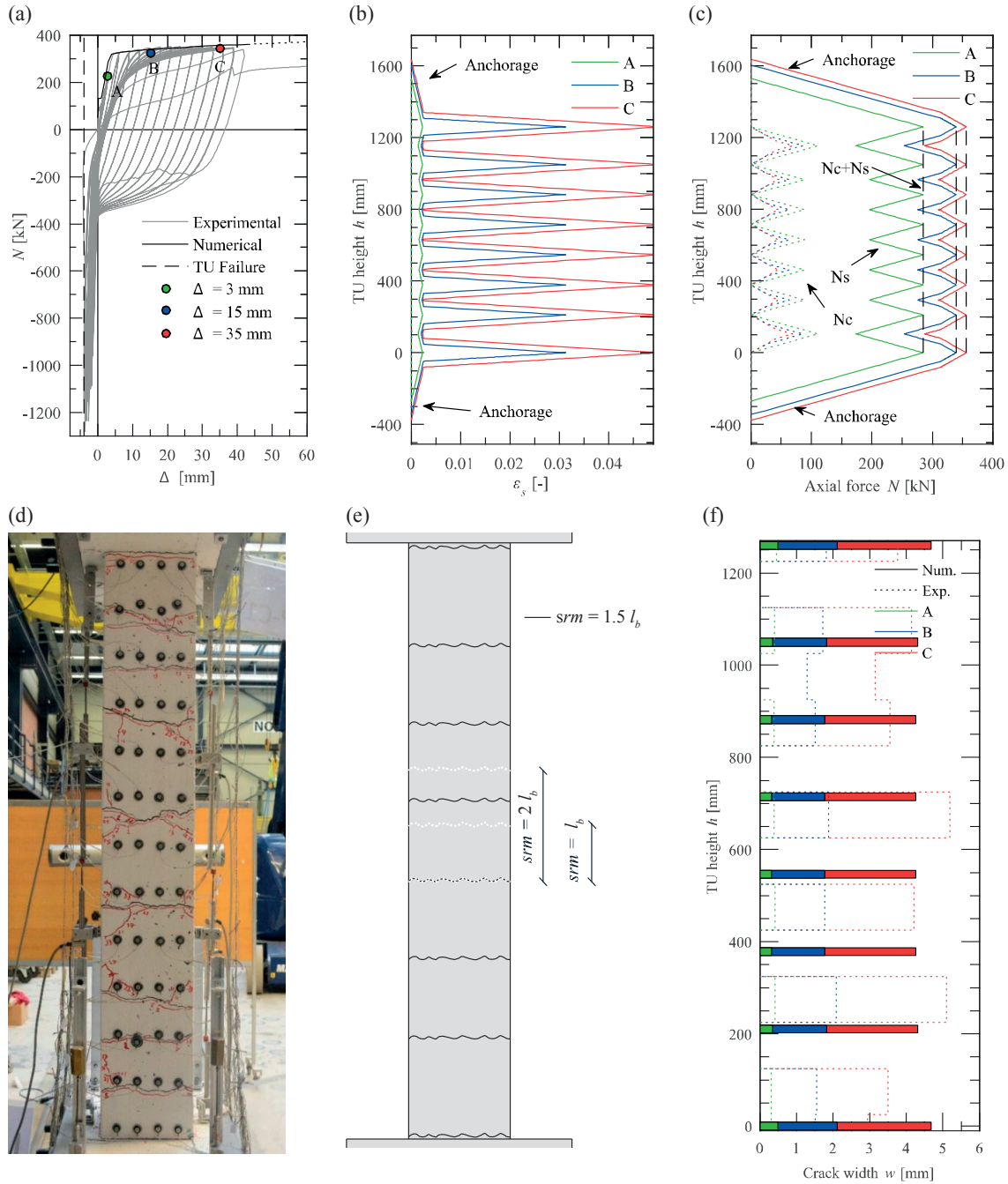


Figure 7.9: TU LAP-C1: (a) Experimental vs numerical force-displacement response; (b) Simulated steel strain profile; (c) Simulated steel and con-crete force profiles; (d) Photo of crack pattern; (e) Numerical crack pattern obtained for different srm to l_b ratios; (f) Experimental vs numerical crack width.

The discretization of the boundary element is shown in Figure 7.9 (e) and consists in two anchorage and seven basic tension chord elements, corresponding to a crack spacing $srm = 1.5 \cdot l_b$. The same figure also includes, for comparison purposes, the minimum and maximum theoretical crack spacing ($srm = l_b$ and $srm = 2 \cdot l_b$), whereas the real crack pattern observed during the test is reported in Figure 7.9 (d).

Finally, experimental and numerical crack widths are compared, for the three levels of displacement A, B and C, in Figure 7.9 (f). Experimental values, computed as displacement difference between markers located on the same vertical line, are represented with a dotted line, whereas numerical values are displayed in the form of bar plots at crack location. It is found that the model describes satisfactorily the experimental results for all considered displacement levels, concerning both cracks along the TU as well as foundation/top beam interface cracks. Namely, as it will be shown in Figure 7.11 (b), the model error associated to the simulation of the average crack width is smaller than 5%.

7.4.2 TUs with lap splices

In Figure 7.10, results from the mechanical model are compared against experimental data obtained from three TUs with lap splices differing in terms of both lap splice length (l_s) and confining reinforcement ratio (ρ_t). In particular, LAP-P4 had the shortest lap-splice length, $l_s = 350$ mm ($25 \cdot \phi_t$) and $\rho_t \approx 0.3\%$, followed by LAP-P16, $l_s = 560$ mm ($40 \cdot \phi_t$) and $\rho_t \approx 0.2\%$, whereas the longest lap-splice length was part of LAP-P5, $l_s = 840$ mm ($60 \cdot \phi_t$) and $\rho_t \approx 0.1\%$. Differently from the model used to simulate the TU with continuous reinforcement, the one used in the present subsection included a lap-splice element above the bottom anchorage element.

From shorter to longer lap splice lengths, the comparison in terms of global force-displacement is shown in plots (a), (d) and (g). In all three cases, the numerical pushover follows satisfactorily the tensile backbone curve of the cyclic experimental results. Moreover, the ultimate displacement capacity is also rather well predicted (relative error below 20%); the numerical failure is triggered by the attainment of the ultimate lap-splice displacement. For each state (A, B, C) represented by a coloured dot in the force-displacement curves, plots (b), (e) and (h) display the numerical vs experimental crack width. A good match between the two quantities can be observed, the model being able to capture the crack evolution as well as the different opening of cracks within and outside the lap-splice region. Namely, the former are considerably smaller than the latter and the difference in crack width increases with the spread of inelasticity. The distribution of rebar steel strains along the lap splice length is also adequately simulated by the model. In plots (c), (f) and (i), the bottom-anchored rebar of the spliced pair is considered for comparison (the top anchored rebar would show similar but mirrored results). A good fit is again apparent for the three lap-splice lengths, which validates the model assumption of neglecting the concrete deformations within the lap-splice region. Unfortunately, the comparison could not be performed close to the two splice-end cracks, where steel deformations are maximum, since no strain measure was available at that location.

In order to further validate the proposed mechanical model, the entire set of RC wall boundary elements presented in Chapter 5 was simulated. The results are summarized in Figure 7.11 in terms of relative error concerning the prediction of: (a) the failure displacement; (b) the average crack width outside the lap splice region; and (c) the average crack width within the lap splice region. The relative error η is expressed by the following equation:

$$\eta = \frac{v_{num} - v_{exp}}{v_{exp}} \quad (7.31)$$

where v_{num} and v_{exp} represent the considered numerical and experimental quantities, respectively.

From Figure 7.11 (a), it is apparent that the relative error between the experimental and numerical ultimate displacement is smaller than 25%, for all specimens. Black dots are used to individuate the TUs depicted in Figure 7.10 (i.e., LAP-P4, LAP-P16 and LAP-P5) and to demonstrate that the good model performance was not restricted to those cases. A remark is due to the fact that the database used for the current validation is the same employed to calibrate the deformation capacity of lap splices (Chapter 5), and therefore acceptable matches were more likely regarding the ultimate displacement. However, to the author's knowledge, no other experimental tests are available in the literature investigating the ductility of lap splices. Moreover, the predictive equation proposed in Chapter 6 was derived from the experimental data including assumptions on the mechanical behaviour of the structural member (e.g., the contribution factor to the interface crack $\alpha = 0.5$). The performed validation hence strengthens the validity of such hypotheses, moreover confirming the dependability of the adopted mechanical approach.

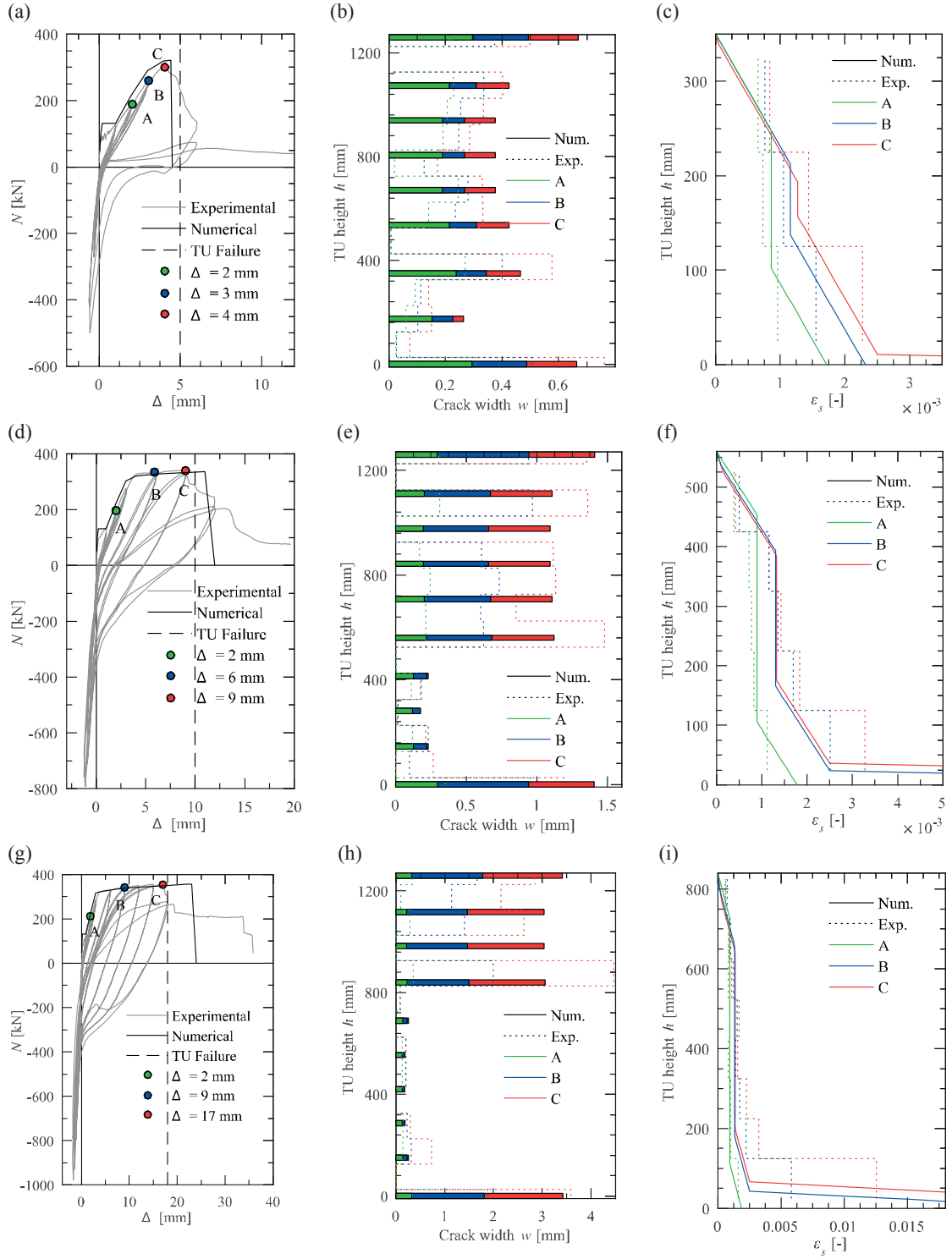


Figure 7.10: Experimental vs numerical comparison for TU LAP-P4 ($l_s = 25 \varnothing$), LAP-P16 ($l_s = 40 \varnothing$) and LAP-P5 ($l_s = 60 \varnothing$): (a), (d), (g) Force-displacement response; (b), (e), (h) Crack width; (c), (f), (i) Steel strains within the lap-splice region for the bottom anchored rebar.

Figure 7.11 (b) and (c) show the relative average crack width error, for cracks located outside and within the lap-splice region, respectively. For each TU, the numerical and experimentally-measured crack widths of all cracks located in either of these two regions is computed and then averaged at each experimental peak tensile displacement. Again, the TUs used for validation in Figure 7.10 are depicted with black lines; the points corresponding to the states A, B, and C, at

which the crack widths were compared, are reported with the same marker notation. Results for all other TUs are represented in grey. For both cracks located outside and within the lapped zone, an error $\eta_w < 20\%$ (approximately) can be observed for all TUs and displacement levels. Exception is made for cracks along the lap-splice zone and low imposed displacements ($\Delta_{tot} < 3\text{mm}$), where the error can arrive to 40%. This deviation can be partly attributed to the fact that experimental cracks, at such small tensile demands, may still evolve along the member (i.e. new cracks can open at different locations) while the points in which they are evaluated are fixed.

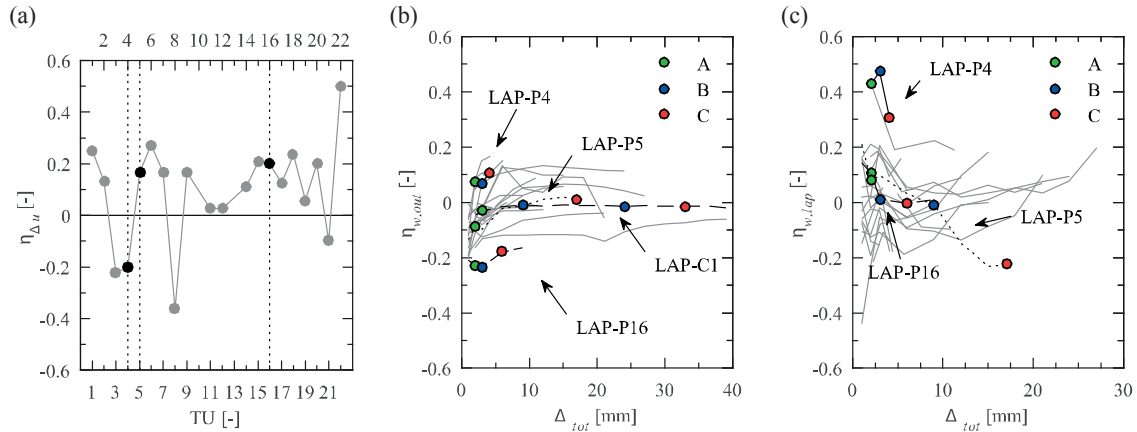


Figure 7.11: Relative error for the simulation of: (a) Ultimate element displacement; (b) Average crack width outside the lap-splice region; (c) Average crack width along the lap-splice region.

7.5 Conclusions

Reinforced concrete walls often have lap splices above the foundation level, where the expected seismic demand is maximum. A proper detailing of lap splices is of fundamental importance for the cyclic response of the structural member as it can result in a significant reduction of its strength and deformation capacity. Boundary elements represent the most strained region of the RC wall, and therefore the one where lap splice failure is triggered.

In this Chapter, a mechanical model for the simulation of RC wall boundary elements with lap splices is presented. It corresponds to an extension of the tension chord model, with which it shares the hypotheses on both material and bond constitutive relations. The model comprises three different types of elements connected in series: an anchorage element accounting for the strain penetration of the reinforcement into the foundation, a lap-splice element describing the deformation occurring within the spliced region and a basic tension chord element modelling the response outside the lapped zone. The newly proposed lap-splice element builds on the hypothesis that the force is transferred from the anchored to the free end (unloaded) rebar through concrete bond; however, similarly to the anchorage element, the concrete is assumed to remain undeformed; it serves to transfer the force from one rebar to the other. The model is highly versatile and allows any combination and number of the above-mentioned elements. A stable iterative solution procedure is proposed to solve the global nonlinear problem. The average lap splice strain at failure suggested in the previous Chapter is used to determine the ultimate displacement of boundary elements with lap splices.

Finally, the model was validated against a set of 24 tests on RC wall boundary elements with both continuous and spliced longitudinal reinforcement. Different lap-splice lengths and confining reinforcement were also considered. Comparisons were made in terms of force-displacement response, crack width and strain distribution along the pair of spliced rebars. In all cases, a good match is found between numerical and experimental results; relative errors regarding the ultimate displacement and crack widths are on average below 20%.

7.6 Acknowledgments

The financial support by the Swiss Federal Roads Office (FEDRO) to the project number AGB 2015/002, under which the present study is carried out, is acknowledged. The author would like to thank Dr. Michele Godio for his precious help with the design of some figures.

8 Conclusions

Past experimental research mainly focused on the evaluation of lap splice strength, typically through tests on RC beams under monotonic loading. Investigations on the cyclic behaviour of lap splices are scarce, predominantly performed on RC beams and columns. Although the presence of lap splices in the plastic hinge region of RC walls was identified as a critical source of damage in recent earthquakes [26], only few studies are available concerning these structural members, for the most part performed in the last decade. In particular, the quantification of their displacement capacity is fundamental in the framework of performance-based earthquake engineering, where displacement rather than forces are compared to the seismic demand. However, expressions to estimate the deformation capacity of poorly designed lap splices are lacking in the literature, as well as simple tools for practicing engineers to simulate the nonlinear response of spliced RC walls. In fact, available finite element models generally account for the deformation contribution brought about by the presence of lap splices with complex interface elements and local bond-slip models.

The objective of this thesis is to contribute to the understanding of the behaviour of RC walls with lap splices as well as to propose suitable tools for predicting their nonlinear response under cyclic loading. In the following, the main contributions of the present work are reviewed, the main limitations are outlined, and future experimental and numerical developments are discussed.

8.1 Contributions and findings

The main contributions of the present thesis are:

- The assembly of a database of past tests on RC walls with lap splices and the determination of the main parameters affecting their displacement capacity: lap splice length, confining reinforcement, moment gradient and loading history;
- The calibration of an equivalent, uniaxial steel constitutive law for lap splices and the proposal of a detailed shell element model to simulate the response of RC walls with lap splices;
- The development of a new beam element model that allows to account for tension shift effects in RC members;
- The completion of an experimental programme involving the testing of 24 RC wall boundary elements, 22 of which with lap splices. Several global and local deformation quantities were continuously monitored with optical and hard-wired measurement systems. The data are now publicly available from the Zenodo platform at the DOI: 10.5281/zenodo.1205887.
- The calibration of a new expression for the strain capacity of lap splices, which only considers deformation contributions originating within the lap splice region. The proposed equation is function of lap splice length, confining reinforcement and casting position.
- The proposal of a mechanical model, based on the tension chord model, describing the behaviour of lap splices in tension. It allows computing the distribution of steel stresses and strains along the pair of spliced rebars as well as the crack width.

In the next subsections, findings obtained from the experimental work, numerical and mechanical modelling are presented in greater detail.

8.1.1 Main findings from experimental tests

8.1.1.1 Tests on RC walls with lap splices

Past experimental programmes on RC walls featuring lap splices, constituted by 16 walls with lap splices and 8 reference units with continuous reinforcement, are collected and key parameters tabulated. The test of two large-scale walls (TW2 without and TW3 with lap splices) performed at the structural laboratory of EPFL are included. They complement the existing tests by investigating a member with a shear span ratio $L_s/h < 2$, which is the smallest among the dataset, allowing

to further evaluate the influence of the moment gradient on the lap splice performance. By comparing the behaviour of all the units collected in the database, the following specific observations can be made regarding the displacement capacity of RC walls with lap splices:

- In RC walls designed according to modern detailing rules with adequately long and well-confined lap splices, the plastic hinge is forced to relocate above the lap splice region. Damage concentrates there in the form of concrete crushing and rebar buckling/fracture, leaving the spliced zone almost undamaged. Nonetheless, shifting the plastic hinge to a section above the lap splice increases the shear demand on the wall and may reduce the member ductility with respect to a member with continuous reinforcement;
- Non code-compliant RC walls with average horizontal reinforcement ratios ($\rho_h < 0.25\%$) and medium long lap splices ($l_s < 40\text{--}45 d_{bl}$), develop splitting cracks along the spliced length. With the increase of the imposed displacement demand, bar slippage leads to the build-up of horizontal cracks forming at the top and bottom of the lap splice region;
- RC walls with medium length lap splices ($l_s > 40 d_{bl}$) and insufficient confinement ($\rho_h < 0.25\%$) typically attain the peak force but their deformation capacity is significantly reduced;
- RC walls with short and not well-confined lap splices ($l_s < 30 d_{bl}$, $\rho_h < 0.2\%$) show brittle failure occurring before the attainment of the flexural yield capacity.
- Three types of lap splices failure may occur: (i) tension failure, (ii) tension failure upon load reversal after concrete crushing in compression took place, and (iii) compression failure of the lap splice in conjunction with crushing of the concrete. The two first modes were both observed while the latter is uncommon in RC walls.
- The failure of the outermost lap splices layer typically signals a marked degradation in the RC wall strength, which can be assumed as member failure.
- The existence of a moment gradient (shear) over the spliced length of a RC wall increases the deformation (average strain) capacity of the lap splices.
- Confining reinforcement, moment gradient, lap splice length, and loading history are the parameters affecting the most the displacement ductility of RC walls with lap splices.

8.1.1.2 Tests on RC wall boundary element with lap splices

Twenty-four RC wall boundary elements were tested under uniaxial cyclic loading at the structural laboratory of EPFL, of which 22 had lap splices and two were reference units with continuous reinforcement. The variable parameters of the test programme included lap splice length, confining reinforcement and loading history, with the former two chosen to be representative of both pre-seismic and code-compliant central European construction practice. The collected data allowed a deeper understanding of the behaviour of lap splices and the following quantification of their deformation capacity. Hereunder the main observations and results obtained from the experimental activity are listed:

- All the spliced units behaved similarly until the onset of failure, which occurred due to the opening of vertical splitting cracks along the lap splice length. Depending on the amount of provided confining reinforcement, a splitting-unzipping or splitting-explosive failure mode could be observed.
- The lap splice failures occurred at very different strain demands, which depended on the lap splice length, the confining reinforcement, the casting position and, to a lesser extent, on the loading history.
- For long lap splices ($l_s = 60 d_{bl}$) adequately confined ($\rho_t > 0.15\%$), the splices did not fail and the rupture of the top anchored rebar occurred. This typically happened after core concrete crushing, determining the specimen failure.
- An expression for predicting the strain at failure of lap splices is derived, in which only the deformation contributions from the lapped region are considered. Anchorage slip due to strain penetration or rebar slip from member locations outside the lap splice region are removed. The proposed equation accounts for the confining reinforcement ratio, the lap splice length (as function of the bar diameter) and the rebar casting position. Compared to these three parameters, the loading history was found to have only a minor influence and the data basis insufficient for its quantification.
- The deformation capacity of lap splices increases with the splice length, irrespectively of the provided confining reinforcement.
- The effectiveness of the confining reinforcement depends instead on the lap splice length. Namely, the deformation capacity of short lap splices ($l_s = 25\phi_t$) is insensitive to the confining reinforcement ratio; on the other extreme, even very low levels of confining reinforcement are sufficient to increase the deformation capacity of long lap splices ($l_s = 60\phi_t$); for intermediate lap-splice lengths the splice deformation capacity increases with confining reinforcement only beyond a certain ratio ($\rho_t > 0.15\%$).

- Larger deformation capacities were reached by bottom-casted splices with respect to top-casted, underlining the importance of concrete quality.
- Larger imposed compression levels reduce the deformation capacity of lap splices. However, further testing is required for an appropriate quantitative characterization of the loading history.

8.1.2 Developed numerical models

8.1.2.1 *Shell element model with equivalent uniaxial steel constitutive law for lap splices*

The response of all the RC walls collected in the database was simulated through advanced 2D shell element models. Once validated, these models allowed to obtain important information on the deformation capacity of lap splices as well as to develop a simple, yet reliable model to account for the presence of lap splices in RC walls. The novel aspects of the proposed approach are:

- Strain values from the validated numerical models were used to calibrate a semi-empirical relationship for the deformation capacity of lap splices. It depends on the equivalent yield strain, confining reinforcement ratio and ratio of lap splice length to shear span, which were identified as the quantities mostly influencing the displacement capacity of spliced RC walls.
- An equivalent, uniaxial steel stress-strain relationship is proposed representing the monotonic envelope of the cyclic response of spliced rebars in RC walls up to the onset of strength degradation. It is characterized by two points defining an equivalent yield state and ultimate condition.
- The constitutive relationship is used in combination with plane shell element models to simulate the force-displacement response of the spliced set of RC walls. Good predictions in terms of both force and displacement capacity of the members were obtained. The accuracy and simplicity of the numerical model make it a suitable tool for engineering practice (i.e. the use of complex interface bond-slip element to account for the lap splice response is not required).
- Beyond the point of strength degradation, the prediction of the wall lateral resistance becomes non-dependable and it is not addressed by the model.

8.1.2.2 *Axially equilibrated displacement-based beam element model*

A nonlinear beam formulation is proposed that can be used to account for tension shift effects in RC members. The latter represent one of the main reason for the mismatch between experimental and numerical local level results when using beam element models. Beam element models are a suitable modelling technique for engineering practice as they represent a good compromise between accuracy and computational cost. A reliable prediction of local level quantities is fundamental in the framework of performance-based earthquake engineering as they are strictly related to structural damage. The main differences and advantages of the proposed beam formulation with respect to classical force-based and displacement-based formulations are:

- In the proposed displacement-based beam element model axial equilibrium is strictly verified along the element length. An intra-element procedure updates the imposed set of axial sectional deformations to attain constant axial force in all integration points, and equal to the applied axial load. This solves one major drawback of displacement-based formulations where the axial forces are equilibrated only in an average sense, causing a poor simulation of global and local level quantities.
- Linear curvature profiles are assumed along the element length, allowing to indirectly account for the effect of tension shift in RC members. These effects cannot be captured by current force-based formulations which, although satisfying equilibrium exactly, can only capture the effect of the moment gradient.
- The axially equilibrated displacement-based element is validated against two sets of cyclic tests on RC cantilever piers and walls. Assuming an appropriate member discretization, with the length of the bottom element equal to the extent of plasticity, it provides accurate results in terms of global and local scale response. Namely, the simulation of experimental curvatures and strains show a significant improvement when compared with models using classical force-based or displacement-based elements.
- From a computational viewpoint, the proposed element performs faster than classical force-based elements but slower than classical-displacement based elements (no intra-element iteration is required for their state determination).

The presence of lap splices may be accounted for by assigning the strain limits provided by equations (6.8) to (6.11) for the steel stress-strain law of the rebar fibers located within the lap splice region. Satisfactorily results were obtained when simulating the global force-displacement response of the spliced RC walls tested by Bimschas [29] and Hannewald [57],

as showed in the following Figure 8.1. Further development and validation is required at the local level, where the reduced deformations occurring within the lap splice region prior to failure are currently not accounted for.

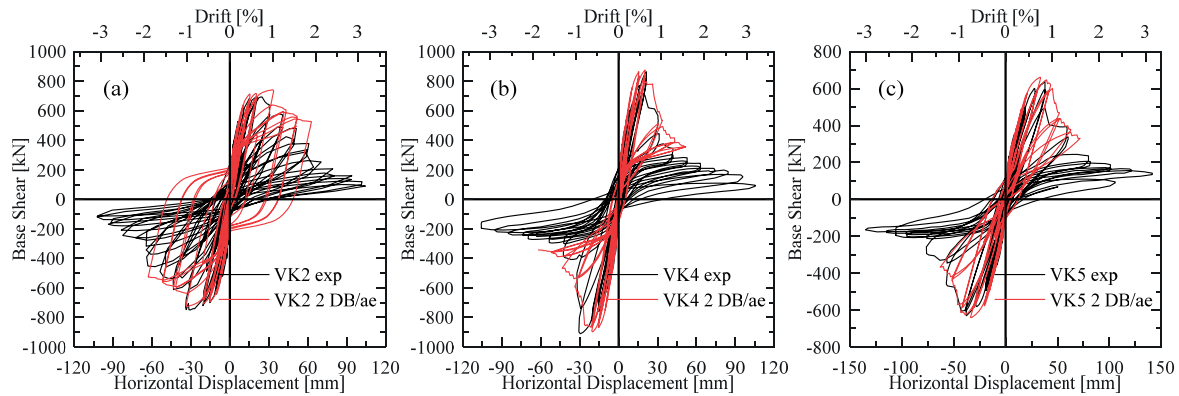


Figure 8.1: Comparison of the experimental and numerical (model with 2 DB/ae with the length of the bottom element equal to the height of the lap splice region) force-displacement response of the spliced TUs: (a) VK2; (b) VK4; (c) VK5.

8.1.3 Developed mechanical model

An extended tension chord model for simulating the response of RC wall boundary elements accounting for strain penetration effects and the presence of lap splices is proposed. The main features and novel aspects with respects to the classical tension chord model are:

- The model is composed of an assembly of components, each one accounting for a different source of deformation. Namely: (i) an anchorage-slip element accounts for the strain penetration of the longitudinal reinforcement into the foundation; (ii) a basic tension chord element evaluates the response outside the lap splice zone; and (iii) a lap splice element describes the behaviour within the lap splice region.
- In the lap splice element, it is assumed that the concrete remains undeformed and has only the function of transferring the force from one bar to another. Although this is a simplification of the real behaviour, it represents a reasonable approximation up to the point of lap splice failure.
- The model gives as output the concrete and steel stress and strain distributions, including the stress and strain distribution of the spliced and anchored rebars. Moreover, it provides the crack distribution and widths. Input quantity can be the global imposed tensile force or displacement: a direct and iterative procedure is necessary in the former and latter case, respectively.
- For poorly detailed spliced members, the ultimate displacement is computed through the relationship derived from the experimental programme on spliced RC wall boundary elements.
- The model is validated against global and local level results obtained from the tests on RC wall boundary elements with and without spliced longitudinal reinforcement. Different lap splice lengths and confining reinforcement were considered. A good match is found between numerical and experimental results in terms of force-displacement response, crack width and strain distribution along the pair of spliced rebars. Relative errors in the computation of the ultimate displacement and crack widths averaged below 20%.

8.2 Limitations and outlook

The main limitations of the present work are pinpointed in the following paragraphs; building on them, future developments are outlined and discussed.

Although in the last decades several tests were performed on RC walls with lap splices, the database of experimental programmes on such type of structural member remains rather limited. Further testing is required in order to broaden the understanding of the cyclic behaviour of spliced RC walls, possibly using standardized specimen where the influence of separate parameters can be clearly identified. Moreover, all tests to date were performed under quasi-static cyclic loading; it would be therefore of interest to investigate the effect that dynamic loading has on the bond deterioration occurring within the lap splice zone.

Based on the restricted dataset of RC walls with lap splices, a semi-empirical expression for the evaluation of the strain capacity of lap splices was calibrated in Chapter 3. The latter should not be applied to RC walls with mechanical and geometrical features outside the range of those included in the database. Following, an equivalent uniaxial steel constitutive law was proposed, which represents the backbone response of lap splices in RC walls. Although it was calibrated against cyclic tests on RC walls, it is only applicable for monotonic loading, i.e. pushover analysis. The development of mathematical relations to capture the unloading and reloading branches of the lap splice response represent a primary extension of the model, so that it could be used in cyclic static and dynamic analyses. Moreover, the equivalent stress-strain law was only validated by employing it within truss elements in 2D shell element models. Although in principle it can be used in different modelling approaches resorting to uniaxial material stress-strain laws (e.g. beam element models), further validation should be carried out.

The axially equilibrated displacement-based formulation presented in Chapter 4 is a plane frame element and, as a first step, should be extended to space frame element for its use in three-dimensional analyses. Moreover, the discretization of the actual RC member is at present required in order to capture tension shift effects, as one finite element has to be associated to each inelastic region. The latter evolves with the imposed demands, which is also not accounted for in the present formulation. The use of bilinear, adaptive shape functions for the curvature profiles represents thus a further improvement as it would allow, on the one side, to capture the evolution of the extent of plasticity and, on the other, to simulate each structural member with a single finite element.

The experimental programme on RC wall boundary elements outlined in Chapter 5 featured lap splice length, confining reinforcement and loading history as variable parameters. Although these are deemed the parameters controlling the most the deformation capacity of lap splices, the influence of several other factors can be experimentally investigated such as: longitudinal and transversal rebar diameter, concrete strength, steel strength and ductility, relative rib area etc. Furthermore, other tests are required for a proper quantification of the effect of loading history, which could be only qualitatively assessed and thus was not included in the predictive equation of the lap splice strain capacity proposed in Chapter 6. Eventually, from a broader dataset of standardized uniaxial tests on lap splices, a full-cyclic stress-strain relationship might also be calibrated. The latter could be then included in the developed beam element model to simulate, both at the global and local level, the behaviour of RC walls with lap splices.

The mechanical model described in Chapter 7 is developed for isolated RC wall boundary elements; a first improvement may therefore be to extend it for simulating the entire wall behaviour. Moreover, the lap splice basic element builds on assuming that the concrete remains undeformed, serving only to transfer the stresses from the anchored to the free end rebar. Although it was proved not to lead to significant errors in the estimation of the spliced rebar strains, this simplifying hypothesis on the lap splices behaviour can be removed in order to obtain more accurate predictions of the local-level response.

References

- [1] Tepfers R. A theory of bond applied to overlapped tensile reinforcement splices for deformed bars. PhD Thesis, Calmers University of Technology, Goteborg, Sweden., 1973.
- [2] Panahshahi N, White RN, Gergely P. Reinforced concrete compression lap splices under inelastic cyclic loading. *ACI Struct J* 1992;89:164–75.
- [3] Canbay E, Frosch RJ. Bond strength of lap-spliced bars. *ACI Struct J* 2005;102:605–14.
- [4] Aristizabal-Ochoa JD. Earthquake Resistant Tensile Lap Splices. *J Struct Eng* 1983;109:843–58. doi:10.1061/(ASCE)0733-9445(1983)109:4(843).
- [5] Kilic SA, Sozen MA. Evaluation of effect of August 17, 1999, Marmara earthquake on two tall reinforced concrete chimneys. *ACI Struct J* 2003;100:357–64.
- [6] Song C, Pujol S, Lepage A. The collapse of the Alto Río building during the 27 February 2010 Maule, Chile, earthquake. *Earthq Spectra* 2012;28:301–34. doi:10.1193/1.4000036.
- [7] Kim S, Shiohara H. Dynamic response analysis of a tall RC chimney damaged during 2007 Niigata-ken Chuetsu-Oki earthquake. 15th World Conf. Earthq. Eng., Lisbon, Portugal: 2012.
- [8] Lukose K, Gergely P, White R. Behavior of reinforced concrete lapped splices for inelastic cyclic loading. *ACI J Proc* 1982.
- [9] Gergely P, White R. Seismic Design of Lapped Splices in Reinforced Concrete. *Proc Seveth World Conf Earthq Eng* 1980;4:281–8.
- [10] Paulay T. Lapped splices in earthquake-resisting columns. *ACI J* 1982;79:458–69.
- [11] Lynn AC, Moehle JP, Mahin SA, Holmes WT. Seismic evaluation of existing reinforced concrete building columns. *Earthq Spectra* 1996;12:715–39.
- [12] Melek M, Wallace JW, Conte JP. PEER Report 2003/04: Experimental assessment of columns with short lap splices subjected to cyclic loads. 2003.
- [13] Villalobos E, Escolano-Margarit D, Ramirez-Márquez AL, Pujol S. Seismic response of reinforced concrete walls with lap splices. *Bull Earthq Eng* 2017;15:2079–100. doi:10.1007/s10518-016-0051-0.
- [14] Hardisty JN, Villalobos E, Richter BP, Pujol S. Lap splices in unconfined boundary elements. *Concr Int* 2015;37:51–8.
- [15] Lowes LN, Lehman DE, Birely AC, Kuchma DA, Marley KP, Hart CR. Earthquake response of slender planar concrete walls with modern detailing. *Eng Struct* 2012;43:31–47. doi:10.1016/j.engstruct.2012.04.040.
- [16] NZS 3101-Part 1. Concrete structures standard, Part 1 - The design of concrete structures. Stand Counc Concr Des Committee, P-3101 2006:697.
- [17] ACI 318M-11. Building code requirements for structural concrete. *Am Concr Inst* 2011:509. doi:10.1016/0262-5075(85)90032-6.
- [18] EN 1992-Part 1-1. Eurocode 2: Design of concrete structures Part 1-1: General rules and rules for buildings. 2004.
- [19] SIA 262. Concrete structures. Swiss Stand Assoc 2003:90.
- [20] SIA 260. Basis of structural design. Swiss Stand Assoc 2003:44.
- [21] Wenk T. Beurteilung der Erdbebensicherheit bestehender Strassenbrücken (assessment or earthquake safety of existing road bridges). *Doc Fed Roads Off FEDRO* 2005.
- [22] Bimschas M, Dazio A. Seismic safety of existing bridges. *FEDRO Report*, Bern, Switzerland: 2014.
- [23] Hannewald P, Beyer K. Seismic Safety of Existing Bridges – Cyclic Inelastic Behaviour of Bridge Piers. *FEDRO Report*, Bern, Switzerland: 2014.
- [24] Hannewald P. Seismic behavior of poorly detailed RC bridge piers. PhD Thesis, École Polytech Fédérale Lausanne 2013:pp 183.
- [25] Mortezaei A, Ronagh HR. Plastic hinge length of reinforced concrete columns subjected to both far-fault and near-fault ground motions having forward directivity. *Struct Des Tall Spec Build* 2013;926:903–26. doi:10.1002/tal.

-
- [26] Sritharan S, Beyer K, Henry RS, Chai YH, Kowalsky M, Bull D. Understanding poor seismic performance of concrete walls and design implications. *Earthq Spectra* 2014;30:307–34. doi:10.1193/021713EQS036M.
 - [27] Aaleti S, Brueggen BL, Johnson B, French CE, Sritharan S. Cyclic response of reinforced concrete walls with different anchorage details: Experimental investigation. *J Struct Eng* 2013;139:1181–91. doi:10.1061/(ASCE)ST.1943-541X.0000732.
 - [28] Layssi H, Mitchell D. Experiments on Seismic Retrofit and Repair of reinforced Concrete Shear Walls. *Proc. 6th Int. Conf. FRP Compos. Civ. Eng. -CICE*, Rome, Italy, June 13-15, 2012, p. 1–8.
 - [29] Bimschas M. Displacement based seismic assessment of existing bridges in regions of moderate seismicity. PhD Thesis, ETH Zurich 2010.
 - [30] Paterson J, Mitchell D. Seismic retrofit of shear walls with headed bars and carbon fiber wrap. *J Struct Eng* 2003;129:606–14. doi:10.1061/(ASCE)0733-9445(2003)129:5(606).
 - [31] Priestley MJN, Seible F, Calvi GM. *Seismic design and retrofit of bridges*. New York: John Wiley & Sons; 1996.
 - [32] Biskinis D, Fardis MN. Flexure-controlled ultimate deformations of members with continuous or lap-spliced bars. *Struct Concr* 2010;11.
 - [33] Almeida JP, Tarquini D, Beyer K. Modelling approaches for inelastic behaviour of RC walls: Multi-level assessment and dependability of results. *Arch Comput Methods Eng* 2016;23:69–100.
 - [34] Ciampi V, Eligehausen R, Bertero V, Popov E. Analytical model for deformed bar bond under generalized excitations 1981:53–67.
 - [35] Tastani SP, Brokalaki E, Pantazopoulou SJ, Asce M. State of Bond along Lap Splices. *J Struct Eng* 2015;141:1–14. doi:10.1061/(ASCE)ST.1943-541X.0001243.
 - [36] Marti P, Alvarez M, Kaufmann W, Sigrist V. Tension Chord Model for Structural Concrete. *Struct Eng Int* 1998;8. doi:10.2749/101686698780488875.
 - [37] Orangun CO, Jirsa JO, Breen JE. A reevaluation of test data on development length and splices. *ACI J* 1977;74:114–22.
 - [38] Zuo J, Darwin D. Splice strength of conventional and high relative rib area bars in normal and high-strength concrete. *ACI Struct J* 2000;97:630–41.
 - [39] Tepfers R. Cracking of concrete cover along anchored deformed reinforcing bars. *Mag Concr Res* 1979;31:3–12. doi:10.1680/mac.1979.31.106.3.
 - [40] ACI. Report on bond of steel reinforcing bars under cyclic loads. *Am Concr Inst - Jt ACI-ASCE Comm* 408 2012:39.
 - [41] EERI. Buildings (EERI Reconnaissance Report Guam). *Earthq Spectra* 1995;11:63–137.
 - [42] Birely A. Seismic performance of slender reinforced structural concrete walls. PhD Thesis, Univ Washingt 2012:983.
 - [43] EERI-GEER. Preliminary observations on the Niigata-Chuetsu Oki, Japan, earthquake of July 16, 2007. *EERI Spec Earthq Rep* 2007:1–12.
 - [44] Gergely P, Fagundo F, White RN. Bond and splices in reinforced concrete for seismic loading. *CEB Bull d'Information* No 132, AICAP-CEB Symp 1979.
 - [45] Fagundo F. Behavior of lapped splices in R.C. beams subjected to cyclic loads. PhD Thesis, Cornell Univ 1979.
 - [46] Tocci AD, Gergely P, White RN. Report No. 81-1, The behavior and strength of lapped splices in R/C beams subjected to repeated loads. *Dep Struct Eng Cornell Univ Ithaca* 1981:256.
 - [47] Sivakumar B, Gergely P, White RN. Suggestions for the design of R/C lapped splices for seismic loading. *Concr Int* 1983;5:46–50.
 - [48] Sparling B, Rezanoff T. The effect of confinement on lap splices in reversed cyclic loading. *Can J Civ Eng* 1986;13:681–92. doi:10.1139/l86-103.
 - [49] Rezanoff T, Zacaruk JA, Topping R. Tensile lap splices in reinforced concrete beams under inelastic cyclic loading. *ACI Struct J* 1988;85:46–52.
 - [50] Aboutaha RS, Engelhardt MU, Jirsa JO, Kreger MF. Retrofit of concrete columns with inadequate lap splices by the use of rectangular steel jackets. *Earthq Spectra* 1996;12:693–714. doi:10.1193/1.1585906.
 - [51] Chai YH, Priestley MJN, Seible F. Seismic retrofit of circular bridge columns for enhanced flexural performance.

- ACI Struct J 1991;88:572–84.
- [52] Valluvan R, Kreger ME, Jirsa JO. Strengthening of column splices for seismic retrofit of nonductile reinforced concrete frames. *ACI Struct J* 1993;90:432–40.
- [53] Melek M, Wallace JW. Cyclic behavior of columns with short lap splices. *ACI Struct J* 2004;101:802–11.
- [54] Pam HJ, Ho JCM. Effects of steel lap splice locations on strength and ductility of reinforced concrete columns. *Adv Struct Eng* 2010;13:199–214. doi:10.1260/1369-4332.13.1.199.
- [55] Biskinis D, Fardis MN. Deformations at flexural yielding of members with continuous or lap-spliced bars. *Struct Concr* 2010;11:127–38.
- [56] Elnady EMM. Seismic rehabilitation of RC structural walls. PhD Thesis, McMaster Univ 2008.
- [57] Hannewald P, Bimschas M, Dazio A. Quasi-static cyclic tests on RC bridge piers with detailing deficiencies. *Inst Fur Baustatik Und Konstr Bericht Nr 352*, ETH Zurich, Switzerland 2013;pp 133.
- [58] Villalobos EJF. Seismic response of structural walls with geometric and reinforcement discontinuities. PhD Thesis, Purdue Univ 2014.
- [59] Almeida JP, Prodan O, Tarquini D, Beyer K. Influence of lap-splices on the cyclic inelastic response of reinforced concrete walls. I: Database assembly, recent experimental data, and findings for model development. *J Struct Eng* 2017;143.
- [60] Almeida JP, Prodan O, Rosso A, Beyer K. Tests on thin reinforced concrete walls subjected to in-plane and out-of-plane cyclic loading. *Earthq Spectra* 2016. doi:10.1193/101915EQS154DP.
- [61] Eligehausen R, Popov EP, Bertero V V. Local bond stress-slip relationships of deformed bars under generalized excitations. Rep UCB/EERC-83/23 1983:162.
- [62] Calabrese A, Almeida JP, Pinho R. Numerical issues in distributed inelasticity modeling of RC frame elements for seismic analysis. *J Earthq Eng* 2010;14:38–68. doi:10.1080/13632469.2010.495681.
- [63] Almeida JP, Das S, Pinho R. Adaptive force-based frame element for regularized softening response. *Comput Struct* 2012;102–103:1–13. doi:10.1016/j.compstruc.2012.03.018.
- [64] Chinn J, Ferguson PM, Thompson JN. Lapped splices in reinforced concrete beams. *ACI J* 1955;52:201–13.
- [65] Ferguson PM, Krishnaswamy CN. Tensile lap splices, Part II: Design recommendations for retaining wall, Splices and large bar splices. Texas Highw Dep Coop with US Dep Transp Rep 113-2 Cont, Fed Highw Adm Bur Public Roads 1971:67.
- [66] ACI 408. Development and Splice Lengths of Uncoated Bars. Am Concr Inst 2001.
- [67] Seliem HM, Hosny A, Rizkalla S, Zia P, Briggs M, Miller S, et al. Bond characteristics of ASTM A1035 steel reinforcing bars. *ACI Struct J* 2009;106:530–9.
- [68] Ferguson PM, Briceno EA. Tensile lap splices Part I: retaining wall type, varying moment zone. Texas Highw Dep Res Rep No 113-2 1969.
- [69] Priestley MJN, Calvi GM, Kowalsky MJ. Displacement-based seismic design of structures. IUSS Press; 2007.
- [70] Aristizabal-Ochoa JD, Fiorato AE, Corley WG. Tension lap splices under severe load reversals. 7th World Conf. Earthq. Eng., Ankara, Turkey: Kelaynak Printing Company; 1980, p. 1–5.
- [71] Muhlenbruch CW. The effect of repeated loading on the bond strength of testing materials. *ASTM Proc* 1948;48:977–85.
- [72] Hester CJ, Salamizavaregh S, Darwin D, McCabe SL. Bond of epoxy-coated reinforcement: Splices. *ACI Struct J* 1993;90:89–102.
- [73] Paulay T, Priestley MJN. *Seismic Design of Reinforced Concrete and Masonry Buildings*. New York: Wiley and Son; 1992.
- [74] Syntzirma DV, Pantazopoulou SJ. Deformation capacity of RC members with brittle details under cyclic loads. *Concr Int* 2006;236:1–22. doi:10.14359/18204.
- [75] Ngo D, Scordelis AC. Finite element analysis of reinforced concrete beams. *ACI J* 1967;64:152–63. doi:10.14359/7551.
- [76] Nilson AH. Internal measurements of bond slip. *ACI J* 1972;69:439–41.
- [77] Harajli MH, Mabsout ME. Evaluation of bond strength of steel reinforcing bars in plain and fiber-reinforced concrete. *ACI Struct J* 2002;99:509–17.

REFERENCES

- [78] Harajli MH, Hamad BS, Rteil AA. Effect of confinement on bond strength between steel bars and concrete. *ACI Struct J* 2004;101:595–603. doi:10.1007/s11595-006-4584-y.
- [79] Harajli MH. Bond stress–slip model for steel bars in unconfined or steel, FRC, or FRP confined concrete under cyclic loading. *J Struct Eng* 2009;135:509–18. doi:10.1061/(ASCE)0733-9445(2009)135:5(509).
- [80] Lowes LN, Moehle JP, Govindjee S. Concrete-steel bond model for use in finite element modeling of reinforced concrete structures. *ACI Struct J* 2004;101:501–11.
- [81] Ichinose T, Kanayama Y, Inoue Y, Bolander JE. Size effect on bond strength of deformed bars. *Constr Build Mater* 2004;18:549–58. doi:10.1016/j.conbuildmat.2004.03.014.
- [82] Esfahani MR, Rangan BV. Influence of transverse reinforcement on bond strength of tensile splices. *Cem Concr Compos* 2000;22:159–63. doi:10.1016/S0958-9465(00)00005-6.
- [83] Sozen M, Moehle J. Development and lap-splice lengths for deformed reinforcing bars in concrete. *Tech Rep to Portl Cem Assoc Urbana*, 1990:111.
- [84] Cairns J. Strength of compression splices: a reevaluation of test data. *ACI J* 1985;82:510–6.
- [85] Lettow S, Eligehausen R. FIB task Group 4.5: Formulation of application rules for lap splices in the new model code. *PPT Present Univ Calif Berkeley* 2006.
- [86] Sakurada T, Morohashi N, Tanaka R. Effect of transverse reinforcement on bond splitting strength of lap splices. *Trans Japan Concr Inst* 1993;15:573–80.
- [87] Esfahani MR, Rangan BV. Bond between normal strength and high-strength concrete (HSC) and reinforcing bars in splices in beams. *ACI Struct J* 1998;95:272–80. doi:10.1617/s11527-013-0143-0.
- [88] ACI committee 408. Bond and development of straight reinforcing bars in tension (ACI 408R-03). *Rep by ACI Comm 408* 2003:1–49.
- [89] FIB. *Model Code for Concrete Structures* 2010 2013:434. doi:10.1002/9783433604090.
- [90] Cho J, Pincheira JA. Inelastic analysis of reinforced concrete columns with short lap splices subjected to reversed cyclic loads. *ACI Struct J* 2006;103:280–90.
- [91] FEMA 356. *Prestandard and Commentary for the Seismic Rehabilitation of Buildings*. 2000.
- [92] Mander JB, Priestley MJN, Park R. Observed Stress-Strain Behavior of Confined Concrete. *J Struct Eng* 1988;114:1827–49.
- [93] Biskinis D, Fardis MN. Effect of lap splices on flexural resistance and cyclic deformation capacity of RC members. *Beton- Und Stahlbetonbau* 2007;102:51–9. doi:10.1002/best.200710105.
- [94] Xiao Y, Ma R. Seismic retrofit of RC circular columns using prefabricated composite jacketing. *J Struct Eng* 1997;123:1357–64. doi:10.1061/(ASCE)0733-9445(1997)123:10(1357).
- [95] Popovics S. A numerical approach to the complete stress-strain curve of concrete. *Cem Concr Res* 1973;3:583–99. doi:10.1016/0008-8846(73)90096-3.
- [96] Binici B, Mosalam KM. Analysis of reinforced concrete columns retrofitted with fiber reinforced polymer lamina. *Compos Part B Eng* 2007;38:265–76. doi:10.1016/j.compositesb.2006.01.006.
- [97] Talaat MM, Mosalam KM. *PEER Report 2007/10: Computational modeling of progressive collapse in reinforced concrete frame structures*. 2008.
- [98] Kim T-H, Kim B-S, Chung Y-S, Shin HM. Seismic performance assessment of reinforced concrete bridge piers with lap splices. *Eng Struct* 2006;28:935–45. doi:10.1016/j.engstruct.2005.10.020.
- [99] Kim T-H, Shin HM, Chung Y-S, Hong H-K. Seismic performance assessment of reinforced concrete bridge columns with lap splices using shaking table tests. *Mag Concr Res* 2009;61:705–19. doi:10.1680/macr.2008.61.9.705.
- [100] Girard C, Bastien J. Finite-element bond-slip model for concrete columns under cyclic loads. *J Struct Eng* 2002;1502–10.
- [101] Chowdhury SR, Orakcal K. An analytical model for reinforced concrete columns with lap splices. *Eng Struct* 2012;43:180–93. doi:10.1016/j.engstruct.2012.05.019.
- [102] Wong PS, Vecchio FJ, Trommels H. *VecTor2 - Nonlinear analysis of two-dimensional reinforced concrete membrane structures* 2014.
- [103] Vecchio FJ, Collins MP. The modified compression-field theory for reinforced concrete elements subjected to

- shear. ACI J 1986;83:219–31.
- [104] Hognestad E, Hanson, N. W, McHenry D. Concrete stress distribution in ultimate strength design. ACI J Proc 1955:455–80.
- [105] Park R, Priestley MJN, Gill WD. Ductility of square-confined concrete columns. J Struct Div 1982;108:929–50.
- [106] Kupfer H, Hilsdorf HK, Rusch H. Behavior of concrete under biaxial stresses. ACI J 1969;66:656–66.
- [107] Richart FE, Brandtzaeg A, Brown RL. A study of the failure of concrete under combined compressive stresses. Univ Illinois Bull 1928;XXVI.
- [108] Seckin M. Hysteretic behaviour of cast-in-place exterior beam column sub-assemblies. PhD Thesis, Dep Civ Eng Univ Toronto, 266 Pp 1982.
- [109] Palermo D, Vecchio FJ. Compression field modeling of reinforced concrete subjected to reverse loading: Formulation. ACI Struct J 2003;100:616–25. doi:10.14359/12803.
- [110] Palermo D, Vecchio FJ. Compression field modeling of reinforced concrete subjected to reverse loading: Verification. ACI Struct J 2004;101:155–64. doi:10.14359/12803.
- [111] Palermo D, Vecchio FJ. Simulation of Cyclically Loaded Concrete Structures Based on the Finite-Element Method. J Struct Eng 2007;133:728–38. doi:10.1061/(ASCE)0733-9445(2007)133:5(728).
- [112] Pugh JS. Numerical Simulation of Walls and Seismic Design Recommendations for Walled Buildings. PhD Thesis, Univ Washingt 2012.
- [113] Vecchio FJ. Towards cyclic load modeling of reinforced concrete. ACI Struct J 1999;96.
- [114] Berry MP, Lehman DE, Lowes LN. Lumped-plasticity models for performance simulation of bridge columns. ACI Struct J 2008;105:270–9.
- [115] Zhao J, Sritharan S. Modeling of strain penetration effects in fiber-based analysis of reinforced concrete structures. ACI Struct J 2007;104:133–41.
- [116] Monti G, Spacone E. Reinforced concrete fiber beam element with bond-slip. J Struct Eng 2000;654–61.
- [117] Spacone E, Filippou FC, Taucer FF. Fibre Beam-Column Model for Non-linear Analysis of R/C Frames: Part 1. Formulation. Earthq Eng Struct Dyn 1996;25:711–25. doi:10.1002/(SICI)1096-9845(199607)25:7<711::AID-EQE576>3.0.CO;2-9.
- [118] Yazgan U, Dazio A. Simulating maximum and residual displacements of RC structures: I. Accuracy. Earthq Spectra 2011;27:1187–202. doi:10.1193/1.3650479.
- [119] Yazgan U, Dazio A. Simulating maximum and residual displacements of RC structures : II. Sensitivity. Earthq Spectra 2011;27:1203–18. doi:10.1193/1.3650478.
- [120] Scott MH, Hamutcuoglu O.M. Numerically consistent regularization of force-based frame elements. Int J Numer Methods Eng 2008;76:1612–31. doi:10.1002/nme.
- [121] SeismoSoft. SeismoStruct - A Computer Program for Static and Dynamic Nonlinear Analysis of Framed Structures 2013.
- [122] McKenna F, Fenves GL, Scott MH, Jeremic B. Open System for Earthquake Engineering Simulation (OpenSees). Berkeley, California, U.S.A.: 2000.
- [123] Goodnight JC, Kowalsky MJ, Nau JM. Effect of Load History on Performance Limit States of Circular Bridge Columns. J Bridg Eng 2013;18:1383–96. doi:10.1061/(ASCE)BE.1943-5592.0000495.
- [124] Hines EM. Seismic Performance of Hollow Rectangular Reinforced Concrete Bridge Piers with Confined Corner Elements. PhD Thesis, Univ Calif 2002.
- [125] Hose YD, Seible F, Priestley MJN. Strategic Relocation of Plastic Hinges in Bridge Columns. Struct Syst Res Proj 97/05, Univ Calif 1997.
- [126] Chai YH, Priestley MJN, Seible F. Flexural retrofit of circular reinforced concrete bridge columns by steel jacketing: experimental studies. Struct Syst Res Proj 91/06, Univ Calif 1991:151.
- [127] Goodnight JC, Kowalsky MJ, Nau JM. A new look at strain limits and plastic hinge lengths for reinforced concrete bridge columns. 10th U.S. Natl. Conf. Earthq. Eng., Anchorage: 2014.
- [128] Izzuddin B, Karayannis C, Elnashai A. Advanced nonlinear formulation for reinforced concrete beam-columns. J Struct Eng 1994;120:2913–34.
- [129] De Souza R. Force-based Finite Element for Large Displacement Inelastic Analysis of Frames. PhD Diss Dep

- Civ Environ Eng Univ California, Berkeley, USA 2000.
- [130] Almeida JP, Tarquini D. SAGRES: Software for Analysis of GRadiant Effects in Structures. Progr Dev Matlab 2016.
 - [131] Goodnight JC, Feng Y, Kowalsky MJ, Nau JM. The Effects of Load History and Design Variables on Performance Limit States of Circular Bridge Columns. Volume 2: Experimental Observations. Report, Alaska Dep Transp Public Facil Res 2015;4000.
 - [132] Scott MH, Fenves GL. Plastic Hinge Integration Methods for Force-Based Beam–Column Elements. J Struct Eng 2006;132:244–52. doi:10.1061/(ASCE)0733-9445(2006)132:2(244).
 - [133] Neuenhofer A, Filippou FC. Evaluation of nonlinear frame finite-element models. J Struct Eng 1997;123:958–66.
 - [134] Goodnight JC, Kowalsky MJ, Nau JM. Modified Plastic-Hinge Method for Circular RC Bridge Columns. J Struct Eng 2016. doi:10.1061/(ASCE)ST.1943-541X.0001570.
 - [135] Menegotto M, Pinto PE. Method of analysis for cyclically loaded RC plane frames including changes in geometry and non-elastic behaviour of elements under combined normal force and bending. IABSE Symp. Resist. Ultim. Deform. Struct. acted by well Defin. repeated loads - Final Rep., 1973.
 - [136] Mander JB, Priestley MJN, Park R. Theoretical Stress-Strain Model for Confined Concrete. J Struct Eng 1988;114:1804–26.
 - [137] Dazio A, Beyer K, Bachmann H. Quasi-static cyclic tests and plastic hinge analysis of RC structural walls. Eng Struct 2009;31:1556–71.
 - [138] Park R. Ductility evaluation from laboratory and analytical testing. Proc. 9th World Conf. Earthq. Eng., 1988.
 - [139] Hines EM, Restrepo JJ, Seible F. Force-displacement characterization of well-confined bridge piers. ACI Struct J 2004;101:537–48.
 - [140] Beyer K, Dazio A, Nigel Priestley MJ. Shear deformations of slender reinforced concrete walls under seismic loading. ACI Struct J 2011;108:167–77.
 - [141] Mergos PE, Beyer K. Modelling shear-flexure interaction in equivalent frame models of slender reinforced concrete walls. Struct Des Tall Spec Build 2014;23:1171–89. doi:10.1002/tal.
 - [142] Tarquini D, Almeida JP, Beyer K. Influence of lap-splices on the cyclic inelastic response of reinforced concrete walls. II: Shell element simulation and equivalent uniaxial model. J Struct Eng 2017;143.
 - [143] SIA. SIA 162, Material tests 1989.
 - [144] Hottinger Baldwin Messtechnik GmbH (HBM). Catman Data acquisition Software. Darmstadt, Deutschland 2000.
 - [145] NDI. Optotrack certus HD, Northern Digital Inc. Waterloo, Ontario, Canada 2009.
 - [146] Ferguson PM, Breen JE. Lapped Splices for High Strength Reinforcing Bars. ACI J Proc 1965;62:1063–8.
 - [147] Chamberlin SJ. Spacing of Spliced Bars in Beams. ACI J Proc 1958;54:689–97.
 - [148] Thompson MA, Jirsa JO, Breen JE, Meinheit DF. The Behavior of Multiple Lap Splices in Wide Sections. Res Rep 154-1, Cent Highw Res Univ Texas Austin 1975:75.
 - [149] Rezansoff T, Konkankar US, Fu C. Confinement limits for tension lap splices under static loading. Can J Civ Eng 1991;19:447–53.
 - [150] Rezansoff T, Akanni A, Sparling B. Tensile Lap Splices under Static Loading : A Review of the Proposed ACI 318 Code Provisions. ACI Struct J 1993;90.
 - [151] Sagan VE, Gergely P, White RN. The behaviour and design of noncontact lap splices subjected to repeated inelastic tensile loading. Tech Rep NCEER-88-0033, Dep Struct Eng Cornell Univ Ithaca, New York 1988:164.
 - [152] Hamad BS, Mansour M. Bond Strength of Noncontact Tension Lap Splices. ACI Struct J 1997;93:1–11.
 - [153] Cairns J, Arthur PD. Strength of Lapped Splices in Reinforced Concrete Columns. ACI J Proc 1979;76:277–96.
 - [154] Pfister JF, Mattock AH. High strength bars as concrete reinforcement, part 5. Lapped splices in concentrically loaded columns. J Portl Cem Assoc Res Dev Lab 1963;5:27–40.
 - [155] Chun S, Lee S, Oh B. Compression Lap Splice in Unconfined Concrete of 40 and 60 MPa (5800 and 8700 psi) Compressive Strengths. ACI J Proc 2010;107:170–8.

-
- [156] Chun S, Lee S, Oh B. Compression Splices in High-Strength Concrete of 100 MPa (14 , 500 psi) and Less. *ACI Struct J* 2011;108:715–24.
 - [157] Askar HS. An experimental investigation on contact compression lap splice in circular columns. *HBRC J* 2016;12:137–46. doi:10.1016/j.hbrj.2014.12.002.
 - [158] Harries KA, Ricles JR, Pessiki S, Sause R. Seismic Retrofit of Lap Splices in Nonductile Square Columns Using Carbon Fiber-Reinforced Jackets. *ACI Struct J* 2006;103:874–84.
 - [159] Juntanalikit P, Jirawattanasomkul T, Pimanmas A. Experimental and numerical study of strengthening non-ductile RC columns with and without lap splice by Carbon Fiber Reinforced Polymer (CFRP) jacketing. *Eng Struct* 2016;125:400–18. doi:10.1016/j.engstruct.2016.07.019.
 - [160] Elsouri AM, Harajli MH. Seismic Repair and Strengthening of Lap Splices in RC Columns : Carbon Fiber – Reinforced Polymer versus Steel Confinement. *J Compos Constr* 2011;15:721–31. doi:10.1061/(ASCE)CC.1943-5614.0000213.
 - [161] Darwin D, Tholen ML, Idun EK, Zuo J. Splice strength of high relative rib area reinforcing bars. *ACI Struct J* 1996;93:95–107.
 - [162] DeVries RA, Moehle JP, Hester W. Lap Splice of Plain and Epoxy-Coated Reinforcements: An Experimental Study Considering Concrete Strength, Casting Position, and Anti-Bleeding Additives. Rep No UCB/SEMM-91/02 Struct Eng Mech Mater Univ California, Berkeley, Calif 1991:86.
 - [163] Treece RA, Jirsa J. Bond Strength of Epoxy-Coated Reinforcing Bars. *ACI Mater J* 1990;86:167–74.
 - [164] Cleary DB, Ramirez JA. Bond Strength of Epoxy-Coated Reinforcement. *ACI Mater J* 1992;88:146–9.
 - [165] Choi C, Hadje-Ghaffari H, Darwin D, McCabe SL. Bond of Epoxy-Coated Reinforcement : Bar Parameters. *ACI Mater J* 1992;88:207–17.
 - [166] Azizinamini A, Chisala M, Ghosh SK. Tension development length of reinforcing bars embedded in high-strength concrete. *Eng Struct* 1995;17:512–22.
 - [167] Hwang S, Lee Y, Lee C. Effect of Silica Fume on the Splice Strength of Deformed Bars of High-Performance Concrete. *ACI Struct J* 1995;91:294–302.
 - [168] Hamad BS, Machaka MF. Effect of transverse reinforcement on bond strength of reinforcing bars in silica fume concrete. *Mater Struct* 1999;32:468–76.
 - [169] Hamad BS, Itani MS. Bond Strength of Reinforcement in High-Performance Concrete : The Role of Silica Fume, Casting Position, and Superplasticizer Dosage. *ACI Mater J* 1999;95.
 - [170] Kadoriku. Study on Behavior of Lap Splices in High-Strength Reinforced Concrete Members. PhD Thesis, Kobe Univ Japan 1994:201.
 - [171] El-azab A, Mohamed HM. Effect of tension lap splice on the behavior of high strength concrete (HSC) beams. *HBRC J* 2014;10:287–97. doi:10.1016/j.hbrj.2014.01.002.
 - [172] Hamad BS, Harajli MH, Jumaa G. Effect of Fiber Reinforcement on Bond Strength of Tension Lap Splices in High-Strength Concrete. *ACI Struct J* 2001;98:638–47.
 - [173] Lagier F, Massicotte B, Charron J. Bond strength of tension lap splice specimens in UHPFRC. *Constr Build Mater* 2015;93:84–94. doi:10.1016/j.conbuildmat.2015.05.009.
 - [174] Harajli MH, Salloukh KA. Effect of Fibers on Development / Splice Strength of Reinforcing Bars in Tension. *ACI Mater J* 1998;94:317–424.
 - [175] Hassan MN, Feldman LR. Behavior of Lap-Spliced plain steel bars. *ACI Struct J* 2012;109:235–44.
 - [176] Verderame GM, Fabbrocino G, Manfredi G. Seismic response of R. C. columns with smooth reinforcement. Part I: Monotonic tests. *Eng Struct* 2008;30:2277–88. doi:10.1016/j.engstruct.2008.01.025.
 - [177] Verderame GM, Fabbrocino G, Manfredi G. Seismic response of R. C. columns with smooth reinforcement. Part II: Cyclic tests. *Eng Struct* 2008;30:2289–300. doi:10.1016/j.engstruct.2008.01.024.
 - [178] Goksu C, Yilmaz H, Chowdhury SR, Orakcal K, Ilki A. The Effect of Lap Splice Length on the Cyclic Lateral Load Behavior of RC Members with Low-Strength Concrete and Plain Bars. *Adv Struct Eng* 2014;17:639–58. doi:10.1260/1369-4332.17.5.639.
 - [179] Luke JJ, Hamad BS, Jirsa JO, Breen JE. The influence of casting position on development and splice length of reinforcing bars. Res Rep 242-1, Cent Highw Res Univ Texas Austin 1981.
 - [180] Sigrist V. Zum Verformungsvermögen von Stahlbetonträgern (On the deformation capacity of reinforced concrete

- girders, in German). Tech Report, Inst Struct Eng Swiss Fed Inst Technol Zurich, Switzerland 1995;210.
- [181] Sigrist V, Marti P. Ductility of structural concrete: A contribution. Proc. Work. Dev. EN 1992 Relat. to New Res. Results to CEB-FIP Model Code 1990, Czech Tech. Univ. Prague, Czech Republic, 211-223., 1994.
- [182] Kaufmann W. Strength and deformations of structural concrete subjected to in-plane shear and normal forces. Tech Report, Inst Struct Eng Swiss Fed Inst Technol Zurich, Switzerland 1998.
- [183] Kaufmann W, Marti P. Structural concrete: Cracked membrane model. J Struct Eng 1998;124:1467–75.
- [184] Alvarez M. Einfluss des Verbundverhaltens auf das Verformungsvermögen von Stahlbeton (Influence of bond behavior on the deformation capacity of structural concrete, in German). Tech Rep , Inst Struct Eng Swiss Fed Inst Technol Zurich, Switzerland 1998.
- [185] Muttoni A, Fernandez MR. Structures en béton. Course Notes, École Polytech Fédérale Lausanne, Switzerland 2010.
- [186] CEB. Model Code for Concrete Structures. vol. Third Ed., Paris, France: Comité Euro International du Béton; 1978.
- [187] FIP-CEB. Model Code 1990, Lausanne, Switzerland: Fédération Internationale du Béton; 1990.
- [188] Sousa R, Almeida JP, Correia AA, Pinho R. Shake Table Blind Prediction Tests: Contributions for Improved Fiber-based Frame Modelling. J Earthq Eng 2018;1–42. doi:10.1080/13632469.2018.1466743.
- [189] Feng DC, Xu J. An efficient fiber beam-column element considering flexure–shear interaction and anchorage bond-slip effect for cyclic analysis of RC structures. Bull Earthq Eng 2018;1–28. doi:10.1007/s10518-018-0392-y.
- [190] Sezen H, Setzler EJ. Reinforcement Slip in Reinforced Concrete Columns. ACI Struct J 2008;105:280–9.
- [191] Mazzoni S, McKenna F, Scott MH, Fenves GL. OpenSees command language manual 2006.
- [192] NEES@UCSD. Concrete Column Blind Prediction Contest 2010.

9 Appendix:

9.1 Implementation of the axially equilibrated displacement-based beam element in Opensees and application to dynamic analysis of structures

The axially equilibrated displacement-based element was implemented in the open source software OpenSees [122]. At present it is available as an external software library and it will be provided upon request to the author of this thesis.

The DB/ae element presents no difference in use with respect to other available nonlinear beam column elements for 2D (planar frame) analysis. The label required to call it within the software environment is ‘dispBeamColumnAxEq’². The input parameters to be defined are the same required for the ‘dispBeamColumn’ element (i.e., OpenSees label used to call classical DB element) except for the fact that the tolerance limit must be additionally explicitly defined. The latter expresses the maximum axial force unbalance accepted between different integration sections. Appropriate documentation and verification examples will be provided by the author together with the external library containing the element implementation until the DB/ae will be officially included in the software core. An appropriate documentation will be added to the software user’s manual and within the several online documentation websites.

In the following two subsections results from several models employing DB/ae elements are illustrated and discussed, both in the framework of nonlinear static and dynamic analysis. OpenSees models are also compared to the corresponding SAGRES [130] models with a two-fold objective: on the one side to validate the FE implementation and on the other to compare the computational time.

9.1.1 Nonlinear static analysis

A simple case study corresponding to a virtual 3 m cantilever column—Figure 9.1 (a)—is used to validate the implementation of the DB/ae in OpenSees. The square 200x200 mm RC section is composed by 20 concrete fibers (discretized only in the bending direction) and 12 steel fibers representing 10 mm-diameter rebars. The OpenSees material models [191] Concrete04 and Steel02 are employed for concrete and steel fibers respectively. The main material parameters are listed in Table 9.1. A single finite element with four Gauss-Lobatto integration sections is used to discretize the structural member.

Figure 9.1 (b) displays the results of three pushover analyses for three values of axial load ratios (ALR): 1%, 5%, and 10%. DB/ae elements are used in all three cases. The label OS (OpenSees) and SA (SAGRES) stand for the software used to perform the simulation. As expected, the force capacity increases with the imposed ALR while the perfect superposition between the curves for the same ALR confirms the good implementation of the DB/ae element in OpenSees.

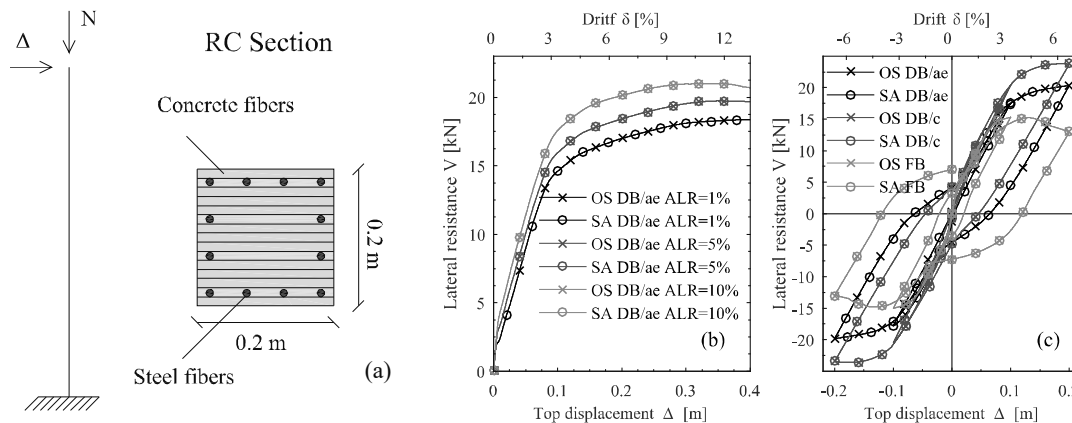


Figure 9.1: (a) Sketch of the structure and sectional discretization; Comparison between OpenSees and Sagres Models: (b) Pushover analysis for different ALR; (c) Cyclic analysis.

² It may vary once the element is officially released. Always refer to the OpenSees online guide: <http://opensees.berkeley.edu/wiki/index.php>

Table 9.1: Steel and concrete material parameters used in the OpenSees models for static analysis.

Concrete			Reinforcing steel		
f'_c [MPa]	ε_c [‰]	E_c [GPa]	f_y [MPa]	E_s [GPa]	b [‰]
40	2	30	500	200	5

Nonlinear cyclic static analyses from three models involving a single FB, DB/c and DB/ae element are compared in Figure 9.1 (c). The strongest and stiffest response is provided by the DB/c element model due to the constraints imposed in both the axial and transversal displacement fields. By imposing axial equilibrium, and thus removing the axial strain constraint, the model using one DB/ae element shows a reduction in the simulated lateral strength. However, the latter is still larger than the solution provided by the FB formulation, where no displacement fields are assigned and exact equilibrium is satisfied. Again, the fact that no difference can be seen between results from the same model but originating from different software confirms that the DB/ae is correctly implemented.

Computational time for both pushover and cyclic analyses, using the same central processing unit, are displayed in Table 9.2 showing that: (i) The performance of the DB/ae is similar to both DB/c and FB models; and (ii) The OpenSees model runs much faster than the same model in SAGRES, which is a consequence of the different programming language in which the two software were developed (C++ *versus* Matlab).

The sectional axial forces and average axial strains at all IPs were recorded during the pushover analysis (1% ALR) for both the DB/ae and DB/c element model implemented in OpenSees; they are depicted in Figure 9.2 (a) and Figure 9.2 (b). For the DB/c case, the axial forces are different in the four IPs and equal only in average to the applied axial load (12 kN). On the other hand, for the DB/ae element model the axial force is constant during the analysis in all IPs and equal to the applied external axial load. The opposite behaviour is instead observed for the generalized axial strains: they are the same in all IPs for the DB/c (the axial displacement field is constrained to be linear) while they assume different values for the DB/ae.

Table 9.2: Computational time for different models and analysis.

Model	Static		Dynamic
	Monotonic T[s]	Cyclic T[s]	T[s]
SA DB/ae	37	212	[-]
OS DB/ae	2	21	290
OS DB/c	2	18	330
OS FB	2	20	260

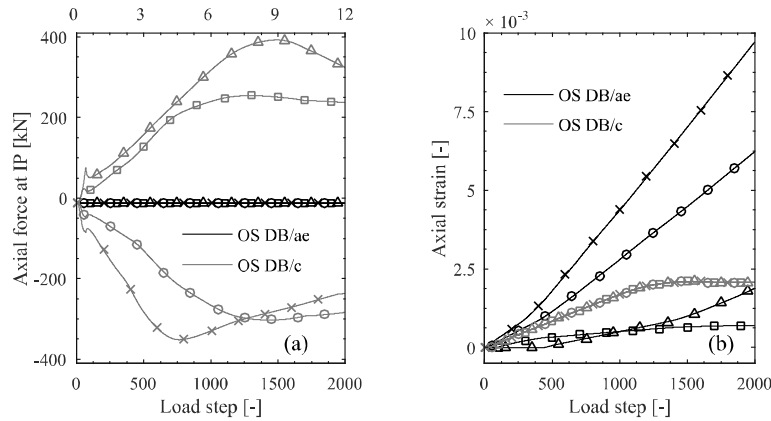


Figure 9.2: Axial force (a) and axial strain (b) evolution at all IPs for DB/ae and DB/c element models during pushover analysis with OpenSees, ALR 1%.

9.1.2 Nonlinear time history analysis

One advantage of implementing the DB/ae formulation in OpenSees is that it can be used for nonlinear time history simulations as well. Such analysis type is not available in SAGRES, which currently features only the nonlinear static analysis solver [130]. A RC column tested at the UCSD's Englekirk Structural Engineering Center in occasion of the 'Concrete Column Blind Prediction Contest 2010' [192] is used as case study. The finite element models selected to carry out the analysis discretize the structural member with a single FB, two DB/c and two DB/ae elements; the height of the bottom element is taken as twice the plastic hinge length computed according to the formula proposed by Priestley et al. [69]. This length was deemed a good estimate of the maximum height over which the plastic curvature profile intersects the elastic one, as discussed in Chapter 4. Each FE has four integration sections; different fibers are used to model cover concrete, core concrete and longitudinal reinforcing bars. The material models and respective main parameters are summarized in Table 9.3. A zero-length element is employed to simulate the strain penetration of the flexural reinforcement into the footing, as suggested by Zhao and Sritharan [115]. Tangent stiffness proportional damping (1% at the first vibration mode) is assumed and nonlinear geometrical effects are considered through the use of the corotational formulation.

The numerical *versus* experimental top displacement histories are illustrated in Figure 9.3; in order to ease the comparison the experimental results are displayed alone in Figure 9.3 (a). It can be observed that the numerical response is similar for all the considered FE models and that the match with the experimental results is reasonably good, at least up to the pulse of the fourth ground motion. After this point there is a residual displacement which is not captured by any of the considered models which causes the offset between numerical and experimental results. Finally, from the computational time viewpoint, the DB/ae model analysis (which consists of around 170000 time steps) takes around 5 minutes to run in a regular office PC, which is similar to the computing time when DB/c or FB elements were used (see Table 9.2).

Table 9.3: Steel and concrete material models and parameters used in OpenSees for dynamic analysis.

Concrete (Concrete04)					Reinforcing steel (Steel02)		
f'_c [MPa]	ϵ_c [‰]	E_c [GPa]	f'_{cc} [MPa]	ϵ_c [‰]	f_y [MPa]	E_s [GPa]	b [‰]
41.5	2.8	30	50	5.5	518	200	8

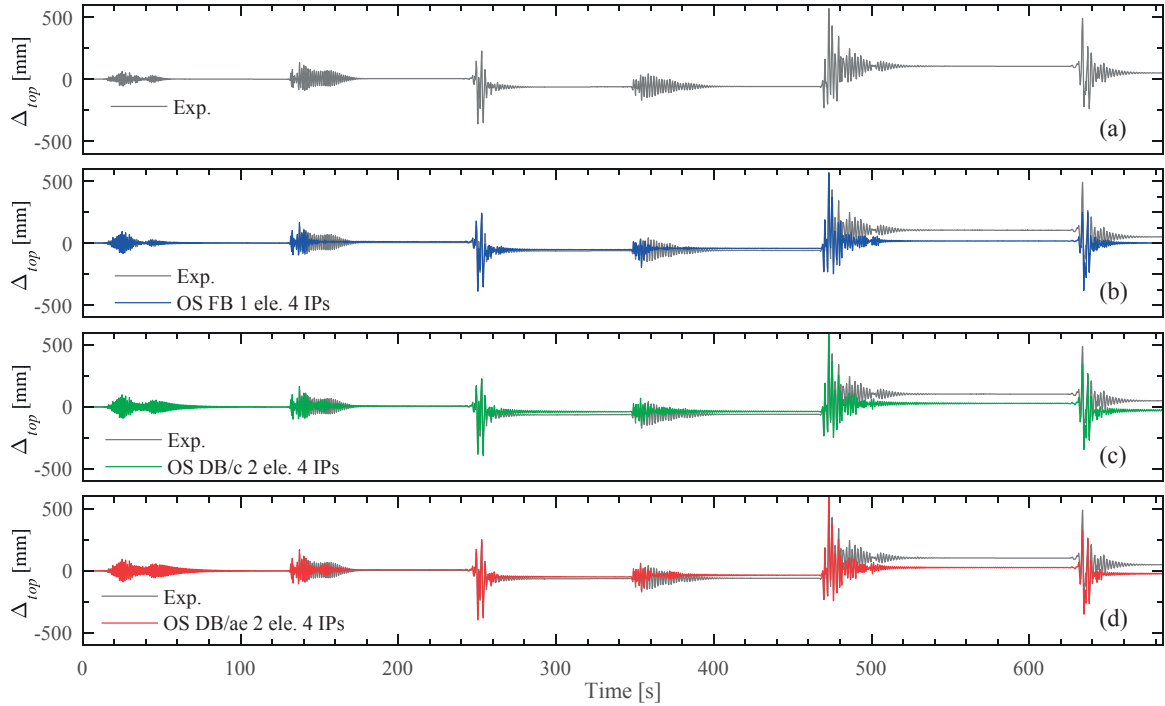


Figure 9.3: (a) Experimental top displacement time histories; Numerical *versus* experimental top displacement time histories: (b) FB; (c) DB/c; (d) DB/ae.

9.2 Mechanical interpretation and calibration of the parameter α

The discussion of the calibration process for the parameters α_1 and α_2 requires some considerations based on the observed pre-failure cracking behaviour of the test units:

- (i) In the TUs with continuous reinforcement, the width of the cracks located at the foundation and top-beam interfaces is approximately equal. Additionally, a similar width is also observed for cracks located along the member, as illustrated in Figure 6.2 (d). This implies that the contribution to the crack width due to anchorage strain penetration (w_{anc}) is, for the current test units, approximately equal to the one given by the steel-concrete slip accumulated along half of the average crack spacing distance. Note that, considering a reference TU as a tension chord [36], the width of a crack along the column height can be expressed as:

$$w = \int_{-\frac{sr}{2}}^{\frac{sr}{2}} (\varepsilon_s - \varepsilon_c) dx \quad (9.1)$$

where sr represents the average crack spacing, and ε_s and ε_c are the steel and concrete strains. On the other hand, the width of a top beam or foundation interface crack in the unit with continuous reinforcement (denoted respectively by w_{TBI} and w_{FI}) is the sum of two contributions:

$$w_{TBI} = \int_0^{l_{anc}} \varepsilon_s dx + \int_{-\frac{sr}{2}}^0 (\varepsilon_s - \varepsilon_c) dx \quad (9.2)$$

$$w_{FI} = \int_{-l_{anc}}^0 \varepsilon_s dx + \int_0^{\frac{sr}{2}} (\varepsilon_s - \varepsilon_c) dx \quad (9.3)$$

where l_{anc} is the anchorage length. The first integral term for each crack refers to the anchorage strain penetration (the concrete is assumed to be unstrained), while the second term refers to the steel-concrete slip in the column. When the anchored rebar is bent inside the foundation (such as in the current TUs), l_{anc} can be estimated as $l_{anc} = l_0 + 5\phi_l$, where l_0 is the straight anchored length [190]. From the two equations above, and building on the observation that $w \approx w_{TBI} \approx w_{FI}$ the following equation (9.4) can be derived:

$$\int_0^{l_{anc}} \varepsilon_s dx = \int_{-l_{anc}}^0 \varepsilon_s dx \approx \int_0^{\frac{sr}{2}} (\varepsilon_s - \varepsilon_c) dx = \int_{-\frac{sr}{2}}^0 (\varepsilon_s - \varepsilon_c) dx \quad (9.4)$$

It is underlined that the approximation above is not valid in general for other configurations of rebar diameters (which is the quantity that mainly governs sr) and/or anchorage configurations.

- (ii) In the TUs with lap splices, up until lap splice failure and independently of the lapped length or the confining reinforcement content, the top and bottom splice-end cracks showed a comparable width (i.e. $w_{TOP} \approx w_{BOT}$), which was also similar to cracks located outside the lapped zone (e.g. see Figure 6.2 (b)). While the latter can be expressed through equation (9.1), w_{TOP} and w_{BOT} are described by the following equations (9.5) and (9.6).

$$w_{TOP} = \int_{-\frac{sr^{ls}}{2}}^0 (\varepsilon_s^{ls} - \varepsilon_c^{ls}) dx + \int_0^{\frac{sr}{2}} (\varepsilon_s - \varepsilon_c) dx \quad (9.5)$$

$$w_{BOT} = \int_{-l_{anc}}^0 \varepsilon_s dx + \int_0^{\frac{sr^{ls}}{2}} (\varepsilon_s^{ls} - \varepsilon_c^{ls}) dx \quad (9.6)$$

where the appendix ls indicates that the quantity refers to the lap splice region. The observation above ($w_{TOP} \approx w_{BOT} \approx w$) implies that the contribution to w_{TOP} and w_{BOT} coming from the lap splice zone (w_{ls}) is approximately equal to the one due to deformations occurring above ($w_{TOP,out}$) or below ($w_{BOT,out}$) the lapped region:

$$w_{ls} = \int_0^{\frac{srml^s}{2}} (\varepsilon_s^{ls} - \varepsilon_c^{ls}) dx = \int_{-\frac{srml^s}{2}}^0 (\varepsilon_s^{ls} - \varepsilon_c^{ls}) dx \approx w_{TOP,out} = \int_0^{\frac{srml}{2}} (\varepsilon_s - \varepsilon_c) dx \approx w_{BOT,out} = \int_{l_{anc}}^0 \varepsilon_s dx \quad (9.7)$$

Given a similar crack spacing within and outside the lap-splice region ($srml^s \approx srml$), which was observed in the experimental tests, equation (9.7) turns into equation (9.4). In other words the rebar steel strain integral (slip) along $srml^s$ of the splice loaded-end contributing to the end crack width (w_{ls}) is similar to the slip provided by a continuous bar ($w_{TOP,out}$) along $srml$. This fact ($w_{ls} \approx w_{TOP,out}$) is not surprising since at a lap splice end the entire load is carried by a single bar while the contiguous cut-off rebar is unloaded.

- (iii) Within the lapped region, horizontal cracks cross the spliced rebars that do not share the same amount of stress. In each pair, one bar is more stressed than the other; from equilibrium considerations, the stress sum has to equal the input stress at each rebar loaded end. If bond is degraded by the more stressed bar (with eventual stress loss), causing slip and crack opening, the less stressed rebar is forced to accommodate the increased crack width [35] and take over the eventual stress shed by the companion bar. The crack width, which results from the slip accumulation over both crack edges, is thus governed by the more stressed bar of the pair.

From the considerations (i) and (ii) above, a relation $\alpha_1 \approx \alpha_2 \approx 0.5$ can be expected for the present TUs. A validation was performed by comparing Δ_{proc} , as computed according to the procedure of subsection 6.4.1, with the displacement Δ_{int} obtained by integrating, along the lap splice length, the envelope of the top and bottom anchored rebar strains (i.e. equation (9.8)) for the case depicted in Figure 6.4 (c)).

$$\Delta_{int} = \varepsilon_{TE} \cdot l_E + \varepsilon_{AB}^{TA} \cdot l_{0,AB} + \varepsilon_{BC}^{TA} \cdot l_{0,BC} + \varepsilon_{CD}^{TA} \cdot l_{0,CD} + \varepsilon_{DE}^{BA} \cdot l_{0,DE} + \varepsilon_{EF}^{BA} \cdot l_{0,EF} + \varepsilon_{BE} \cdot l_E \quad (9.8)$$

The strain envelope (black thick line in Figure 6.4 (c)) is used in view of consideration (iii) and it is computed by means of the optical markers directly glued on the spliced rebars, see Figure 6.4 (b) and (c). The displacement Δ_{int} includes contributions from the splice-end strains (ε_{BE} and ε_{TE}), which, due to the unavailability of a measurement point, were retrieved from the experimental (monotonic) steel stress-strain law. The input quantity to the constitutive law was the bar-loaded-end stress, derived from the global imposed axial force N (Figure 6.4 (c)). A simplified constant integration weight $l_E = 12.5$ mm was associated to both strains ε_{BE} and ε_{TE} , roughly corresponding to half the distance between the closest LED and the end crack. As the largest deformations occurred at the lap-ends, neglecting the contribution due to ε_{BE} and ε_{TE} would result in a significant underestimation of Δ_{int} , especially for imposed displacement demands beyond yielding of the longitudinal reinforcement.

Although from a theoretical viewpoint Δ_{int} is the measure best representing the pure lap splice deformation, it was comparatively more difficult to obtain than Δ_{proc} because: (i) the detachment of one or more markers glued on the spliced rebars was more likely than the detachment of those glued on the concrete; and (ii) after the failure of the first lap splice the calculation of the steel stresses at the lap loaded end was highly unreliable. In fact, they depended on the unknown residual force carried by the failed lap splices as well as on the force redistribution between the still-holding splices. Note that, due to the reduced steel stiffness, after rebar yielding any miscalculation of the rebar stress would yield large differences in the estimated strain. For the cases in which the calculation of Δ_{int} was indeed possible, the validation of the assumption $\alpha_1 \approx \alpha_2 \approx 0.5$ was carried out and is depicted in Figure 6.4 (d).

CURRICULUM VITAE – DANILO TARQUINI

Address : Rue de la Paix 27, 1020 Renens (VD), Switzerland
E-mail : daniilo.tarquini@epfl.ch
Mobile : +41 78 6407337
Nationality : Italian **Date of birth :** 24/06/1986



EDUCATION

DEGREES	2014 – 2019	Ph.D. in Earthquake Engineering and Structural Dynamics <i>École Polytechnique Fédérale de Lausanne (EPFL), Lausanne, Switzerland.</i>
	2012 – 2014	2nd Level Master Degree in Earthquake Engineering and Engineering Seismology <i>ROSE School programme, Institute for Advanced Studies IUSS, Pavia, Italy.</i> Scholarship (tuition fee waiver) winner, awarded on curriculum basis.
	2005 – 2011	B.S. and M.Sc. with honors in Civil and Environmental Engineering <i>University of Perugia, Perugia, Italy</i> Scholarship (tuition fee waiver) winner, awarded on curriculum basis.
TRAINING COURSES	2016 – 2017	Four semester courses: • Modélisation numérique des solides et structures • Effective communication for research engineers • Scientific programming for engineers • Optimization and simulation. <i>EPFL, Lausanne, Switzerland.</i>
	03.2014	One-week intensive course (40 hours): Seismic Analysis of Tall Buildings. <i>UME Graduate School, Pavia, Italy.</i>

RESEARCH-RELATED EXPERIENCE

PROJECTS	2016 – 2019	Research project, EPFL, Lausanne, Switzerland. Project title : ‘Modelling the seismic response of RC bridge piers with lap splices in the plastic hinge region’. Funded by <i>FEDRO</i> Switzerland. Main tasks : • Development of mechanical and finite element models to simulate the response of RC members • Advanced numerical modelling of RC structures • Experimental cyclic testing of RC members. Teaching : • Three-times teaching assistant for the Master course ‘ <i>Nonlinear Finite Element Analysis</i> ’ • Co-supervisor of 7 Master projects. Software development : • Implementation of a user-element in the FE software for seismic analysis OpenSees (C++) • Developer of the FE Software SAGRES (Matlab/ Python): re-structuring and extension of the software solver.
	06.2014 – 09.2014	Research internship, Iowa State University (ISU), Ames, USA. Project title : ‘Investigation on the design specifications of wall-type bridge piers in the US seismic guidelines’ Main tasks : • Assessment of the appropriateness of US codes specifications with respect to the design of wall-type bridge piers • Detailed FE modelling of squat RC walls • Proposal of new guidelines for design requirements.

PROFESSIONAL EXPERIENCE

2011 – 2012	Structural Engineer <i>Studio di Ingegneria di Santucci Egidio, Montappone (FM), Italy.</i> Main tasks : • Assessment, planning and retrofit of two masonry buildings • Structural design of a 4-storey RC residential building • Drafting of metric preliminary calculations
-------------	---

SKILLS

LANGUAGES	Italian : Mother tongue; English : C1; French : C1; German : A2.
COMPUTER	Programming Languages : Matlab, C++, Python; FE softwares : OpenSees, Abaqus, Diana, SAP2000, SeismoStruct; CAD : Autocad, SolidWorks; Others : Microsoft Office, Adobe Illustrator, Adobe Photoshop.

ADDITIONAL INFORMATION

EXTRACURRICULAR ACTIVITIES	2010 – 2014	Vice-President and co-founder of the youth association ‘Il Cilindro’ (organization of sport tournaments, group trips and musical events);
	2009 – 2013	Council member of the town of Montappone (FM), Italy.
SPORTS AND INTERESTS	Bouldering (regular bi-weekly practice), climbing, mountaineering, skiing, football (semi-professional player for 10 years), table tennis, chess (member of a chess club).	

PUBLICATIONS

JOURNAL PAPERS	<u>Tarquini D.</u> , Almeida J.P., Beyer K., (2019). <i>Mechanical model for simulating the response of RC wall boundary elements with lap splices</i> . ACI Structural Journal (under submission).	
	<u>Tarquini D.</u> , Almeida J.P., Beyer K., (2019). <i>Experimental investigation on the deformation capacity of lap splices under cyclic loading</i> . Bulletin of Earthquake Engineering (under review).	
	<u>Tarquini D.</u> , Almeida J.P., Beyer K., (2018). <i>Uniaxial cyclic tests on reinforced concrete members with lap splices</i> . Earthquake Spectra (accepted for publication).	
	<u>Tarquini D.</u> , Almeida J.P., Beyer K., (2017). <i>Axially equilibrated displacement-based beam element for simulating the cyclic inelastic behaviour of RC members</i> , Earthquake Engineering and Structural Dynamics 46 (9)	
	<u>Tarquini D.</u> , Almeida J.P., Beyer K., (2017). <i>Influence of lap splices on the deformation capacity of RC walls II: Shell element simulation and equivalent uniaxial model</i> , ASCE Journal of Structural Engineering 143 (12)	
	Almeida J.P., Prodan O., <u>Tarquini D.</u> , Beyer K., (2017). <i>Influence of lap splices on the deformation capacity of RC walls I: Database assembly, recent experimental data, and findings for model development</i> , ASCE Journal of Structural Engineering 143 (12)	
	Almeida J.P., <u>Tarquini D.</u> , Beyer K., (2017). <i>Modelling approaches for inelastic behaviour of RC walls: multi-level assessment and dependability of results</i> , Archives of Computational Methods in Engineering 23 (1)	
CONFERENCE PROCEEDINGS	<u>Tarquini D.</u> , Almeida J.P., Beyer K., (2018). <i>Experimental investigation on the behaviour of lap splices under uniaxial cyclic loading</i> . 16th ECEE, Thessaloniki, Greece.	
	<u>Tarquini D.</u> , Almeida J.P., Beyer K., (2017). <i>Axially equilibrated displacement-based beam element: implementation in OpenSees and application to dynamic analysis of structures</i> . COMPDYN 2017, Rhodes, Greece.	
	<u>Tarquini D.</u> , Almeida J.P., Beyer K., (2017). <i>An enhanced displacement-based element to account for tension shift effects</i> . 16th World Conference On Earthquake Engineering, Santiago, Chile.	
	<u>Tarquini D.</u> , Almeida J.P., Beyer K., (2016). <i>Elemento de viga baseado em formulação de rigidez enriquecido com funções de forma adaptativas para garantir equilíbrio axial</i> . Congresso Nacional de Sismologia e Engenharia Sísmica, Ponta Delgada, Portugal.	
	<u>Tarquini D.</u> , Almeida J.P., Beyer K., (2014). <i>From plastic hinge to shell models: recommendations for RC wall models</i> . 2nd European Conference on Earthquake Engineering and Seismology, Istanbul, Turkey.	
	<u>Tarquini D.</u> , Almeida J.P., Beyer K., (2014). <i>Adequabilidade de deformações locais como parâmetro na avaliação sísmica de paredes de betão armado</i> . Congresso Nacional de Sismologia e Engenharia Sísmica, Lisbon, Portugal.	

